Ultrasound-mediated transport of nanoparticles and the influence of particle density

Harriet Elizabeth Lea-Banks
Magdalen College

Supervisors
Professor Constantin C. Coussios
Professor Eleanor Stride

January 2018

A thesis submitted for the degree of Doctor of Philosophy

Abstract

Cancer therapeutics are limited in efficacy by poor penetration into tumour tissue. This doctoral thesis aims to explore how changing the density of a therapeutic could influence its ultrasound-mediated delivery and penetration depth, thereby testing the hypothesis that increasing particle density increases penetration depth of nanoparticles under ultrasound exposure. Density-enhanced transport in the presence of ultrasound-induced cavitation is studied utilising a combination of numerical simulations, *in vitro* and *in vivo* experimental models.

The penetration depth of nanoparticles of different densities was first predicted using a computational model to assess the magnitude of acoustic and fluid dynamic forces on a spherical nanoparticle in the presence or absence of a cavitating microbubble. This simulation showed that a denser particle will be transported further when exposed to ultrasound. Furthermore, cavitation was identified as fundamental for enhanced transport, with forcing due to microstreaming dominating the transport behaviour. These predictions were validated and supported experimentally using an *in vitro* model, where a fivefold increase in particle density resulted in a 43 % increase in peak particle penetration depth.

To form a closer analogue to the tumour environment, a three-dimensional flow-vessel phantom was then implemented, where the penetration depths of three density-contrasting nanoparticles with unique fluorescent tags – co-delivered with either a micro- or a nano-scale cavitation agent – were studied. A trend between nanoparticle density and extravasation depth was again discernible, with the densest particles penetrating the furthest. However, the choice of cavitation agent often had a greater influence on particle transport.

Finally, experiments were performed in a tumour-bearing mouse model, where the bio-distribution of fluorescent nanoparticles was assessed after ultrasound exposure. A bistatic HIFU setup was used to activate cavitation agents, and passive acoustic mapping was implemented to detect cavitation activity within the tumour site. Density-contrasting fluorescent nanoparticles were used as mock therapeutics, and were successfully detected in *ex vivo* tumours through IVIS imaging. However, due to experimental limitations, the influence of nanoparticle density on ultrasound-mediated drug delivery *in vivo* could not be determined, and so recommendations are made for how the hypothesis can be further validated.

Statement of Originality

I hereby declare that this submission is my own work and, to the best of my knowledge, it contains no materials previously published or written by another person, or substantial proportions of material which have been accepted for the award of any other degree or diploma at the University of Oxford or any other educational institution, except where due acknowledgement is made in the thesis.

Any contribution made to the research by others, with whom I have worked at the University of Oxford or elsewhere, is explicitly acknowledged in the thesis.

I also declare that the intellectual content of this thesis is the product of my own work, except to the extent that assistance from others in the project's design and conception or in style, presentation and linguistic expression is acknowledged.

Harriet Lea-Banks

November 2017

Acknowledgements

This thesis would not have been possible without the kind support of so many people. I would like to thank the Engineering and Physical Sciences Research Council for sponsoring my doctoral studentship. I am grateful to my supervisors for entrusting me with this research, for supporting me through the successes and failures of the project, and for their pivotal role in my journey from student to researcher. My heartfelt gratitude goes to the BUBBL team, for all their assistance and countless discussions over coffee (at least some of which were about science). Particular thanks go to Prof. Robert Carlisle, Dr Christophoros Mannaris, Sheena Wallington, Megan Grundy and Jamie Wallis who made Chapter 4 possible, as well as to Dr Boon Teo and Dr Luca Bau for teaching chemistry to an engineer. I would like to thank Jane Clark, my dyslexia support tutor, for teaching me how to read and write all over again. For patient listening and ceaseless encouragement, I thank my parents. And finally, I thank my husband, for his kindness and support, restoring my sense of perspective time after time.

Statement of Contributions

I gratefully acknowledge the following who contributed to this doctoral research.

Chapter 2

- **Dr Boon Teo**: Supported implementing and trouble-shooting nanoparticle fabrication procedure and characterisation.
- **James Fisk**: Fabricated agarose cylindrical phantom.

Chapter 3

- **Dr Boon Teo and Dr Luca Bau**: Supported establishing protocol for fabrication of fluorescently labelled density-modified nanoparticles, including selection of fluorophores.
- **Dr Christophoros Mannaris and Megan Grundy:** Designed agarose vessel phantom.
- **James Fisk:** Fabricated agarose vessel phantom.
- **Graham Brown:** Offered confocal microscopy training and support in establishing correct fluorescence filters for detecting labelled density-modified nanoparticles.

Chapter 4

- **Dr Luca Bau**: Supported establishing protocol for fabrication of fluorescently labelled biocompatible density-modified nanoparticles, and for advice on stability study procedure.
- **Megan Grundy:** Operated the IVIS throughout this chapter – *in vitro*, *in vivo* and *ex vivo* imaging.
- **Prof. Robert Carlisle:** Performed all inoculations for mice used in the study.
- **Jamie Wallis:** Cultured the cell line used in the inoculations, performed tumour sizing, culling and tumour excising.
- **Dr Christophoros Mannaris:** Operated bistatic HIFU setup for all *in vivo* exposures.
- **Sheena Wallington:** Performed cannulations and injections for all *in vivo* treatments.

Dissemination

Peer-Reviewed Journal Publications

Lea-Banks, H., Teo, B., Bau, L., Stride, E. and Coussios, C.C., *'Bespoke fluorescent density-modified nanoparticles: Fabrication and characterisation of a nanoscale tool for pharmacokinetic studies'* (in preparation)

Lea-Banks, H., Mannaris, C., Stride, E. and Coussios, C.C., '*Delivering density-modified nanoparticles with ultrasound: A comparison between micro- and nano-scale cavitation nuclei*' (in preparation)

Mannaris, C., Grundy, M., Bau, L., Gray, M., **Lea-Banks, H.**, Seth, A., Carlisle, R., Stride, E. and Coussios, C.C., *'Investigation of ultrasound exposure parameters for extravasation and drug delivery using submicron cavitation nuclei'*, Ultrasound in Medicine and Biology (in review)

Lea-Banks, H., Teo, B., Stride, E. and Coussios, C.C., *'The effect of particle density on ultrasound-mediated transport of nanoparticles'*, Physics in Medicine and Biology, 2016, 61(22), 7906.

Conference Presentations

Lea-Banks, H., Mannaris, C., Grundy, M., Stride, E.P. and Coussios, C.,. *'Enhanced delivery of a density-modified therapeutic using ultrasound: Comparing the influence of micro-and nano-scale cavitation nuclei'*, The Journal of the Acoustical Society of America, 2017, 141(5), 4011-4011.

Coussios, C., Myers, R., Kwan, J., **Lea-Banks, H.**, Mo, S., Grundy, M., Mannaris, C., Duffy, M., Paverd, C., Carugo, D. and Coviello, C., '*Cavitation-mediated extravasation and transtumoral drug delivery by microstreaming: What role do the gas nuclei and the physical properties of the therapeutic play?*', The Journal of the Acoustical Society of America, 2016, 140(4), 2985-2985.

Lea-Banks, H., Stride, E. and Coussios, C.C., *'Ultrasound-mediated transport of nanoparticles and the influence of particle density'*, The Journal of the Acoustical Society of America, 2016, 139(4), 2093-2093.

Prizes

Best Student Paper Award for Biomedical Acoustics for the paper '*Ultrasound-mediated transport of nanoparticles and the influence of particle density*', 171st Meeting of the Acoustical Society of America, Salt Lake City, Utah, May 2016.

Contents

List of figures

List of tables

Acronyms and abbreviations

Ad	Adenovirus
AMCA	AMCA-X, SE (6-((7-amino-4-methylcoumarin-3-acetyl)amino)hexanoic acid, succinimidyl ester)
ANOVA	Analysis of variance
Au	Gold
AuNP	Gold nanoparticle
BALB/c	Albino laboratory mouse
BSA	Bovine serum albumin
CAPIR	Circulation, accumulation, penetration, internalisation and release
CT26	Murine colon carcinoma cell line
Cy5	Cyanine-5 fluorescent dye
Cy5-AuNP	Cyanine-5 labelled gold nanoparticle
Cy5-PEG-NHS	Cyanine-5 labelled polyethylene glycol (2000 Da) with NHS ester
Cy5-PEG-SH	Cyanine-5 labelled polyethylene glycol (2000 Da) with thiol group
Cy5-PSNP	Cyanine-5 labelled polystyrene nanoparticle
DAQ	Data acquisition
DI	Deionised
DiI	1,1'-Dioctadecyl-3,3,3',3'-Tetramethylindocarbocyanine Perchlorate ('DiI'; $DiIC_{18}(3)$) fluorescent dye
DLS	Dynamic light scattering
DMF	N,N-Dimethylformamide
DMSO	Dimethyl sulfoxide
DPPG.Na	Dipalmitoylphosphatidylglycerol sodium
DSPC	Distearoyl-phosphatidylcholine
EPR	Enhanced permeability and retention
FITC	Fluorescein isothiocyanate
GFP	Green fluorescent protein
HCl	Hydrochloric acid
HIFU	High-intensity focussed ultrasound
iNC	Inactive NanoCups
IVIS	*In Vivo* Imaging System
mPEG-NHS(SC)	Succinimidyl polyethylene-glycol (2000 Da) with NHS ester
mPEG-SH	Polyethylene-glycol (2000 Da) with thiol group
$NaHCO_3$	Sodium bicarbonate

NC	NanoCups
NH_2	Amine group
NTA	Nanoparticle tracking analysis
PAM	Passive acoustic mapping
PCD	Passive cavitation detection
PDA	Poly-dopamine
PDA-Au	Poly-dopamine coated gold nanoparticle
PDA-PS	Poly-dopamine coated polystyrene nanoparticle
PDA-SiO_2	Poly-dopamine coated silica nanoparticle
PdI	Polydispersity index
PEG	Polyethylene glycol
PIFE	Protein induced fluorescence enhancement
PRF	Pulse repetition frequency
PS	Polystyrene
PSNP	Polystyrene nanoparticle
PVP	Polyvinylpyrrolidone
RFP	Red fluorescent protein
RITC	Rhodamine B isothiocyanate
ROI	Region of interest
SF_6	Sulphur hexafluoride
SiO_2	Silica
SV	SonoVue®
TEM	Transmission electron microscopy
Tris	Tris(hydroxymethyyl) aminomethane
US	Ultrasound
Zp	Zeta potential

Symbols

c	Speed of sound
f	Acoustic frequency
F_{AR_1}	Primary acoustic radiation force
F_{AR_2}	Secondary acoustic radiation force
F_{D_1}	Acoustic streaming force
F_{D_2}	Microstreaming force
F_y	Yield stress force
I	Acoustic intensity
k	Effective viscosity
L_{ms}	Microstreaming boundary layer
m	Effective particle mass
m_{added}	Added mass
m_p	Particle mass
p	Pressure
p_0	Hydrostatic pressure
P_a	Acoustic pressure
p_g	Gas pressure
p_l	Liquid pressure
p_v	Vapour pressure
p_σ	Laplace pressure
q_s	Rate of temperature change
r	Initial particle location
R	Instantaneous bubble radius
$\dot{R}$	Bubble radial velocity
$\ddot{R}$	Bubble radial acceleration
R_0	Equilibrium bubble radius
$R_{break-up}$	Break-up bubble radius
$R_{buckling}$	Buckling bubble radius
$R_{ruptured}$	Rupture bubble radius
R_p	Particle radius
t	Time
u_1	Acoustic streaming velocity
u_2	Microstreaming velocity

V	Volume
v_p	Particle velocity
z_p	Penetration distance
α	Attenuation
γ	Ratio of specific heats
δ_p	Particle penetration depth
δ_v	Viscous penetration depth
κ	Polytropic gas exponent
κ_s	Shell surface viscosity
λ	Wavelength
μ	Dynamic viscosity
μ_L	Liquid viscosity
ρ_L	Liquid density
ρ_p	Particle density
σ	Surface tension
σ_{water}	Surface tension of water
χ	Elastic compression modulus
ω	Acoustic angular frequency

Chapter 1: **Literature Review and Research Objectives**

1.1 Drug Delivery for Cancer Therapy

1.1.1 Pharmacological Cancer Therapies

In the treatment of cancer, systemic administration of cytotoxic drugs is often favoured when, in addition to the primary tumour, there is a high chance of metastatic disease elsewhere in the body. Pharmacological cancer therapies may be used in isolation, before or after surgery, or during and complementary to non-invasive therapies. Many anti-cancer drugs target fast-growing cells such as cancer cells, bone marrow cells, cells in the digestive system and hair follicles. Since healthy cells are also damaged during treatment, use of these therapeutics may lead to a number of side effects, most commonly a weakened immune system, nausea and hair loss. Hence, there are significant ongoing efforts to facilitate targeted drug delivery for cancer, with the aim of both reducing systemic dose and enhancing therapeutic efficacy.

There has been a recent trend in new cancer therapeutics towards multi-functional particles for increased accumulation and penetration, as well as biological agents, such as viruses and antibodies, for selective targeting. In this review, a summary of current challenges and proposed solutions for enhancing drug delivery will be discussed. Conclusions will be drawn about the persistent barriers to cancer treatment and the pathways to enhanced delivery that appear most promising.

1.1.2 Challenges in Oncological Drug Delivery

'Cancer cells break the most basic rules of cell behaviour' (Alberts *et al.* 2008); because of this, a single cell mutation can lead to years of treatment, suffering and eventually death.

However, in identifying these cellular rules and understanding why cancer cells are so successful in invading healthy tissue, growing awareness of cancer physiology is aiding the development of new oncological drug delivery techniques which attempt to overcome the barriers to effective delivery.

The challenges in oncological drug delivery are three-fold: (1) the chaotic and irregular nature of the tumour environment, (2) the high interstitial fluid pressure within a dense extracellular matrix, and (3) the increased distance between a viable cell and the nearest blood vessel.

Firstly, the chaotic architecture associated with a cancerous tumour is a characteristic that stems from the initial genetic mutation and is facilitated by the rapid growth (Carmeliet *et al.* 2000). Angiogenesis is the process whereby cancerous tumours encourage new blood vessels to form and feed the growing tumour. However, this process is rapid and erratic, resulting in leaky and poorly organised vessel structures, with a wide range of capillary diameters (table 1.1). Poorly organised vasculature throughout the tumour results in a patchwork of perfused and oxygenated, and non-perfused and hypoxic tissue. Designing drug delivery systems that function effectively in this heterogeneous environment is a challenge.

Table 1.1 *Vascular dimensions in healthy human tissue and primary human tumour tissue (values taken from [*]Baronzio 2009 and [†]Jain 1987).*

	Healthy human tissue	*Primary human tumour*
Capillary diameter	5 – 10 µm[*]	5 – 80 µm[*]
Volume of interstitial space	3 – 20 %[†]	6 – 40 %[†]
Endothelium pore size	20 nm[*]	2 µm[*]
Interstitial pressure	0 – 6 mmHg[*]	25 – 30 mmHg[*]

Secondly, the tumour environment displays high interstitial fluid pressure (table 1.1). In healthy tissue, pressure is regulated by an equilibrium of incoming fluid and outgoing fluid, through the vascular and lymphatic supplies. However, in cancerous tissue the lack of viable

lymphatic vessels results in limited lymphatic drainage. A build-up of fluid results in high intratumoral pressure, providing a high resistance for drug molecules leaving the vasculature which limits successful drug delivery (Bae *et al.* 2013).

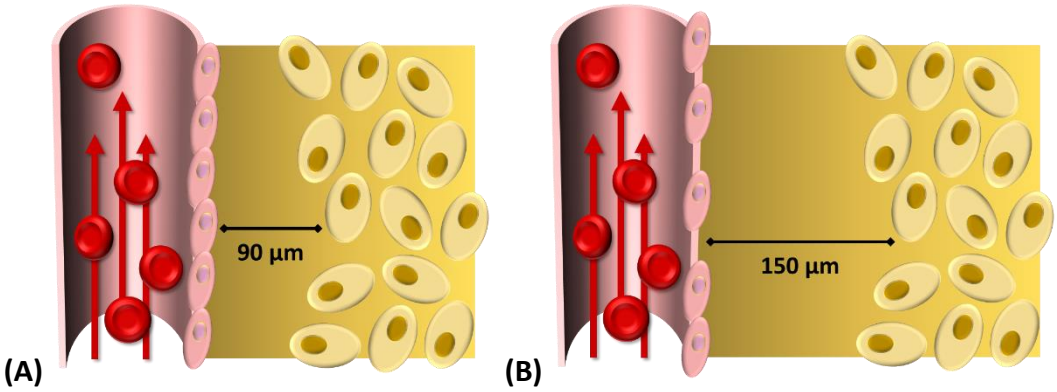

Figure 1.1 *An illustration of a blood vessel lined with endothelial cells, separated from the surrounding tissue cells by interstitial space in* ***(A)*** *healthy tissue and* ***(B)*** *diseased tissue.*

Thirdly, cancerous tissue exhibits increased interstitial space, meaning the space separating the vasculature from the surrounding tissue cells is substantially larger than in healthy tissue. Baronzio *et al.* (2009) describe how the increase in interstitial space, from 90 µm in healthy tissue to 150 µm in cancerous tissue, means drug particles have a greater distance to travel from vessel to tumour tissue, further increasing the difficulty of drug delivery (figure 1.1).

This pressurised and heterogeneous environment is often described as presenting 'drug barriers' (Baronzio *et al.* 2009). To overcome the barriers to drug delivery posed by cancerous tumours, two types of solution – pharmacological and mechanical – have been explored and are discussed in the following sections.

1.1.3 Pharmacological Approaches to Enhancing Drug Delivery

Although the tumour is a challenging environment, several pharmacological approaches for enhancing drug delivery have been developed. To combat the fast clearance and low

specificity of free drug molecules, emerging delivery methods have sought to encapsulate small molecular therapeutics inside nanoscale drug-carriers, including the use of lipid shells known as liposomes. In designing a drug carrier there are several characteristics that must be considered, including size, shape, and surface charge; ability to target antibodies or blood vessels; and capacity to integrate a release mechanism (Jain *et al.* 2010).

Quantifying the success of a delivery mechanism requires an understanding of the full pharmacokinetic process. One example of a cascade used to assess the success of a drug delivery system is known as CAPIR – circulation, accumulation, penetration, internalisation and release (Sun *et al.* 2014). The five stages of the CAPIR cascade describe the journey of a therapeutic agent from injection to treatment. Firstly, the lifetime of the therapeutic within the blood circulation must be sufficient to accumulate at the target site before being cleared through various filtration and immune clearance mechanisms. Secondly, the accumulation of the therapeutic at the target site must be sufficient for a therapeutic effect. This may be achieved using a targeting mechanism, such as tuning the drug size to escape through the leaky vasculature, or surface modifications. Thirdly, the drug construct needs to escape the confines of the blood vessel and penetrate into the surrounding tumour tissue. Once in the target tissue, the drug construct may need to be internalised by the cell to induce cell death, and once internalised release the therapeutic payload. This cascade illustrates that it is not enough simply to have a long circulation time and good accumulation; without the drug penetrating into the tissue, treatment will not be successful. It can thus be used in the assessment of drug delivery strategies.

Notwithstanding the usefulness of the CAPIR cascade, there exist a number of limitations. If the therapeutic in question is a virus, circulation, accumulation and penetration remain important factors. However, the virus binds to receptors on the outside of cancer cells,

negating the need to internalise the whole agent or to release any kind of drug payload. Rather, genetic material from the bound virus enters the cell, before viral replication and rupturing of the cell; after which, the replicated viruses escape and bind to the next cancer cell. It should also be noted that the steps in this cascade are not necessarily sequential; for example, ThermoDox (see section 1.3.1) releases doxorubicin from a liposomal shell when heated, and therefore does not require internalisation before release, but rather releases the payload into the interstitial fluid surrounding the target cells, where the free doxorubicin is internalised by the cell. Nevertheless, although consideration of the specific application is required, the CAPIR cascade is often helpful for assessing the likely efficacy of a therapeutic construct.

The first set of pharmacological approaches to enhance drug delivery aim to exploit the enhanced permeability and retention (EPR) effect by optimising particle size. The origin of the EPR effect is two-fold: firstly, the leaky vascular associated with tumours allows nanometre-sized therapeutics to pass from blood vessels into surrounding tissue; then secondly, the nanoagents are retained in the surrounding tumour tissue since drainage is prevented by the lack of viable lymphatic vessels. The combined effect of easy exit from the vasculature and retention in surrounding tissue allows drug particles, designed within a specific size distribution, to accumulate through the natural effect of EPR. Optimising particle size to be delivered through the EPR effect is one form of passive targeting (Lammers *et al.* 2012). The size-dependent transportation exhibited by nanoparticles *in vivo* has been confirmed through fluorescent imaging studies (Popović *et al.* 2010): a mouse xenograft model was used to show particles of hydrodynamic diameter 12 nm penetrated far deeper into the surrounding tumour tissue than those of 125 nm. In current medical practice, Doxil (PEGylated liposomal doxorubicin) is one example of a clinically approved nanomedicine that exploits passive targeting, fabricated at 87 nm diameter to fall within an optimal range (Soundararajan *et al.*

2009) – large enough to achieve prolonged circulation and small enough to leak through the pores in the vasculature. A clarifying summary is provided by Jain *et al.* (2010) who describes endothelial pore sizes in tumour blood vessels as spanning 200 nm – 2 μm, depending on the tumour type and stage of growth. As an illustrative example, a 90 nm particle accumulates in the perivascular space, but is not able to penetrate the dense extracellular matrix.

Multistage nanoparticles are a creative solution currently being developed to overcome the contrasting size limitations within the pharmacokinetic journey of a nanoparticle (Wong *et al.* 2011). Using a nanoparticle that is initially at a size of 100 nm which degrades overtime to 10 nm allows the particle to be at optimal size for delivery in each location – namely large enough to remain in the vascular and prolong circulation (100 nm), and then small enough to penetrate into cancerous tissue when at the target site (10 nm).

However, it has been suggested that the magnitude and significance of the EPR effect is often exaggerated, with some arguing that it is such a heterogeneous effect, varying in both an inter- and intra-subject fashion, that drawing conclusions about its value as an effective delivery mechanism is inherently limited (Lammers *et al.* 2012). Moreover, this phenomenon has largely been studied in animal models, where the tumour has been grown specifically for scientific study and its growth rate is much more rapid than for a human patient, causing increased leaky vasculature and a greater EPR effect. For these reasons Lammers *et al.* (2012) conclude that the EPR effect is 'overrated' and should not be relied on for human drug delivery. A recent study by Wilhelm *et al.* (2016) emphasises this point. Using a multivariate analysis approach and by compiling results from 232 data sets produced over the last 10 years, the group ascertained that regardless of the size, shape, material, targeting strategy and zeta potential of the nanoparticle drug-carrier, less than 1 % (median) of drug is successfully delivered to the target site. Not only does this lead to sub-therapeutic doses,

increasing the likelihood of drug resistance, it also implies that over 99 % of the injected dose interacts with healthy tissue, increasing the risk of toxicity and side-effects. Furthermore, the study concluded that the choice of cancer model often had the greatest influence on the level of delivery efficiency.

An alternative pharmacological approach is known as vascular normalisation. As previously mentioned, the growth of tumour vasculature is governed by angiogenesis and is inherently disorganised and leaky in its structure and composition. Vascular normalisation aims to bring order to the vascular architecture, regulating the distribution of vessels to be closer to that in normal tissue before administering the cancer therapeutic (Goel *et al.* 2012, Baronzio *et al.* 2009). This is a pharmacological approach which uses antiangiogenic agents – namely drugs that block the signalling protein VEGF (vascular endothelial growth factor) – so that well-organised blood vessels can grow, with better perfusion and lower interstitial fluid pressure (Jain 2013).

Vascular normalisation has been shown to be advantageous for the delivery of small molecule therapeutics, through the reduction of interstitial fluid pressure within the tumour. However, restoration of the vasculature leads to pores in the leaky vessels becoming smaller, ultimately preventing larger nanoscale therapeutics from passing through. Therefore, although normalisation has been shown to increase accumulation, enhanced penetration and distribution away from vessels is yet to be proven, with some studies suggesting an inhibitory effect that prevents the delivery of nanoparticles (~100 nm) (Chauhan *et al.* 2012).

Yet another approach utilises the targeting and binding ability of ‘reprogrammed’ viruses to selectively infect cancerous cells (Cattaneo *et al.* 2008, Alberts *et al.* 2008). One example of oncolytic virotherapy uses an adenovirus to exploit cancer-cell-specific receptors, which

enables binding and subsequent particle internalisation. Once the viral DNA has been internalised by the cell nucleus, viral replication takes place. Cellular death may then occur as the replicating viruses burst the cell membrane and escape – a death mechanism known as cellular lysis. However, cancer cells are not unique in all surface proteins expressed, and the potential for a biological therapeutic to inadvertently infect healthy cells is a possible risk (Russell *et al.* 2007). Further investigation is needed to fully understand the pharmacokinetics of oncolytic viruses, as well as an ability to accurately quantify the proportion of successfully infected cancerous cells and the proportion of virus left circulating in the body.

Each of these pharmacological or biological approaches aims to exploit the characteristics of the host environment. However, all are united by a common limitation of poor delivery and low penetration depth. To overcome this limitation, pairing pharmacological techniques with device-based approaches has been explored and is discussed below.

Finally, it should be acknowledged that the efficacy of targeting therapeutics and delivery strategies will ultimately be limited if the target site lacks vascularity. Section 1.1.2 described the heterogeneous and chaotic nature of the tumour blood vessels, and without sufficient perfusion the delivery of therapeutics is inherently limited.

1.1.4 Device-Based Approaches to Enhancing Drug Delivery

Engineering techniques are also being developed to enhance drug delivery, often alongside pharmacological approaches. These device-based approaches utilise a variety of energy sources, such as electromagnetic radiation, magnetic fields and sound. Device-based approaches can be broadly categorised as either invasive or minimally/non-invasive.

Invasive techniques for drug delivery by definition require the skin barrier to be breached. Two common examples of invasive device-based approaches to enhance drug delivery are internal radiotherapy and microwave ablation. These treatments are given alongside chemotherapy to induce enhanced cellular uptake of the therapeutic. For modalities that implement microwaves, high-energy x-rays and gamma rays, the associated wavelength is very short (on the order of micrometres, nanometres and picometres respectively), leading to high attenuation and a shallow penetration depth. These methods have shown promise for cancers in superficial locations, such as rectal cancer, cervical cancer and superficial bladder cancer (NICE 2007). However, the invasive implanting of radioactive materials is often required for cancers located deeper than superficial sites, a treatment known as brachytherapy. Rupturing the skin can be detrimental, causing patient discomfort and an increased risk of infection; therefore, finding non-invasive alternatives is desirable.

Examples of non-invasive device-based approaches to enhance drug delivery include external radiotherapy, magnetic targeting and photodynamic therapy. In contrast to its invasive and internal counterpart, external radiotherapy is a relatively painless procedure, utilising a linear accelerator to transmit beams of electrons into the body, to collide with and terminate cancer cells (Brahme 1987). Alongside software developments for treatment planning, advances in beamforming using multileaf collimators have been shown to improve the accuracy of radiation delivery (Powlis *et al.* 1993). However, limitations in accuracy still persist, and patient movement, respiration movement and drift of external markers may lead to erroneous delivery of radiation to healthy tissue.

A second non-invasive device-based technique is magnetic targeting (Veiseh *et al.* 2010), a method achieved by incorporating iron oxide nanoparticles into liposomal structures. The magnetic drug-carrier may then be attracted to the target site using an external magnet.

However, this method is depth-limited and heavily dependent on the magnetic field gradient. Although this technique has shown positive results in small rodent models, questions remain about the field strength required to achieve useful penetration distances in larger mammals or humans (Dobson 2006). Furthermore, a compromise is needed in particle size: larger magnetic drug-carriers have a greater drug-loading capacity and stronger magnetic attraction, but have also been found to aggregate more rapidly, forming clumps that can no longer penetrate through tissue. Therefore, although magnetic targeting is able to enhance accumulation of therapeutics, penetration is limited depending on tumour location and magnet strength (Sunderland *et al.* 2006).

Table 1.2 *Penetration depths into tissue for different modalities.*

Modality	**Penetration depth**	
Light	0.5 – 2 cm	(Dougherty *et al.* 1998)
Microwave therapy	2 – 4 cm	(Brace 2010)
Radiotherapy	Up to 5 cm	(Gazda *et al.* 2001)
Ultrasound	Up to 30 cm	(Chan *et al.* 2011)

Thirdly, light may also be used to instigate cancerous death. Photochemotherapy or photodynamic therapy, a term made common by Dougherty (1984), utilises a chemical agent to induce photosensitivity in cancer cells. Once cells are in a photosensitive state, an infrared light source, often administered through a fibre optic catheter, may be applied to cause cellular death (Lammers *et al.* 2012). However, cellular death is only possible in regions where sufficient levels of light energy are achieved. This approach is therefore depth-limited, since infrared light is readily absorbed through tissue. As with magnetic targeting, the advantages of this device-based approach are very dependent on tumour location; it is most effective for superficial sites where the required penetration depth is minimal (table 1.2).

A common limitation uniting these techniques of radiotherapy, microwave therapy, magnetic targeting and photodynamic therapy, is treatment depth (see table 1.2). Returning to the CAPIR cascade, many of these depth-limited techniques perform well in accumulation, showing clear increased dosage, but remain limited in penetration which caps the effectiveness of treatment (Dougherty *et al.* 1998, Brace 2010, Gazda *et al.* 2001). A possible solution to this problem is the use of ultrasound. This non-invasive, low-cost modality allows for simultaneous delivery and monitoring (Coussios and Roy 2008). Although attenuation by tissue is still a concern with high-frequency sound waves, transducer design and beamforming algorithms are able to achieve a variety of focal lengths, optimised for the depth and location of each target site.

For optimal transmission, ultrasound requires an acoustically homogeneous medium, i.e. one in which the acoustic impedance is consistent throughout. This modality is limited therefore by the presence of tissue/bone or tissue/air interfaces, where a sudden change in acoustic impedance is encountered. Increasing the transmitted ultrasonic intensity may help to achieve the required intensity at the target, but potential adverse effects such as heating or cavitation in the pre-focal path become more likely at higher intensities.

1.2 Physical Principles of Ultrasound

Ultrasound can enhance drug delivery through both mechanical and thermal effects. In order to gain an understanding of how these effects are mediated, a brief literature review of the key physical principles is presented.

1.2.1 Wave Propagation, Attenuation, Absorption and Scattering

As an acoustic wave passes through a medium, particles are displaced locally, generating regions of high and low density and pressure, known respectively as compressional and

rarefactional regions. In soft tissue ultrasound propagates primarily as longitudinal compressional waves, i.e. particles are displaced parallel to the direction of wave propagation. Ultrasound is defined as having a frequency greater than 20 kHz (the approximate upper threshold of human hearing). As ultrasound propagates through a medium, energy can be lost in two ways: through absorption and/or through scattering. Absorption occurs as a result of viscous dissipation in the medium and molecular relaxation processes, and thus, in general, increases with increasing frequency (Goss *et al.* 1980). Absorption converts acoustic energy into heat.

By contrast, scattering occurs when a propagating acoustic wave encounters a region of varying acoustic impedance that causes deviations in the direction of energy propagation (Rayleigh 1896). In doing so, the amplitude of the wave is attenuated along the original direction of propagation without acoustic energy being converted into heat. The way in which an acoustic scatterer embedded in the medium will alter the sound field is dependent on its acoustic impedance and size. If the wavelength of the incident propagating wave is significantly smaller than the size of the scatterer, geometric scattering is exhibited. If the wavelength of the incident propagating wave is significantly larger than the size of the scatterer, Rayleigh scattering is exhibited. The microbubbles used in clinical applications (diameter range 1 – 10 μm) in diagnostic ultrasound conditions (frequency range 0.2 – 20 MHz) act as Rayleigh scatterers (Leighton 1994), since they are substantially smaller in diameter than the wavelength of the highest frequencies used (i.e. 74 μm).

1.2.2 Acoustic Radiation Force and Acoustic Streaming

As discussed above, a propagating acoustic wave will be attenuated and induce a pressure field (p) as it travels through a medium. The effect of the resulting pressure gradient $(\vec{\nabla}p)$

across a finite volume (V), induces a force upon that volume in the direction of propagation, known as the primary acoustic radiation force (F_{AR_1}) and defined by:

$$F_{AR_1} = V\vec{\nabla}p \tag{1.1}$$

If a body is immersed in a fluid and subject to an acoustic field, that body will experience both acoustic and hydrodynamic forces. The absorption of momentum generates a net motion of the surrounding fluid known as acoustic streaming. This will also produce a force (F_{D_1}) on a body of finite volume (V) immersed in the fluid, which can be related to the velocity of acoustic streaming (u_1) and fluid viscosity (μ_L) through the following relationship (Beyer 1974):

$$F_{D_1} = -V\mu_L\nabla^2 u_1 \tag{1.2}$$

In degassed, stationary fluid, the equations describing the forces on a body due to acoustic radiation (1.1) and streaming (1.2) are adequate to approximate the driving forces acting on a suspended nanoparticle in an acoustic field. However, when microbubbles are introduced to enhance transport, additional forces must be noted, namely the secondary acoustic radiation force and those produced by microstreaming.

1.2.3 Ultrasound-Induced Cavitation and Microstreaming

The term cavitation is used to describe a variety of bubble-related phenomena – from the nucleation of a bubble in a champagne glass, to the violent bubble collapse responsible for propeller pitting. In the following manuscript the term cavitation will be used to refer to the response and oscillation of micro- and nano-scale bubbles to ultrasonic excitation.

Cavitation activity is a complex phenomenon, and dependent upon the properties of the bubble, the surrounding fluid and the incident acoustic field. Pre-existing gas/vapour bubbles undergo volumetric oscillations when exposed to ultrasound as a result of the fluctuating

pressure field. Figure 1.2 shows a cross-section through a bubble, illustrating the hydrostatic pressure in the surrounding fluid (p_0), the Laplace pressure resulting from surface tension (p_σ) and the acoustic pressure at the bubble wall (P_a), all acting inwards towards the bubble centre. In opposition, the gas pressure (p_g) and vapour pressure (p_v) act outwards from the bubble centre. As the liquid pressure in the surrounding fluid rises and falls due to the propagating sound wave, the bubble dynamically responds to equate internal $(p_g + p_v)$ and external pressure terms $(p_0 + p_\sigma + P_a)$.

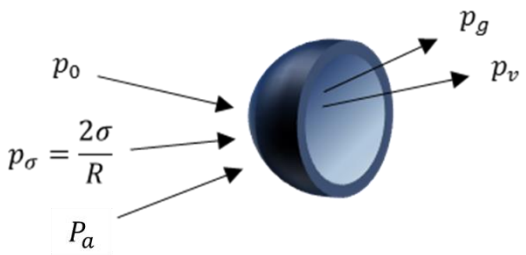

Figure 1.2 *Bubble cross-section illustrating external and internal pressure terms (adapted from Leighton 1994).*

Over the last century several individuals have looked to describe cavitation behaviour mathematically. One of the most widely used expressions was developed by Rayleigh and Plesset in 1960 (Plesset 1960). This expression describes the relationship between the acoustic force, liquid inertia and bubble radial response. Later contributions by Neppiras and Noltingk (1950, 1951) and Poritsky (1952) account for liquid viscosity and surface tension, forming what is now widely referred to as the Rayleigh-Plesset equation (equation 1.3). This non-linear second-order differential equation is able to describe the bubble response for radial excursions that are relatively slow and small compared to the equilibrium radius. It can be seen from equation 1.3 that the Rayleigh-Plesset model considers one spatial dimension and therefore assumes axisymmetric spherical expansion and collapse. The Rayleigh-Plesset model assumes that the liquid is incompressible.

$$R\ddot{R} + \frac{3\dot{R}^2}{2} = \frac{1}{\rho_L}\left(\left(p_0 + \frac{2\sigma}{R_0} - p_v\right)\left(\frac{R_0}{R}\right)^{3\kappa} + p_v - \frac{2\sigma}{R} - \frac{4\mu\dot{R}}{R} - p_0 - P_a(t)\right) \quad (1.3)$$

However, as the acoustic wavelength (λ) tends to the bubble radius (R) it can no longer be assumed that the whole bubble experiences the same pressure; rather, one part of the bubble may experience compressional pressure while another part experiences rarefactional (Leighton 1994). In this scenario the bubble no longer pulsates with spherical symmetry, but begins to exhibit surface modes.

Furthermore, as the bubble responds more violently, and radial velocity $(\dot{R})$ tends to the speed of sound (c), liquid compressibility becomes important. To account for this limitation, in 1980, Keller and Miksis developed an expression for bubble oscillations of large amplitude (equation 1.4). Here, they were able to account for compressibility in the surrounding fluid and were therefore no longer limited to relatively slow and small amplitude bubble expansion.

$$\ddot{R} = \left(\frac{1}{2}\dot{R}^3 + \dot{R}\Delta(R) - c\left(\frac{3}{2}\dot{R}^2 + \frac{4\mu\dot{R}}{\rho_L R} + \frac{2\sigma}{\rho_L R} - \Delta(R)\right) + R\dot{R}\Delta'(R) + \left(1 + \frac{\dot{R}}{c}\right)\frac{P_a(t)c}{\rho_L}\right)\left(\frac{4\mu}{\rho_L} - R(\dot{R} - c)\right)^{-1}$$
$$\text{where } \Delta(R) = \left(\left(p_0 + \frac{2\sigma}{R_0}\right)\left(\frac{R_0}{R}\right)^{3\kappa} - p_0\right)\rho_L^{-1} \quad (1.4)$$

Since all bubbles used clinically require a stabilising coating, they cannot technically be described as free bubbles. Therefore further models have been developed to describe the influence of surface coatings – additional damping (viscosity) and stiffness terms, as well as non-linear surface tension dependent on the instantaneous bubble radius have been added. Marmottant (2005) describes the behaviour of a coated bubble using a modified Rayleigh-Plesset model through three different regimes, namely buckling, elastic and rupture states

(equation 1.5). The relative importance of these coatings in a therapeutic regime will be described further in chapter 2.

$$R\ddot{R} + \frac{3\dot{R}^2}{2} = \frac{1}{\rho_L}\left(\left(p_0 + \frac{2\sigma(R_0)}{R_0}\right)\left(\frac{R_0}{R}\right)^{-3\kappa}\left(1 - \frac{3\kappa}{c}\dot{R}\right) - \frac{2\sigma(R)}{R} - \frac{4\mu\dot{R}}{R} - \frac{4\kappa_s\dot{R}}{R^2} - p_0 - P_a(t)\right)$$

$$\text{where } \sigma(R) = \begin{cases} 0 & if\ R \le R_{buckling} \\ \chi\left(\frac{R^2}{R_{buckling}} - 1\right) & if\ R_{buckling} \le R \le R_{break-up} \\ \sigma_{water} & if\ ruptured\ and\ R \ge R_{ruptured} \end{cases} \quad (1.5)$$

Cavitation thresholds and detection

Throughout the following chapters cavitation activity will broadly be separated into two categories: inertial and non-inertial cavitation. Inertial cavitation (first termed 'transient') was defined by Flynn (1975) as the dynamic behaviour of a bubble when controlled by the inertial forces of the surrounding fluid during the contraction phase of an oscillatory cycle. In contrast, non-inertial cavitation is dominated by the pressure forces.

When detecting cavitation experimentally, acoustic emissions may be recorded using an ultrasonic transducer, and can be analysed to assess magnitude, duration and type of cavitation activity. Violent bubble collapse associated with inertial cavitation produces characteristic broadband emissions due to shockwave formation – a phenomenon short in the time domain but broadband in the frequency domain. In contrast, non-inertial cavitation produces harmonic emissions. The source of these harmonic emissions is associated with two key sources of nonlinearity: firstly the nonlinear oscillations of the bubble (as seen in the nonlinear equations 1.3 and 1.4 of Rayleigh-Plesset and Keller-Miksis discussed previously), and secondly the nonlinear relationship between the incident pressure field and the radiated pressure field produced by the bubble. Chapter 3 will examine whether these cavitation emissions can be used as a predictor of therapeutic delivery.

Furthermore, as the incident ultrasonic wave propagates through the lossy medium, it may undergo nonlinear distortions. Nonlinearity in the incident pressure field will lead to harmonics in the pressure incident on the bubble. Nonlinear distortion of the incident field becomes increasingly likely at higher pressures, higher frequencies and longer propagation distances. Careful frequency filtering and choice of 'passive cavitation detector' (section 2.3.1) can help to distinguish between nonlinearity from cavitation and nonlinearity from the incident field.

Microstreaming

Volumetric pulsations of a bubble transfer momentum to the surrounding fluid inducing motion termed microstreaming. Whether stably oscillating or transiently collapsing, acoustically excited bubbles have the potential to induce substantial movement in the surrounding fluid, which in turn imparts momentum to nearby structures.

In the case of a stably non-inertially cavitating microbubble, acoustically driven microstreaming originates in a narrow layer of fluid around the surface of the oscillating bubble. This region is defined as the microstreaming boundary layer and has a thickness described by $L_{ms} = \sqrt{2\mu/\rho_L \omega}$ (Landau and Lifshitz 1987). For a microbubble suspended in water responding to a 0.5 MHz acoustic excitation, this boundary is found to be 0.8 μm in thickness. As the expression suggests, this value becomes even smaller for increased frequencies, following an inverse power law trend.

This phenomenon can be observed experimentally. The original experimental observations performed by Elder (1959), consisted of both acoustic and optical measurements taken to assess microstreaming velocities under a variety of low amplitude exposures. Microstreaming close to the surface of the bubble was shown to induce 'inner vortices' within a thin layer, as

defined by the microstreaming boundary layer (L_{ms}). Through high shear stresses, these inner vortices have the potential to drive larger 'outer vortices' that rotate in the opposite direction, and are responsible for fluid circulation over distances that can be large compared to the bubble and experimentally observed (Tho *et al.* 2007). However it should be noted that the original observations by Elder (1959) studied semi-spherical bubbles adhered to a rigid surface. In a clinical context microbubbles exhibit both pulsation and translational motion, which many of the later models take into account (Davidson *et al.* 1970, Longuet-Higgins *et al.* 1997).

Several attempts have been made to derive numerical expressions to describe microstreaming behaviour. Of note is the 1996 publication by Wu and Du, which describes the microstreaming produced by a single air bubble in water, and generated theoretical predictions in agreement with the aforementioned experimental observations by Elder (1959). A more versatile numerical model is derived by Doinikov *et al.* (2010), who states that the Wu and Du model only applies to very low fluid viscosities (less than that of water) and that this leads to a severe underestimate of microstreaming velocities. However, it should be noted that currently there is no mathematical model for microstreaming that truly captures nonlinear bubble behaviour across a full excitation spectrum, including large-amplitude expansion.

1.3 Ultrasound-Enhanced Drug Delivery for Cancer

Ultrasonic waves can be used to enhance drug delivery through mechanical and/or thermal effects. Three key mechanisms have been shown to promote drug delivery: (1) triggered release, (2) increased cellular uptake and (3) enhanced extravasation and tissue penetration.

Firstly, triggered release aims to optimise dosage by delivering the drug encased in micro-scale capsules, to be deposited at the target site. A liposome is one example of a drug carrier

that may be designed to open and release the therapeutic payload under certain conditions, such as a specific pH environment, when heated above a chosen threshold (Needham *et al.* 2001) or as a result of mechanical damage through cavitation (Pitt *et al.* 2004). However, an important compromise in the design of liposomal capsules is that of size. The liposome must be small enough to extravasate from the vasculature into the tumour, but large enough that the payload capacity is sufficient to deliver a cytotoxic dosage (Lammers *et al.* 2012).

Secondly, ultrasound has been shown to enhance cellular uptake (Delalande *et al.* 2013). Once the therapeutic has reached a cancerous cell, exposure to ultrasound can increase the permeability of cellular membranes, allowing the therapeutic to traverse the membrane and enter the cell. The opening of cellular membranes in the presence of ultrasound is known as sonoporation and has been shown to facilitate a high therapeutic dosage inside cells. Different mechanisms of sonoporation are associated with different acoustic regimes: low intensity ultrasound (producing non-inertial cavitation) is thought to induce endocytotic uptake, whilst high intensity ultrasound (producing inertial cavitation) is thought to induce cytoplasmic uptake (Lentacker *et al.* 2010) (section 1.3.2). The same phenomenon may be seen across tissue membranes, where the permeability of groups of cells is altered, such as the blood brain barrier (Hynynen *et al.* 2005). However, relatively little is known about the exact biological effects induced by opening membranes and altering permeability. For example, the blood brain barrier exists to prevent the entry of toxic materials, and so removing this barrier has the potential to leave healthy cells vulnerable to toxins. Minimising the duration of enhanced permeability may prove to be important in protecting healthy tissue.

Thirdly, ultrasound has also been found to enhance the transport of free drug molecules. The penetration depth of conventional therapeutics that are injected into the blood stream may be enhanced by acoustically driven microbubbles (Arvanitis *et al.* 2011, Mo *et al.* 2012).

Micrometre-sized gas-filled bubbles were originally developed as ultrasonic imaging contrast agents. The presence of acoustically excited microbubbles is able to increase the penetration depth of therapeutics into the surrounding tissue through a combination of dynamic phenomena, primarily acoustic radiation forces and microstreaming.

1.3.1 Heat-Mediated Drug Delivery by Ultrasound

As described previously, ultrasonic waves have the ability to induce localised heating. Heating is also associated with long acoustic pulse lengths or continuous wave excitation. In a high duty cycle regime there is little time for cooling to occur, resulting in the build-up of a thermal region. Therefore the time-averaged intensity is a helpful measure when predicting heating. The heat deposited by ultrasound may be described in terms of the source power density (or rate of heat transfer per unit volume) (q_s), from an ultrasonic plane wave of frequency (f) and local acoustic intensity (I), travelling through a medium with frequency-dependent attenuation (α) (purely defined by absorption), as (Pierce 1981):

$$q_s = 2\alpha(f)I \tag{1.6}$$

The Pennes bioheat transport equation (Pennes 1948) relates this power density to heating through the consideration of the heating caused by the source (in this application due to ultrasound), and cooling from convection, perfusion, conduction and energy storage.

By exploiting the heating generated by acoustic absorption, thermal effects can enhance drug delivery. Triggered release may be achieved using thermosensitive liposomes, lipid capsules that release their therapeutic payload under specified thermal conditions. A key example of this technique is found in the liposomal encapsulation of doxorubicin. Known originally as lyso-thermosensitive liposomal doxorubicin (LTLD), LTLD is now commercially available as ThermoDox® and is the first clinically approved thermosensitive liposomal form of

doxorubicin. The first evidence of ultrasound-mediated release of ThermoDox® was identified (Dromi *et al.* 2007) by comparing thermosensitive and non-thermosensitive liposomes in a murine *in vivo* model. Pulsed HIFU was used to induce hyperthermia within the tumour region, activating the ThermoDox®, releasing doxorubicin and inducing an enhanced therapeutic effect when compared to the non-thermosensitive carrier.

A further study by Staruch *et al.* (2012) confirmed that applying a hyperthermia-activated shell increases circulation time and accumulation of the therapeutic at the target site. Not only does a larger construct avoid clearance mechanisms, like the immune system and filtration through the liver, encapsulating the active drug also prevents off-target interactions with healthy tissue, which results in a larger percentage of the dose arriving intact and active at the target site. By administering LTLD compared to free doxorubicin, using an *in vivo* rabbit model, the group were able to achieve a 26.7-fold enhancement in drug delivery with thermosensitive liposomal doxorubicin in heated tumours, showing both increased local concentration and enhanced penetration.

However, necrosis due to cytotoxic dosage was not the only form of cellular death exhibited in the Staruch (2012) study. To reach temperatures sufficient to activate the drug-carrying liposomes, high levels of thermal energy are required, often inducing inadvertent tissue damage. Therefore accurate, real-time monitoring techniques were deemed to be required during hyperthermia treatments (Hynynen *et al.* 1993). A number of monitoring techniques for hyperthermia exist. Firstly the use of an interstitial probe to monitor tissue temperature during treatment provides a low-cost and widely available solution. However this technique is invasive and requires the skin barrier to be breached. Interstitial probes for measuring heating are also associated with limited accuracy. Hynynen *et al.* (1989) explored the influence of temperature sensing probes on distortions in the acoustic field and temperature

measurement errors. Distortions in the ultrasound field were found to be dependent on probe size, whilst temperature measurement errors were apparent even for the smallest probes and dependent on additional probe features, such as their material and orientation. To mitigate heating artefacts a non-ultrasound-absorbing coating around the sensor is recommended, as well as orientating the probe parallel to the ultrasound beam.

Secondly, a superior solution for monitoring tissue temperature during treatment may be achieved using magnetic resonance imaging (MRI) (Le Bihan *et al.* 1989). MR imaging-derived temperature information is spatially localised, allowing a temperature map to be produced that is free from artefacts caused by implanted temperature probes. Furthermore, this technique is non-invasive, avoiding unnecessary pain and keeping the skin barrier intact. However, MRI is expensive and not widely available. The technology also suffers from sensitivity to patient movement and has poor performance when detecting temperature changes in fatty tissue (McDannold *et al.* 2004).

Overall, heat-mediated drug delivery is a promising technique and has now been implemented in preliminary clinical trials (Lyon *et al.* 2017). Clinical translation of this technique has been achieved, albeit without MR thermometry or particularly precise temperature monitoring, with very promising results. However, challenges for clinical adoption are threefold. Firstly the need to encapsulate a therapeutic in a thermal-sensitive casing requires modification of the therapeutic. Secondly, many modern biological therapeutics, such as viruses and antibodies, are not stable or do not survive in heated environments. Thirdly, MR-guided hyperthermia is a costly and lengthy procedure, the technology for which is currently only available in a few centres worldwide.

1.3.2 Mechanical Enhancement of Drug Delivery by Ultrasound

As an alternative to heating tissue, forces produced by the mechanical effects of ultrasound may be exploited for enhanced drug delivery. As previously discussed, the acoustic radiation force occurs due to a pressure gradient across a volume, such that when an object is placed in an acoustic field, a driving force is experienced. This effect is true for microbubbles and drug-carriers (Dayton *et al.* 1999, Zhao *et al.* 2004), where the applied driving force is able to push therapeutics deeper into the target site. In addition to the acoustic radiation force, a drug carrier is also acted upon by fluid forces generated by acoustically driven microbubbles. The fluid motion generated by microstreaming induces circulation patterns around the oscillating bubble, imparting momentum to the nearby particle and enabling transport from the vasculature, through the endothelium, and into surrounding tissue.

These mechanical effects may also be paired with triggered release and sonoporation. Just as radiation forces and cavitation may be exploited to move a drug particle, so too can these forces be used to split open a liposome or degrade a micelle, delivering the therapeutic payload. Nelson *et al.* (2002) have shown how using an encapsulated chemotherapeutic, when delivered using low-frequency ultrasound, leads to significant tumour response. In a study of 42 rodent models, 70 kHz ultrasound was used to successfully enhance the efficacy of treatment, assessed through a reduction in tumour volume compared to controls which did not receive ultrasound. This enhanced treatment was attributed to ultrasound activating the release of doxorubicin from the micelle. However, no adequate monitoring or measuring systems were in place during treatment to verify this. More recently a cavitation-sensitive liposome was developed by Graham *et al.* (2014) and used to deliver luciferin in a murine tumour model. The liposome was co-delivered with SonoVue® microbubble contrast agent, which when excited with ultrasound provided the cavitation trigger for release of the liposome payload. This mechanism was demonstrated using passive cavitation detection (see

section 1.3.3), where inertial cavitation was found to be a necessary requirement for the release of luciferin.

Similarly, sonoporation may also be attributed to these mechanical effects. There are competing schools of thought on the true underlying physical and biological mechanisms of sonoporation. One hypothesis is that the shearing forces provided by nearby cavitating bubbles encourage gaps within biological membranes to open. These gaps have been shown to be sufficient in size to allow drug molecules to enter. *In vitro* studies have shown correlation between acoustic pressure, the number of cells with increased permeability, and the duration of increased permeability (Lammertink *et al.* 2015). However, only very limited inferences about drug delivery in humans may be drawn from *in vitro* experiments. Microbubble-cell membrane interactions may be substantially different when in flow conditions, as experienced in the vasculature, primarily because the interactions between a stationary cell and a bubble entrained in flow can be fleeting.

Ultrasound has the ability to move and excite bubbles, which in turn can trigger the release of drugs from bubble-like capsules (*triggered release*), or open pores in cells and tissue membranes (*sonoporation*). However, these mechanical effects, and the biological phenomena they trigger, are still not fully understood.

1.3.3 Enhanced Particle Transport

This thesis is primarily concerned with the transportation of therapeutics from the vasculature and their penetration into tissue. Particle transport using ultrasound has been studied in a variety of applications, from acoustic levitation – suspending particles of various sizes, shapes and densities in a standing wave field (Brandt 2001, Xie *et al.* 2002) – to sorting cells – utilising

ultrasound in microfluidic devices to separate cell types (Johansson *et al.* 2009, Franke *et al.* 2010).

In the 2010 study by Rifai *et al.* the delivery of a macromolecule, a dye-labelled protein used as a model drug, was enhanced using ultrasound and cavitation in an obstructed bifurcated vessel phantom. Cavitation was induced using hydrophobic talc microparticles and monitored acoustically in real time. The use of passive cavitation detection (PCD), first implemented for biomedical frequencies (where cavitation could not be heard by ear) by Atchley *et al.* (1988), is now widely used for monitoring bubble activity in many branches of biomedical acoustics, from established techniques such as lithotripsy (Coleman *et al.* 1992, Cleveland *et al.* 2000), to emerging fields such as opening the blood-brain barrier (McDannold *et al.* 2006).

Rifai *et al.* (2010) aimed to implement this technique for monitoring drug delivery *in vitro*. The final volume of deposited macromolecules was measured optically and correlated to the acoustic emissions. It was found that in the presence of cavitation nuclei the transport of macromolecules was significantly enhanced. Furthermore, acoustic emissions, associated with inertial cavitation activity (i.e. broadband emissions), were found to correlate strongly with the amount of delivered macromolecule. To understand the mechanisms behind this enhanced transport, the author describes how the transport behaviour indicates a convective rather than a diffusive mechanism, since there was seen to be a clear boundary between regions where the macromolecule was in high and low concentration. Furthermore, since broadband emissions where strongly correlated to delivery, inertial cavitation was identified as the dominant mechanism for the enhanced convective mixing.

Ultrasonic enhancement has also been studied for the delivery of oncolytic adenoviruses (Arvantis *et al.* 2011, Bazan-Peregrino *et al.* 2012, 2013) – viruses which possess the ability to

selectively infect cancerous cells, and are over 100 nm in diameter, several orders of magnitude larger than the macromolecules used by Rifai *et al.* (2010) previously described. Ultrasound-enhanced delivery of adenoviruses was first explored *in vitro* using a cell-embedded vessel phantom and luciferase-expressing adenovirus, with the primary aim of identifying the ultrasound exposure parameters (peak negative pressure, pulse repetition frequency and duty cycle) required to induce non-inertial and inertial cavitation respectively (Arvantis *et al.* 2011). The highest pressure regime, where inertial cavitation was most prominent, was found to induce the greatest luciferase expression whilst still being biologically safe, as assessed through cell viability studies.

Building on this, in the 2013 study by Bazan-Peregrino *et al.*, enhanced delivery of a virus was achieved in an *in vivo* murine model by co-injecting the adenovirus and a microbubble contrast agent, where targeting and penetration depth of the virus into the tumour was enhanced upon exposure to ultrasound. Passive cavitation monitoring was implemented to record acoustic emissions and, in agreement with the previous *in vitro* study, acoustic emissions (specifically broadband emissions) were found to correspond to enhanced delivery of the construct. However, no direct correlation was found between the magnitude of acoustic emissions and the number of viral particles delivered. The author emphasises that lack of spatial information associated with the acoustic emissions is a key limitation, whereby the emissions are effectively integrated over the detection focus. Since the tumour contains a heterogeneous vessel structure, the distribution of cavitation agents is also poorly spread, leading to regions of high and low cavitation activity, something that it is not possible to detect using the single element PCD.

To enhance circulation time within the body and tumour targeting ability, polymer stealthing of adenoviruses has also been investigated (Carlisle *et al.* 2013). It has been shown that

coating the oncolytic adenovirus in a specifically developed polymer enables it to travel to the target site without being identified and removed by the body's immune system. By increasing circulation half-life in this manner and supplementing delivery with microbubble-nucleated inertial cavitation, the group demonstrated for the first time that it is possible to deliver oncolytic viruses to distances in excess of 100 µm, and up to 180 µm, from the nearest blood vessel. This milestone is significant as the farthest distance that a live cancer cell can lie from vasculature has been shown to be 150 µm (Jain 1987). For a self-amplifying therapeutic such as a virus, this increased transport distance of a few particles might be sufficient for effective treatment. However, for non-amplifying therapeutics, achieving delivery at a therapeutic concentration at these greater penetration depths in tumour tissue remains a barrier.

The first observation that density could have an impact on ultrasound-enhanced particle transport in the context of drug delivery was published by Mo *et al.* (2015), who combined the technique of polymer stealthing adenoviruses (Ad-PEG) with a surface coating of gold nanoparticles. When tested *in vivo*, the gold-coated viral nanoagent was found to accumulate over one hundred times more effectively in the target tumour when compared to the accumulation of the bare adenovirus. Using this method the combined advantages of long circulation half-life, specificity in targeting cancer cells and enhanced penetration depth were achieved.

A number of *in vivo* studies have now illustrated the effectiveness of cavitation in drug delivery and the importance of passive cavitation detection as an indicator of successful ultrasound-mediated drug delivery through the detection of sustained inertial cavitation emissions (Bazan-Peregrino *et al.* 2013, Carlisle *et al.* 2013, Mo *et al.* 2015). The previously described *in vitro* studies (Rifai *et al.* 2010, Arvanitis *et al.* 2011) shed light on the underlying

physical mechanisms, namely the enhanced mass transport and mixing that result from inertial cavitation.

1.4 Thesis Objectives

This chapter has reviewed the previous research concerning the design of drug-encapsulating particles to optimise release, targeting and mapping under different imaging modalities. It has shown that with adequate real-time monitoring of cavitation and heating, ultrasound offers a safe, non-invasive and low-cost solution for enhancing drug-delivery for cancer therapy that has recently been the subject of preliminary clinical trials (Dimcevski *et al.* 2016, Lyon *et al.* 2017).

However, relatively little attention has been given to optimising the transport of therapeutic-carriers through tissue. Furthermore, few studies exist that investigate how sound may be exploited to transport nanoparticles – i.e. bodies larger than molecular agents but smaller than microbubbles.

Previous work has demonstrated that simply increasing particle density can significantly enhance tissue penetration of a nano-scale therapeutic, transported by ultrasound-mediated cavitation activity (Mo *et al.* 2015). However, questions still remain about the influence of particle density in enhancing delivery and the optimal acoustic conditions for maximum transport. Therefore, the aims of the work described in this thesis are twofold: firstly to investigate the role of density in nanoparticle transport, both through computational modelling and experimental validation; and secondly to explore the ultrasound conditions most favourable for cavitation-enhanced therapeutic delivery, using both *in vitro* and *in vivo* models.

1.4.1 Research Questions

In order to explore the influence of nanoparticle density in ultrasound-mediated drug delivery, this thesis endeavours to answer the following research questions:

1) How does nanoparticle density influence the ultrasound-mediated transport and penetration depth of density-contrasting nanoparticles?

2) What influence does the choice of ultrasound exposure parameters have on the transport of density-contrasting nanoparticles, and is this dominated by acoustic streaming and radiation force effects, or by cavitation-mediated microstreaming?

3) What influence does the choice of cavitation agent have on the cavitation-enhanced transport of density-contrasting nanoparticles?

4) Can acoustic emissions be used to predict the transport and penetration depth of density-contrasting nanoparticles?

5) What is the influence of nanoparticle density on ultrasound-mediated drug delivery *in vivo*?

References

Alberts, B., Johnson, A., Lewis, J., Raff, M., Roberts, K., Walter, P., '*Molecular Biology of the Cell*', fifth edition, Garland Science, 2008.

Atchley, A.A., Frizzell, L.A., Apfel, R.E., Holland, C.K., Madanshetty, S. and Roy, R.A., '*Thresholds for cavitation produced in water by pulsed ultrasound*', Ultrasonics, 1988, 26(5), 280-285.

Arvanitis, C.D., Bazan-Peregrino, M., Rifai, B., Seymour, L. W., and Coussios, C.C., '*Cavitation-enhanced extravasation for drug delivery*', Ultrasound in Medicine and Biology, 2011, 37(11), 1838-1852.

Bae, Y.H., Mrsny, R.J. and Park, K., '*Cancer Targeted Drug Delivery - An Elusive Dream*', Springer, 2013.

Baronzio, G., Freitas, I., Baronzio, A., Baronzio, M., Crespi, E. and Netti, P.A., '*Cancer Microenvironment and Therapeutic Implications',* Chapter 5, '*Barriers to Drug Delivery in Cancer: Clinical Implications*', Springer, 2009.

Bazan-Peregrino, M., Arvanitis, C.D., Rifai, B., Seymour, L.W. and Coussios, C.C., '*Ultrasound-induced cavitation enhances the delivery and therapeutic efficacy of an oncolytic virus in an in vitro model*', Journal of Controlled Release, 2012, 157(2), 235-242.

Bazan-Peregrino, M., Rifai, B., Carlisle, R.C., Choi, J., Arvanitis, C.D., Seymour, L.W. and Coussios, C.C., '*Cavitation-enhanced delivery of a replicating oncolytic adenovirus to tumors using focused ultrasound*', Journal of Controlled Release, 2013, 169(1), 40-47.

Beyer, R.T., '*Nonlinear Acoustics*', Chapter 7, '*Streaming*', American Institute of Physics, 1974.

Blake, F.G., '*Technical memo 12',* Acoustics Research Laboratory, Harvard University, Cambridge, MA, 1949.

Brace, C.L., '*Microwave tissue ablation: biophysics, technology, and applications*', Critical Reviews™ in Biomedical Engineering, 2010, 38(1).

Brahme, A., '*Design principles and clinical possibilities with a new generation of radiation therapy equipment: a review*', Acta Oncologica, 1987, 26(6), 403-412.

Brandt, E.H., *'Acoustic physics: suspended by sound'*, Nature, 2001, 413(6855), 474-475.

Carlisle, R., Choi, J., Bazan-Peregrino, M., Laga, R., Subr, V., Kostka, L., and Seymour, L.W., '*Enhanced tumor uptake and penetration of virotherapy using polymer stealthing and focused ultrasound*', Journal of the National Cancer Institute, 2013, 105(22), 1701-1710.

Carmeliet, P. and Jain, R.K., *'Angiogenesis in cancer and other diseases'*, Nature, 2000, 407(6801), 249-257.

Chan, V., and Perlas, A., '*Basics of ultrasound imaging',* from *'Atlas of Ultrasound-Guided Procedures in Interventional Pain Management*', Springer New York, 2011, 13-19.

Chauhan, V.P., Stylianopoulos, T., Martin, J.D., Popović, Z., Chen, O., Kamoun, W.S., Bawendi, M.G., Fukumura, D. and Jain, R.K., '*Normalization of tumour blood vessels improves the delivery of nanomedicines in a size-dependent manner*', Nature nanotechnology, 2012, 7(6), 383-388.

Cleveland, R.O., Sapozhnikov, O.A., Bailey, M.R. and Crum, L.A., *'A dual passive cavitation detector for localized detection of lithotripsy-induced cavitation in vitro'*, The Journal of the Acoustical Society of America, 2000, 107(3), 1745-1758.

Coleman, A.J., Choi, M.J., Saunders, J.E. and Leighton, T.G., '*Acoustic emission and sonoluminescence due to cavitation at the beam focus of an electrohydraulic shock wave lithotripter*', Ultrasound in Medicine and Biology, 1992, 18(3), 267-281.

Coussios, C.C., and Roy, R.A. '*Applications of acoustics and cavitation to noninvasive therapy and drug delivery'*, The Annual Review of Fluid Mechanics, 2008, 40, 395-420.

Davidson, B.J. and Riley, N., '*Cavitation microstreaming*', Journal of Sound and Vibration, 1971, 15(2), 217-233.

Davis, M.E., and Shin, D.M., '*Nanoparticle therapeutics: an emerging treatment modality for cancer*', Nature Reviews Drug Discovery, 2008, 7(9), 771-782.

Dayton, P., Klibanov, A., Brandenburger, G. and Ferrara, K., *'Acoustic radiation force in vivo: a mechanism to assist targeting of microbubbles*', Ultrasound in Medicine and Biology, 1999, 25(8), 1195-1201.

Delalande, A., Kotopoulis, S., Postema, M., Midoux, P. and Pichon, C., '*Sonoporation: mechanistic insights and ongoing challenges for gene transfer',* Gene, 2013, 525(2), 191-199.

Dimcevski, G., Kotopoulis, S., Bjånes, T., Hoem, D., Schjøtt, J., Gjertsen, B.T., Biermann, M., Molven, A., Sorbye, H., McCormack, E. and Postema, M., '*A human clinical trial using ultrasound and microbubbles to enhance gemcitabine treatment of inoperable pancreatic cancer*', Journal of Controlled Release, 2016, 243, 172-181.

Dobson, J., '*Magnetic Nanoparticles for Drug Delivery*', Drug Development Research, 2006, 67, 55–60.

Doinikov, A. A., and Bouakaz, A., '*Acoustic microstreaming around a gas bubble*', The Journal of the Acoustical Society of America, 2010, 127(2), 703-709.

Dougherty, T.J., '*Photodynamic therapy (PDT) of malignant tumors*', Critical Reviews in Oncology/Hematology, 1984, 2(2), 83-116.

Dougherty, T.J., Gomer, C.J., Henderson, B.W., Jori, G., Kessel, D., Korbelik, M., Moan, J., and Peng, Q., '*Photodynamic therapy*', Journal of the National Cancer Institute, 1998, 90(12), 889-905.

Dromi, S., Frenkel, V., Luk, A., Traughber, B., Angstadt, M., Bur, M., Poff, J., Xie, J., Libutti, S.K., Li, K.C. and Wood, B.J., '*Pulsed-high intensity focused ultrasound and low temperature–sensitive liposomes for enhanced targeted drug delivery and antitumor effect*', Clinical Cancer Research, 2007, 13(9), 2722-2727.

Elder, S.A., '*Cavitation microstreaming*', The Journal of the Acoustical Society of America, 1959, 31(1), 54-64.

Flynn, H.G., *'Cavitation dynamics. II. Free pulsations and models for cavitation bubbles'*, The Journal of the Acoustical Society of America, 1975, 57(6), 1379-1396.

Franke, T., Braunmüller, S., Schmid, L., Wixforth, A. and Weitz, D.A., *'Surface acoustic wave actuated cell sorting (SAWACS)'*, Lab on a Chip, 2010, 10(6), 789-794.

Gazda, M.J., and Coia, L.R., '*Principles of radiation therapy*', Chapter 2 of '*Cancer Management: A Multidisciplinary Approach: Medical, surgical and radiation oncology*'. Melville: PRR, Inc, 2001, 9-19.

Goel, S., Wong, A.H.K., and Jain, R.K., '*Vascular normalization as a therapeutic strategy for malignant and nonmalignant disease*', Cold Spring Harbor Perspectives in Medicine, 2012, 2(3), a006486.

Goss, S.A., Frizzell, L.A., Dunn, F. and Dines, K.A., '*Dependence of the ultrasonic properties of biological tissue on constituent proteins*', The Journal of the Acoustical Society of America, 1980, 67(3), 1041-1044.

Graham, S.M., Carlisle, R., Choi, J.J., Stevenson, M., Shah, A.R., Myers, R.S., Fisher, K., Peregrino, M.B., Seymour, L. and Coussios, C.C., *'Inertial cavitation to non-invasively trigger and monitor intratumoral release of drug from intravenously delivered liposomes'*, Journal of Controlled Release, 2014, 178, 101-107.

Hynynen, K. and Edwards, D.K., '*Temperature measurements during ultrasound hyperthermia*', Medical Physics, 1989, 16(4), 618-626.

Hynynen, K., Darkazanli, A., Damianou, C.A., Unger, E. and Schenck, J.F., '*Tissue thermometry during ultrasound exposure',* European Urology, 1993, 23, 12-16.

Hynynen, K., McDannold, N., Sheikov, N.A., Jolesz, F.A. and Vykhodtseva, N., *'Local and reversible blood–brain barrier disruption by noninvasive focused ultrasound at frequencies suitable for trans-skull sonications*', Neuroimage, 2005, 24(1), 12-20.

Jain, R.K., '*Transport of Molecules in the Tumor Interstitium: A Review',* American Association for Cancer Research 1987, 47, 3039-3051.

Jain, R.K. and Stylianopoulos, T., '*Delivering nanomedicine to solid tumors*', Nature Reviews Clinical Oncology, 2010, 7(11), 653-664.

Jain, R.K., '*Normalizing tumor microenvironment to treat cancer: bench to bedside to biomarkers*', Journal of Clinical Oncology, 2013, 31(17), 2205-2218.

Johansson, L., Nikolajeff, F., Johansson, S. and Thorslund, S., *'On-chip fluorescence-activated cell sorting by an integrated miniaturized ultrasonic transducer'*, Analytical Chemistry, 2009, 81(13), 5188-5196.

Keller, J.B., and Miksis, M., '*Bubble oscillations of large amplitude*', The Journal of the Acoustical Society of America, 1980, 68(2), 628-633.

Kwan, J.J., Graham, S., and Coussios, C. C., '*Inertial cavitation at the nanoscale*', Acoustical Society of America, In Proceedings of Meetings on Acoustics, 2013, 19(1), 075031.

Lammers, T., Kiessling, F., Hennink, W.E., and Storm, G., '*Drug targeting to tumours: Principles, pitfalls and (pre-) clinical progress*', Journal of Controlled Release 2012, 161, 175-187.

Landau, L.D. and Lifshitz, E.M., 1987, '*Fluid Mechanics, V. 6 of Course of Theoretical Physics*', 2nd English edition. Revised.

Le Bihan, D., Delannoy, J. and Levin, R.L., '*Temperature mapping with MR imaging of molecular diffusion: application to hyperthermia*', Radiology, 1989, 171(3), 853-857.

Leighton, T., '*The Acoustic Bubble*', Academic Press, 1994.

Lentacker, I., De Cock, I., Deckers, R., De Smedt, S. C., and Moonen, C. T. W., '*Understanding ultrasound induced sonoporation: Definitions and underlying mechanisms*', Advanced Drug Delivery Reviews, 2010, 72, 49-64.

Longuet-Higgins, M.S., '*Viscous streaming from an oscillating spherical bubble*', Proceedings of the Royal Society of London A: Mathematical, Physical and Engineering Sciences, 1998, 454(1970), 725-742.

Lyon, P.C., Griffiths, L.F., Lee, J., Chung, D., Carlisle, R., Wu, F., Middleton, M.R., Gleeson, F.V. and Coussios, C., '*Clinical trial protocol for TARDOX: a phase I study to investigate the feasibility of targeted release of lyso-thermosensitive liposomal doxorubicin (ThermoDox®) using focused ultrasound in patients with liver tumours*', Journal of Therapeutic Ultrasound, 2017, 5(28), 1-8.

Marmottant, P., van der Meer, S., Emmer, M., Versluis, M., de Jong, N., Hilgenfeldt, S. and Lohse, D., *'A model for large amplitude oscillations of coated bubbles accounting for buckling and rupture'*, The Journal of the Acoustical Society of America, 2005, 118(6), 3499-3505.

McDannold, N., Fossheim, S.L., Rasmussen, H., Martin, H., Vykhodtseva, N., and Hynynen, K., '*Heat-activated Liposomal MR Contrast Agent: Initial in Vivo Results in Rabbit Liver and Kidney 1*', Radiology, 2004, 230(3), 743-752.

McDannold, N., Vykhodtseva, N. and Hynynen, K., '*Targeted disruption of the blood–brain barrier with focused ultrasound: association with cavitation activity*', Physics in Medicine and Biology, 2006, 51(4), 793-807.

Mo, S., Coussios, C.C., Seymour, L., and Carlisle, R., '*Ultrasound-enhanced drug delivery for cancer*', Expert opinion on drug delivery, 2012, 9(12), 1525-1538.

Mo, S., Carlisle, R., Laga, R., Myers, R., Graham, S., Cawood, R., Ulbrich, K., Seymour, L. and Coussios, C.C., '*Increasing the density of nanomedicines improves their ultrasound-mediated delivery to tumours*', Journal of Controlled Release, 2015, 210, 10-18.

Morris, H., Rivens, I., Shaw, A., and ter Haar, G., '*Investigation of the viscous heating artefact arising from the use of thermocouples in a focused ultrasound field*', Physics in Medicine and Biology, 2008, 53(17), 4759.

Morse, P.M., and Ingard, K.U., '*Theoretical acoustics*', Princeton University Press, 1968.

National Institute for Health and Care Excellence (NICE), '*Intravesical microwave hyperthermia with intravesical chemotherapy for superficial bladder cancer'*, Issued: October 2007, NICE Interventional Procedure Guidance 235, www.nice.org.uk/ipg235.

Nelson, J.L., Roeder, B.L., Carmen, J.C., Roloff, F., and Pitt, W.G., *'Ultrasonically activated chemotherapeutic drug delivery in a rat model*', Cancer Research, 2002, 62(24), 7280-7283.

Neppiras, E.A. and Noltingk, B.E., '*Cavitation produced by ultrasonics: theoretical conditions for the onset of cavitation*', Proceedings of the Physical Society, Section B, 1951, 64(12), 1032.

Noltingk, B.E. and Neppiras, E.A., *'Cavitation produced by ultrasonics'*, Proceedings of the Physical Society. Section B, 1950, 63(9), 674.

Pennes, H.H., '*Analysis of tissue and arterial blood temperatures in the resting human forearm'*, Journal of Applied Physiology, 1948, 1(2), 93-122.

Pitt, W.G., Husseini, G.A., and Staples, B.J., '*Ultrasonic drug delivery-a general review',* Expert Opinion on Drug Delivery, 2004, 1(1), 37-56.

Plesset, M.S. and Hsieh, D.Y., *'Theory of gas bubble dynamics in oscillating pressure fields'*, The Physics of Fluids, 1960, 3(6), 882-892.

Pluen, A., Netti, P.A., Jain, R.K., and Berk, D.A., *'Diffusion of macromolecules in agarose gels: comparison of linear and globular configurations*', Biophysical Journal, 1999, 77(1), 542-552.

Popović, Z., Liu, W., Chauhan, V.P., Lee, J., Wong, C., Greytak, A.B. and Bawendi, M.G., '*A nanoparticle size series for in vivo fluorescence imaging'*, Angewandte Chemie, 2010, 122(46), 8831-8834.

Powlis, W.D., Smith, A.R., Cheng, E., Galvin, J.M., Villari, F., Bloch, P., and Kligerman, M.M., '*Initiation of multileaf collimator conformal radiation therapy*', International Journal of Radiation Oncology, Biology, Physics, 1993, 25(2), 171-179.

Pierce, A.D., '*Acoustics: An introduction to its physical principles and applications*', McGraw-Hill Book Company, 1981.

Rayleigh, J. W. Strutt, Baron, '*Theory of Sound'*, 1896, Volume 2, 282.

Rifai, B., Arvanitis, C.D., Bazan-Peregrino, M., and Coussios, C.C., '*Cavitation-enhanced delivery of macromolecules into an obstructed vessel*', The Journal of the Acoustical Society of America, 2010, 128(5), EL310-EL315.

Russell, S.J. and Peng, K.W., '*Viruses as anticancer drugs*', Trends in Pharmacological Sciences, 2007, 28(7), 326-333.

Soundararajan, A., Bao, A., Phillips, W.T., Perez, R. and Goins, B.A., *'[186 Re] Liposomal doxorubicin (Doxil): in vitro stability, pharmacokinetics, imaging and biodistribution in a head and neck squamous cell carcinoma xenograft model'*, Nuclear medicine and biology, 2009, 36(5), 515-524.

Starritt, H.C., Duck, F.A., and Humphrey, V.F., '*An experimental investigation of streaming in pulsed diagnostic ultrasound beams*', Ultrasound in Medicine and Biology, 1989, 15(4), 363-373.

Staruch, R.M., Ganguly, M., Tannock, I.F., Hynynen, K., and Chopra, R., '*Enhanced drug delivery in rabbit VX2 tumours using thermosensitive liposomes and MRI-controlled focused ultrasound hyperthermia*', International Journal of Hyperthermia, 2012, 28(8), 776-787.

Sun, Q., Sun, X., Ma, X., Zhou, Z., Jin, E., Zhang, B., Shen, Y., Van Kirk, E.A., Murdoch, W.J., Lott, J.R., Lodge, T.P., Radosz, M., Zhaoet, Y., '*Integration of nanoassembly functions for an effective delivery cascade for cancer drugs',* Advanced Materials, 2014, 26(45), 7615-7621.

Sunderland, C.J., Steiert, M., Talmadge, J.E., Derfus, A.M., and Barry, S.E., '*Targeted nanoparticles for detecting and treating cancer*', Drug Development Research, 2006, 67(1), 70-93.

Tho, P., Manasseh, R. and Ooi, A., '*Cavitation microstreaming patterns in single and multiple bubble systems*', Journal of Fluid Mechanics, 2007, 576, 191-233.

Veiseh, O., Gunn, J.W. and Zhang, M., '*Design and fabrication of magnetic nanoparticles for targeted drug delivery and imaging'*, Advanced Drug Delivery Reviews, 2010, 62(3), 284-304.

Wilhelm, S., Tavares, A.J., Dai, Q., Ohta, S., Audet, J., Dvorak, H.F. and Chan, W.C., '*Analysis of nanoparticle delivery to tumours*', Nature Reviews Materials, 2016, 16014.

Wong, C., Stylianopoulos, T., Cui, J., Martin, J., Chauhan, V.P., Jiang, W., and Fukumura, D., '*Multistage nanoparticle delivery system for deep penetration into tumor tissue*', Proceedings of the National Academy of Sciences, 2011, 108(6), 2426-2431.

Wu, J. and Du, G., *'Streaming Generated by a Bubble in an Ultrasound Field'*, Journal of Acoustical Society of America, 1997, 101(4), 1899-1907.

Xie, W.J. and Wei, B., *'Dependence of acoustic levitation capabilities on geometric parameters'*, Physical Review E, 2002, 66(2), 026605.

Zhao, S., Borden, M., Bloch, S.H., Kruse, D., Ferrara, K.W. and Dayton, P.A., '*Radiation-force assisted targeting facilitates ultrasonic molecular imaging*', Molecular Imaging, 2004, 3(3), 135-148.

Chapter 2: **The effect of particle density on ultrasound-mediated transport of nanoparticles**

Abstract

A significant barrier to successful drug delivery is the limited penetration of nanoscale therapeutics beyond the vasculature. Building on recent *in vivo* findings in the context of cancer drug delivery, this chapter investigates whether modification of nanoscale drug-carriers to increase their density can be used to enhance their penetration into viscoelastic materials under ultrasound exposure. A computational model is first presented to predict the transport of identically sized nanoparticles of different densities in an ultrasonic field in the presence of an oscillating microbubble, by a combination of primary and secondary acoustic radiation forces, acoustic streaming, and microstreaming. Experiments are then described in which near monodisperse (polydispersity index < 0.2) nanoparticles of approximate modal average diameter 200 nm and densities ranging from 1.01 g/cm^3 to 5.58 g/cm^3 were fabricated and delivered to a tissue-mimicking material in the presence or absence of a microbubble ultrasound contrast agent, at ultrasound frequencies of 0.5 MHz and 1.6 MHz and a peak negative pressure of 1 MPa. Both the theoretical and experimental results confirm that denser particles exhibit significantly greater ultrasound-mediated transport than their lower density counterparts, indicating that density is a key consideration in the design of nanoscale therapeutics.

This chapter has been published in an alternative form in Lea-Banks *et al.* (2016) *Physics in Medicine and Biology*.

2.1 Introduction

Cancerous tissue is highly heterogeneous in terms of perfusion and the pressure and composition of the extracellular matrix, posing a number of significant barriers to drug delivery. Consequently, current methods of systemic drug delivery often do not enable therapeutics to penetrate sufficiently deep into tumour tissue for effective treatment (Minchinton *et al.* 2006). This is particularly problematic for relatively large therapeutics such as nanoparticles. Strategies for enhancing the transport of nanoscale drug carriers have included modifying their size, shape and surface chemistry – primarily surface charge and biological targeting (Blanco *et al.* 2015). Tailoring the size and shape of nanoparticles can increase their ability to pass through pores in the 'leaky' vasculature that is characteristic of cancerous blood vessels and be retained in the surrounding tumour tissue – an effect known as enhanced permeability and retention (EPR) (Maeda *et al.* 2010, Prabhakar *et al.* 2013). Exploiting the EPR effect in this way is classified as passive targeting. In contrast, using surface charge or ligands to enable particles to bind to specific receptors on cancer or endothelial cells is classed as active targeting (Kamaly *et al.* 2012).

As discussed in chapter 1, it has been shown that neither passive (Popović *et al.* 2010) nor active targeting alone can provide significant enhancements in nanoparticle delivery (Wilhelm *et al.* 2016). In combination with physical stimuli, however, much greater penetration depths can be achieved. These stimuli include magnetic fields (Lübbe *et al.* 2001), electromagnetic radiation (such as photodynamic therapy) (Dougherty *et al.* 1992) and ultrasound. Of these, ultrasound has been shown to achieve the greatest penetration depths and has the advantage of being cost-effective and already clinically approved as an imaging and therapeutic modality (Mo *et al.* 2012). The combination of a nanoparticle with microbubbles driven in a sustained inertial cavitation regime has shown promise as a means of enhancing transport, enabling the

delivery of nanoparticulate therapeutics to some 200 micrometres from the nearest blood vessel (Carlisle *et al.* 2013). Although size and shape modifications have been quite extensively explored, relatively little attention has been given to the influence of particle density on the delivery and penetration distance of nanoscale drug carriers when exposed to ultrasound.

It has been shown previously that coating an adenovirus of mean size 140 nm with gold nanoparticles can enhance its ultrasound-mediated transport in a mouse model in the presence of a microbubble ultrasound contrast agent (Mo *et al.* 2015). It was hypothesised that this enhancement was due to the polymer-gold coating providing both reduced immunogenicity, and hence increased circulation time, and an increase in density that facilitates transport by cavitation-induced microstreaming. The current study aims to test this hypothesis and to determine how the ultrasound-mediated transport of a nanoscale object is affected by its density. Additionally, the influence of ultrasound exposure conditions and the incidence of cavitation will also be examined.

2.1.1 Research Questions

In this chapter the first research question will be addressed:

1) How does nanoparticle density influence the ultrasound-mediated transport and penetration depth of density-contrasting nanoparticles?

The influence of particle density will be explored through a computational model assessing the dominant forces present during ultrasound-mediated drug delivery, and experimental validations using density-modified nanoparticles and acoustically-driven microbubbles.

2.2 Numerical Model

2.2.1 Methodology

A simple computational model was first developed to compare the magnitude of the different forces acting on a 200 nm diameter nanoparticle suspended in water and subjected to an ultrasound field, under different exposure conditions, in the presence or absence of a 3 µm diameter microbubble (see appendix A4 for all associated code). This model was then used to predict the distance that the particle would travel beyond a planar water/agarose boundary into agarose gel. Agarose was used here both in the computational and experimental models as a tissue-mimicking material, having similar density, acoustic properties and pore size to those of human tissue (Maaloum *et al.* 1998). A particle size of 200 nm was chosen as being representative of larger nanoparticulate therapeutics, such as viruses or liposomes, whilst still being small enough to extravasate through leaky tumour vasculature (Hobbs *et al.* 1998).

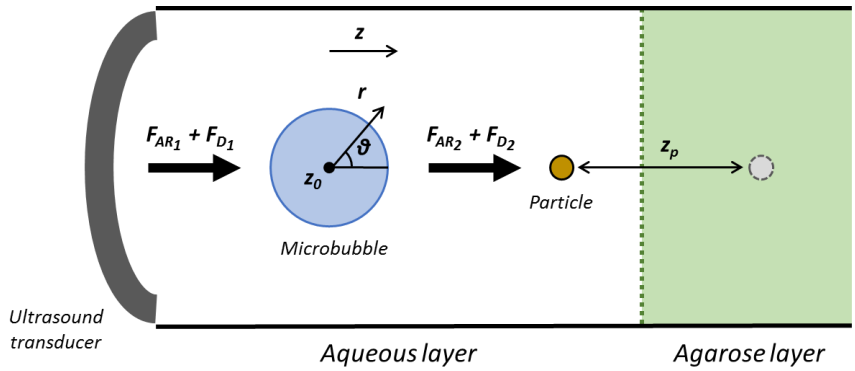

Figure 2.1 *Schematic of the model-system used to estimate the primary acoustic radiation force (F_{AR1}), acoustic streaming force (F_{D1}), secondary radiation force (F_{AR2}) and microstreaming force (F_{D2}) on a 200 nm solid particle in aqueous suspension, and predict the resultant penetration distance (z_p).*

A schematic of the system is shown in figure 2.1. In the absence of the microbubble, the particle will experience an acoustic radiation force (F_{AR1}) due to the propagating ultrasound field and a second force due to acoustic streaming (F_{D1}). The latter was calculated using Stoke's equation for drag (equation 2.1). This was deemed to be justified since the regimes

considered relate to a nanoscale object and low streaming velocities (~cm/s), producing Reynolds numbers on the order of 1×10^{-3}.

In the presence of the microbubble, the particle will experience two additional forces: a secondary acoustic radiation force (F_{AR2}) and a force due to microstreaming (F_{D2}). The response of a 3 µm diameter microbubble (the median diameter of a SonoVue® microbubble) in free-field conditions was modelled using the Keller-Miksis equation (equation 2.2) (Keller *et al.* 1980) and the predicted radial oscillations for driving frequencies of 0.5 MHz and 1.6 MHz and a peak negative pressure of 1 MPa are shown for a coated and uncoated bubble in figure 2.2 and 2.3 respectively. Driving frequencies of 0.5 MHz and 1.6 MHz were chosen such that the same experimental setup could be used to excite the bubble in two different regimes – below and near resonance – with the same transducer, driven at the fundamental or third harmonic frequency. To account for the sulphur hexafluoride encapsulated inside the SonoVue® microbubbles (Bracco Imaging, France) used in the experiments, a specific heat ratio (γ) of 1.098 was used to describe the internal gas (Schneider *et al.* 1995). The effect of the microbubble coating was neglected since initial simulations indicated that the influence of the coating on microbubble dynamics, for the ultrasound exposure parameters used in the study, was negligible (figure 2.2).

Dynamics of a coated and free microbubble

The amplitude of oscillation is predicted for a free bubble (as predicted by Keller *et al.* 1980) and for a coated bubble (as predicted by Marmottant *et al.* 2005) (equation 1.5). Figure 2.2 shows a comparison of oscillation amplitudes for a 3 µm bubble driven at 0.5 MHz or 1.6 MHz, at 1 MPa. The shell of the coated bubble is defined using experimentally derived parameters for a SonoVue® microbubble (Marmottant *et al.* 2005) shown below. It can be seen that at

these acoustic exposures this type of coating has very little influence on the amplitudes of oscillation.

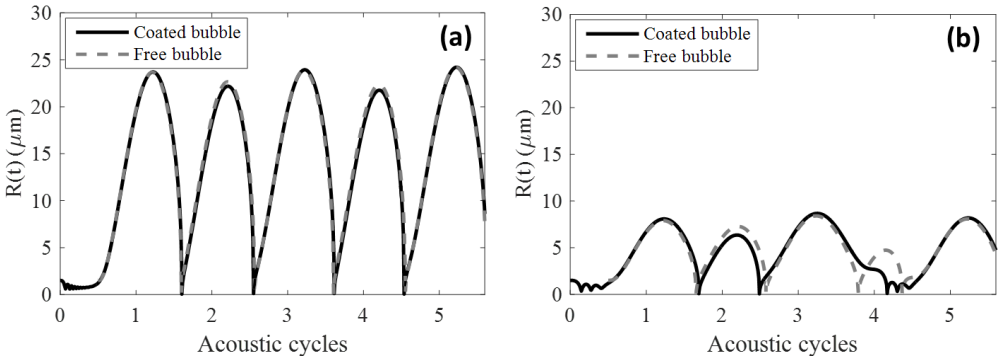

Figure 2.2 *Simulated radius-time curves for a coated and free 3 µm bubble as determined by the Marmottant coated bubble model (Marmottant et al. 2005) and the free Keller Miksis model (Keller et al. 1980) respectively, driven at 1 MPa and **(a)** 0.5 MHz and **(b)** 1.6 MHz.*

Table 2.1 *Table of variables and associated symbols and values*

R_0	Equilibrium bubble radius	$1.50\ \mu m$
$R_{buckling}$	Buckling bubble radius	$1.50\ \mu m$
$R_{ruptured}$	Ruptured bubble radius ($R_{ruptured} = R_{buckling}(1 + \sigma_{water}/\chi)^{1/2}$)	$1.55\ \mu m$
χ	Shell elasticity	$1\ N/m$
κ_s	Shell friction ($\kappa_s = 3\mu_{sh}\varepsilon_{sh}$)	$15 \times 10^{-9} N$
μ_{sh}	Shell viscosity	
ε_{sh}	Shell thickness	
$\sigma_{break-up}$	Maximum surface tension before rupture	$> 1\ N/m$
σ_{water}	Surface tension of water	$0.072\ N/m$
κ	Polytropic gas exponent of SF_6	1.095
ρ_l	Liquid density	$1000\ kg/m^3$
μ	Liquid viscosity	$0.001\ Pa\ s$
c	Liquid sound speed	$1480\ m/s$

The radiated pressure (p_{rad}) field may be calculated from the corresponding potential flow theory (equation 2.3) (Vokurka 1990), which was in turn used to determine the magnitude of the secondary radiation force (also known as the secondary Bjerknes force). The

microstreaming model published by Doinikov (2010) was implemented to assess the velocity field around the microbubble (equation 32, Doinikov 2010). The radial component of microstreaming taken in the positive 'r' direction (i.e. towards the water/agar boundary) was used to determine the corresponding force on the particle that would lead to penetration into the agar, again assuming Stoke's drag.

The relative magnitudes of the four forces acting on the particle are shown in table 2.3. These values illustrate that within the regimes of interest for this study the greatest of the four forces is provided by the microstreaming, which dominates the particle's motion. Since depth of penetration was the primary quantity of interest, only the z-axis component of these forces was considered. The nanoparticle was assumed to be located initially at a distance of twice the viscous penetration depth from the bubble outer surface (equation 2.4) (1.6 µm and 0.9 µm from the surface at 0.5 MHz and 1.6 MHz respectively) and to be travelling at the velocity of the fluid by the time it had reached the aqueous/agarose boundary (equation 2.5). The effective particle mass accounts for the mass of the particle and the added mass due to the inertia of the displaced fluid (equation 2.6).

The predicted penetration depth of the nanoparticle is defined as the distance the particle penetrates into agar assuming no further propulsion, i.e. the particle is travelling due to the momentum imparted to it when in the fluid layer. The particle ultimately comes to rest because of the drag experienced in the agar. Penetration depth into the agarose gel was predicted using a non-Newtonian fluid model (equation 2.7) (de Bruyn *et al.* 2004), in which agarose viscosity and yield strength are free parameters that may be determined from experimental observations. Since published parameters vary considerably however, for the purposes of this study, the predicted penetration depths were normalised to the peak

penetration depth found across any of the ultrasound exposure conditions, with the maximum normalised value being 1000.

$$F_{D1} = 6\pi R_p \mu(u_1 - v_p), \qquad F_{D2} = 6\pi R_p \mu(u_2 - v_p) \tag{2.1}$$

where u_1 and u_2 are determined from the microstreaming model

$$\ddot{R} = \left(\frac{1}{2}\dot{R}^3 + \dot{R}\Delta(R) - c\left(\frac{3}{2}\dot{R}^2 + \frac{4\mu\dot{R}}{\rho_L R} + \frac{2\sigma}{\rho_L R} - \Delta(R)\right) + R\dot{R}\Delta'(R) + \left(1 + \frac{\dot{R}}{c}\right)\frac{P_a c}{\rho_L}\sin\omega\left(t + \frac{R}{c}\right)\right)\left(\frac{4\mu}{\rho_L} - R(\dot{R} - c)\right)^{-1} \tag{2.2}$$

$$\text{where } \Delta(R) = \left(\left(p_0 + \frac{2\sigma}{R_0}\right)\left(\frac{R_0}{R}\right)^{3\gamma} - p_0\right)\rho_L^{-1}$$

$$p_{rad} = \left(\left(1 - \frac{\dot{R}}{c}\right)R\dot{R}\rho_L + \frac{3}{2}\left(1 - \frac{\dot{R}}{3c}\right)\dot{R}^2\rho_L - \frac{R}{c}\frac{dP_a}{dt}\right)\left(1 + \frac{\dot{R}}{c}\right)^{-1} \tag{2.3}$$

$$r = R_0 + 2\delta_v \text{ , where } \delta_v = \sqrt{2\mu/\rho_L\omega} \quad \text{(Doinikov 2010)} \tag{2.4}$$

$$v_p = (u_1 + u_2) \tag{2.5}$$

$$m = m_p + m_{added} = \frac{4}{3}\pi R_p^3 \rho_p + \frac{2}{3}\pi R_p^3 \rho_L \tag{2.6}$$

$$\delta_p = \frac{m v_p}{k} - \frac{F_y m}{k^2}\ln\left(1 + \frac{v_p k}{F_y}\right) \text{ (de Bruyn } \textit{et al.}\text{ 2004)} \tag{2.7}$$

Table 2.2 *Table of variables and constants, with associated symbols and values.*

Variables

F_{AR1}	*Acoustic radiation force*	R	*Instantaneous radius*
F_{AR2}	*Secondary acoustic radiation force*	$\dot{R}$	*Radial velocity*
F_{D1}	*Acoustic streaming force*	$\ddot{R}$	*Radial acceleration*
F_{D2}	*Microstreaming force*	R_p	*Particle radius*
F_y	*Yield stress force of agarose*	u_1	*Acoustic streaming velocity*
k	*Effective viscosity*	u_2	*Microstreaming velocity*
m	*Effective particle mass*	v_p	*Particle velocity*
m_{added}	*Added mass*	δ_p	*Particle penetration depth*
m_p	*Particle mass*	δ_v	*Viscous penetration depth*
P_a	*Acoustic pressure*	ρ_p	*Particle density*
r	*Initial particle location*	ω	*Acoustic angular frequency*

Constants

c	*Sound speed in surrounding medium*	$1480\ m/s$
p_0	*Static pressure*	$1 \times 10^5 Pa$
R_0	*Equilibrium bubble radius*	$1.5\ \mu m$
R_p	*Particle radius*	$100\ nm$
ρ_L	*Liquid density*	$1000\ kg/m^3$
μ	*Liquid viscosity*	$0.001\ kg/ms$
σ	*Surface tension*	$0.0725\ N/m$
γ	*Ratio of specific heats*	1.098

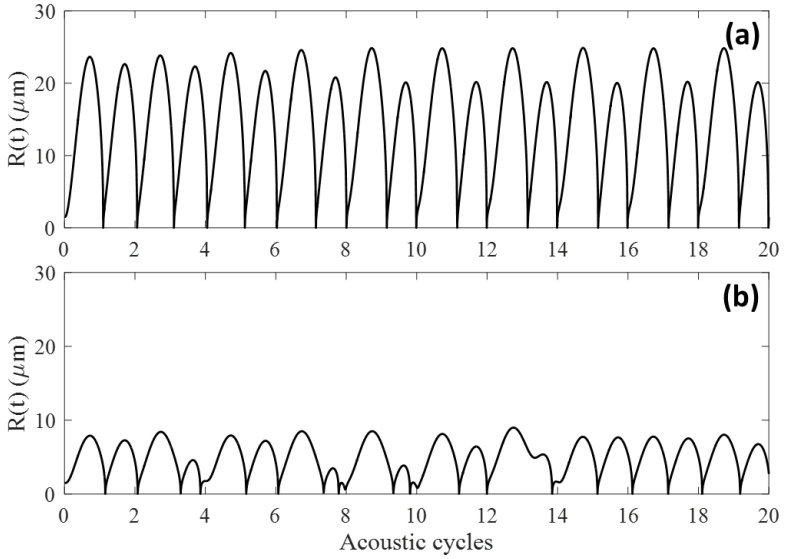

Figure 2.3 *Radius-time curves predicted by the Keller-Miksis model (Keller et al. 1980) for the dynamic response of a 3 µm bubble driven at 1 MPa at **(a)** 0.5 MHz and **(b)** 1.6 MHz for the first 20 acoustic cycles.*

Table 2.3 *Predicted force magnitudes on a 200 nm solid particle at a distance of twice the viscous penetration depth from the surface of an oscillating 3 µm bubble at a peak negative pressure of 1 MPa.*

	1.6 MHz + SV	**0.5 MHz + SV**
Primary acoustic radiation force (F_{AR_1})	$5.0 \times 10^{-13}\ N$	$7.7 \times 10^{-14}\ N$
Acoustic streaming force (F_{D_1})	$8.1 \times 10^{-11}\ N$ $(u_1 = 4.31\ cm/s)$	$7.8 \times 10^{-13}\ N$ $(u_1 = 0.41\ cm/s)$
Secondary acoustic radiation force (F_{AR_2})	$1.7 \times 10^{-11}\ N$	$1.4 \times 10^{-11}\ N$
Microstreaming force (F_{D_2})	$2.9 \times 10^{-10}\ N$ $(u_2 = 15.4\ cm/s)$	$6.3 \times 10^{-10}\ N$ $(u_2 = 33.6\ cm/s)$

2.2.2 Results

The penetration depth was predicted for particles of three different densities, each with a core of either polystyrene (PS), silica (SiO_2) or gold (Au) and a polymer coating, giving final particle densities of 1.01 g/cm^3, 1.41 g/cm^3 or 5.58 g/cm^3 respectively, under four acoustic regimes (figure 2.4). The first two acoustic regimes correspond to the case in which no cavitation nuclei are present. Therefore the particle is driven only by the primary acoustic radiation force (F_{AR1}) and the force due to acoustic streaming (F_{D1}). In this non-cavitational regime the model predicts greater penetration depths at 1.6 MHz compared to 0.5 MHz. This is as expected because at higher frequencies the ultrasound energy is more attenuated by the surrounding fluid and transfer more momentum from the propagating wave to the fluid, which in turn induces greater acoustic streaming velocities. Even at the higher frequency, however, the predicted penetration depth is relatively small compared to that observed with a microbubble present.

When an oscillating microbubble was introduced, much greater penetration depths were predicted for all three types of particles. For example, the greatest predicted penetration depth achieved by the gold nanoparticle without cavitation is 0.2 % of the greatest predicted penetration depth achieved by the gold nanoparticle with cavitation. In this cavitation regime the particles experience the additional secondary acoustic radiation force (F_{AR2}) and the force generated by microstreaming (F_{D2}). With cavitation nuclei at 0.5 MHz, the predicted penetration depths are greater for all three particles than in the 1.6 MHz regime. As shown in figure 2.3 (a), at 0.5 MHz the 3 µm bubble experiences a longer negative pressure phase than at 1.6 MHz (figure 2.3 (b)), and is therefore able to achieve greater expansion ratios that are associated with greater microstreaming velocities (table 2.3).

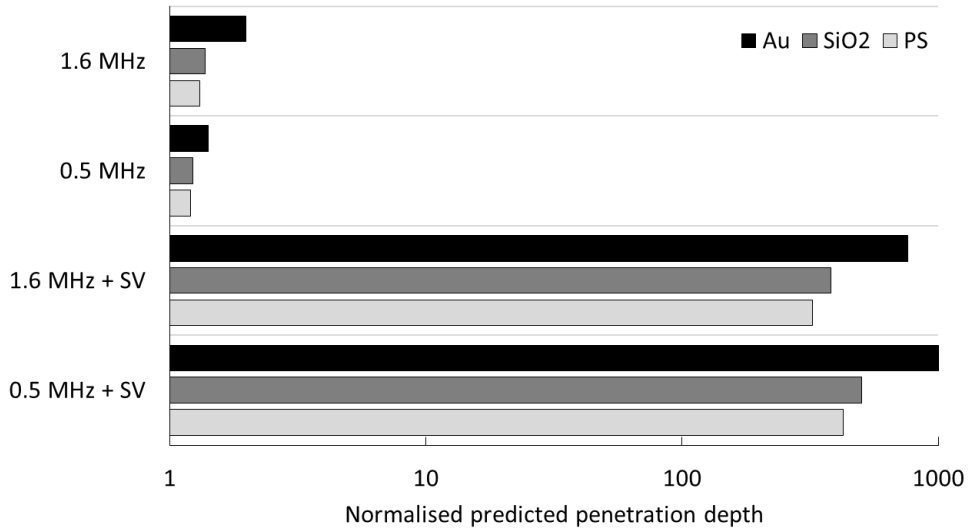

Figure 2.4 *Normalised predicted penetration depths of 200 nm particles of three different densities (Au = 5.58 g/cm^3, SiO_2 = 1.41 g/cm^3, PS = 1.01 g/cm^3) under ultrasound exposure in four acoustic regimes with and without a SonoVue® (SV) microbubble. A microbubble diameter of 3 µm was used and a peak negative pressure of 1 MPa over 100 acoustic cycles. Predicted depths are normalised to the peak penetration depth in any of the acoustic regimes.*

2.3 Experimental Investigations

2.3.1 Methodology

Ultrasound-mediated transport of contrasting-density nanoparticles was investigated experimentally using the apparatus shown in figure 2.5, building on similar experimental setups used in previous studies (Bhatnagar *et al.* 2014). A high-intensity focussed ultrasound (HIFU) single element transducer with circular cut-out (H-107F-18; Sonic Concepts, USA) was used. The HIFU transducer has an element diameter of 64 mm, geometric focus of 60 mm, a fundamental frequency of 0.5 MHz and a third harmonic at approximately 3.3 times that, at 1.6 MHz (with -3 dB bandwidth of 0.4 – 0.6 MHz and 1.44 – 1.76 MHz at the fundamental and third harmonic respectively). This transducer was chosen such that two contrasting acoustic regimes could be studied with the same experimental setup. Ultrasound was delivered at a pulse repetition frequency of 10 Hz and 2 % duty cycle, with pulse repetition period of 100 ms over a total exposure time of 10 s, at a peak negative pressure of 1.0 MPa.

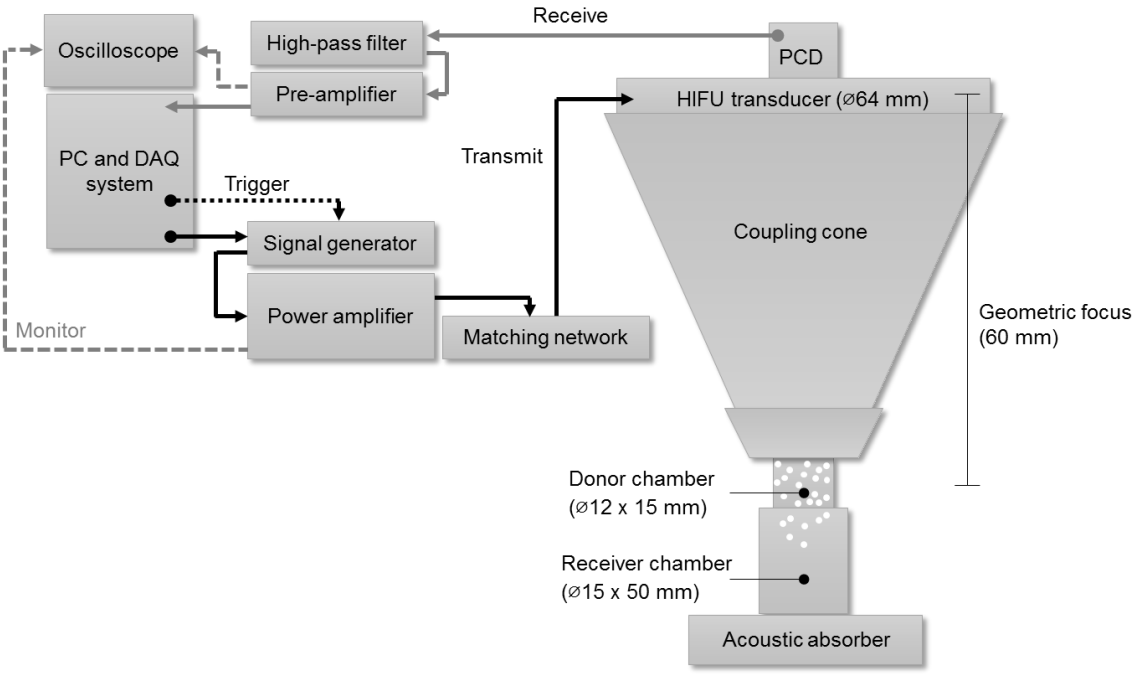

Figure 2.5 *Schematic representation of ultrasound transmission, trigger, receive, and monitor circuit; with high-intensity focussed ultrasound (HIFU) transducer and passive cavitation detection (PCD) transducer. The coupling cone, filled with degassed water, allows transmission of ultrasound from the HIFU transducer into the donor chamber, filled with fluid, nanoparticles and SonoVue® (SV). Nanoparticles are transported from the donor chamber to the receiver chamber, filled with agarose gel and placed upon an acoustic absorber.*

Transmission of ultrasound from the HIFU transducer to the aqueous sample of nanoparticles was achieved using a Perspex coupling cone containing degassed deionised (DI) water (figure 2.5). Average cavitation signals were captured using a passive cavitation detection (PCD) transducer (V320; Panametrics, Olympus NDT U.K. Ltd, England) coaxially aligned with the HIFU transducer. The PCD was spherically focussed, with centre frequency 7.5 MHz, element diameter 12.5 mm and geometric focus 75.0 mm. High-pass filtering at 5 MHz, using a passive precision filter (FILT-HP5-A, Allen Avionics, USA), was implemented to condition the PCD signal. This form of conditioning was implemented to isolate high frequency signals, to remove any direct reflections of the transducer driving frequency and associated lower harmonics produced by nonlinear propagation, in order to identify harmonics and broadband signals exclusively emitted by the cavitating microbubbles.

As shown in figure 2.5, the 'donor' chamber, a Perspex cylinder with diameter 12 mm and internal volume of 1.7 mL, was placed beneath the coupling cone and filled with each population of density-contrasting nanoparticle in aqueous suspension and SonoVue® (SV) microbubbles, at a 20-fold dilution of the stock concentration (approximately 10^7 bubbles/mL). Nanoparticles were transported from the donor chamber into the receiver chamber, which was filled with a volume of 1 % concentration (weight/volume %) agarose gel. An acoustic absorber was placed beneath the receiver chamber to prevent standing waves forming in the chambers above. Control studies allowed particles to diffuse into agar without exposure to ultrasound, and were performed over the same time frame as the other studies, i.e. accounting for set-up, alignment and ultrasound exposure duration.

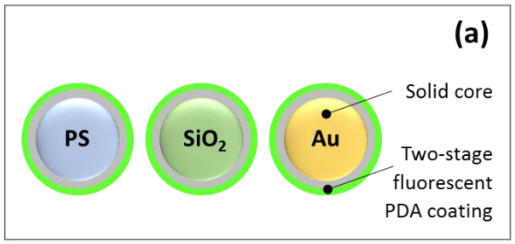

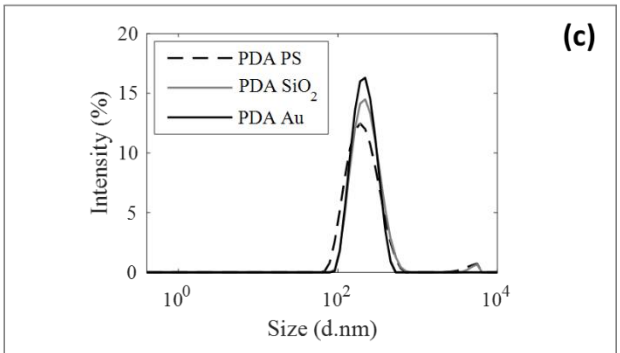

Particle type	*Hydrodynamic diameter (nm)*	*Polydispersity index (PdI)*	*Zeta potential (mV)*
PDA PS	193.7	0.194	-26.2
PDA SiO_2	215.9	0.176	-27.6
PDA Au	194.7	0.134	-27.0

Figure 2.6 *Bespoke density-modified nanoparticles formed from contrasting density cores of polystyrene (PS), silica (SiO_2) or gold (Au) with a fluorescent poly-dopamine (PDA) coating. Particles are shown as **(a)** a schematic illustration and **(b)** a transmission electron microscopy (TEM) image of PDA-PS (left) and PDA-Au (right). The size distribution of each particle type is shown in **(c)** as measured by dynamic light scattering (DLS).*

Bespoke density-modified nanoparticles were fabricated using a 100 nm diameter core of polystyrene (PS), silica (SiO_2) or gold (Au), coated with a 50 nm thick poly-dopamine (PDA) shell in a two-phase coating procedure described by Chen *et al.* (2014) (figure 2.6). Dr Boon

Teo is gratefully acknowledged for her support in implementing and trouble-shooting this procedure. The final coated nanoparticles were characterised using dynamic light scattering (DLS), and had a modal average diameter of 200 nm and size distribution of 0.17 ± 0.03, quantified using the normalised second cumulant (i.e. *variance/mean*^{2}) known as the polydispersity index (PdI). All batches used in the study were also similar in terms of zeta potential (-27 mV ± 2), fluorescence (excitation 400 nm, emission 480 nm) and concentration (10^{10} particles/mL), but contrasting in density (PDA-PS 1.10 g/cm^3, PDA-SiO_2 1.41 g/cm^3, PDA-Au 5.58 g/cm^3). It should be noted that variation in the polymerisation process led to surface variations, allowing the nanoparticle shape to derivate from spherical (clearly visible through TEM in figure 2.6b). However, it is assumed that these small surface features will be associated with a very small increase in drag coefficient, and for the purposes of this transport study can be assumed to be negligible.

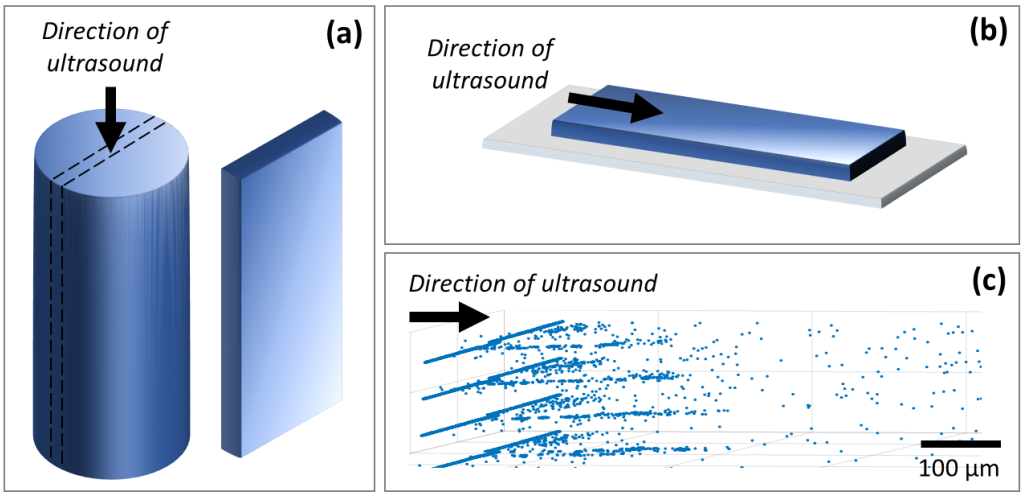

Figure 2.7 *Schematic representation of **(a)** gel sample and **(b)** preparation for confocal microscopy by slicing the central plane and applying to a microscope slide. Confocal microscopy was used to obtain **(c)** a volumetric scan of the sample and particle detection to locate and map the distribution of nanoparticles.*

The agarose sample was removed from the receiver chamber, sliced to a thickness of approximately 4 mm and prepared for microscopy, as illustrated in figure 2.7. Confocal

microscopy was used to capture a volumetric scan of the sample. These data were then processed by applying a thresholding function to detect the location of each particle. By locating each particle and measuring the distance from the agarose boundary, a value for penetration depth was obtained. Statistical significance was assessed using analysis of variance, comparing the variation between groups with the variation within groups, and was felt to be a more robust measure than a simple t test. A p-value < 0.05 was used to disprove the null hypothesis.

2.3.2 Results

Figure 2.8 shows the results from three sets of experiments. In the absence of ultrasound exposure, the average penetration by diffusion alone is limited to less than 30 µm. In the presence of acoustic excitation, the penetration depth exceeds 80 µm in all cases. It can be seen that in each of the acoustic regimes the penetration depth was greatest for the densest particle.

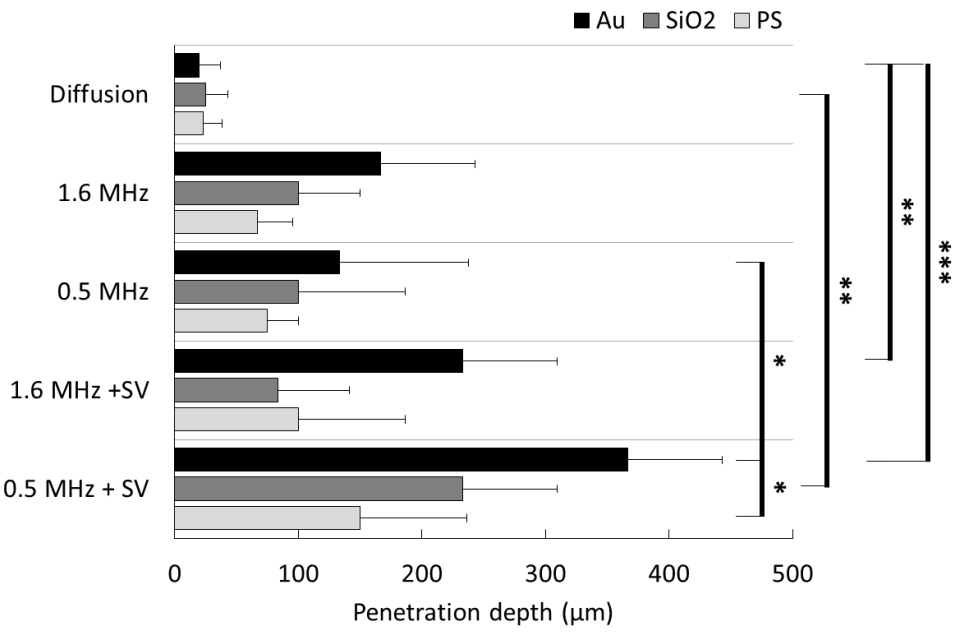

Figure 2.8 *Penetration depths of density-contrasting particles under ultrasound exposure in four acoustic regimes. Statistical significance is assessed using one-way ANOVA testing:* $*\ (p < 0.05)$ *,* $**\ (p < 0.01)$ *,* $***\ (p < 0.001)$ *where* $n = 3$*.*

Table 2.4 *Statistical significance and p-values assessed through one-way ANOVA testing.*

Groups compared		***p-value***
Group 1	***Group 2***	
Diffusion ***Au***	*0.5 MHz + SV* ***Au***	4.09×10^{-5}
Diffusion ***Au***	*1.6 MHz + SV* ***Au***	0.004
Diffusion ***SiO_2***	*0.5 MHz + SV* ***SiO_2***	0.006
0.5 MHz ***Au***	*0.5 MHz + SV* ***Au***	0.02
0.5 MHz + SV ***Au***	*0.5 MHz + SV* ***PS***	0.05

The addition of SV enhanced the average penetration depths of all particles at 0.5 MHz. In particular, the penetration depth of gold nanoparticles with SV at 0.5 MHz was found to be statistically significantly greater than the penetration of gold nanoparticles without SV, illustrated In figure 2.8. An ultrasound frequency of 0.5 MHz was found to be most favourable for particle transport when compared to exposure at 1.6 MHz, in agreement with the theoretical predictions.

Figure 2.9a summarises the detected cavitation emissions. It is important to note that cavitation activity was detected without SV present at both 1.6 MHz and 0.5 MHz, where the detected peak cavitation power was raised above baseline. This spontaneous activity is likely to be attributed to gas in dissolution in the water and gas trapped on the surface of the density-contrasting nanoparticles. However, the addition of SV significantly increased the cavitation activity when compared to ultrasound alone ($p < 0.001$). Figure 2.9b and 2.9c show the frequency composition of typical example measurements of PCD data during ultrasound exposure with SV at 1.6 MHz and 0.5 MHz. More harmonic peaks were seen during insonation at 1.6 MHz, whereas greater broadband frequency content was seen during insonation at 0.5 MHz.

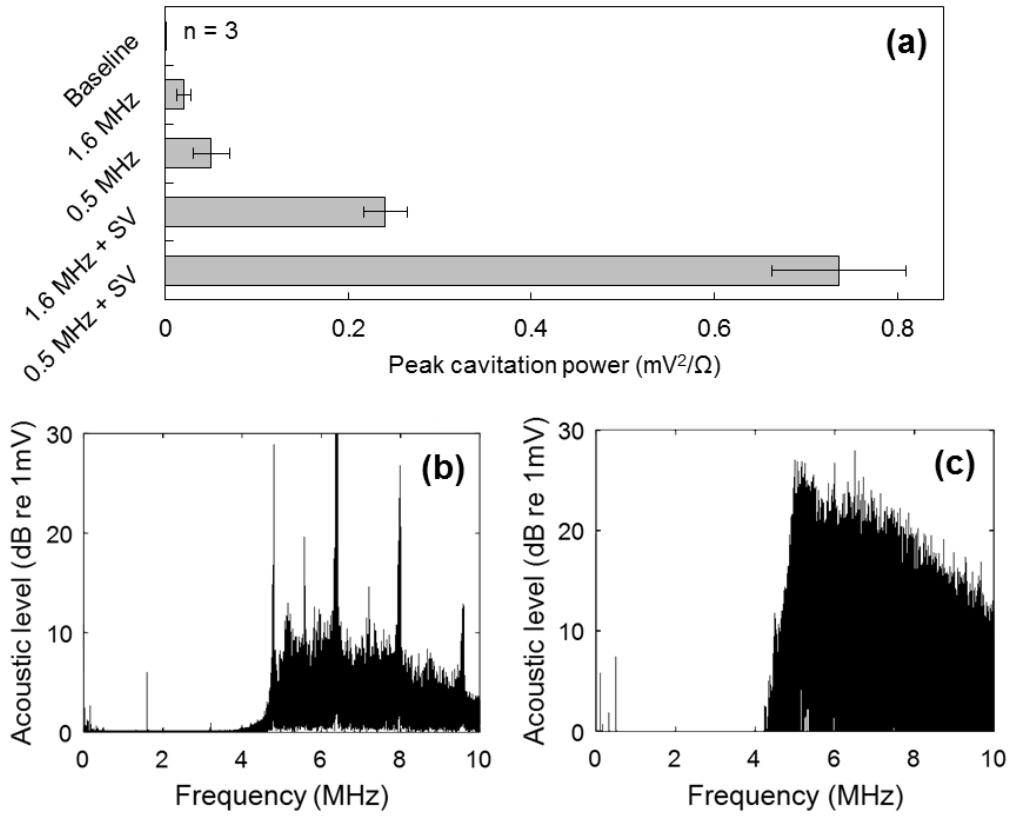

Figure 2.9 *Cavitation emissions **(a)** summarised as peak cavitation power for each experimental group, and typical examples of Fourier transforms of the passive cavitation detection (PCD) signals captured during exposure with SonoVue® microbubbles at 1 MPa for **(b)** 1.6 MHz and **(c)** 0.5 MHz.*

2.4 Discussion

2.4.1 Comparison of Predictions and Results

When comparing the computational and experimental results it can be seen that the model predicts almost negligible penetration distances in the non-cavitation regime. However in practice, cavitation activity was detected even without artificially introduced cavitation nuclei. The peak power of cavitation emissions was calculated by $\frac{peak\ PCD\ voltage(mV)^2}{circuit\ resistance(\Omega)}$, and was found to be raised above the baseline level when the sample was exposed to ultrasound alone at 1.6 MHz and 0.5 MHz. This spontaneous cavitation activity resulted in some particle transport, even without a cavitation agent present. However, as expected, peak cavitational power was significantly greater when SV microbubbles were introduced, giving over 12 times

more cavitation power when compared to ultrasound alone. Figure 2.9 shows the cavitation behaviour recorded during exposure using SV at 1.6 MHz and 0.5 MHz, with clear harmonic peaks present at 1.6 MHz and a broadband frequency response at 0.5 MHz.

Greater qualitative agreement for penetration depths is seen when computational predictions and experimental observations are compared in the cavitation regime, supporting the hypothesis that increasing particle density increases penetration depth. Furthermore, SV excited at 0.5 MHz was both predicted and observed to induce greater particle transport than at 1.6 MHz. It should be emphasised, however, that the computational model implemented in the current study is a substantial simplification of the true experimental conditions experienced by the suspended nanoparticle. Firstly, the simulation is only concerned with a single-bubble-single-particle interaction, negating bubble-bubble or particle-particle interactions. In reality a population of microbubbles was observed, with a size distribution spanning a range of radii and resonant frequencies. Furthermore the nanoparticle is assumed to be rigid and sufficiently small that the scattered pressure field is negligible; therefore the incident pressure field is assumed to be unchanged by the presence of the particle.
The value of using a simple numerical model to predict ultrasound-mediated transport of nanoparticles has been shown in the context of elucidating the impact of nanoparticle density on penetration depth. In future work, however, it may be advantageous to add complexity to such a simulation, allowing the confines of a viscoelasticity vessel to be accounted for (Sassaroli *et al.* 2005), rather than a free-field bubble, as well as bubble-bubble interactions (Parlitz *et al.* 1999, Lauterborn *et al.* 2010) (section 5.3.1).

The tissue mimicking phantom, 1 % concentration (weight/volume %) agarose gel, was chosen because of its similar acoustic properties to tissue. The gel also has a porous structure, and at 1 % concentration the pore size has been measured as 200 – 500 nm (Narayanan *et al.* 2006,

Maaloum *et al.* 1998) depending on the measurement technique used, either absorbance or atomic force microscopy. This size range is similar to that of the pore sizes observed between endothelial cells in cancerous vasculature, found to be 50 – 400 nm (Yuan *et al.* 1995). However, the homogeneity of this model must be acknowledged, and thus an agarose gel is inherently limited in representing the complex and chaotic structure of the cancerous tumour. Nevertheless, many studies have shown good agreement between penetration depths achieved in *in vitro* experiments carried out in cell-embedded agarose phantoms and *in vivo* studies (Carlisle *et al.* 2013, Mo *et al.* 2015). To enable translation into an *in vivo* context, further investigations using a more realistic vessel model to study the influence of particle density on ultrasound-mediated transport are recommended. Potential methods include using a dissected section of vessel or a tissue-engineered vascular graft (Mitchell *et al.* 2003).

As discussed in the introduction, the results support the hypothesis that increased density played a significant role in enhancing the penetration depth of the modified adenovirus studied by Mo *et al.* (2015), where the influence of a 2.4 times density increase was studied between an unmodified and a gold-coated virus. In the current study PDA-Au particles (5.58 g/cm^3) provided a 5.1 times increase in density compared to PDA-PS (1.10 g/cm^3), and achieved significantly greater ultrasound-mediated penetration depths compared to their less dense counterparts ($p < 0.05$).

The potential applications of the current findings have applicability far beyond the field of virotherapy, arguably to all five major categories of tumour-targeted therapeutic – liposomal drug carriers, polymer-based carriers, micelles, solid nanoparticles (lipid-based, viral and 'multistage') and antibodies – which could incorporate an inert, biocompatible heavy metal, such as gold.

2.5 Conclusions

The overall conclusion of this study is that the penetration depth achieved by a nanoparticle under ultrasound exposure is significantly influenced by particle density. It has been shown that a denser particle will be transported further when exposed to ultrasound and cavitating microbubbles than its less dense counterpart, and hence the first research question has been addressed. Having a greater mass means a particle will have greater momentum when entering the tissue. This momentum leads to an enhanced penetration depth, as expressed through the ballistics model used in section 2.2.1 (equation 2.7).

It has also been shown that SonoVue® microbubbles exposed to ultrasound at a frequency of 0.5 MHz induce greater nanoparticle transport than during exposure at 1.6 MHz, due to the higher microstreaming velocities. A far greater impact on particle transport was predicted and observed in regimes with substantial cavitation activity (and associated microstreaming), relative to regimes where acoustic streaming and radiation force alone were active. Since limited penetration depth of nanoscale therapeutics is a current limitation in oncolytic drug delivery, these findings are important in designing density-modified drug carriers that can penetrate deep into cancerous tumours.

However, the limitations of this work should be addressed. Firstly the transport of nanoparticles from a stationary fluid bears limited resemblance to a clinical context where therapeutics are transported from flow conditions found within the vasculature. Furthermore, a limited range of cavitation behaviour was investigated in the current study, namely only one type of cavitation agent, at one concentration and in a stationary fluid. As the field of ultrasound-mediated drug delivery has grown, a variety of cavitation agents have been developed to enhance delivery, offering the potential for smaller and more stable agents than

SonoVue®. The following chapter will look to address these limitations, developing the *in vitro* model to a flow vessel phantom, and comparing micro- and nano-scale cavitation agents.

In summary, the clinical application of nanoscale therapeutics often require the use of a protective coating – to hide the therapeutic from the immune system, to slow clearance from the blood stream, or to encapsulate smaller drug molecules. It is possible then to conceive designing a coating not only for pharmacological benefits but also for density-enhanced delivery

References

Bhatnagar, S., Schiffter, H. and Coussios, C.C., '*Exploitation of Acoustic Cavitation-Induced Microstreaming to Enhance Molecular Transport*', Journal of Pharmaceutical Sciences, 2014, 103(6), 1903-1912.

Blanco, E., Shen, H. and Ferrari, M., '*Principles of nanoparticle design for overcoming biological barriers to drug delivery*', Nature Biotechnology, 2015, 33(9), 941-951.

de Bruyn, J.R., and Walsh, A. M., '*Penetration of spheres into loose granular media*', Canadian Journal of Physics, 2004, 82(6), 439-446.

Carlisle, R., Choi, J., Bazan-Peregrino, M., Laga, R., Subr, V., Kostka, L., Ulbrich, K., Coussios, C.C. and Seymour, L.W., '*Enhanced tumour uptake and penetration of virotherapy using polymer stealthing and Focused Ultrasound*', Journal of the National Cancer Institute, 2013, 105(22), 1701–1710.

Chen, X., Yan, Y., Müllner, M., van Koeverden, M. P., Noi, K. F., Zhu, W., and Caruso, F., '*Engineering fluorescent poly (dopamine) capsules*', Langmuir, 2014, 30(10), 2921-2925.

Doinikov, A. A., and Bouakaz, A., '*Acoustic microstreaming around a gas bubble*', The Journal of the Acoustical Society of America, 2010, 127(2), 703-709.

Dougherty, T.J. and Marcus, S.L., '*Photodynamic therapy*', European Journal of Cancer, 1992, 28(10), 734-1742.

Hobbs, S.K., Monsky, W.L., Yuan, F., Roberts, W.G., Griffith, L., Torchilin, V.P. and Jain, R.K., '*Regulation of transport pathways in tumor vessels: role of tumor type and microenvironment*', Proceedings of the National Academy of Sciences, 1998, 95(8), 4607-4612.

Kamaly, N., Xiao, Z., Valencia, P.M., Radovic-Moreno, A.F. and Farokhzad, O.C., '*Targeted polymeric therapeutic nanoparticles: design, development and clinical translation*', Chemical Society Reviews, 2012, 41(7), 2971-3010.

Keller, J.B., and Miksis, M., '*Bubble oscillations of large amplitude*', The Journal of the Acoustical Society of America, 1980, 68(2), 628-633.

Lauterborn, W. and Kurz, T., '*Physics of bubble oscillations*', Reports on Progress in Physics, 2010, 73(10), 1-88.

Lea-Banks, H., Teo, B., Stride, E. and Coussios, C.C., *'The effect of particle density on ultrasound-mediated transport of nanoparticles'*, Physics in Medicine and Biology, 2016, 61(22), 7906-7918.

Lübbe, A.S., Alexiou, C. and Bergemann, C., '*Clinical applications of magnetic drug targeting*', Journal of Surgical Research, 2001, 95(2), 200-206.

Narayanan, J., Jun-Ying, X., and Xiang-Yang, L., '*Determination of agarose gel pore size: Absorbance measurements vis a vis other techniques*', Journal of Physics: Conference Series, 2006, 28, 83–86.

Maaloum, M., Pernodet, N. and Tinland, B., '*Agarose gel structure using atomic force microscopy: gel concentration and ionic strength effects*', Electrophoresis, 1998, 19(10), 1606-1610.

Maeda, H., '*Tumor-selective delivery of macromolecular drugs via the EPR effect: background and future prospects*', Bioconjugate chemistry, 2010, 21(5), 797-802.

Marmottant, P., van der Meer, S., Emmer, M., Versluis, M., de Jong, N., Hilgenfeldt, S. and Lohse, D., '*A model for large amplitude oscillations of coated bubbles accounting for buckling and rupture*', The Journal of the Acoustical Society of America, 2005, 118(6), 3499-3505.

van der Meer, S.M., Dollet, B., Voormolen, M.M., Chin, C.T., Bouakaz, A., de Jong, N., Versluis, M. and Lohse, D., '*Microbubble spectroscopy of ultrasound contrast agents*', The Journal of the Acoustical Society of America, 2007, 121(1), 648-656.

Minchinton, A.I. and Tannock, I.F., '*Drug penetration in solid tumours*', Nature Reviews Cancer, 2006, 6(8), 583-592.

Mitchell, S.L., and Niklason, L.E., '*Requirements for growing tissue-engineered vascular grafts*', Cardiovascular Pathology, 2003, 12(2), 59-64.

Mo, S., Coussios, C.C., Seymour, L. and Carlisle, R., '*Ultrasound-enhanced drug delivery for cancer*', Expert Opinion on Drug Delivery, 2012, 9(12), 1525-1538.

Mo, S., Carlisle, R., Laga, R., Myers, R., Graham, S., Cawood, R., Ulbrich, K., Seymour, L., Coussios, C.-C., '*Increasing the density of nanomedicines improves their ultrasound-mediated delivery to tumours*', Journal of Controlled Release, 2015, 210, 10-18.

Parlitz, U., Mettin, R., Luther, S., Akhatov, I., Voss, M. and Lauterborn, W., '*Spatio–temporal dynamics of acoustic cavitation bubble clouds*', Philosophical Transactions of the Royal Society of London A: Mathematical, Physical and Engineering Sciences, 1999, 357(1751), 313-334.

Popović, Z., Liu, W., Chauhan, V.P., Lee, J., Wong, C., Greytak, A.B., Insin, N., Nocera, D.G., Fukumura, D., Jain, R.K. and Bawendi, M.G., '*A nanoparticle size series for in vivo fluorescence imaging*', Angewandte Chemie, 2010, 122(46), 8831-8834.

Prabhakar, U., Maeda, H., Jain, R.K., Sevick-Muraca, E.M., Zamboni, W., Farokhzad, O.C., Barry, S.T., Gabizon, A., Grodzinski, P. and Blakey, D.C., '*Challenges and key considerations of the enhanced permeability and retention effect for nanomedicine drug delivery in oncology*', Cancer Research, 2013, 73(8), 2412-2417.

Sassaroli, E. and Hynynen, K., '*Resonance frequency of microbubbles in small blood vessels: a numerical study*', Physics in Medicine and Biology, 2005, 50(22), 5293 - 5305.

Schneider, M., Arditi, M., Barrau, M.B., Brochot, J., Broillet, A., Ventrone, R. and Yan, F., '*BR1: a new ultrasonographic contrast agent based on sulfur hexafluoride-filled microbubbles'*, Investigative Radiology, 1995, 30(8), 451-457.

Vokurka, K., '*Amplitudes of free bubble oscillations in liquids',* Journal of Sound and Vibration, 1990, 141(2), 259-275.

Wilhelm, S., Tavares, A.J., Dai, Q., Ohta, S., Audet, J., Dvorak, H.F. and Chan, W.C., 2016. '*Analysis of nanoparticle delivery to tumours*', Nature Reviews Materials, 2016, 1, 1-12.

Yuan, F., Dellian, M., Fukumura, D., Leunig, M., Berk, D. A., Torchilin, V. P., and Jain, R. K., '*Vascular permeability in a human tumor xenograft: molecular size dependence and cutoff size*', Cancer Research, 1995, 55(17), 3752-3756.

Chapter 3: **Enhanced delivery of density-modified nanoparticles using ultrasound: Comparing the influence of micro- and nano-scale cavitation nuclei**

Abstract

New strategies are required to enhance the penetration and tumour-wide distribution of cancer therapeutics, including viruses, antibodies and oligonucleotides. It was shown in the previous chapter that increasing the density of a nanoparticle can enhance its ultrasound-mediated transport, particularly under the influence of cavitation-induced microstreaming. The current study investigates how the physical characteristics and dynamics of different cavitation nucleation agents affect the cavitation-mediated transport of density-modified therapeutics. SonoVue® (Bracco, Milan, Italy), a microbubble contrast agent with a median diameter of 3 μm and polymeric gas-entrapping nanoparticles with a mean particle diameter of 480 nm were compared. Under the same ultrasound exposure conditions (centre frequencies of either 0.5 MHz or 1.6 MHz, and peak negative pressures from 0.2 MPa to 3.5 MPa) the acoustic emissions from the two agents were found to differ in magnitude, frequency composition and duration. The resultant penetration depths of co-injected bespoke density-modified nanoparticles in a tissue-mimicking phantom were also found to vary, with the polymeric gas-entrapping nanoparticles giving rise to greater penetration distances for the same acoustic energy. These results demonstrate that both the characteristics of the therapeutic and the cavitation nuclei can significantly influence ultrasound-mediated drug delivery.

3.1 Introduction

In the treatment of cancer, scientists and clinicians have an ever-growing toolbox of biological therapeutics at their disposal. Families of biological therapeutic agents such as viruses, antibodies and oligonucleotides have been shown to have high efficacy in treating cancerous cells in many *in vitro* models (Mo *et al.* 2015, Tanaka *et al.* 2007, Lee *et al.* 2017) when the therapeutic is in close proximity to the target cell (figure 3.1(A)). However, each of these families of biological agents all face the same delivery challenge: moving from the vasculature and penetrating deep into the surrounding tumour tissue. Histological studies have shown 150 µm to be the furthest distance a viable cancer cell can survive from the nearest vessel (Jain 1987) (figure 3.1(C)). This sets the target length scale for enhanced therapeutic penetration.

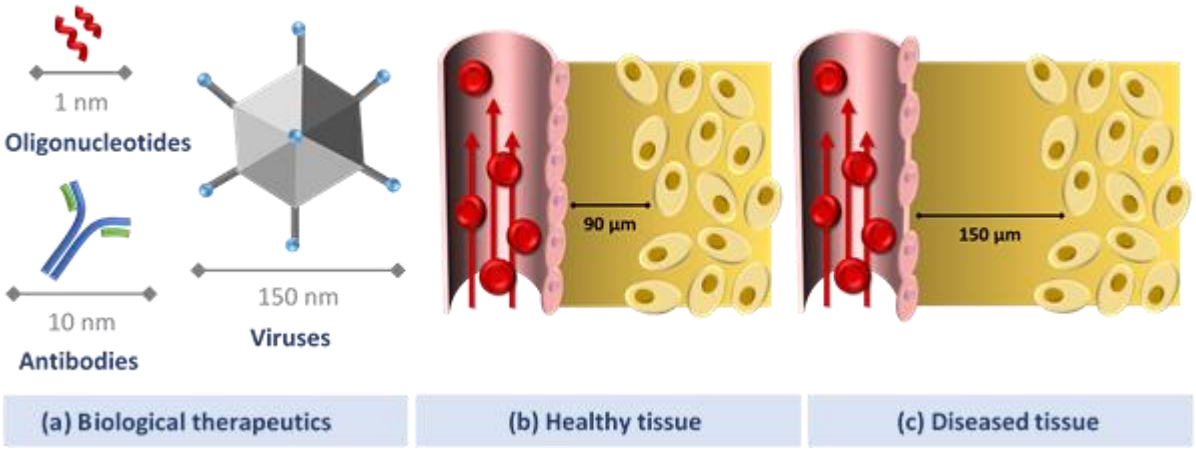

Figure 3.1 *Schematics of **(A)** biological therapeutics, including oligonucleotides, antibodies and viruses; **(B)** healthy tissue, including a cross-section of blood vessel with tight endothelial cells and surrounding tissue cells separated by 90 µm of interstitial space; **(C)** diseased tissue, including a cross-section of blood vessel with leaky endothelial cells and surrounding tissue cells separated by 150 µm of interstitial space.*

The following chapter will investigate whether penetration depths of this order can be achieved *in vitro* through (1) the choice of cavitation agent – either a commercially available ultrasound contrast agent or a polymeric gas-entrapping nanoparticle – and (2) the density modification of a mock therapeutic, with particle densities spanning 1.1 to 5.3 g/cm^3.

3.1.1 Research Questions

In the previous chapter it was demonstrated that particle density influences the peak penetration depth of nanoparticles when transported by ultrasound-mediated cavitation activity in a simple static tissue phantom. However, the specific acoustic excitation conditions needed to observe density-enhanced transport require further investigation: is a particular magnitude or duration of cavitation activity required? The effect of flow in the surrounding medium, as found in blood vessels, must also be investigated.

In the previous chapter the commercially available contrast agent SonoVue® was used to generate cavitation. In this chapter both SonoVue® – a micro-scale lipid-coated bubble – and a nano-scale polymeric gas entrapping nanoparticle will be utilised to investigate the effect of the type of cavitation agent upon particle transport.

Finally, this chapter will investigate whether there is a relationship between the acoustic emissions produced by cavitation and nanoparticle extravasation, with a view to determining the viability of real-time non-invasive treatment monitoring.

Thus this chapter aims to answer research questions 2-4, outlined in chapter 1:

2) What influence does the choice of ultrasound exposure parameters have on the transport of density-contrasting nanoparticles, and is this dominated by acoustic streaming and radiation force effects, or by cavitation-mediated microstreaming?

3) What influence does the choice of cavitation agent have on the cavitation-enhanced transport of density-contrasting nanoparticles?

4) Can acoustic emissions be used to predict the transport and penetration depth of density-contrasting nanoparticles?

3.2 Methodology

Dr Boon Teo and Dr Luca Bau are gratefully acknowledged for their help in establishing the following protocol for the fabrication of fluorescently labelled density-modified nanoparticles.

3.2.1 Bespoke fluorescent density-modified nanoparticles

To investigate further the role of particle density in ultrasound-mediated delivery of nanoparticles, density contrasting nanoparticles with unique fluorescent tags were fabricated. The following section describes a two-stage protocol for fabricating and characterising a set of three bespoke fluorescent density-modified nanoparticles, consisting of a polystyrene (PS), silica (SiO_2) or gold (Au) core, surrounded by a poly-dopamine (PDA) shell and an outer fluorescent protein corona formed from a bovine serum albumin (BSA)-dye conjugate (figure 3.2). The final particles were characterised using a variety of techniques including transmission electron microscopy (TEM) to assess shape and size, dynamic light scattering (DLS) to assess size and zeta-potential, nanoparticle tracking analysis (NTA) to measure concentration and confocal imaging for fluorescence characterisation.

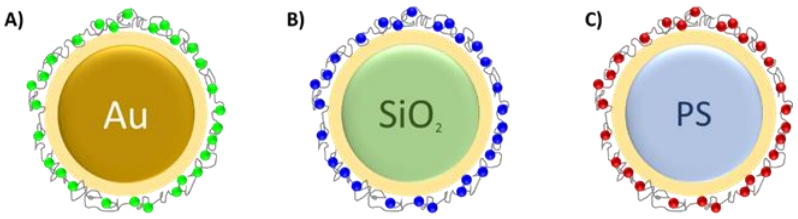

Figure 3.2 *Schematic of bespoke fluorescent density-modified nanoparticles **(A)** gold BSA-FITC-PDA-Au, **(B)** silica BSA-AMCA-PDA-SiO2, **(C)** polystyrene BSA-RITC-PDA-PS.*

3.2.1.1 Nanoparticle synthesis

Materials

Polyvinylpyrrolidone (PVP) (M_w ~ 10,000), N,N-Dimethylformamide (DMF) (99.8 %), gold(III) chloride trihydrate (99.9 %), sodium citrate dihydrate (99 %), tris(hydroxymethyyl) aminomethane (Tris) (99.8 %), hydrochloric acid (HCl), dopamine hydrochloride (98 %), bovine

serum albumin (98 %) (BSA), fluorescein 5(6)-isothiocyanate (90 %) (FITC), rhodamine B isothiocyanate (mixed isomers) (RITC), dimethyl sulfoxide (DMSO), sodium bicarbonate ($NaHCO_3$) and sucrose (for molecular biology) (99.5 %) were all purchased from Sigma-Aldrich (Dorset, UK) and used without further purification. Additionally, AMCA-X, SE (6-((7-amino-4-methylcoumarin-3-acetyl)amino)hexanoic acid, succinimidyl ester) (AMCA) was purchased from Fisher Scientific (Loughborough, UK). Deionised (DI) Milli-Q water was used throughout the fabrication. Polystyrene and silica 100 nm spherical particles were sourced from Sigma-Aldrich (Dorset, UK) and nanoComposix (San Diego, CA, US) respectively. Gold 100 nm particles were fabricated following the protocol described by Chirea (2013) using a seed-mediated method and citrate reduction. The dense cores were characterised in size and zeta potential using DLS, results from which are shown in table 3.1.

Polymerisation of dopamine to form a shell of poly-dopamine (PDA) around the dense nanoparticle core was carried out in order to give each particle the same surface chemistry, and, in the case of the gold construct, to create a buffer between the core and the fluorophore with the aim of reducing quenching. The PDA shell was formed following the protocol described by Barbosa *et al.* (2010), by oxidative self-polymerisation of dopamine onto the particle surface. PDA-coated nanoparticles were prepared in a 10 mM Tris buffer at pH 8.5. Dopamine hydrochloride was added to particles in suspension in the Tris buffer, in weight/weight ratio of 1:1, dopamine to particles, i.e. to 2 mL of Tris buffer was added 20uL of 10 % solid dense particle cores and 2 mg of dopamine chloride. The suspension was stirred for 30 mins, or until an increase in particle diameter of 100 nm was observed, resulting in PDA-coated particles of 200 nm.

Table 3.1 *Nanoparticle characterisation measurements taken with dynamic light scattering (DLS), showing size, size distribution and zeta potential of particles during fabrication stages.*

	Sizing (Z-average)			***Zeta potential (zp)***		
Dense core 	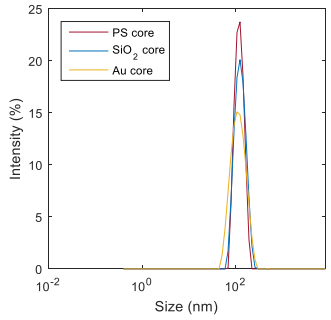			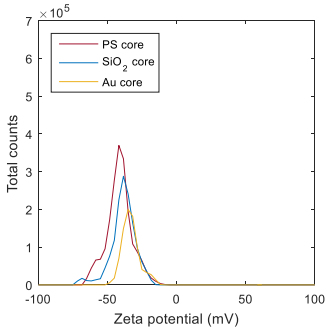		
	PS	**SiO_2**	**Au**		**PS**	**SiO_2**	**Au**
Size (d.nm)	115.9 ± 2.3	118.5 ± 2.1	94.0 ± 4.6	***zp (mV)***	-41.5 ± 1.0	-39.2 ± 1.2	-34.3 ± 1.2
PdI	0.01	0.06	0.18				
PDA-coated particle 	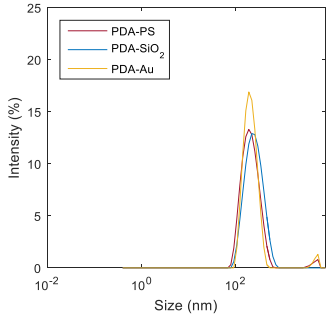			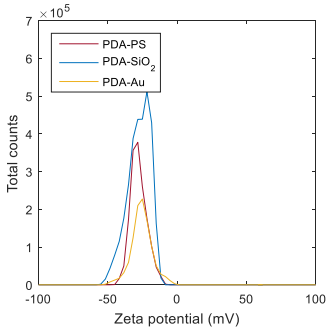		
	PS	**SiO_2**	**Au**		**PS**	**SiO_2**	**Au**
Size (d.nm)	196.1 ± 3.8	219.4 ± 4.1	205.3 ± 5.5	***zp (mV)***	-28.7 ± 0.8	-27.1 ± 0.5	-25.0 ± 0.8
PdI	0.18	0.15	0.19				
BSA-dye labelled particle 	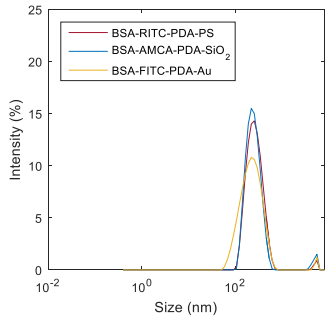			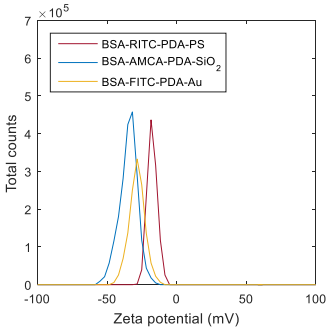		
	PS	**SiO_2**	**Au**		**PS**	**SiO_2**	**Au**
Size (d.nm)	251.9 ± 3.7	243.7 ± 3.9	252.0 ± 5.1	***zp (mV)***	-17.7 ± 0.5	-34.4 ± 0.6	-27.4 ± 1.3
PdI	0.19	0.21	0.19				

The PDA-coated particles, in aqueous suspension at pH 7.4, were characterised in terms of their size and zeta potential (zp) using DLS, the results from which are shown in table 3.1. DLS uses a laser to characterise particle movement through the change in the speckle pattern caused by scattered light from the sample. A prediction of particle size is calculated from the rate of movement due to Brownian motion, which is dependent on the hydrodynamic diameter of the particle (Berne *et al.* 1976). The zeta potential describes the electrostatic potential or the magnitude of charge between particles at the particle surface, and is dependent on, amongst other things, the ionic strength of the surrounding fluid (Hunter 2013).

Selection of fluorophores

It should be noted that fluorescence may be induced simply by adding hydrogen peroxide, inducing oxidation which in turn produces a fluorescent signal (excitation 400 nm, emission 480 nm) (Chen *et al.* 2014) as shown in chapter 2. However, attaching commercial fluorophores gives a more intense signal and allows greater flexibility in emission colour.

Selection of the fluorophores was based on two requirements. First, the need to provide the correct functional group to achieve coupling with BSA, and second, compatibility of emission and excitation wavelengths between dyes to achieve good separation of emission peaks. To form the BSA-dye conjugate, compatible dyes were selected; these were amine-reactive so that they could bind with the ε-amino group of lysines of albumin (De Lumen *et al.* 1970) (figures 3.3(A)-(C)). To ensure no cross-talk between fluorophores, good separation of emission peaks was necessary. To fulfil both of these requirements, FITC (excitation wavelength 495 nm, emissions wavelength 525 nm), RITC (excitation wavelength 543 nm, emission wavelength 580 nm) and AMCA (excitation wavelength 353 nm, emission wavelength 442 nm) were chosen (figure 3.3(D)).

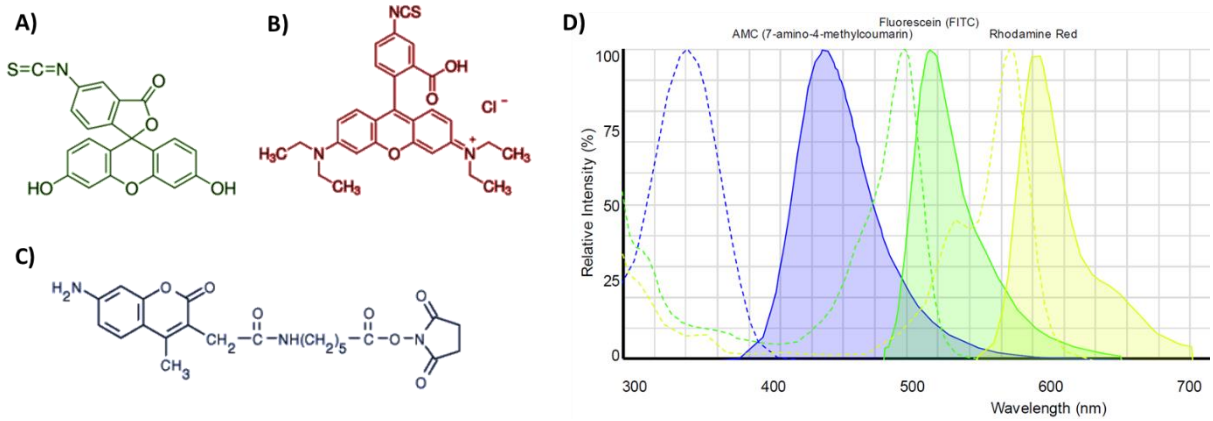

Figure 3.3 *Structural formulae of **(A)** Fluorescein 5(6)-isothiocyanate, **(B)** Rhodamine B isothiocyanate, **(C)** AMCA-X, SE (6-((7-amino-4-methylcoumarin-3-acetyl)amino)hexanoic acid, succinimidyl ester), with respective excitation and emission peaks **(D)** ('Fluorescence SpectraViewer', Thermo Scientific).*

Fabrication of protein-dye conjugate

BSA-dye conjugates were prepared by dissolving BSA (5 mg/mL) into a 0.05 M solution of $NaHCO_3$ at pH 10. The dry fluorophore was then dissolved in DMSO at a ratio of 1 mg dye to 100 µL solvent. 300 µL of dye solution was combined dropwise to 6 mL of protein solution and stirred in dark conditions overnight. The combined protein-dye solution was then freeze dried at -30 °C for 48 hours. Freeze drying the BSA-dye conjugates allowed stable storage and resulted in efficient BSA-dye loading onto the nanoparticle.

The BSA-dye was added to the PDA-particle solution (1 mg/mL), stirring, for 12 hours before thorough washing by centrifugation in DI Milli-Q. Adsorption of the BSA-dye conjugate onto PDA surface formed a fluorescent protein corona (Zhu *et al.* 2011, Rahman *et al.* 2013), inducing a further increase in hydrodynamic radius (table 3.1).

3.2.1.2 Nanoparticle characterisation

The final constructs were again characterised using DLS to determine their size, size distribution and zeta potential (table 3.1). Nanoparticle Tracking Analysis (NTA) using the NanoSight (LM-20, Malvern Instruments, Malvern, UK) was used to assess the concentration of the final constructs, which were found to have an average value of $8.01 \pm 1.3 \times 10^9$ particles/mL. NTA was also used to perform a second size measurement, values from which agree with DLS measurements to within 8 %. Shape and size were further characterised using TEM, where the shape of each coated particle tends to spherical in each case (figure 3.4).

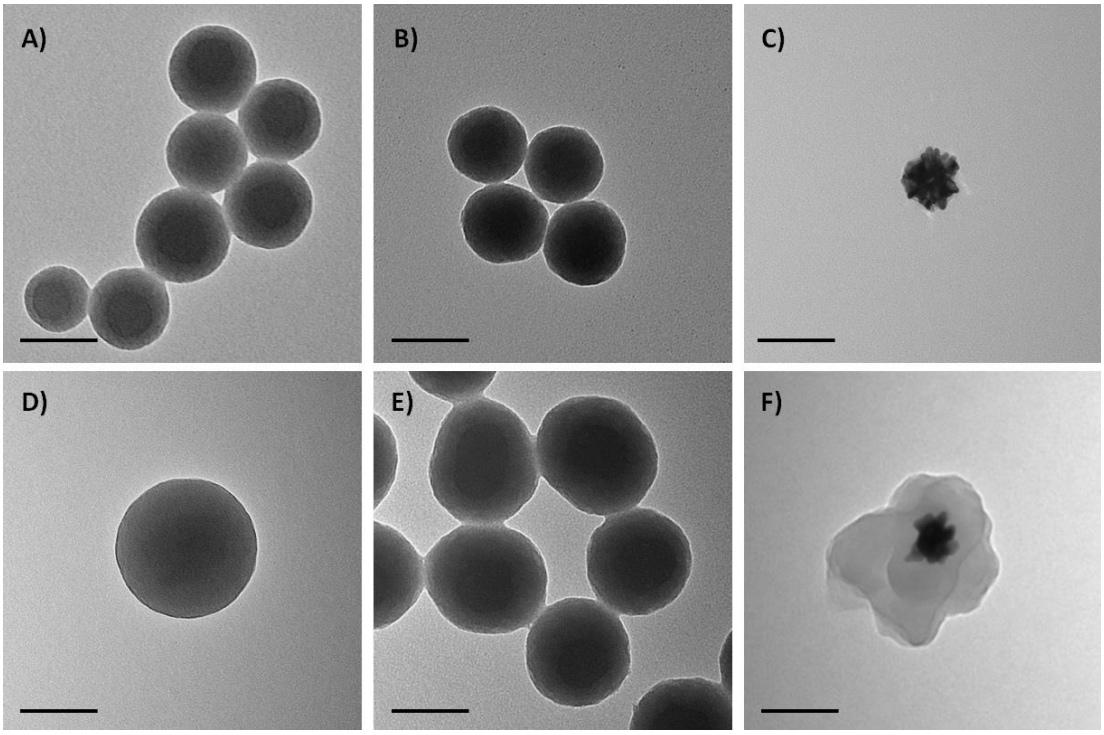

Figure 3.4 *TEM images of dense nanoparticle cores* ***(A)*** *polystyrene,* ***(B)*** *silica,* ***(C)*** *gold and BSA-PDA coated particles with cores of* ***(D)*** *polystyrene,* ***(E)*** *silica,* ***(F)*** *gold. Scale bar 100 nm.*

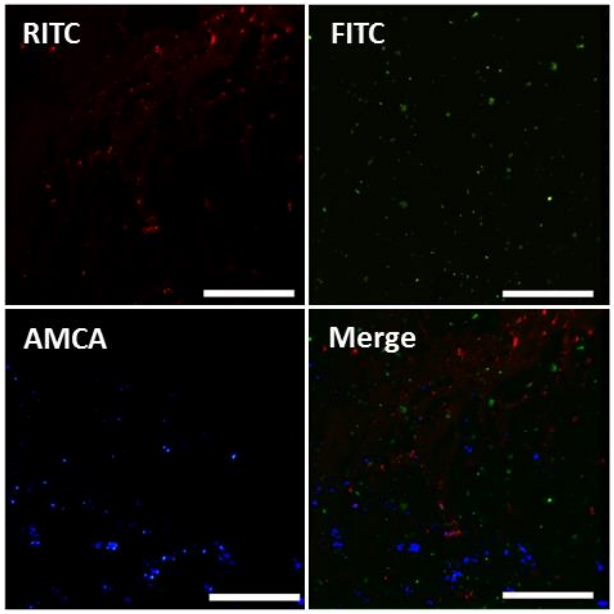

Figure 3.5 *Fluorescence confocal microscopy images of bespoke fluorescent density-modified nanoparticles, acquired with Plan-Apochromat objective at 63x magnification, showing each fluorescence channel individually and merged. Scale bar 100 µm.*

The final constructs were also imaged with a point-scanning fluorescence confocal microscope (Zeiss 780, Zeiss, Cambridge, UK). Figure 3.5 shows a three-channel image acquired using a 63x magnification oil immersion lens (Plan-Apochromat 63x/1.40 Oil DIC M27), where the BSA-RITC-PDA-PS, BSA-FITC-PDA-Au, and BSA-AMCA-PDA- SiO_2 particles are visible on the red, green and blue channels respectively. Confocal imaging confirmed that the particles had distinct locations across channels, showing minimal cross-bleed between channels, and sufficient fluorophore loading for particles to be detectable.

Density gradient centrifugation

A centrifugal separation method was chosen to quantify the particle density of the final constructs (Griffith 2010). The density gradient was formed in a 50 mL falcon tube using layered solutions of sucrose in weight percentage concentrations from 20 % to 70 % sucrose in aqueous solution. The layering was achieved by slowly pipetting each solution down the wall of the tube. Two sucrose density gradients were prepared: a control column using

nanoparticles with known densities, and the density study using the bespoke fluorescent density-modified nanoparticles. Both columns were prepared in the same way, with the top layer being a mixture of density particles. The control column used 200 nm particles of silver and silica (both nanoComposix, San Diego, CA, US), and 200 nm yellow polystyrene latex beads (Sigma-Aldrich, Dorset, UK), with known densities of 10.50 g/cm^3, 2.65 g/cm^3 and 1.04 g/cm^3 respectively (figure 3.6(A)).

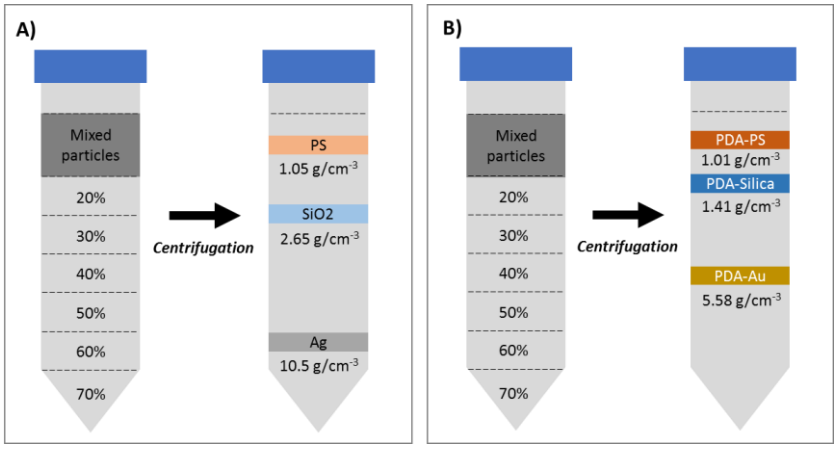

Figure 3.6 *Schematic of sucrose density gradients before and after centrifugation for the **(A)** control column and **(B)** density study using bespoke nanoparticles.*

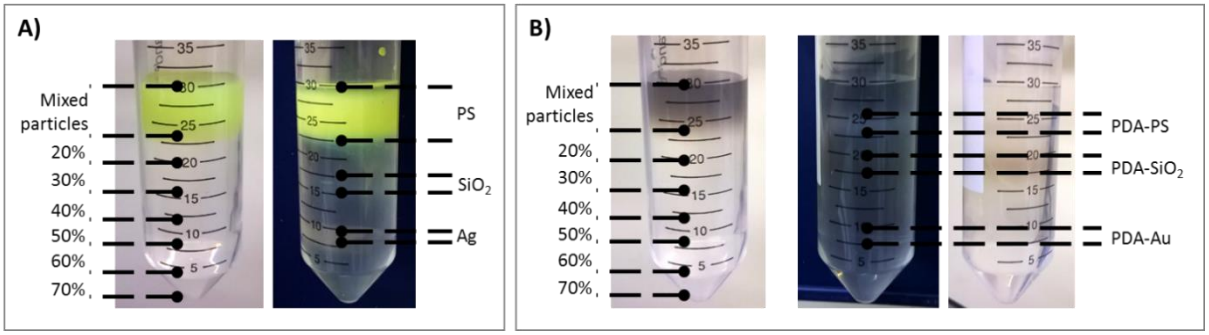

Figure 3.7 *Photographs of sucrose density gradients before and after centrifugation for the **(A)** control column and **(B)** density study using bespoke nanoparticles.*

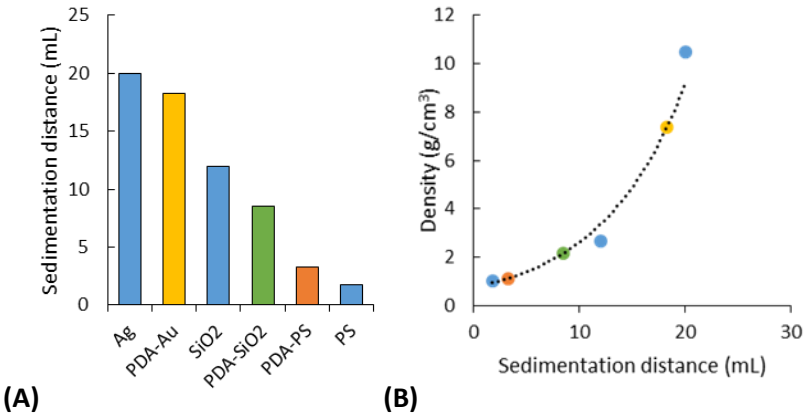

(A) **(B)** **(C)**

Particle	*Density (g/cm^3)*
Ag	10.50
PDA-Au	7.37
SiO_2	2.65
PDA- SiO_2	2.18
PDA-PS	1.13
PS	1.04

Figure 3.8 *Sedimentation distances of each particle population **(A)** used to form a standard curve **(B)** by correlating sedimentation distance and density. **(C)** Known (control particles Ag, SiO_2, PS) and measured (bespoke particles PDA-Au, PDA-SiO_2, PDA-PS) particle density values obtained from sucrose density gradient study.*

After centrifugation at 2190 g for 20 minutes, the three populations of particles in each tube were separated (figures 3.6 and 3.7). The sedimentation distances of the control populations were used to form a standard curve correlating particle density and sedimentation distance after 20 minutes. By reference to this curve the densities of the bespoke particles were quantified (figure 3.8).

3.2.2 *In vitro* experimental design

A flow channel phantom holder, with internal dimensions 100.0 x 50.0 x 5.0 mm, was designed by Dr Christophoros Mannaris and Megan Grundy, and machined by James Fisk to create an agarose vessel phantom, with mylar windows allowing entry and exit of ultrasound. Degassed 1 % weight/volume concentration agarose (UltraPure™ Low Melting Point Agarose, Invitrogen) was cast inside the phantom, surrounding three 1.0 mm diameter metal rods. Once the agarose had set (2 hours at 4 °C), the metal rods were removed, leaving three 1.0 mm diameter hollow channels. Using a perfusion pump (Minipuls Evolution, Gilson) attached via thin plastic tubing, the aqueous suspension of bespoke density-modified nanoparticles, co-

infused with the cavitation agent, could be passed through each flow channel in turn, at a rate of 0.6 mL/min to mimic the perfusion rate of human tumour tissue (Kallinowski *et al.* 1989).

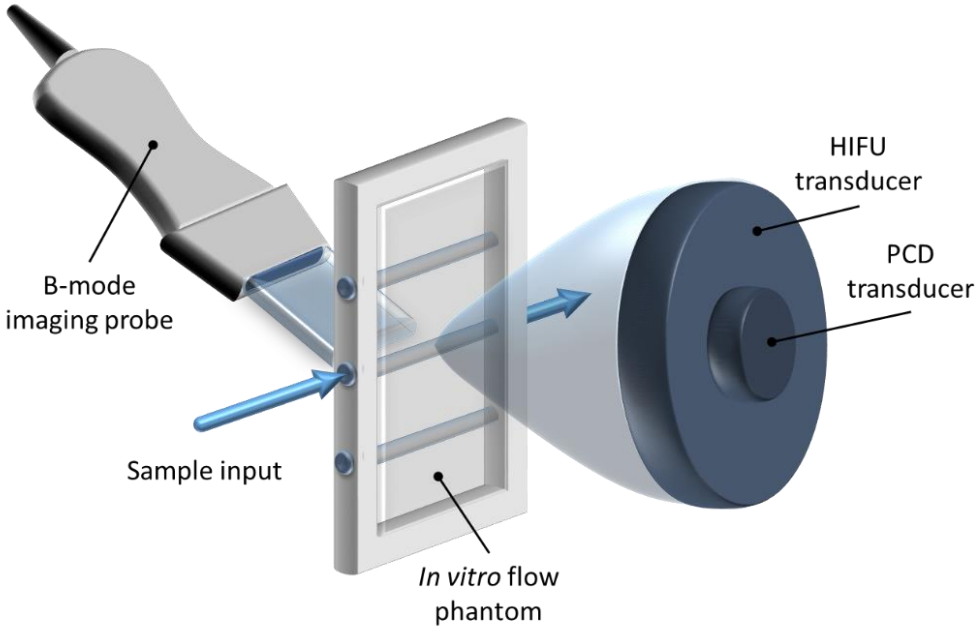

Figure 3.9 *In vitro experimental set-up, including three 1 mm diameter flow channels cast in an agar gel phantom, HIFU transducer, PCD transducer and B-mode imaging probe.*

The flow channel was aligned to the HIFU transducer (H107 013D, Sonic Concepts), centre frequency 0.5 MHz, aperture 64 mm, geometric focus 60 mm and focal size at the fundamental of 3.0 x 21.0 mm and 1.0 x 7.0 mm at the third harmonic (figure 3.9). Alignment was carried out using a pulser/receiver system (DPR300, JSR Ultrasonics), with the air-filled channel acting as a reflector. A single element unfocussed PCD transducer (V319, Panametrics), centre frequency 15 MHz, was housed in the centre of the HIFU transducer, within a circular cut-out, and co-axially aligned to the focus of the HIFU transducer, again aligned using the pulser/receiver system and the air-filled channel as a reflector. Signals detected by the PCD were passed through a high-pass filter (Allen Avionics Inc.), cut-off frequency 5 MHz, and then through a pre-amplifier (SR445A, Stanford Research Systems Inc.), at 5x amplification.

The channel boundaries and cavitation agents were visualised using a B-mode imaging probe (L12-5, Diagnostic Ultrasound System, iU22, Philips), enabling cavitation activity to be monitored qualitatively as bright flashes located at the HIFU focus. The linear probe was positioned at an obtuse angle relative to the PCD to prevent interference of the B-mode with the PCD signal. Amplification was provided by a power amplifier (ENI A300 #019667) connected to the HIFU transducer via a bespoke impedance matching network (S/N 013, Sonic Concepts).

Agarose at 1 % concentration was considered an appropriate tissue model for this model, since the material properties – including pore size and acoustic impedance – are similar to cancerous tissue (Pluen *et al.* 1999). Furthermore the gel is sufficiently optically transparent to enable subsequent microscopic examination.

3.2.3 Cavitation agents: *Comparing micro- and nano-scale cavitation nuclei*

The current study investigates the influence of two cavitation agents on the cavitation-mediated transport of density-modified nanoparticles: the commercially available ultrasound contrast agent, SonoVue® (Bracco, Milan, Italy), which has a distribution of bubble diameters between 1 and 10 µm, and polymeric gas-entrapping nanoparticles, referred to as NanoCups, with an average particle diameter of 480 nm (Kwan *et al.* 2015b). In addition to size, the two agents have a variety of contrasting features including stability (acoustically active lifetime of the agent), acoustic response and concentration, which are summarised in table 3.2.

Table 3.2 *Summary of characteristics for two cavitation agents – SonoVue® microbubbles (Bracco, Milan, Italy) and NanoCups (OxSonics, Oxford, UK).*

	SonoVue® microbubbles	 ***NanoCups***
Size	*Bubble diameter:* 1 – 10 µm	*Hydrodynamic particle diameter:* 480 nm *Crevice diameter:* 260 nm
Composition	*Gas:* Sulphur hexafluoride (SF_6) *Shell:* Mixture of phospholipids and emulsifiers	*Gas:* Air *Cup:* Hydrophobic polymer
Stability *Acoustically active lifetime of the agent*	Stable at room temperature for <2hours	Stable at room temperature for >1 month
Acoustic response		
Onset of narrowband emissions	~0.1 MPa *(at 0.5 MHz)*	No detectable harmonic response in the absence of broadband noise
Onset of broadband emissions	~0.35 MPa *(at 0.5 MHz)*	~0.5 MPa *(at 0.5 MHz)*
Concentration	10^7 bubbles/mL	10^{12} particles/mL
Estimated gas volume fraction	0.005 – 5.235 mm^3/mL	9.201 mm^3/mL
Particle volume fraction	0.005 – 5.235 mm^3/mL	24.347 mm^3/mL

Size

SonoVue® and NanoCups vary in size by approximately an order of magnitude, with SonoVue® spanning a range of bubble diameters from 1 – 10 µm (figure 3.10(A)), and NanoCups having a tighter size distribution, centred at 480 nm with spread quantified by a polydispersity index (PdI) of 0.14 (figure 3.10(B)). Since nanoscale agents have a diameter on the order of the phantom pore size and the fluorescent nanoparticle size, these small agents have the ability to follow particles into the surrounding medium. This feature may allow NanoCups to propel

nanoparticles further, with the combined effects of sustained cavitation response and sustained close proximity.

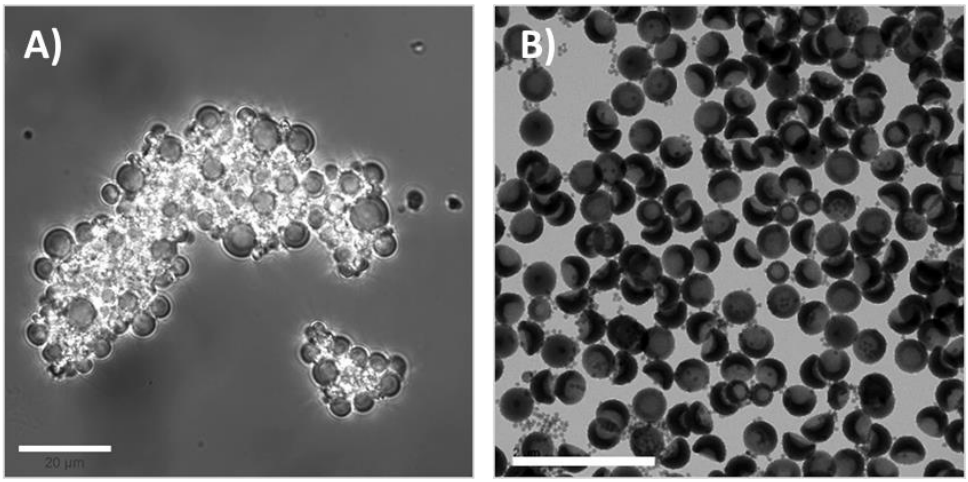

Figure 3.10 *Cavitation agents SonoVue® **(A)** imaged by confocal microscopy (scale bar 20 µm) and **(B)** NanoCups imaged by TEM – image curtesy of OxSonics (scale bar 2 µm).*

Composition

The two agents also differ significantly in composition and structure. SonoVue® consists of a lipid shell containing polyethylene glycol (PEG), distearoyl-phosphatidylcholine (DSPC) and dipalmitoylphosphatidylglycerol sodium (DPPG.Na), enclosing a gas core of sulphur hexafluoride (SF_6). SF_6 is a relatively inert and high molecular weight gas with low aqueous solubility, utilised to prevent premature dissolution of the bubble. In order to stabilise gas in a much smaller volume, NanoCups require a more rigid structure. This rigid semi-circular shell is formed from a copolymer containing methyl methacrylate, 2-hydroxymethyl methacrylate and divinylbenzene. After drying, this cup shaped structure is able to stabilise a gas pocket within the rough hydrophobic crevice (Kwan *et al.* 2015a).

Stability

In a static environment, SonoVue® microbubbles undergo two main forms of change. Firstly bubble coalescence may occur where clusters of bubbles fuse and give rise to larger bubbles.

Secondly, gas dissolution may occur, where the SF_6 within the microbubble can escape into the surrounding solution, forming smaller bubbles over time – a process that has been shown to occur over minutes (Gorce *et al.* 2000). In contrast, the NanoCup is able to stabilise a gas bubble because of its rough crevice shape and its hydrophobic surface. Kwan *et al.* (2015a) describes the comparison with a similar sized smooth polymer sphere which, when exposed to ultrasound parameters that have been shown to cause a NanoCup to inertially cavitate, produced no detectable cavitation emissions. Furthermore, NanoCups that had not been air dried also produced no detectable cavitation emissions, illustrating that both a rough crevice shape and air drying are required for the inertial cavitation behaviour exhibited by NanoCups.

Furthermore, this hydrophobic crevice provided by the polymeric cup prevents gas dissolution over time, producing a stable cavitation agent at room temperature for over a month: assessed using a t-test ($p < 0.01$), there was found to be no statistically significant difference in total acoustic energy when the same batch was used 30 days apart (figure 3.11).

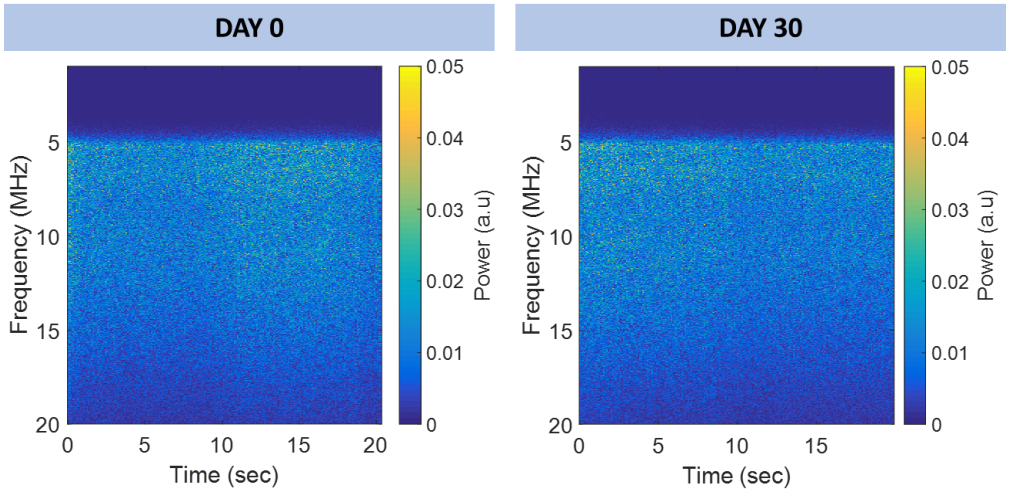

Figure 3.11. *Power spectra showing two samples of NanoCups from the same fabrication batch exposed at centre frequency 0.5 MHz, peak negative pressure 2.0 MPa for 20 seconds, on two occasions 30 days apart after being stored at room temperature.*

Acoustic response

The lipid coating of SonoVue® microbubbles stabilises them against small pressure fluctuations, allowing repeated expansion and contraction. This stable oscillatory motion produces harmonic emissions, an example of which is detected at peak negative pressure 0.2 MPa at 1.6 MHz (table 3.4). However, at higher pressures or lower frequencies the lipid coating is no longer able to contain the gas expansion induced by the rarefactional phase. As predicted by the Marmottant model (equation 1.5), the bubble will reach an expansion ratio whereby the lipid coating undergoes plastic deformation and will rupture. Uncontrolled expansion and violent collapse can be seen at 0.5 MHz at low pressures, giving an inertial cavitation threshold on the order of 0.4 MPa (Arvanitis *et al.* 2011, Lin *et al.* 2017). The term inertial cavitation threshold here is used to describe the lowest pressure for which inertial collapse of the bubble is observed experimentally as indicated by the onset of broadband acoustic emissions.

Added uncertainty in acoustic response from SonoVue® is associated with the size distribution and differences in surface coating (Rademeyer *et al.* 2015), whereby a variety of diameter bubbles are being excited simultaneously, each with a unique resonance frequency and inertial cavitation threshold (Gorce *et al.* 2000). Further complexity is associated with bubble-bubble interactions and shielding (Arora *et al.* 2007).

In contrast, the polymeric structure of NanoCups stabilises them against low and moderate pressure fluctuations, up to 0.5 MPa at 0.5 MHz (Kwan *et al.* 2015a), preventing any substantial detectable bubble response and no detectable harmonic emissions. However, once the activation threshold has been met, ~1.5 MPa (at 0.5 MHz), the gas pocket expands beyond the bounds of the cup, and may be pinched off altogether, forming (momentarily) a

free bubble. The term activation threshold is here used to mean the lowest pressure required to remove the bubble from the crevice.

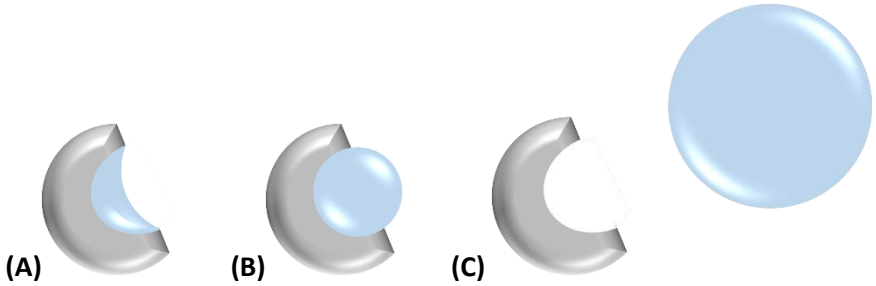

Figure 3.12 *Schematic of a NanoCup at **(A)** static pressure, and during positive and **(B)** negative pressure phases, and **(C)** beyond the inertial cavitation threshold where the bubble is pinched off from the polymeric cup.*

This effect can be studied in further detail by considering a crevice model (Harvey *et al.* 1944), where the shape of the meniscus is dependent on the contact angle of the gas/liquid/solid interface (Apfel 1984, Atchley and Prosperetti 1989). Once ultrasound is applied, the gas pocket will begin to respond to the sequential positive and negative pressure phases. During the positive pressure phase the radius of curvature becomes concave, the surface tension acts outwards towards the fluid, and the gas pocket is stabilised (figure 3.12(A)). During the negative pressure phase the gas pocket forms a convex radius, a radius of curvature positively extruding from the crevice into the surrounding fluid (figure 3.12(B)). In this regime surface tension acts towards the centre of the crevice and the pressure inside the gas-filled cavity drops. As the magnitude or duration of the negative pressure phase increases, the bubble expansion may be great enough to overcome the surface tension pinning the bubble to the cup. Once this threshold is traversed, the bubble may be pinched from the cup and detach into the surrounding fluid (figure 3.12(C)). In this final regime the lifespan of the free bubble is likely to be fleeting, since the pressure required to detach the bubble is equivalent to the pressure required for unstable bubble growth and violent collapse, as modelled by Kwan *et al.* (2015a, 2015b).

Concentration

In this study SonoVue® was used at a concentration corresponding to a 20-fold dilution, resulting in 10^7 bubbles/mL, as has been used previously (Mo *et al.* 2015). In contrast, NanoCups have been used at much higher concentrations, in previous studies and for this study, 10^{12} particles/mL (1 mg/mL) was selected. These particle concentrations give gas volume fractions (i.e. the total volume of gas injected per mL) of 0.005 – 5.232 mm^3 of gas per mL for SonoVue® and 9.201 mm^3 of gas per mL for NanoCups. However, it should be noted that the additional stabilisation provided by the hydrophobic polymeric cup allows a greater molar concentration of gas to be trapped per unit area compared to a lipid-coated bubble. Therefore once the gas has been released from the polymeric cup, the gas volume fraction is likely to be larger. Consequently it is useful to also consider the particle volume fraction, where we can compare the injected volume of cavitation agent, namely between 0.005 – 5.232 mm^3 per mL for SonoVue® and 24.347 mm^3 per mL for NanoCups.

3.2.4 Microscopy: *Sample preparation, imaging and quantification*

After ultrasound exposure, the phantom holder was disassembled and the agar sectioned using a razor blade to enable microscopic examination of the region surrounding the channels. The sections were placed onto a thin microscope slide (figure 3.13 (B)) and images were captured using fluorescence microscopy (Zeiss 780 scanning point laser confocal microscope) with either x10 or x20 magnification. A tile scan was acquired for each sample, by which the three fluorescence channels were captured simultaneously, along with a brightfield image for co-registration of the channel boundary (visible in brightfield) and the location of transported nanoparticles (visible in fluorescence) (figure 3.13 (C)). Thresholding was applied to the images using ImageJ software, to remove background noise and isolate the locations of fluorescent pixels.

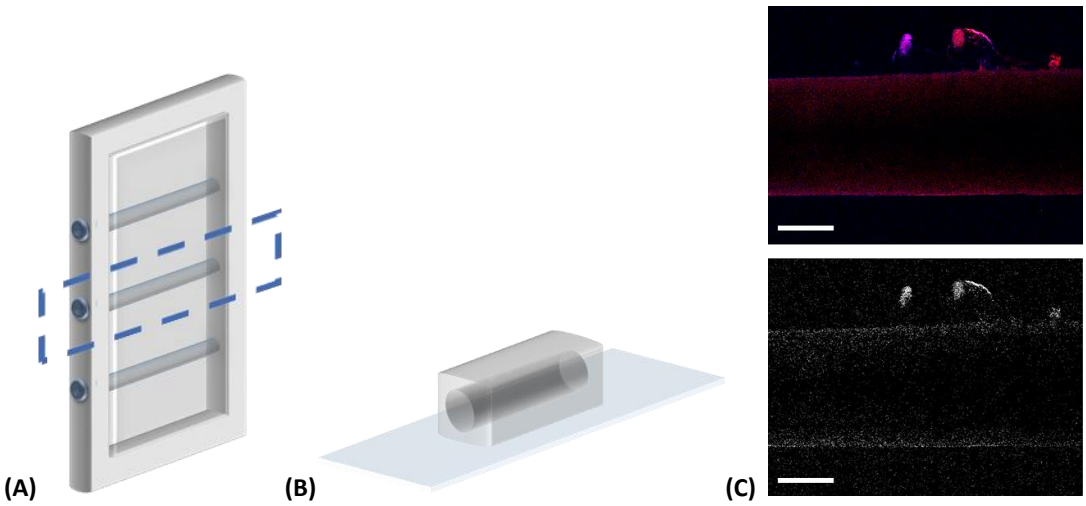

Figure 3.13 *Sample preparation including **(A)** isolation of individual channel from vessel phantom, **(B)** sample preparation for microscopy and **(C)** imaging and thresholding. Scale bars 500 µm.*

The resulting binary images were imported into Matlab to generate matrices of fluorescent pixel locations. In this way the peak penetration depth, i.e. the furthest location of fluorescent nanoparticles from the channel boundary, could be quantified.

3.2.5 Ultrasound exposure

As summarised in table 3.2 the cavitation agents investigated in this study exhibit significantly different acoustic responses, according to the ultrasound excitation. In order to explore a variety of cavitation regimes, peak negative pressures from 0.2 MPa to 3.5 MPa were used at pulse centre frequencies of either 0.5 MHz or 1.6 MHz (exploiting the fundamental and third harmonic frequencies of the HIFU transducer). Exposure duration was varied from 40 pulses to 5000 pulses, with fixed pulse length (5 ms), pulse period (100 ms) and pulse repetition frequency (10 Hz). Duty cycle was fixed between regimes, set at 5 % to encourage extravasation without causing significant thermal effects. Figure 3.14 illustrates the overall experimental matrix.

Total delivered acoustic energy

The parameter matrix below (figure 3.14) was designed such that total delivered acoustic energy might be equated across exposure regimes. Although the two cavitation agents exhibit very different acoustic behaviours, their respective cavitation activity will be exploited to convert a proportion of the incident acoustic energy into effective particle transport. The proposed approach provides a measure of particle transport efficiency for a given input acoustic energy. The total acoustic energy delivered is calculated by $\left(acoustic\ intensity\ (W/m^2) \times\ focal\ area\ (m^2) \times\ exposure\ duration\ (s)\right)$ at each ultrasound exposure regime, and is summarised in table 3.3.

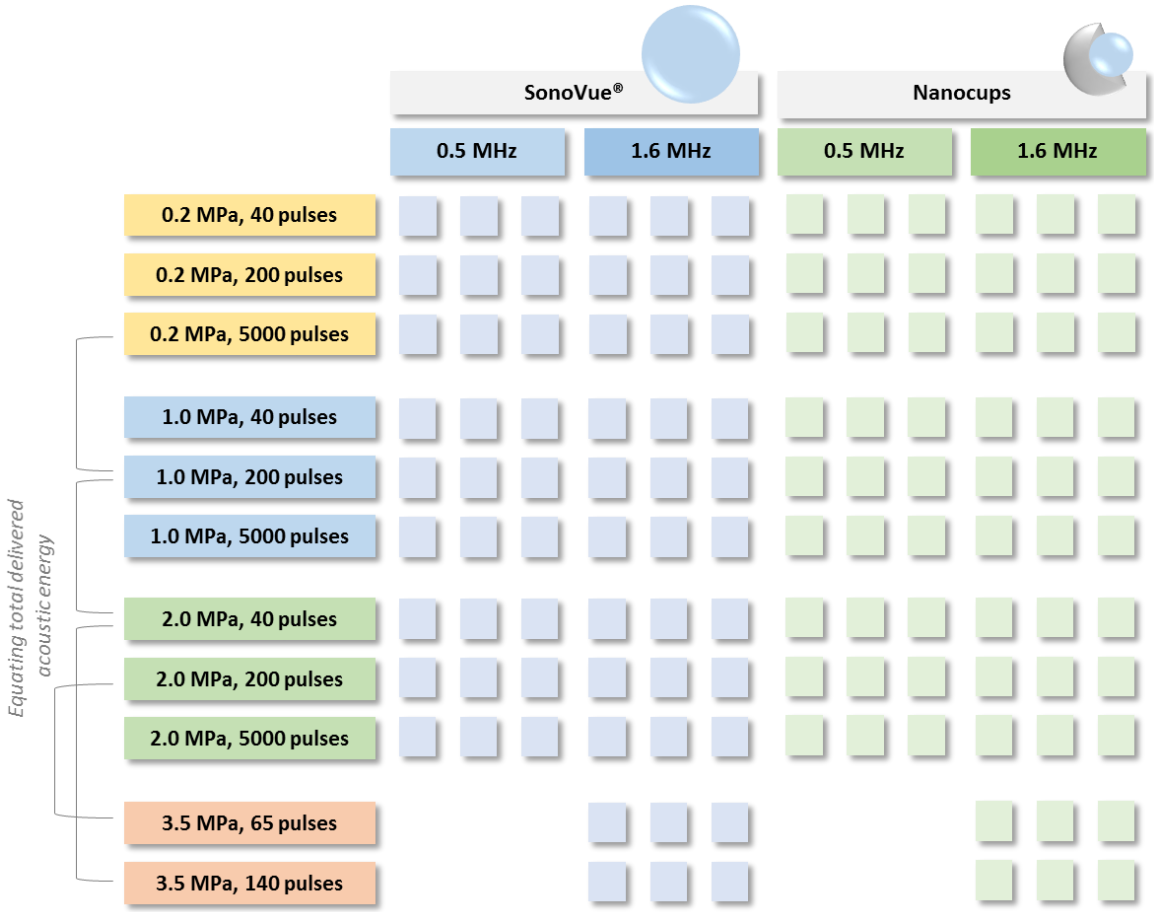

Figure 3.14 *Experimental matrix of ultrasound exposure values; comparing acoustic pressures (0.2 – 3.5 MPa), exposure durations (40 – 5000 pulses), frequency (0.5 or 1.6 MHz) and cavitation agent (SonoVue® or NanoCups), at a fixed duty cycle (5 %), PRF (10 Hz), pulse period (100 ms), and pulse duration (5 ms). Brackets on the left side illustrate the equated total delivered acoustic energy across regimes.*

Table 3.3 *Total delivered acoustic energy across ultrasound exposure regimes.*

Total delivered acoustic energy (J)	Frequency (MHz)	Pressure (MPa)	Number of pulses
4.72	1.6	0.2	5000
		1.0	200
		2.0	40
18.8	1.6	2.0	200
		3.5	65
40.4	0.5	0.2	5000
		1.0	200
		2.0	40
	1.6	3.5	140

3.3 Results

3.3.1 *In vitro* results

Two key measurements were made for each set of exposure conditions: first, the total energy of the detected acoustic emissions, captured using the single element passive cavitation detection (PCD) transducer and calculated from the integral of the frequency spectrum of the PCD signal; second, the peak penetration depth of the transported nanoparticles, captured using fluorescence microscopy.

a) Cavitation behaviour

At 0.5 MHz the relative magnitudes of emissions for each agent differed at each excitation pressure, but were consistently found to produce almost exclusively broadband emissions. At 0.2 MPa SonoVue® was the only agent to produce noticeable emissions (table 3.4), statistically significantly greater in magnitude than the three other exposure regimes (figure 3.15(A)) and in agreement with previous studies (Arvanitis *et al.* 2011). At 1.0 MPa emissions produced by SonoVue® were similar in peak magnitude, but more sustained compared to NanoCups (table 3.5). At 2.0 MPa SonoVue® was destroyed rapidly, but NanoCups produced high magnitude and sustained cavitation emissions, statistically significantly greater in magnitude than the three other exposure regimes (figure 3.17(A)).

At 1.6 MHz both the relative magnitudes and the frequency composition of emissions for each agent differed at each excitation pressure. At 0.2 MPa SonoVue® produced emissions with total acoustic energy less than those at 0.5 MHz, but which contained strong harmonic components (table 3.4), whilst emissions from NanoCups were not detectable. At 1.0 MPa emissions produced by SonoVue® were again similar in peak magnitude to NanoCups, with the frequency spectra becoming dominated by broadband emissions with increasing pressure. Similarly to 0.5 MHz, the rapid destruction of SonoVue at 2.0 MPa led to sporadic and intermittent cavitation emissions, whilst emissions from NanoCups were found to be well sustained.

Table 3.4 *Frequency power spectra of acoustic emissions from SonoVue® (SV) exposed at frequencies 0.5 MHz and 1.6 MHz, and peak negatives pressures from 0.2 MPa to 3.5 MPa.*

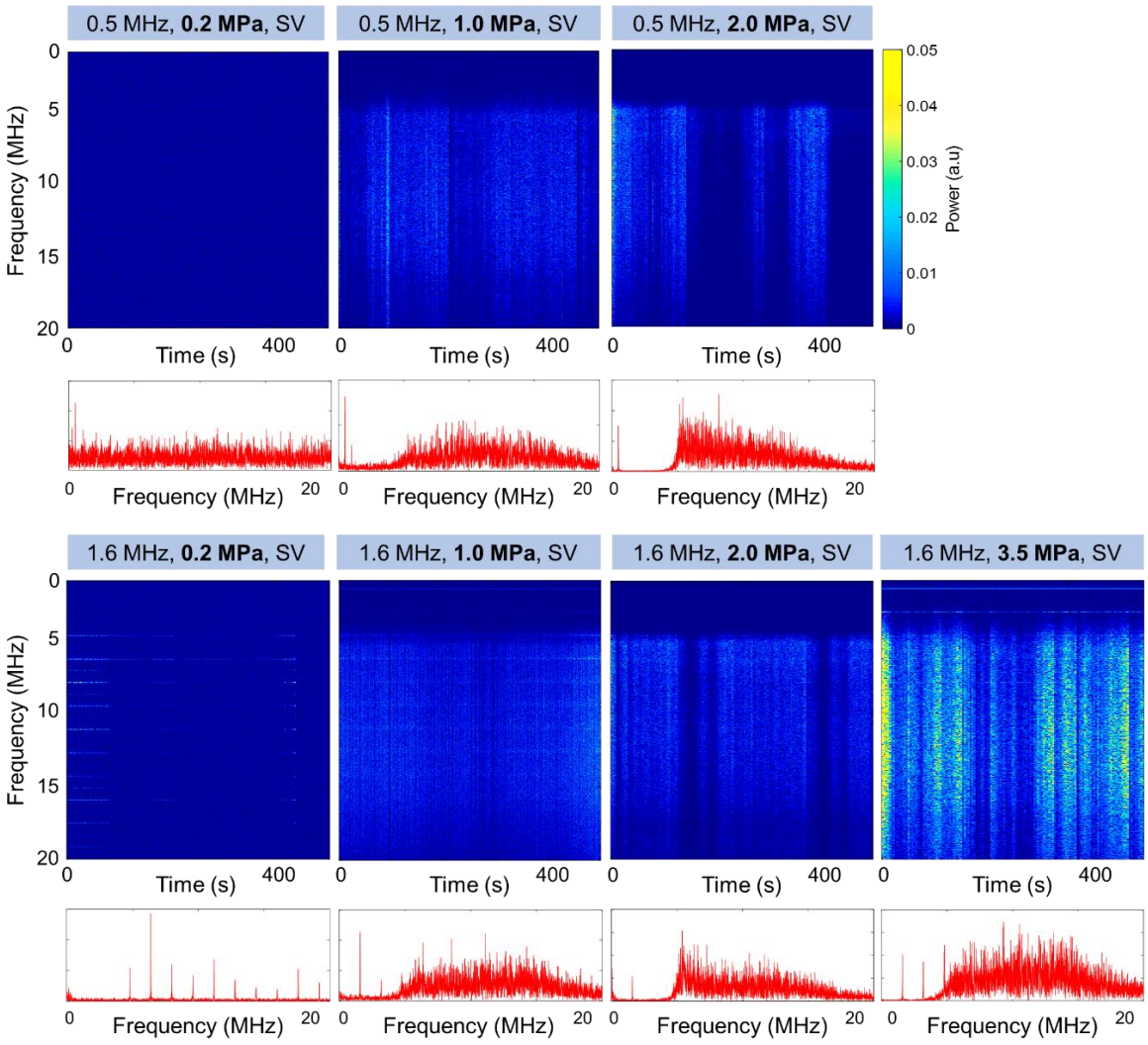

Table 3.5 *Frequency power spectra of acoustic emissions from NanoCups (NC) exposed at frequencies 0.5 MHz and 1.6 MHz, at peak negatives pressures from 1.0 MPa to 3.5 MPa.*

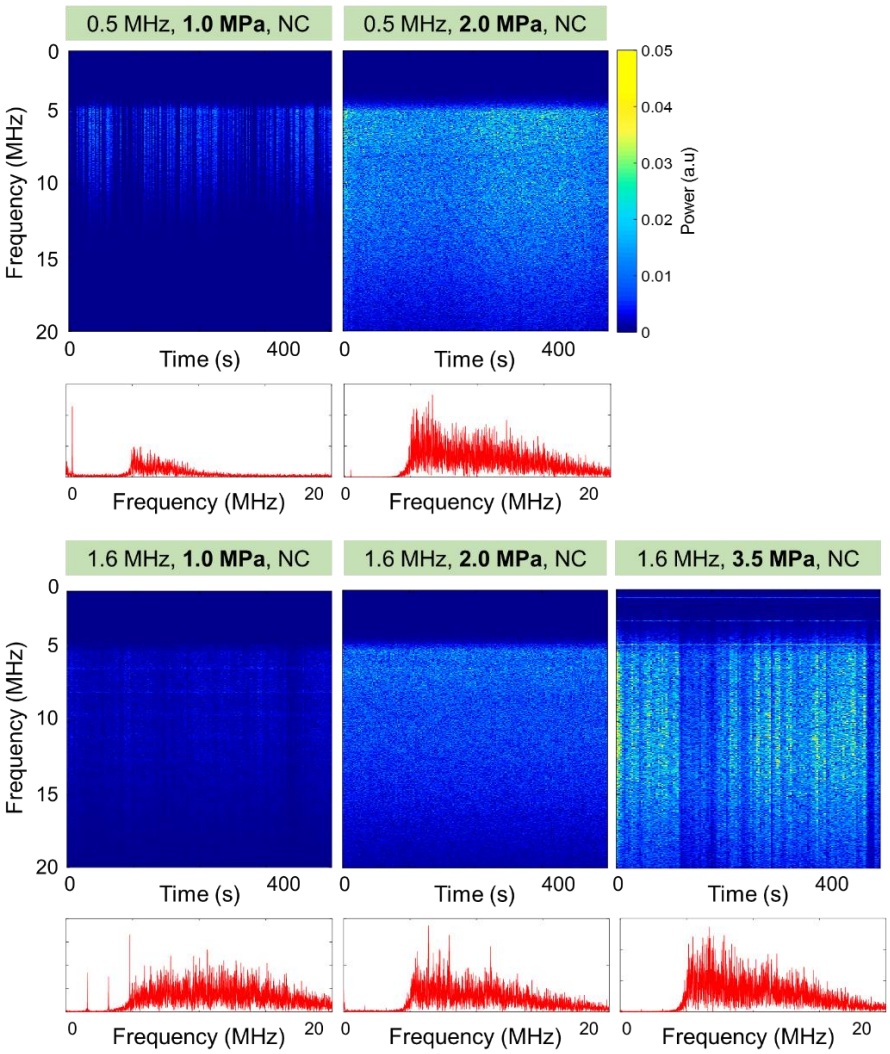

b) Particle penetration depth

The peak penetration depth induced at 0.2 MPa is shown in figures 3.15(B)-(E). Sample confocal images are shown in figure 3.18. Very limited extravasation was observed at 0.2 MPa for both agents, at both frequencies, only exceeding 50 µm when 5000 pulses were used. Although a slight difference in penetration depth with density could be seen in many groups, the discrepancies were not statistically significant.

At 1.0 MPa, SonoVue® produced greater penetration depths than NanoCups in every exposure regime, as predicted by the cavitation emissions. Figures 3.16(B)-(E) show a stronger trend in particle density and penetration depth compared to the other pressure regimes, but particle density only produced statistically significant differences in penetration depth at one exposure regime – namely 1.6 MHz with SonoVue® at 200 pulses.

At 2.0 MPa the high magnitude cavitation emissions are again indicative of the particle penetration depth, as illustrated with the microscopy (figure 3.21). At this higher pressure, the agar vessel model begins to show significant damage, with voids in the agar being created (safety implications from which are discussed in section 3.4.1). This effect prevented the relatively subtle differences in particle density from being observed – as a void is opened up, all of the sample flows to the furthest point, regardless of density. At 1.6MHz this effect was particularly pronounced. The extravasation pattern became much more directional and narrow, with single channels of > 3 mm in length being formed (figure 3.17(E)).

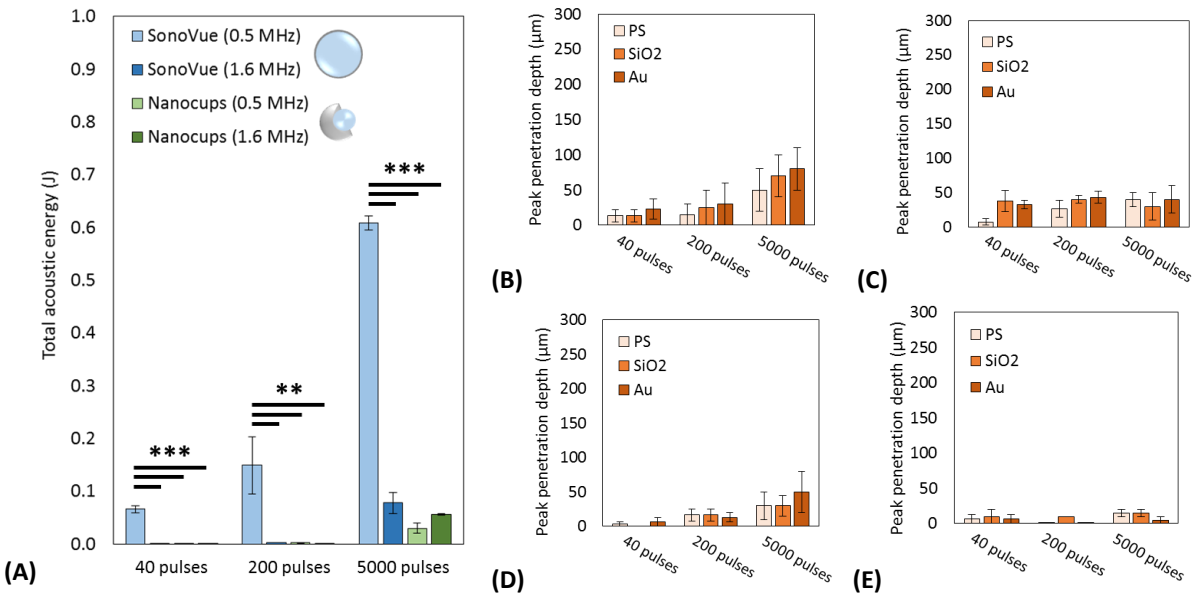

Figure 3.15 *Cavitation emissions* **(A)** *and extravastion distances of density-modified particles with cores of polystyrene (PS), silica (SiO_2) and gold (Au), measured under excitation at 0.2 MPa,* **(B)** *0.5 MHz with SV,* **(C)** *0.5 MHz with NC,* **(D)** *1.6 MHz with SV,* **(E)** *1.6 MHz with NC. Error bars show 1 standard deviation of the data. Statistical significance was assessed using one-way ANOVA testing:* $**$ $(p < 0.01)$, $***$ $(p < 0.001)$, *where* $n = 3$ *for each group.*

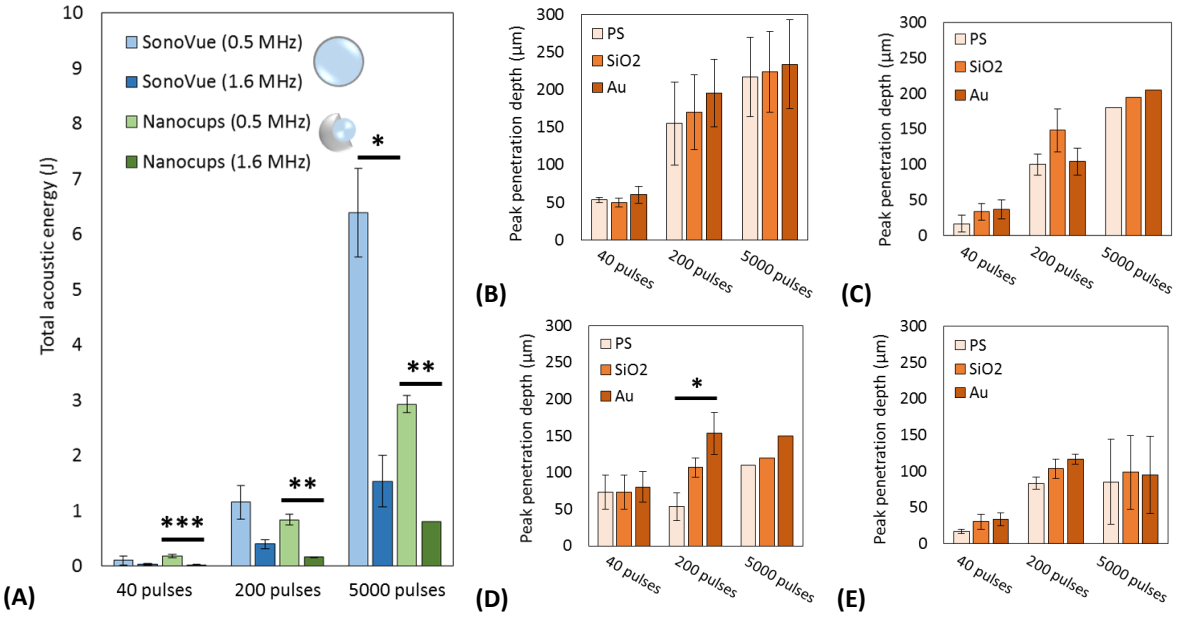

Figure 3.16 *Cavitation emissions* **(A)** *and extravastion distances of density-modified particles with cores of polystyrene (PS), silica (SiO_2) and gold (Au), measured under excitation at 1.0 MPa,* **(B)** *0.5 MHz with SV,* **(C)** *0.5 MHz with NC,* **(D)** *1.6 MHz with SV,* **(E)** *1.6 MHz with NC. Error bars show 1 standard deviation of the data. Statistical significance was assessed using one-way ANOVA testing:* $*$ $(p < 0.05)$, $**$ $(p < 0.01)$, $***$ $(p < 0.001)$, *where* $n = 3$ *for each group.*

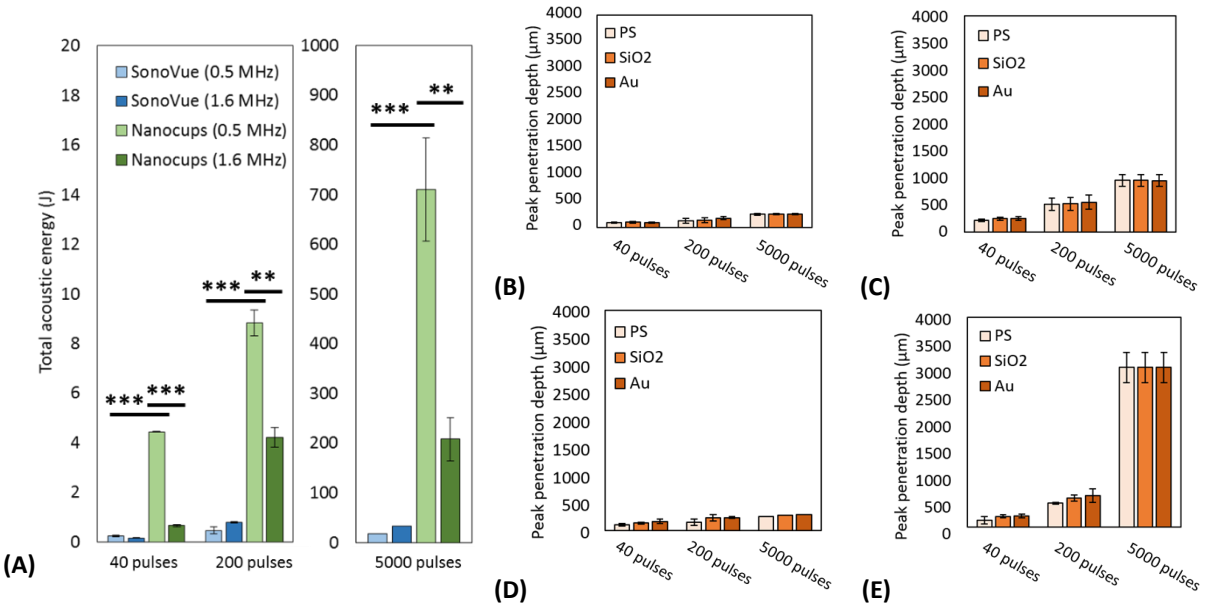

Figure 3.17 *Cavitation emissions* **(A)** *and extravastion distances of density-modified particles with cores of polystyrene (PS), silica (SiO_2) and gold (Au), measured under excitation at 2.0 MPa,* **(B)** *0.5 MHz with SV,* **(C)** *0.5 MHz with NC,* **(D)** *1.6 MHz with SV,* **(E)** *1.6 MHz with NC. Error bars show 1 standard deviation of the data. Statistical significance was assessed using one-way ANOVA testing:* $**$ $(p < 0.01)$, $***$ $(p < 0.001)$, *where* $n = 3$ *for each group.*

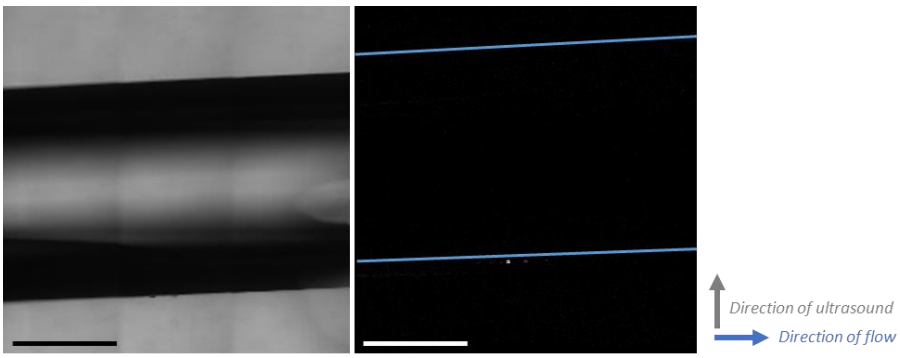

Figure 3.18 *Microscopy images of (left) bright field and (right) fluorescence channels with channel walls marked in blue, illustrating particle extravasation with SonoVue® resultant at 0.2 MPa, 0.5 MHz, 200 pulses.*

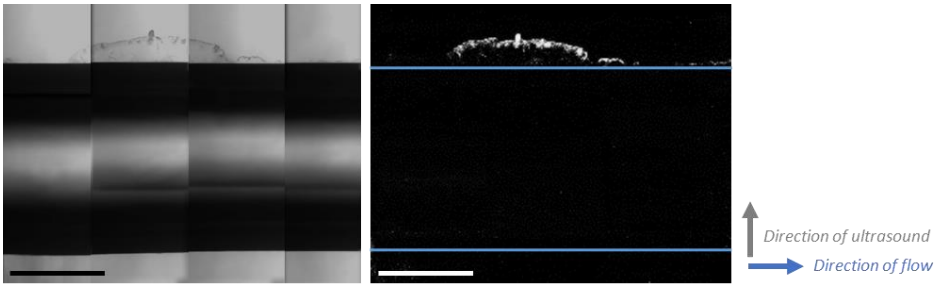

Figure 3.19 *Microscopy images of (left) bright field and (right) fluorescence channels with channel walls marked in blue, illustrating particle extravasation with SonoVue® resultant at 1.0 MPa, 0.5 MHz, 200 pulses.*

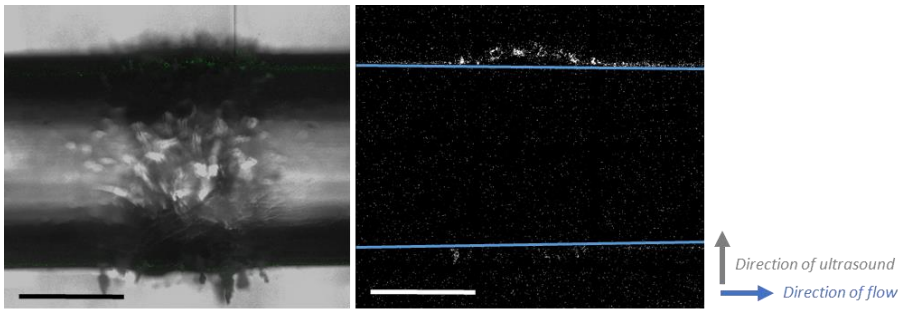

Figure 3.20 *Microscopy images of (left) bright field and (right) fluorescence channels with channel walls marked in blue, illustrating particle extravasation with SonoVue® resultant at 2.0 MPa, 0.5 MHz, 200 pulses.*

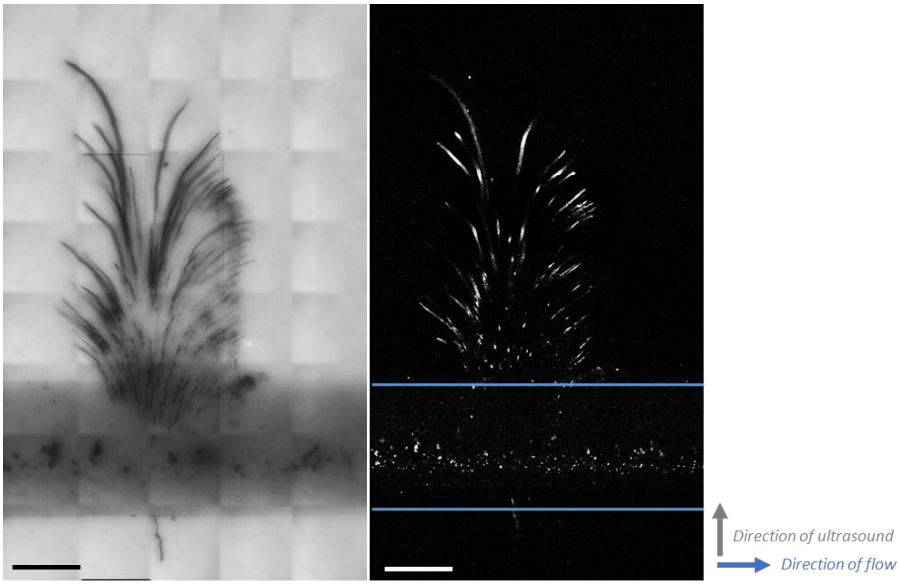

Figure 3.21 *Microscopy images of (left) bright field and (right) fluorescence channels with channel walls marked in blue, showing extravasation with NanoCups, 2.0 MPa, 1.6 MHz, 5000 pulses. Scale bars 500 µm.*

3.3.2 Monitoring and predicting extravasation

Figure 3.22 shows the total energy of acoustic emissions as detected by the PCD, plotted against peak penetration depth of the fluorescent nanoparticles. Figure 3.22(A) shows all data points collected in the study: emissions and extravasation produced by both SonoVue® (blue) and NanoCups (green). Figures 3.22(B) and 3.22(C) show the data split between SonoVue® and NanoCups respectively. The shape of each data point illustrates the type of density-modified nanoparticle.

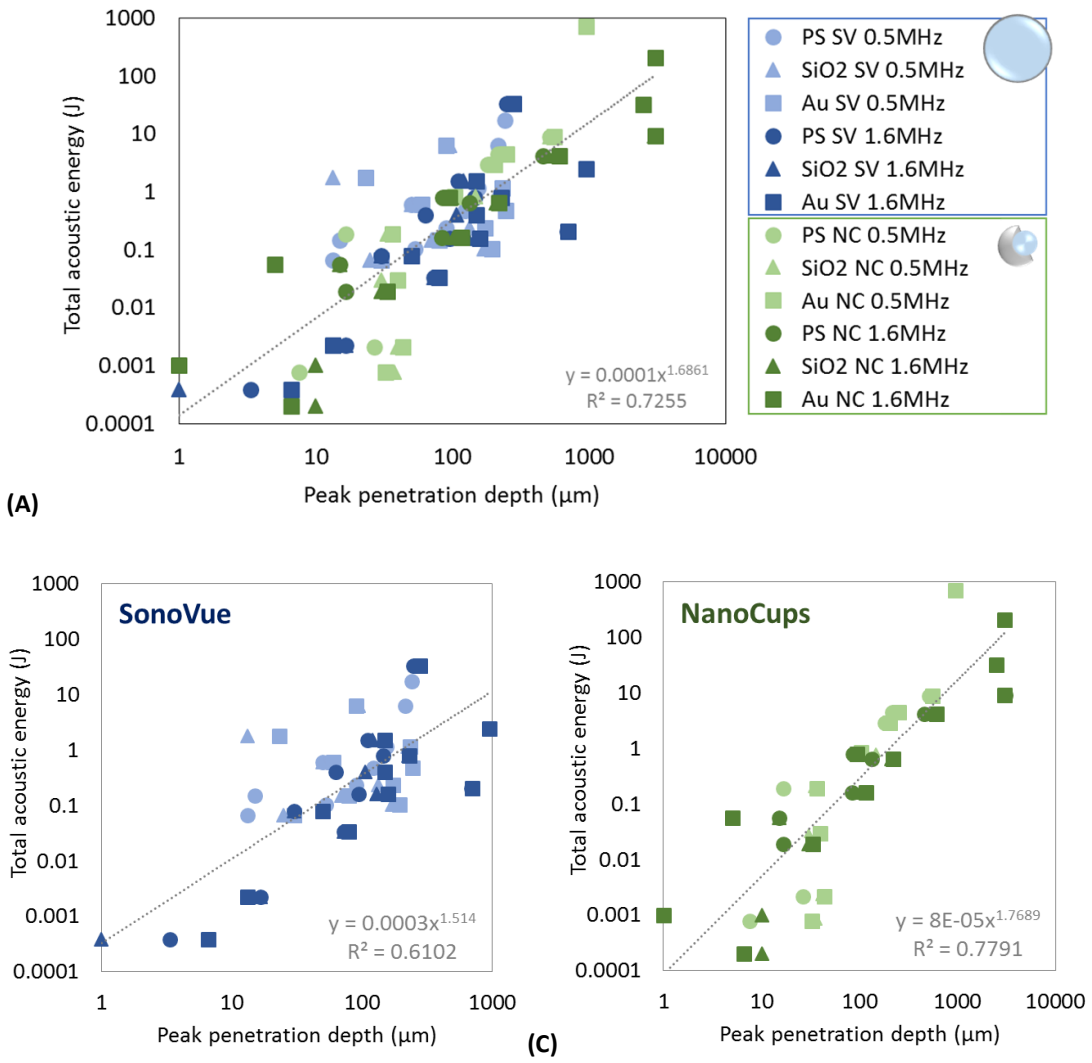

Figure 3.22 *Correlation of acoustic emissions and nanoparticle peak penetration depth for **(A)** all data points, **(B)** SonoVue® and **(C)** NanoCups. Marker shape illustrates each type of density-modified nanoparticle with cores of (●) polystyrene, (▲) silica and (■) gold.*

Cavitation emissions and nanoparticle peak penetration depth were found to have a power-law dependence, with correlation strength described by R^2 as 0.726. The greatest deviations from the power-law trend are seen at the lowest and highest cavitation energies. When the responses of SonoVue® and NanoCups were studied in isolation, correlation between cavitation emissions and peak penetration depth was found to be stronger for NanoCups (R^2 = 0.779) than SonoVue® (R^2 = 0.610). This effect may be attributed to the tight size distribution of NanoCups and consequential high reproducibility in cavitation response. Furthermore, the trend was found to be at a steeper gradient for NanoCups, suggesting that the same increase in penetration depth may be achieved for less cavitation energy: NanoCups are more efficient at converting cavitation activity into nanoparticle penetration compared to SonoVue®. This implies that a smaller gas volume fraction and/or number of cavitation agents may be required to induce the same therapeutic effect. However, further investigation is required to isolate the effect of agar damage.

3.4 Discussion

3.4.1 Influence of acoustic pressure

In general the greater the peak negative pressure of acoustic excitation, the greater the peak penetration depth of the mock therapeutic, a trend that was found to be true for both SonoVue® and NanoCups. However, this relationship between driving pressure and extravasation depth was found to be a nonlinear one.

Designed as an imaging contrast agent, SonoVue® produces sustained non-inertial cavitation at high frequencies, in the typical 1.5 – 5 MHz range used for conventional B-mode imaging. Therefore the harmonic response seen at 1.6 MHz, with peak negative pressures of 0.2 MPa and 1.0 MPa, was expected. However, at higher pressures a nonlinear relationship between

driving pressure and particle extravasation was found, where violent collapses were measured and the destruction of a large volume of microbubbles could be observed on the B-mode imaging probe, particularly at 0.5 MHz when the focal region is large. Often such a large volume of microbubbles were destroyed that the channel could not be replenished before the subsequent acoustic pulse. Therefore for SonoVue® the extravasation achieved at 2.0 MPa was not significantly greater than at 1.0 MPa.

NanoCups also showed a nonlinear relationship between driving pressure and particle extravasation. In this case the nonlinearity stemmed from the existence of a distinct transition from sporadic and small amplitude cavitation events (at 0.5 MHz, 1.0 MPa), to high amplitude and sustained emissions (at 0.2 MPa for both frequencies).

Acoustic pressures of 2.0 MPa and above produced significant amounts of mechanical damage in the vessel phantom at 0.5 MHz and illustrate a key safety implication of this technology. The threshold of mechanical damage in the phantom medium for this particular *in vitro* system was found to be 2.0 MPa for both 0.5 MHz and 1.6 MHz when exposed to more than 200 pulses with cavitation agents present. Cavitation-induced damage might also be expected in tissue at these pressures, as illustrated by Hynynen (1991) in studying the onset of transient cavitation in dog thighs *in vivo* in the context of hyperthermia treatments. A range of frequencies were explored, from 0.25 – 1.68 MHz, and a pressure amplitude value of 5.3 MPa MHz^{-1} was identified as the maximum acceptable pressure to use during ultrasound hyperthermia treatments, since this threshold marked the onset of transient cavitation in tissue. However, it should be noted that the ultrasound was pulsed in a pattern of 1 s of insonation, followed by 30 s without, resulting in a far higher duty cycle and longer pulse length than used in the current study.

3.4.2 Influence of centre frequency

In chapter 1 the theoretical dynamic behaviour of bubbles was discussed, and in chapter 2 the difference in response of a 3 µm bubble to excitation at 0.5 MHz and 1.6 MHz was illustrated computationally and experimentally. In both cases it was shown that the longer rarefactional period of 0.5 MHz excitation leads to greater bubble expansion (figures 2.2 and 2.3). This trend was seen again in the current flow vessel phantom, where at pressures up to 1.0 MPa at 0.5 MHz, the greatest particle extravasation was measured for both SonoVue® and NanoCups.

However, at 1.6 MHz a number of parameters change. Firstly the size of the focus reduces from 3.0 x 21.0 mm at 0.5 MHz, to 1.0 x 7.0 mm, equating to a 30-fold reduction in focal volume, which activates a smaller population of cavitation agents and exposes less of the surrounding agar to acoustic energy. Secondly, due to the shorter wavelength, the pressure gradient within the focus increases, leading to an increase in radiation force experienced by the cavitation agent, and to a lesser extent an increase in primary acoustic streaming. This in turn is likely to push bubbles against the wall of the vessel, enhancing the preferential direction of extravasation away from the transducer. These effects in combination lead to tightly focussed and highly directional extravasation. Long channels were also observed, an effect which might be attributed to individual bubbles tunnelling into the agar, as has been observed in previous studies (Bian *et al.* 2017), generating peak penetration distances of over 3 mm in the case of NanoCups at 2.0 MPa, 1.6 MHz.

3.4.3 Influence of nanoparticle density

In several regimes particle density is seen to influence penetration depth as expected from the results of the previous chapter. Of particular note is the extravasation seen using SonoVue® at 1.6 MHz, exposure at 1.0 MPa for 200 pulses (figure 3.16(D)). In this example we

can see PS nanoparticles reach 60 µm peak penetration depth, whereas Au nanoparticles were propelled to over 150 µm, indicating that this method of therapeutic modification may make the difference between successfully treating the whole tumour volume and not.

However, in contrast to the results shown in Chapter 2, differences in nanoparticle density did not always produce a statistically significant difference in penetration depth. This may be partly attributed to particle-particle interactions. In the experiments described in Chapter 2 particle populations were studied in isolation, i.e. separate delivery studies were carried out for PS, Si and Au nanoparticles respectively. In this study all three populations were delivered simultaneously. Channels created by the motion of denser particles could have allowed less dense particles to follow. Alternatively, denser particles may have pushed less dense particles deeper, both effects leading to less dense particles penetrating deeper into the phantom.

Furthermore, as above, at pressures of 2.0 MPa and higher, significant mechanical damage in the phantom medium was seen. In these regimes nanoparticles of all densities were able to flow into the voids, preventing the observation of density-enhanced transport. The threshold for mechanical damage was found to be 40 J of total delivered acoustic energy for this particular *in vitro* system.

3.4.4 Influence of flow

The previous *in vitro* model used in chapter 2 considered the simple scenario of static fluid, which is arguably more representative of small vasculature. However, in the current study a flow rate of 0.6 mL/min was used to mimic blood flow rate in a tumour (Kallinowski *et al.* 1989). Flow conditions add a number of considerations. Of key importance is the replenishment of cavitation agents. Unlike in the static setup, new cavitation agents are introduced, potentially allowing sustained cavitation activity over the full exposure duration

depending on the pulse repetition frequency (PRF). If the PRF is too high, the exposed channel region will not be replenished before the next acoustic pulse arrives. As previously discussed, even with the same flow rate, the replenishment rate is lower for SonoVue® since a larger volume of cavitation agent is destroyed per pulse. Because of this, the cavitation activity was found to be less consistent with SonoVue® than NanoCups, particularly at 2.0 MPa (table 3.4).

3.4.5 Limitations

First, the extent of density-enhanced transport may be limited in this experimental setup by particle-particle interactions. Future work should look to deliver density-modified therapeutics in isolation, studying each population in turn to avoid interactions.

Second, the agarose phantom does not mimic the complex structure found in tumour tissue. As discussed in Chapter 1, in cancerous tissue a myriad of physical and biological barriers exist to hinder the penetration of therapeutics. In order to address this the following chapter will study the bio-distribution of a density-modified therapeutic in an *in vivo* tumour model. Additionally, in a further effort to move this work towards clinical relevance, cavitation agents should be used at concentrations corresponding to the maximum acceptable clinical dose, rather than simply based on previous work, as is implemented here. This would allow agents to be more fairly and more directly compared.

Third, this study has been concerned exclusively with quantifying therapeutic delivery in terms of peak penetration depth. However, to ensure therapeutic efficacy both penetration depth and total delivered dosage should be considered. The area over which fluorescent nanoparticles are distributed will be influenced by both the size of the ultrasound focus and the volume of activated cavitation agents.

Not only does each driving frequency have an associated focal volume (as discussed previously), acoustic calibrations and pressure maps taken for the source transducer reveal side lobes, characteristic of any circular transducer. When the peak negative pressure in the side lobes exceeds the pressure necessary to induce inertial cavitation, then the active region within the channel becomes significantly larger. For example, at 0.5 MHz, driving the transducer at 2.0 MPa will create side lobes of approximately 0.4 MPa peak negative pressure, located 10 mm away from the focal centre, as can been seen from the pressure field scans in the appendix (appendix A1), which would be sufficient to induce inertial cavitation in a population of SonoVue® (table 3.2). Figure 3.23 illustrates this effect by showing a schematic of the transducer profile overlaid with the channel. The ability of side lobes to activate cavitation agents outside of the main focus and contribute to ultrasound-mediated transport was observed in real-time on B-mode imaging during many of the previous exposures using SonoVue®.

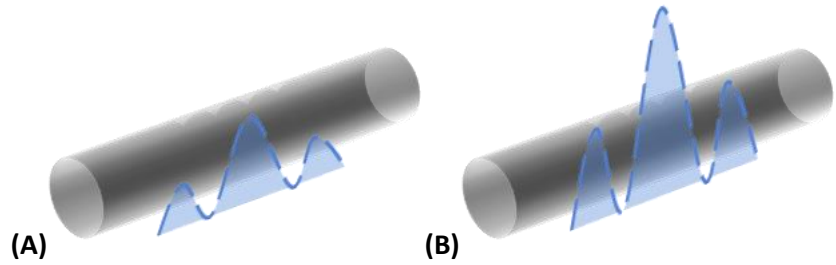

Figure 3.23 *Transducer profile with main lobe and side lobes (blue) overlaid with agarose channel phantom (grey) at **(A)** relatively low and **(B)** relatively high acoustic pressures.*

Furthermore, the volume of activated cavitation agents, for a fixed pressure field, will depend on the cavitation threshold of the specific agent. For example, since SonoVue® responds to lower pressures than NanoCups, a larger volume of SonoVue® will be activated and may contribute to ultrasound-mediated transport, whereas NanoCups are predicted to achieve a tighter distribution of extravasation. However, depending on the replenishment rate, this argument may only hold for the first ultrasound pulse, since, as discussed previously, a significant proportion of SonoVue® is often destroyed in a single pulse. This effect can be

observed in the power frequency spectra in table 3.4, where the cavitation emissions frequently drop to background at during exposure at 2.0 MPa, suggesting the whole detectable population of SonoVue® has been destroyed.

Nevertheless, the distribution of therapeutic agents both in depth and area has clinical implications for ultrasound-mediated drug delivery. Optimising the distribution in terms of penetration depth and total area will be informed by the target volume to be treated, with the ultimate aim being an even distribution of therapeutic material throughout the tumour volume.

3.5 Conclusions

In conclusion, a correlation between nanoparticle density and extravasation depth was discernible, but was found to be less statistically significant than in the work described in the previous chapter. Particle density did not always have a statistical significant effect upon penetration depth, which was found to be more strongly influenced by the type of cavitation agent. Delivering the density-contrasting particles simultaneously may have diluted the effect through particle-particle interactions. Running these studies in parallel could help to identify the extent of these interactions. Furthermore, the effect of density was found to be limited by the threshold for mechanical damage in the phantom medium (2.0 MPa peak negative pressure for this particular *in vitro* system).

Correlation between total acoustic energy and nanoparticle peak penetration distance was found to have a power-law dependence, with the exponent 1.69. This trend between cavitation and penetration was found to be strongest for NanoCups. Overall, in the context of a highly repeatable *in vitro* experiment, total acoustic energy provides a promising metric for predicting the peak penetration distance of density-modified nanoparticles.

References

Apfel, R.E., '*Acoustic cavitation inception'*, Ultrasonics, 1984, 22(4), 167-173.

Arora, M., Ohl, C.D. and Lohse, D., '*Effect of nuclei concentration on cavitation cluster dynamics*', The Journal of the Acoustical Society of America, 2007, 121(6), 3432-3436.

Arvanitis, C.D., Bazan-Peregrino, M., Rifai, B., Seymour, L.W. and Coussios, C.C., *'Cavitation-enhanced extravasation for drug delivery'*, Ultrasound in Medicine and Biology, 2011, 37(11), 1838-1852.

Atchley, A.A. and Prosperetti, A., *'The crevice model of bubble nucleation'*, The Journal of the Acoustical Society of America, 1989, 86(3), 1065-1084.

Barbosa, S., Agrawal, A., Rodríguez-Lorenzo, L., Pastoriza-Santos, I., Alvarez-Puebla, R.A., Kornowski, A., Weller, H. and Liz-Marzán, L.M., '*Tuning size and sensing properties in colloidal gold nanostars'*, Langmuir, 2010, 26(18), 14943-14950.

B.J. Berne and R. Pecora, '*Dynamic light scattering: with applications to chemistry, biology, and physics*', Wiley, 1976.

Bian, S., Seth, A., Daly, D., Carlisle, R. and Stride, E., *'A multimodal instrument for real-time in situ study of ultrasound and cavitation mediated drug delivery'*, Review of Scientific Instruments, 2017, 88(3), 034302.

Chen, Xi, Yan Yan, Markus Müllner, Martin P. van Koeverden, Ka Fung Noi, Wei Zhu, and Frank Caruso, '*Engineering fluorescent poly (dopamine) capsules*', Langmuir, 2014, 30(10), 2921-2925.

Chirea, M., '*Electron transfer at gold nanostar assemblies: a study of shape stability and surface density influence'*, Catalysts, 2013, 3(1), 288-309.

De Lumen, B.O. and Tappel, A.L., '*Fluorescein-hemoglobin as a substrate for cathepsin D and other proteases*', Analytical Biochemistry, 1970, 36(1), 22-29.

Gorce, J.M., Arditi, M. and Schneider, M., *'Influence of bubble size distribution on the echogenicity of ultrasound contrast agents: A study of SonoVue™'*, Investigative Radiology, 2000, 35(11), 661-671.

Griffith, O.M., '*Practical techniques for centrifugal separations*', Thermo Fisher Scientific, 2010.

Harvey, E.N., Barnes, D.K., McElroy, W.D., Whiteley, A.H., Pease, D.C. and Cooper, K.W., '*Bubble formation in animals. I. Physical factors*', Journal of Cellular Physiology, 1944, 24(1), 1-22.

Hunter, R.J., '*Zeta potential in colloid science: principles and applications*', Vol. 2, Academic Press, 2013.

Hynynen, K., '*The threshold for thermally significant cavitation in dog's thigh muscle in vivo*', Ultrasound in Medicine and Biology, 1991, 17(2), 157-169.

Jain, R.K., '*Transport of Molecules in the Tumor Interstitium: A Review',* American Association for Cancer Research, 1987, 47, 3039-3051.

Kallinowski, F., Schlenger, K.H., Runkel, S., Kloes, M., Stohrer, M., Okunieff, P. and Vaupel, P., '*Blood flow, metabolism, cellular microenvironment, and growth rate of human tumor xenografts*', Cancer Research, 1989, 49(14), 3759-3764.

Kwan, J.J., Graham, S., Myers, R., Carlisle, R., Stride, E. and Coussios, C.C., *'Ultrasound-induced inertial cavitation from gas-stabilizing nanoparticles*', Physical Review E, 2015a, 92(2), 023019-1-5.

Kwan, J.J., Myers, R., Coviello, C.M., Graham, S.M., Shah, A.R., Stride, E., Carlisle, R.C. and Coussios, C.C., *'Ultrasound-Propelled Nanocups for Drug Delivery',* Small, 2015b, 11(39), 5305-5314.

Lee, H., Dellatore, S.M., Miller, W.M. and Messersmith, P.B., '*Mussel-inspired surface chemistry for multifunctional coatings',* Science, 2007, 318(5849), 426-430.

Lee, J.Y., Crake, C., Teo, B., Carugo, D., de Saint Victor, M., Seth, A. and Stride, E., '*Ultrasound-Enhanced siRNA Delivery Using Magnetic Nanoparticle-Loaded Chitosan-Deoxycholic Acid Nanodroplets*', Advanced Healthcare Materials, 2017, 6(8), 2192-2659.

Leighton, T., '*The Acoustic Bubble*', Academic Press, 1994.

Lin, Y., Lin, L., Cheng, M., Jin, L., Du, L., Han, T., Xu, L., Alfred, C.H. and Qin, P., '*Effect of acoustic parameters on the cavitation behavior of SonoVue microbubbles induced by pulsed ultrasound'*, Ultrasonics Sonochemistry, 2017, 35, 176-184.

Mo, S., Carlisle, R., Laga, R., Myers, R., Graham, S., Cawood, R., Ulbrich, K., Seymour, L. and Coussios, C.C., '*Increasing the density of nanomedicines improves their ultrasound-mediated delivery to tumours*', Journal of Controlled Release, 2015, 210, 10-18.

Pluen, A., Netti, P.A., Jain, R.K. and Berk, D.A., *'Diffusion of macromolecules in agarose gels: comparison of linear and globular configurations'*, Biophysical Journal, 1999, 77(1), 542-552.

Rahman, M., Laurent, S., Tawil, N., Mahmoudi, L.Y.M., '*Protein-Nanoparticle Interactions'*, Springer Series in Biophysics, 2013, 15.

Rademeyer, P., Carugo, D., Lee, J.Y. and Stride, E., *'Microfluidic system for high throughput characterisation of echogenic particles'*, Lab on a Chip, 2015, 15(2), 417-428.

Tanaka, T., Williams, R.L. and Rabbitts, T.H., *'Tumour prevention by a single antibody domain targeting the interaction of signal transduction proteins with RAS'*, The EMBO Journal, 2007, 26(13), 3250-3259.

Wilhelm, S., Tavares, A.J., Dai, Q., Ohta, S., Audet, J., Dvorak, H.F. and Chan, W.C., '*Analysis of nanoparticle delivery to tumours',* Nature Reviews Materials, 2016, 1, 16014.

Xu, L.Q., Yang, W.J., Neoh, K.G., Kang, E.T. and Fu, G.D., '*Dopamine-induced reduction and functionalization of graphene oxide nanosheets',* Macromolecules, 2010, 43(20), 8336-8339.

Zhu, L.P., Jiang, J.H., Zhu, B.K. and Xu, Y.Y., '*Immobilization of bovine serum albumin onto porous polyethylene membranes using strongly attached polydopamine as a spacer',* Colloids and Surfaces B: Biointerfaces, 2011, 86(1), 111-118.

Chapter 4: **Density-enhanced delivery of bio-compatible nanoparticles *in vivo***

Abstract

Enhancing the penetration of therapeutics into tumour tissue by modifying their physical properties, specifically density, has been a common theme throughout this thesis. The following *in vivo* study utilises a murine tumour model to assess the density-enhanced delivery of bio-compatible density-contrasting nanoparticles in the presence of ultrasound and micro- or nano-scale cavitation agents. Ultrasound was delivered and monitored using a bistatic configuration of HIFU transducers and linear arrays, to enable the highest possible spatial resolution of the incident ultrasound field and mapping of the acoustic cavitation activity. Fluorescence uptake was quantified through live animal fluorescence imaging and fluorescence measurements of *ex vivo* homogenised tumour tissue. Cavitation activity was significantly enhanced by the presence of cavitation agents, resulting in a corresponding enhancement in fluorescent material in the *ex vivo* tumours. However, the effect of particle density could not be reliably determined using the current *in vivo* protocol. Recommendations are made to develop this study for future work.

4.1 Introduction and motivation

4.1.1 Research questions

In the previous chapter it was demonstrated that although particle density plays an important role in therapeutic transport, the choice of cavitation agent can have a more significant impact on transport distance. It was also shown that a power-law correlation existed between total acoustic energy and nanoparticle peak penetration distance.

However, the *in vitro* models described in chapter 2 and chapter 3 have clear limitations in mimicking real tissue and vasculature. Furthermore, during the simultaneous delivery of multiple particle populations, particle-particle interactions were identified as a limiting factor in the detection of density-enhanced transport. In order to overcome these limitations and study ultrasound-mediated nanoparticle transport *in vivo*, a murine tumour model was used in the work described in this chapter. The bio-distribution of two density-contrasting nanoparticles – delivered with and without cavitation agents – was analysed. The aim of the study was to determine whether particle density would influence the ultrasound-mediated delivery of a mock therapeutic *in vivo*.

4.2 Nanoparticle chemistry

Two types of density-contrasting bio-compatible nanoparticles were fabricated by coating spherical cores of either polystyrene or gold, with a fluorescent polyethylene glycol (PEG) coating. The final constructs had the same size (200 nm diameter), shape, zeta potential and fluorescence labelling in order to minimise differences in their pharmacokinetics *in vivo*. The number of particle types was limited to two, with the greatest density contrast possible, in order to minimise the number of animals required, whilst maximising the opportunity to observe a differential effect *in vivo*. The labelling method used in the previous chapter, a physically adsorbed protein-dye conjugate, offered a convenient coating and labelling

method, but was not appropriate for *in vivo* applications since BSA is likely to be displaced by blood proteins *in vivo*. Therefore PEGylation was implemented for a stable and biologically-compatible coating and labelling method.

A particle size of 200 nm diameter was chosen to imitate the dimensions of a large biological therapeutic such as a virus, while being small enough to fit through the leaky vasculature of the tumour and to be large enough to avoid two key clearance mechanisms (Alexis *et al.* 2008). Firstly, filtration of particles occurs in the liver, through the sinusoidal endothelial cells into the hepatocytes. Clearance from the bloodstream through this mechanism has been shown to occur for agents below 100 nm in humans and agents below 130 nm in murine models. Secondly, complement-mediated clearance through the binding of various receptors has been shown to remove nanoparticles in the range 30 – 200 nm. PEGylating the particles was also designed to avoid the latter mechanism.

The fluorophore Cyanine-5 (Cy5) was chosen because of its long excitation and emission wavelength, with the aim of minimising light attenuation into and out of tissue when imaging with the *In Vivo Imaging System* (IVIS). Cy5 is compatible with both live animal fluorescence imaging and fluorescence measurements of *ex vivo* homogenised tumour tissue.

4.2.1 Methodology and materials

Amine-functionalised polystyrene particles and gold particles stabilised in citrate buffer (both 200 nm diameter) were purchased from Nanocs (New York, USA) and Sigma-Aldrich (Dorset, UK) respectively. Buffer reagents boric acid, sodium tetraborate, sodium phosphate dibasic and sodium phosphate monobasic were purchased from Sigma-Aldrich (Dorset, UK). Polyethylene glycol (PEG) variations, succinimidyl PEG NHS (mPEG-NHS(SC)), Cy5 PEG NHS, thiol PEG (mPEG-SH) and Cy5 PEG thiol (Cy5-PEG-SH), each of 2000 Da mass, were purchased

from Nanocs (New York, USA). Deionised (DI) Milli-Q water was used throughout the fabrication. The following protocol is based on standard chemistry principles, established with the assistance of Dr Luca Bau.

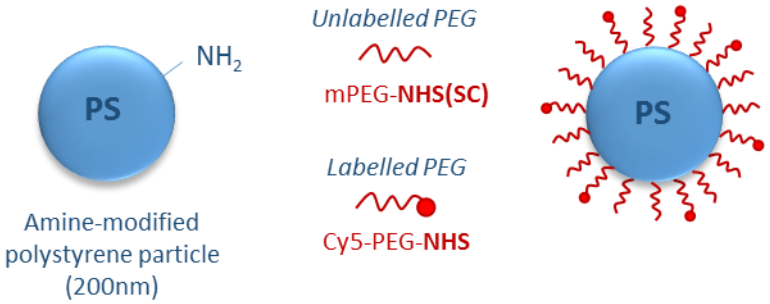

Figure 4.1 *Amine-modified polystyrene nanoparticle of 200 nm diameter, unlabelled and labelled PEG chains and final Cy5-PEG-coated polystyrene nanoparticle.*

Cy5-PEGylated polystyrene nanoparticles were prepared in a solution of 20 mM borate buffer at pH 8.5 (figure 4.1). Both labelled and unlabelled PEG was dissolved into the buffer at ratios of 5:95 Cy5-PEG-NHS to mPEG-NHS(SC). To 5 mL of borate buffer, a total of 1 mg PEG was added, followed by the amine-modified polystyrene particles, at a final concentration of 5×10^{10} particles/mL. The solution was stirred rapidly for 4 hours.

Cy5-PEGylated gold nanoparticles were prepared in a solution of 20 mM sodium phosphate buffer at pH 7.4 (figure 4.2). Both labelled and unlabelled PEG was dissolved into the buffer at ratios of 5:95 Cy5-PEG-thiol to mPEG-thiol. To 5 mL of phosphate buffer, a total of 1 mg PEG was added. Gold nanoparticles were spun down and taken out of the citrate buffer, and were then added to the buffer-PEG solution at a final concentration of 5×10^{10} particles/mL. The solution was stirred rapidly overnight.

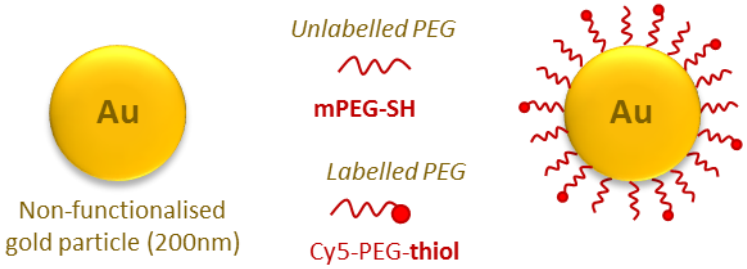

Figure 4.2 *Non-functionalised gold nanoparticles of diameter 200 nm, unlabelled and labelled PEG-thiol chains and final Cy5-PEG-coated gold nanoparticle.*

In both cases a buffer of unlabelled PEG was used to ensure good surface coverage of the particle whilst not inducing self-quenching of the Cy5 label. Self-quenching becomes more likely when fluorophores are brought into close proximity through a targeting or binding technique such as the attachment to a nanoparticle as is used here. Furthermore, by using different ratios of labelled and unlabelled PEG the degree of labelling and final fluorescence brightness could be tuned. The unlabelled PEG formed 95 % of the final PEG coating.

Reagent quantities were based on calculations, considering the nanoparticle surface area and the PEG chain footprint (illustrated in figure 4.3). It was found that 1.14×10^7 PEG (2000 Da) chains were required per 1 mg of nanoparticles (with diameter 200 nm).

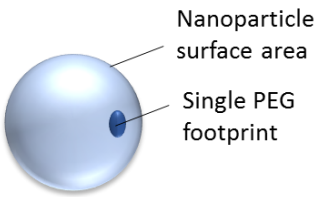

Nanoparticle surface area (nm^2)	125600
PEG (M_N *2000*) chain footprint (nm^2) *(K. Rahme 2013)*	0.25
No. of PEG chains required per 1mg of particles	1.14×10^{17}
Mass of PEG required per 1mg of particles (mg)	0.38

Figure 4.3 *Calculations of reagent quantities including surface area schematic and table of key values.*

Thorough washing was required to ensure all unbound Cy5-PEG and unbound Cy5 (see section 4.2.2) was removed. Centrifugation in 45 mL falcon tubes at 35000 g was carried out for 30 minutes to form a pellet. Washing in the respective buffers was carried out three times, or until the fluorescence intensity of supernatant fell to background levels.

4.2.2 Characterisation results

The final constructs were found to have a tight size distribution around a peak diameter of 200 nm, assessed through dynamic light scattering (DLS) (Zetasizer, Nano – ZS, Malvern Instruments, Malvern, UK). Both constructs were also found to have negative zeta potential when measured in aqueous suspension.

Table 4.1 *Summary of DLS data from Cy5-PEG-PS and Cy5-PEG-Au nanoparticles.*

Cy5-PEG-PS nanoparticles	
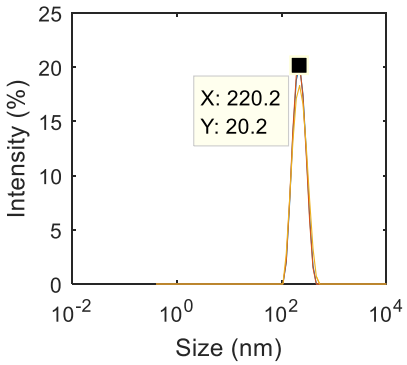	
Z-Average (nm)	210.03 ± 2.10
PdI	0.10 ± 0.04
Zeta potential (mV)	-23.20 ± 0.40
pH	6.8

Cy5-PEG-Au nanoparticles	
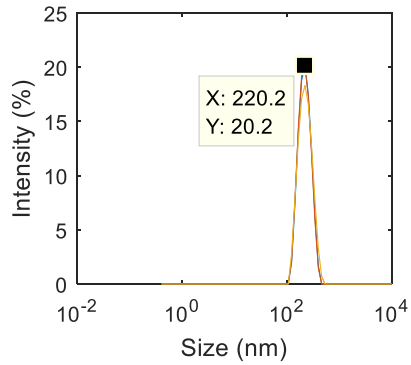	
Z-Average (nm)	212.53 ± 6.37
PdI	0.18 ± 0.02
Zeta potential (mV)	-18.63 ± 1.27
pH	7.3

A) **B)**

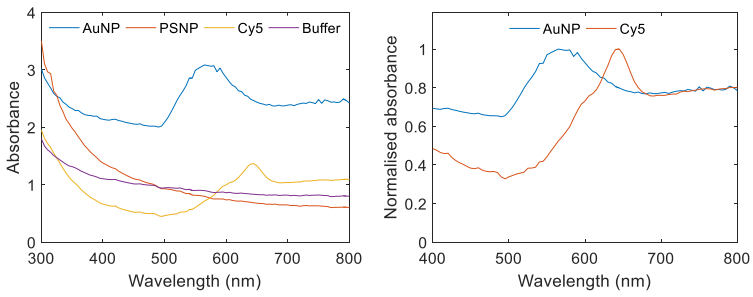

Table 4.2 *Absorbance peak of each component.*

Component	***Absorbance peak***
AuNP	565 nm
PSNP	315 nm
Cy5	640 nm
Buffer	300 nm

Figure 4.4 *Absorbance spectra of construct components,* ***A)*** *200 nm gold nanoparticles (AuNP), 200 nm polystyrene nanoparticles (PSNP), unbound fluorophore (Cy5) and sodium phosphate buffer (Buffer).* ***B)*** *Gold nanoparticles and Cy5 fluorophore show separation of absorbance peaks.*

The absorbance spectrum of each component was measured using the microplate reader (FLUOstar Omega, BMG Labtech, Buckinghamshire, UK) at a wavelength resolution of 5 nm (figure 4.4(A)). Figure 4.4(B) illustrates the separation of absorbance peaks associated with 200 nm gold nanoparticles (AuNP) and the free Cy5 fluorophore. Absorbance peaks are summarised in table 4.2.

Chemical purity of Cy5-PEG

Chemical purity may be defined as 'the fraction of the main component present in a given sample' (Staveley 1971). The chemical purity of the commercially purchased fluorescently labelled PEG was assessed using a size exclusion column. It was found that this commercially sourced Cy5-PEG-NHS contained a significant portion of unbound Cy5. The bound Cy5-PEG and free Cy5 were separated using a PD-10 size exclusion column, also known as a molecular sieve, flushed through with borate buffer (20 mM, pH 8.5). Due to their differences in size and molecular weight, the two components formed two distinct bands (figure 4.5(B)).

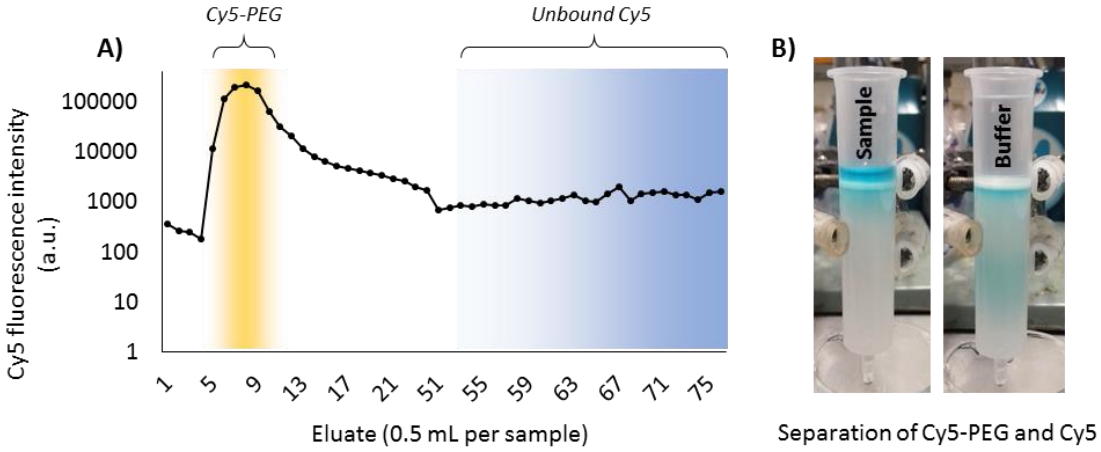

Figure 4.5 *Assessing the purity of Cy5-PEG-NHS using a size exclusion column,* ***A)*** *measuring the fluorescence intensity of each eluate and* ***B)*** *visually observing a separation of blue bands indicating unbound Cy5 (upper band) and Cy5-PEG (lower band).*

The fluorescence intensity of the 0.5 mL eluates was measured in a black flat-bottom 96 well plate, with a peak corresponding to Cy5-PEG-PS and Cy5-PEG occurring at eluates 6 – 9 (figure 4.5(A)). This assessment of purity was used to inform the washing protocol of the particles through centrifugation, to ensure all unbound fluorescence was removed.

Stability study

A stability study was carried out to assess any aggregation over time and decay in fluorescence intensity. The particles were stored in the respective buffers used for fabrication (i.e. 20 mM borate buffer and 20 mM phosphate buffer) and monitored daily over 144 hours. Both constructs were found to be stable in size and size distribution when stored in the buffers used for fabrication (figure 4.6(A)). However, Cy5-PEG-Au nanoparticles were found to decay in fluorescence intensity dramatically over the course of the study, emitting less than 30 % of the original fluorescence intensity 7 days after fabrication (figure 4.6(B)).

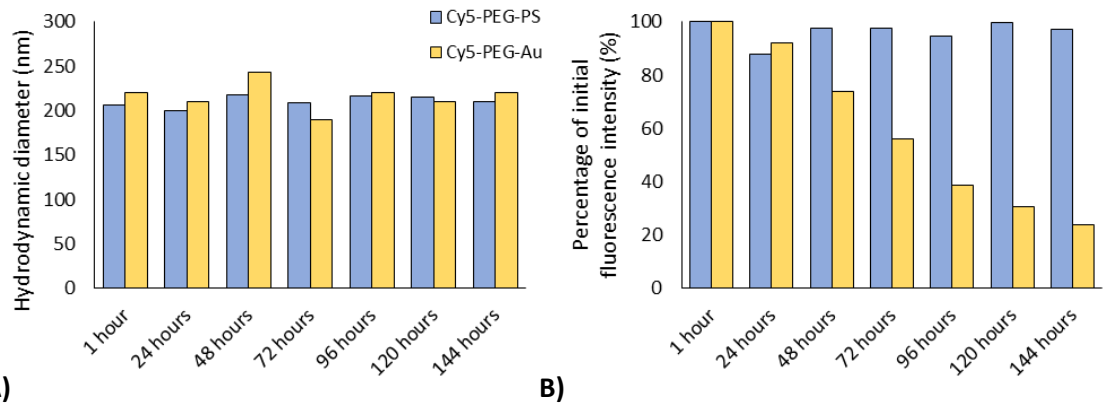

Figure 4.6 *Stability of **A)** hydrodynamic diameter and **B)** fluorescence intensity over 144 hours, comparing Cy5-PEG-PS and Cy5-PEG-Au nanoparticles.*

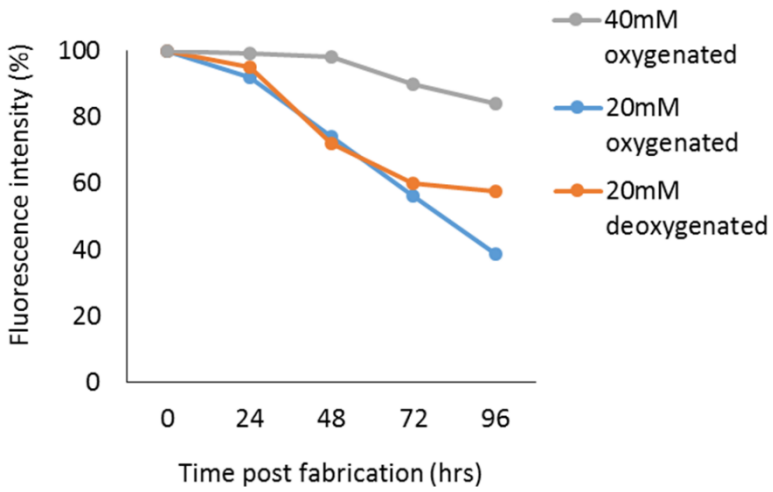

Figure 4.7 *Stability of Cy5-PEG-Au nanoparticles stored in three different conditions: 40 mM phosphate buffer, 20 mM phosphate buffer and 20 mM phosphate buffer deoxygenated.*

To explore this decay in fluorescence, a second stability study was carried out looking exclusively at the Cy5-PEG-AuNPs stored in three different dark conditions: (1) 20 mM phosphate buffer, 4 °C, atmospheric oxygen level, (2) 20 mM phosphate buffer, 4 °C, deoxygenated using nitrogen gas, and (3) 40 mM phosphate buffer, 4 °C, atmospheric oxygen level. Figure 4.7 shows the decay in fluorescence intensity of these three batches over 96 hours. It was found that increasing the buffer concentration to 40 mM significantly increased the fluorescence life time of the Cy5-labelled gold nanoparticles.

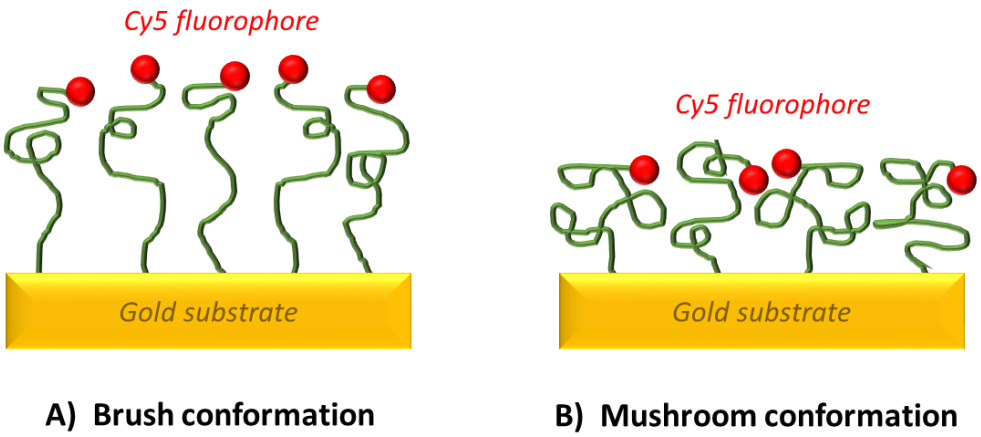

Figure 4.8 *Schematic of PEG chains grafted to gold substrates and attached to Cy5 fluorophores in **(A)** brush and **(B)** mushroom conformations (adapted from Kim et al. 2015).*

The increased stability of the fluorescence at 40 mM buffer concentration is attributed to the conformation of PEG chains at various ionic strengths. PEG chains are characteristically found in either 'brush' or 'mushroom' conformations (Kim *et al.* 2015). A more bunched 'mushroom' conformation brings the fluorophore closer to the gold surface resulting in greater fluorescence quenching, whilst a 'brush' formation retains good separation between the fluorophore and gold surface resulting in a higher fluorescence intensity. Based on literature (Moh *et al.* 2011) it is hypothesised that at 20 mM buffer concentration the PEG conformation tends towards a 'mushroom' conformation (i.e. reducing the fluorescence signal), whilst at 40 mM the conformation is more 'brush'-like (i.e. preserving the fluorescence signal over 48 hours) (figure 4.8). To ensure the greatest fluorescence intensity for the nanoparticles used in this study, the samples were stored in 40 mM concentration buffer and used within 48 hours of fabrication.

Competitive reactions

The efficiency of the Cy5-PEG-NHS-PS reaction is likely to be less than Cy5-PEG-SH-Au due to competitive reactions. Two competitive reactions exist in the formation of the PEG-NHS-PS bond. Firstly, the primary (and desired) reaction of aminolysis depends on both pH and concentration, becoming faster with increased pH and PEG concentration. Secondly, hydrolysis acts in competition to aminolysis, cleaving amine bonds in the presence of water found in the buffer. If the concentration of PEG is too low, the aminolysis rate will become comparable to or lower than the hydrolysis rate, and PEGylation will become very inefficient. Although Cy5-PEG-PS nanoparticles experience these competitive reactions, the effects of quenching appear to be more influential, with Cy5-labelled gold producing a lower fluorescence intensity than Cy5-labelled polystyrene for the same particle concentration.

IVIS detection study

The *In Vivo Imaging System* (IVIS) (PerkinElmer, USA) was used to measure the fluorescence intensity of tumours in live anaesthetised animals, and ultimately to quantify nanoparticle uptake. My role during this study included fabricating the fluorescence nanoparticles, preparing the spiked lysate well plate, designing the calibration study and instructing which images to acquire. Since I do not have the appropriate training to operate the IVIS, Megan Grundy is gratefully acknowledged who operated the IVIS equipment throughout this work.

To calibrate the IVIS, and correlate fluorescence intensity in tumour tissue with quantity of nanoparticles present, tumour lysate (a fluid suspension of lysed or ruptured cells) was spiked with a gradient of nanoparticle concentrations, from 100 % of the injected dose ($1x10^{11}$ particles/mL where no tumour lysate was present) to 0 % (where only tumour lysate was present). The spiked lysate was prepared in a black flat-bottom 96 well-plate and measured using both a conventional microplate reader and the IVIS. It should be noted that the tumour lysate was isolated from the same tumour model (female BALB/c with CT26 cell line inoculation) but had not be given purified diet (section 4.3.1). It is possible therefore that background fluorescence signal may be higher in this control study than the final experiment.

It is also apparent from figures 4.9 that adding the Cy5-labelled nanoparticles to tumour lysate caused an increase in fluorescence emission, resulting in the particle suspension at 50 % concentration having a greater fluorescence intensity than particles alone. This effect is likely attributable to protein binding, a phenomenon termed protein induced fluorescence enhancement (PIFE). PIFE has been reported for a number of cyanine dyes such as Cy5 and Cy3 (Stennett *et al.* 2015, Hwang *et al.* 2011). This enhancement is expected to be present also in the final tumour samples. Furthermore, it should be noted that a pipetting error

occurred for the 0.50 % concentration sample of Cy5-PSNP, indicated with red circles on figures 4.9 – 4.13.

Image acquisition using the IVIS requires a sequential procedure, including optimising the excitation and emission filters, the field of view and the exposure time. Quantification of IVIS images can be achieved through post-processing, where specific regions of interests (ROIs) may be selected to assess the number of fluorescent pixels in a specific region, known as total counts. In this calibration study each occupied well of the 96 well plate was defined as an ROI. Once the system had been fully optimised it was found that 0.10 % of the injected dose ($1x10^8$ particles/mL) could be successfully detected on the IVIS, for both Cy5-AuNP and Cy5-PSNP constructs in tumour lysate. An exposure time of 10 s was used to determine the sensitivity – at longer exposure durations the image became highly saturated and the background signal exceeded 2000 average counts due to specular reflections from the well plate.

1) Optimising IVIS excitation and emission filters

Firstly the fluorescent filters were optimised by testing a variety of combinations of excitation and emission filters. Figure 4.9 shows the total counts detected across a series of ROIs for five different excitation/emission filter combinations, from 570 nm to 675 nm wavelength excitation and 705 nm to 815 nm (labelled as ICG) wavelength emission. Although combinations ex605/em705 and ex640/em705 detect a very similar number of fluorescence pixels, using an excitation of 640 nm requires half the exposure time, suggesting more efficient excitation and therefore a lower likelihood of photobleaching. Therefore an excitation filter at 640 nm and an emission filter at 705 nm were chosen to detect the Cy5 fluorophore on the labelled nanoparticles.

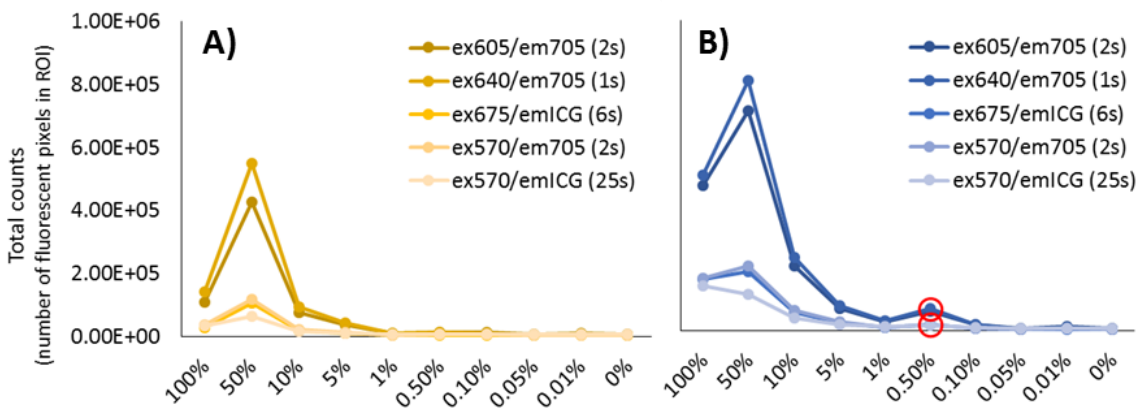

Figure 4.9 *Total counts detected through IVIS imaging for five different excitation and emission filter combinations across a range of particle concentrations for* ***(A)*** *Cy5-AuNPs and* ***(B)*** *Cy5-PSNPs, where the exposure time in seconds is stated in brackets beside each exposure condition. A pipetting error at 0.50 % concentration is identified with red circles.*

2) Optimising IVIS field of view

Secondly, the field of view must be chosen. The field of view in the IVIS is described by letters A – D, and governs how high the camera sits above the target and therefore the size of the imaged field. It was found that by moving from setting D (the largest field of view with an image size of 125 mm x 125 mm) to setting C (closer to the target with an image size of 100 mm x 100 mm) there was a significant enhancement in the fluorescence detection. Figure 4.10 shows the black and white photograph taken by the IVIS for spatial registration at field of view D and C. Figure 4.11 shows the effect changing the size of the field of view has on the number of detected fluorescent pixels. It can be seen that by moving from setting D to C achieves a 3 to 4-fold increase in detection sensitivity.

At low concentrations the detection enhancement of using a smaller field of view is also apparent. For the Cy5-labelled nanoparticles choosing the field of view ‘C’ rather than ‘D’ makes detecting 0.10 % of the injected dose possible (figure 4.12).

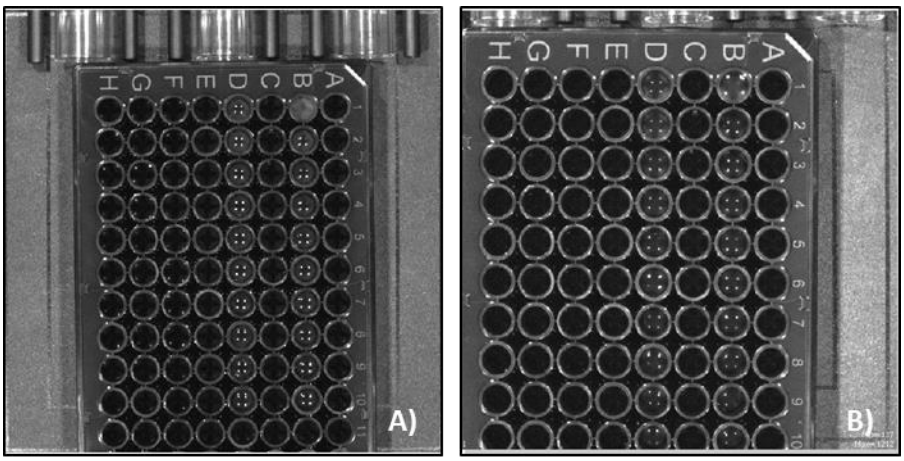

Figure 4.10 *Black and white photographs captured using the IVIS illustrating two different fields of view –* ***A)*** *field of view D (125 mm x 125 mm) and* ***B)*** *field of view C (100 mm x 100 mm).*

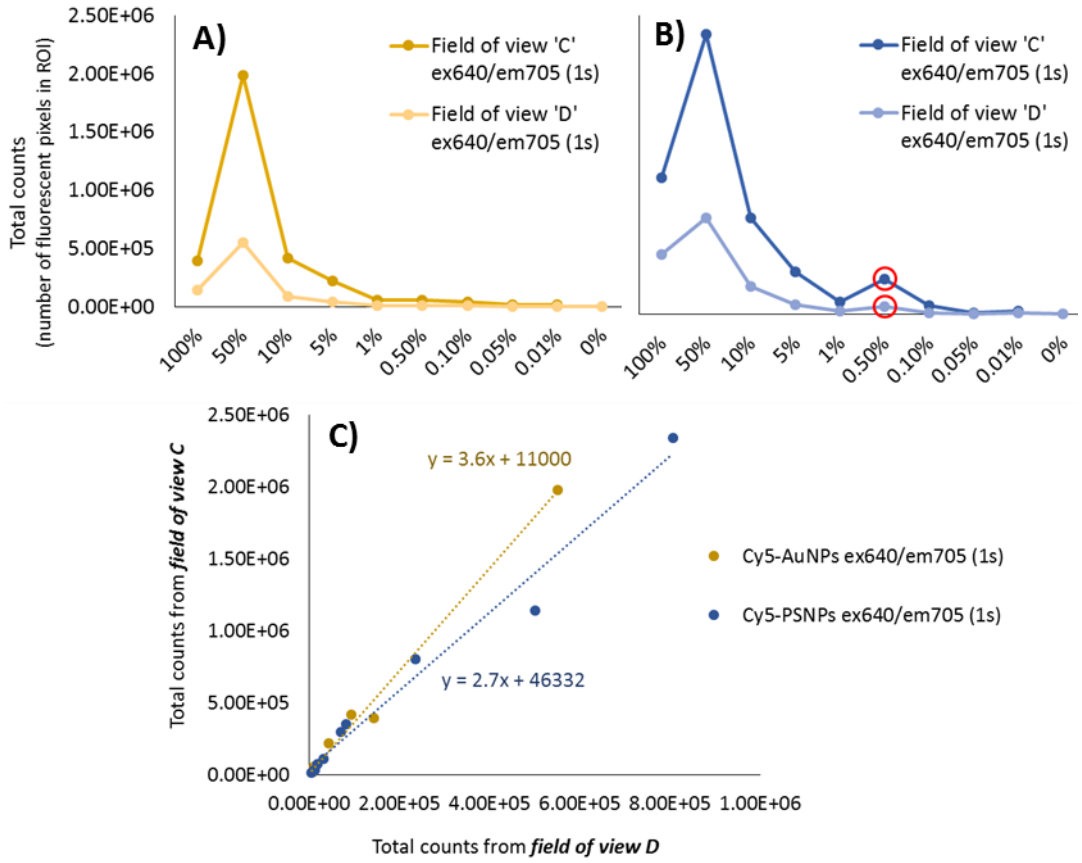

Figure 4.11 *Influence of field of view on detected total counts for* ***(A)*** *Cy5-AuNPs and* ***(B)*** *Cy5-PSNPs,* ***(C)*** *illustrating using field of view C achieves approximately 3 times greater detection of fluorescent pixels than field of view D. A pipetting error at 0.50 % concentration is identified with red circles.*

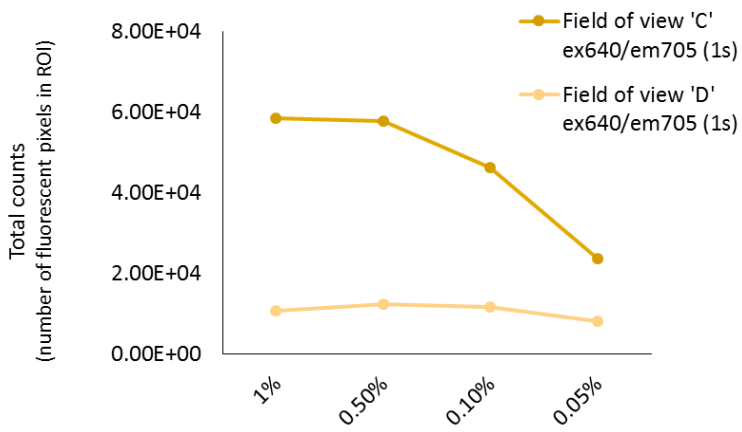

Figure 4.12 *Influence of field of view on detected total counts at low concentrations, comparing field of view D and C.*

3) Optimising IVIS exposure time

A variety of exposure times were tested, from 1 s to 20 s in order to visualise all dilutions (figure 4.13). The maximum exposure time was found to be governed by the saturation level (65000 counts) and the increasing background signal (which was set at 2000 counts in post-processing).

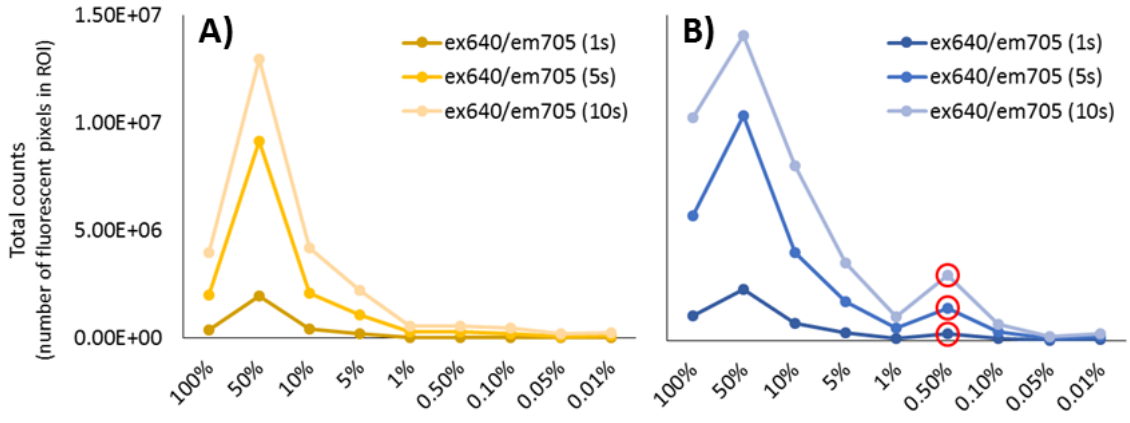

Figure 4.13 *Total counts detected through IVIS imaging for three different exposure times across a range of particle concentrations for **(A)** Cy5-AuNPs and **(B)** Cy5-PSNPs. A pipetting error at 0.50 % concentration is identified with red circles.*

The influence of using saturated or unsaturated images was also studied to assess the influence on fluorescence detection and total count in unsaturated regions. However, it was found that having saturated regions present in an image did not affect the ability to detect pixels in low fluorescence regions, and the total count in these regions was unaffected when a saturated region was either present or obscured in the image. This is an important detail, since in many live animal *in vivo* images, the head, feet and tail of the animal can produce very high fluorescence signals due to the autofluorescence of hair and various skin types. It was important therefore to check that these small regions, which may become saturated, did not affect the integrity of the unsaturated target regions – the tumour tissue.

4) Assessing IVIS photobleaching

It was also important to ensure that imaging using the IVIS did not cause photobleaching of the Cy5 fluorophore. This could be monitored by capturing the same image with identical settings at the beginning and end of the imaging session to measure any decay in fluorescence emission. Initial and final IVIS images captured the same number of total counts (± 0.2e5) suggesting no detectable photobleaching during the imaging session.

5) Defining IVIS regions of interest (ROI)

In post-processing of IVIS images, regions of interest (ROIs) may be defined. Figure 4.14 illustrates the regions of interest selected on the 96 well plate. The IVIS image shows a black and white photograph for spatial registration, with a fluorescence count colour map overlay. Small regions of red appear outside the regions of interest showing high background levels, as well as yellow saturated regions, both indicating that the image is overexposed.

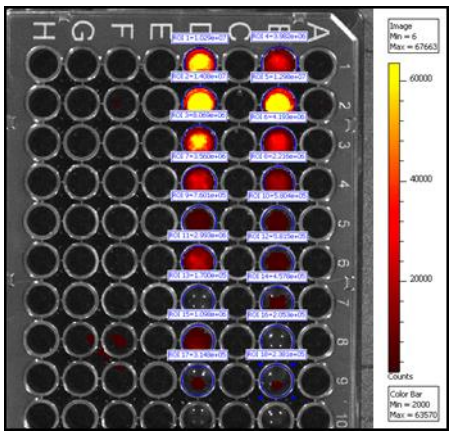

Figure 4.14 *An example IVIS image showing the fluorescence image in colour scale overlaid on a black and white photograph for spatial registration, with blue circles defining regions of interest (ROIs).*

Correlating microplate reader and IVIS measurements

Finally the microplate reader fluorescence intensity measurements were correlated with the total counts detected on the IVIS. Figure 4.15 shows the linear trend between plate reader and IVIS data for both Cy5-AuNP and Cy5-PSNP constructs, comparing fields of view D and C. Good correlation was found between these two independent fluorescence techniques.

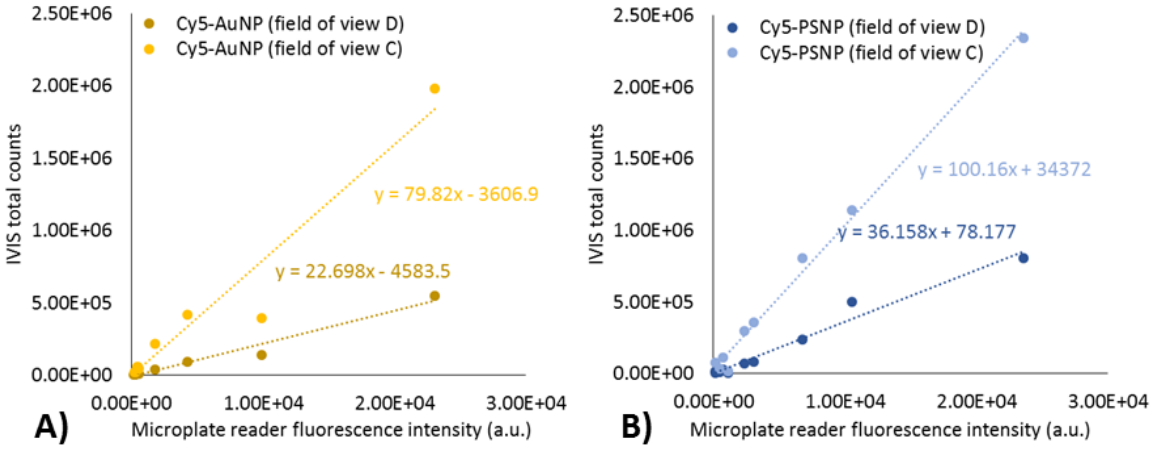

Figure 4.15 *Correlating microplate reader fluorescence intensity and IVIS total count values for* ***(A)*** *Cy5-AuNPs and* ***(B)*** *Cy5-PSNPs imaged under two differently sized fields of view.*

4.3 *In vivo* model

4.3.1 Methodology

My role during the following *in vivo* work included designing the study, the preparation of injections including the fluorescent nanoparticles and cavitation agents, time-keeping and note-taking on the day to co-ordinate the treatment and imaging of 30 mice, and all post-processing and data analysis reported here. Since I did not hold an animal handling licence Professor Robert Carlisle, Sheena Wallington, Dr Christophoros Mannaris, Megan Grundy and Jamie Wallis are all gratefully acknowledged for their expertise and assistance in performing the following work.

In vivo protocol

A tumour model was chosen using BALB/c female mice implanted with the murine colon carcinoma cell line CT26, as used in several previous ultrasound-mediated drug delivery studies (Myers *et al.* 2016, Crake *et al.* 2016, Mo *et al.* 2015). The CT26 cell line forms a well characterised murine tumour model for drug delivery, and is commonly used to mimic human solid tumours because of its fast growing nature and consequential leaky vasculature (Kunjachan *et al.* 2014). However, it should be noted that this tumour model, because of the rapid and chaotic nature of its growth, is also prone to high perfusion variability and ulcerations beyond approximately 500 mm^3 in tumour volume (Smyth *et al.* 2005). 30 mice were inoculated subcutaneously with CT26 cells suspended in RPMI media (Roswell Park Memorial Institute, ThermoFisher) at a concentration of 2×10^5 cells per 100 µL injection. Two tumours were implanted per mouse, one on each flank. Professor Robert Carlisle is gratefully acknowledged for carrying out all the inoculations.

After inoculation, animal weights were measured every 3 days to assess the health of the animals. All animals were found to exhibit gradually increasing weights and remained within 2.5 standard deviations of the group mean weight (figure 4.16).

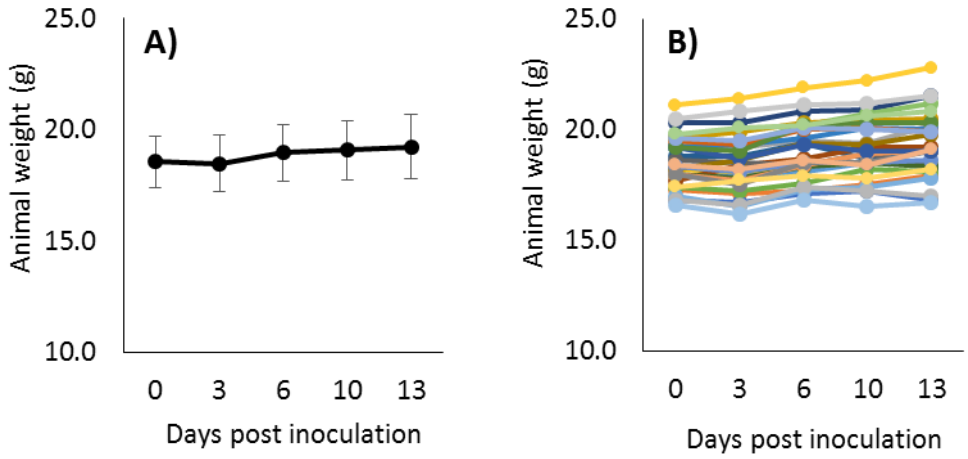

Figure 4.16 *In vivo monitoring of animal weights post inoculation, shown as **(A)** the group mean and **(B)** as individual animals. Error bars show 1 standard deviation of animal weights.*

Purified diet and autofluorescence

5 days before treatment the animals were switched to a purified diet. Removing chlorophyll found in the dehydrated alfalfa meal commonly used in laboratory animal diets has been shown to significantly reduce the autofluorescence of the animal when imaged with IVIS (Troy *et al.* 2004). In a study comparing conventional grain-based lab diets and chlorophyll-free purified diets with adult male C57BL/6 mice, autofluorescence (quantified as fluorescence efficiency at excitation wavelength 675 nm and emission wavelength 720 nm) fell from 4×10^{-5} to 2×10^{-5} after 6 days (figure 4.17) (*PMI Nutrition International*, 2015).

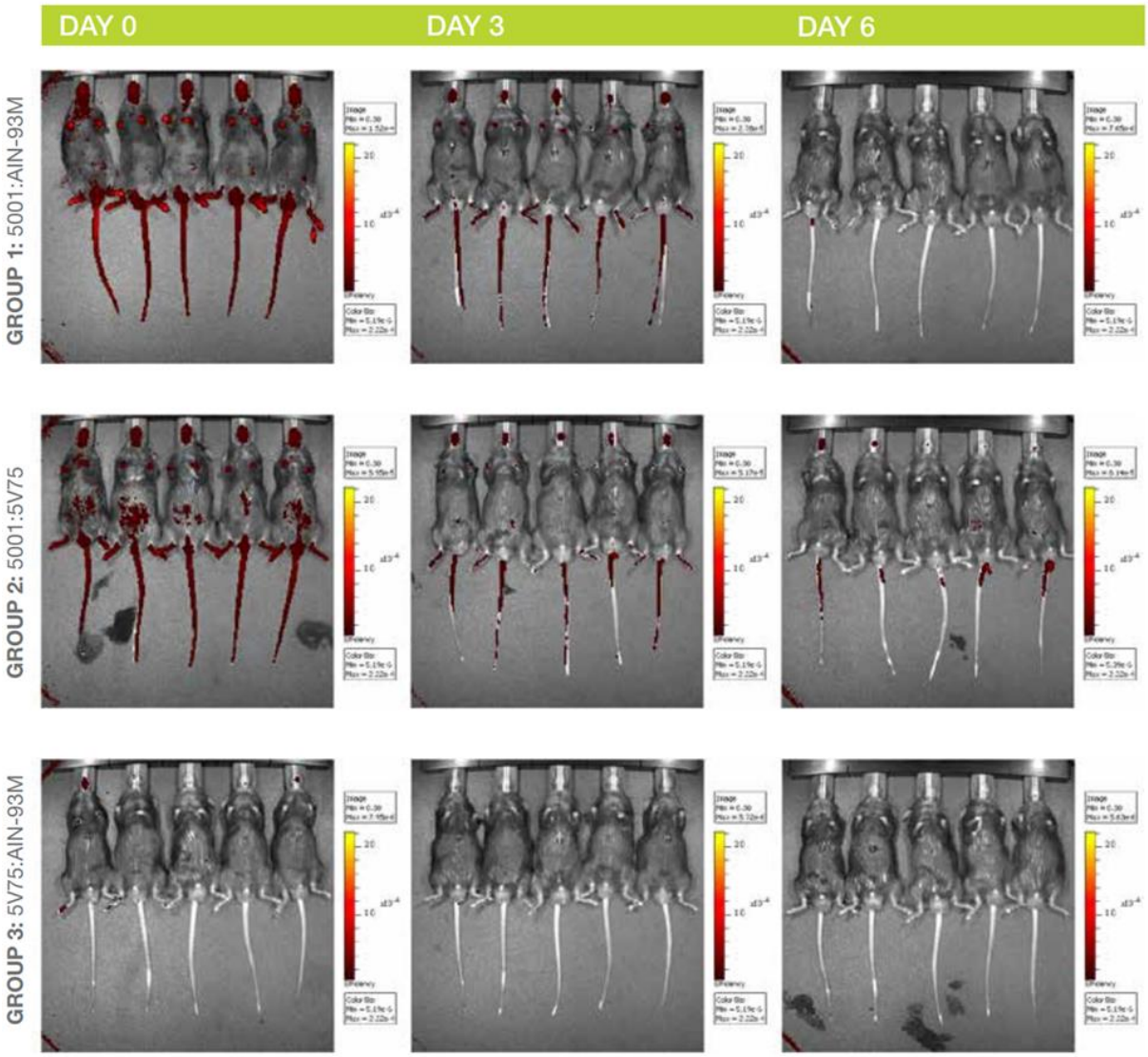

Figure 4.17 *Reduction in autofluorescence when switching from grain-based to purified diet, detected at an emission wavelength of 680 nm wavelength on the IVIS (PMI Nutrition International, 2015).*

In order to see if the PMI Nutrition International (2015) results could be replicated for tumour-bearing female BALB/c mice, IVIS images were captured of 2 mice when on un-purified diet and after 5 days on purified alfalfa-free diet. Alfalfa-free diet (Teklad Irradiated Global 19 % Protein Extruded Rodent Diet) was sourced from Envigo (Madison, WI, USA). Tumour regions were shaved prior to IVIS imaging for tumour sizing. After 5 days on purified feed, a 27.5 % mean decrease was measured for the average counts in the tumour region (contoured in white), showing a significant reduction in autofluorescence (figure 4.18).

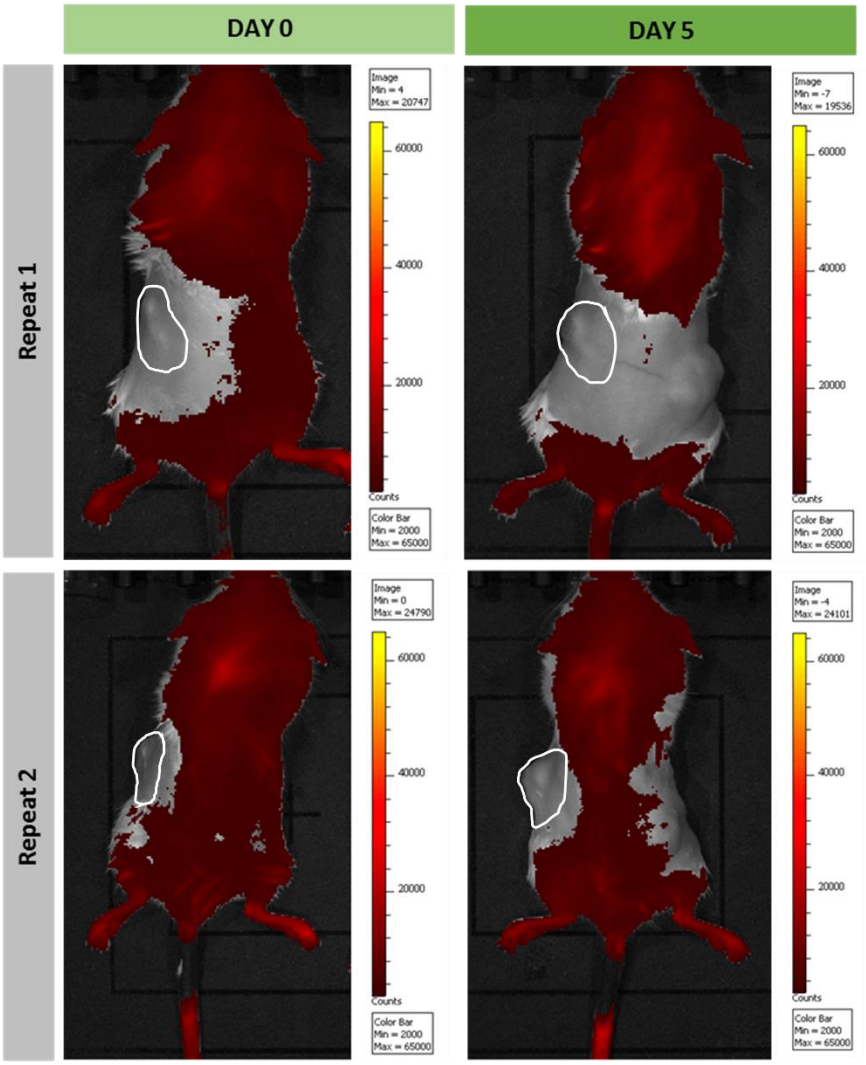

Figure 4.18 *IVIS images illustrating autofluorescence of 2 BALB/c mice before and after 5 days on purified feed, captured using Cy5 optimised filters at an exposure time of 1 s, with tumour regions contoured in white.*

Ultrasound exposure

8 experimental groups were formed in total (table 4.3), with 3 mice per group. Sheena Wallington is gratefully acknowledged for having performed all cannulations and injections during this study. Ultrasound-mediated delivery experiments were performed 18 days after inoculation, when the tumours had reached a combined volume in excess of 200 mm^3 but less than 1000 mm^3 for each animal, measured with callipers. Tumour volumes varied substantially

within and between animals. When separating animals into treatment groups, a distribution of sizes was sought in each group (figure 4.19).

Table 4.3 *Experimental groups 1-9 with mock therapeutic nanoparticle Cy5-PEG-PS or Cy5-PEG-Au, with or without ultrasound (US) exposure, co-injected with an inactive (iNC) or active cavitation agent (NC or SV).*

Group	**Cy5-PEG-PS** Nanoparticle	**Cy5-PEG-Au** Nanoparticle	**US** Exposure	**iNC** Inactive cavitation agent	**NC** Cavitation agent	**SV** Cavitation agent
1	✓					
2		✓				
3	✓		✓	✓		
4		✓	✓	✓		
5	✓		✓		✓	
6		✓	✓		✓	
7	✓		✓			✓
8		✓	✓			✓

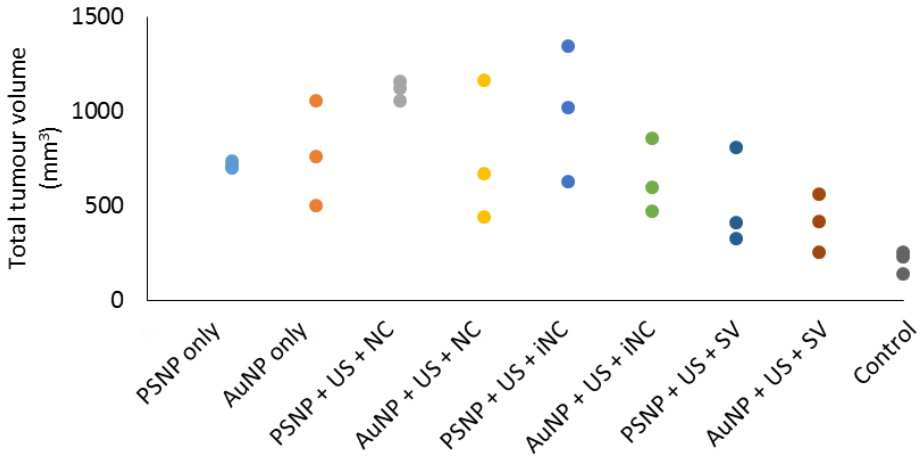

Figure 4.19 *Distribution of total tumour volume per animal before treatment, separated by experimental group.*

Before exposure, anaesthesia was induced using isoflurane gas and maintained throughout the study. Each mouse was cannulated, placed into the water tank and aligned with the ultrasound focus before it received an intravenous injection of 50 µL of PEGylated Cy5-labelled 200 nm gold or polystyrene nanoparticles, co-injected with 50 µL of cavitation agent (either NanoCups or SonoVue® microbubbles, at stock concentration of 20 mg/mL or 10^8

bubbles/mL respectively) or buffer (sterile 5 % glucose). Ultrasound control groups additionally received 10 minutes of ultrasound exposure with or without an inactive cavitation agent. Inactive NanoCups (iNC) are an acoustically unresponsive version of NanoCups, and have been fabricated without an air-drying stage (section 3.2.3 - *Stability*) and therefore do not contain a pocket of gas. iNC were found to show little or no acoustic response at 0.5 MHz with 1.5 MPa, and were used *in vivo* as a control group to mitigate any enhanced delivery associated with the chemical agent alone.

When injecting SonoVue®, a staggered treatment procedure was applied, whereby half of the total volume was initially injected, followed by a 4-minute pause before the next half volume was delivered. This procedure was implemented to account for the extremely short circulation time of SonoVue®, on the order of 60 – 80 s in small animal models (Wu *et al.* 2017, Bazan-Peregrino *et al.* 2013).

Following the treatment injection, the tumour region was exposed to ultrasound at centre frequency 0.5 MHz and 1.5 MPa peak negative pressure, with the intention of inducing sustained inertial cavitation, for 10 minutes (table 4.4). Only one tumour per mouse was exposed to ultrasound, the second untreated tumour provided an internal control. The second mouse was not treated until recovery and health of the first mouse was confirmed.

Ultrasound was delivered using a dual-transducer, dual-array, transmit and receive setup (figure 4.20). A small water tank filled with degassed water, heated to 37 °C, was used to immerse the posterior half of the animal, allowing transmission of ultrasound to the target tumour. Two 0.5 MHz centre frequency HIFU transducers (H-107C-033 and H-107C-034, Sonic Concepts, USA) – each with element diameter 64 mm, geometric focus 63.2 mm, focal size 3.0 x 21.4 mm and rectangular central opening – were aligned to the same focal spot, creating a

combined tight focal region of approximately 3 x 5 mm, which was scanned through the tumour volume throughout the 10 minutes exposure. This orthogonal setup using 2 transducers was chosen to minimise pre-focal cavitation, since the two transducers could each be driven at 0.75 MPa but achieve 1.5 MPa at the focus. This configuration also creates a tight focal volume for accurate positioning inside the tumour volume.

Acoustic emissions were detected using two transducer arrays embedded inside the HIFU transducers. Using two arrays of 'listening' transducers allowed cavitation activity to be monitored in time and space, a technique known as passive acoustic mapping (PAM), discussed later. This bistatic configuration was first described by Elbes *et al.* (2017), where two orthogonal and coplanar L11-5 probes (128-element linear arrays) are used, each with 6.25 MHz centre frequency (Verasonics, USA). Successful activation of the cavitation agents could therefore be monitored in real-time, at sub-millimetre resolution, over a 20 x 20 mm area. Although the data is inherently filtered due to the bandwidth of the probes, additional digital filtering is applied, including a bandpass filter of 5 – 11 MHz and a comb filter to remove harmonic components such that just broadband information remained. Dr Christophoros Mannaris is gratefully acknowledged for operating the ultrasound setup throughout this study.

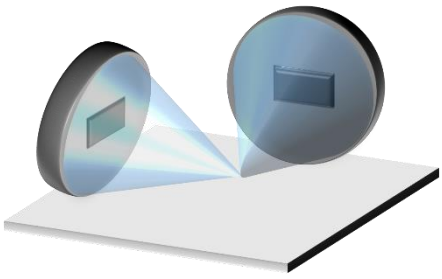

Figure 4.20 *Dual-transducer, dual-array, transmit and receive ultrasound setup.*

Table 4.4 *Ultrasound parameters.*

Frequency	0.5 MHz
Peak negative pressure	1.5 MPa
Pulse repetition frequency	0.5 Hz
Duty cycle	5.0 %
Number of cycles per pulse	50,000 cycles
Total exposure duration	10 mins

Passive Acoustic Mapping

The ultimate aim of PAM is to produce a spatial map showing the estimated locations and strengths of cavitation sources within a specific field of view. Originating from a technique known as Time Exposure Acoustics used in underwater acoustics (Buckingham *et al.* 1992) and seismology (Norton *et al.* 2000), PAM was first used in combination with HIFU to track bubble activity *in vitro* by Gyöngy *et al.* (2008).

An array of elements, with fixed and known spacing, can be used to locate a cavitation source within a map by steering the beam to each pixel location, achieved by applying corresponding delays to each element signal. These signals can also be weighted to account for spherical spreading or to remove noise from interfering sources, before being summed. Together this processing of delay, weight and sum is known as beamforming, and several algorithms have been developed to achieve this (Thomenius 1996, Synnevag *et al.* 2007). In the current work the robust Capon beamformer is used, an adaptive beamformer which continuously optimises the weighting values and time delays to minimise variance in the signal, thus accurately localising the cavitation source (Coviello *et al.* 2015).

In the following work the source strength is defined in terms of '*PAM magnitude*'. This metric is calculated by identifying the peak energy pixel within each PAM frame through time, therefore spatially averaging the signal to a single energy value every 2 s. This metric is also averaged temporally to summarise the cavitation activity across the entire exposure duration; this is described as the '*mean PAM magnitude*' (figure 4.24).

Imaging procedure

The current study will use three different methods to quantify the amount of fluorescence material delivered to the tumours: (1) whole animal live imaging using the IVIS, (2) *ex vivo* imaging of excised tumours using the IVIS and (3) fluorescence measurement of homogenised tumour tissue using the microplate reader.

Fluorescence live-animal imaging was achieved using the Perkin Elmer IVIS. The red Cy5 fluorophore used to label the density-contrasting nanoparticles was visible in the circulatory system of the animals, allowing tumour uptake of the constructs to be mapped. Imaging using IVIS was performed before the first injection to capture a control image of background intensity, after treatment, and of the excised tumours.

All animals used in the study were sacrificed after imaging. At sacrifice, tumours were excised, imaged with IVIS, and snap frozen on dry ice for further analysis. Jamie Wallis is gratefully acknowledged for monitoring animal heath, culling animals and excising tumours. Homogenised tumour tissue was achieved using a handheld mechanical homogeniser (T10 basic Ultra-Turrax, IKA, Oxford, UK), and a 1:1 weight-volume ratio of tumour tissue to DI water, for fluorescence measurements using the microplate reader.

It was known from the fluorescence stability study in section 4.2.2 (figure 4.7) that a decay in fluorescence could occur within hours in the least favourable conditions. In an effort to reduce this time and to remain consistent in imaging each animal at the same time point, each animal was timed precisely using a stopwatch. Post-treatment imaging occurred 20 minutes after the injection, and 10 minutes after ultrasound treatment. The mouse was then in the IVIS for no longer than 5 minutes (including alignment and imaging), before being culled and the *ex vivo* images acquired.

4.3.2 Results

4.3.2.1 Cavitation detection

PAM was able to detect the magnitude and persistence of cavitation activity within each experimental group. Cavitation activity was quantified as 'PAM magnitude', a metric which describes the value of the highest energy pixel in each PAM map. Figures 4.21 – 4.24 show the PAM magnitude data and the mean and peak PAM magnitudes for each treatment group. Differences in peak PAM magnitude were found to be statistically significant between SonoVue® and background, and between SonoVue® and inactive NanoCups. Cavitation emissions detected from the active NanoCups group showed too wide a distribution to achieve statistical significance relative to all other exposure groups.

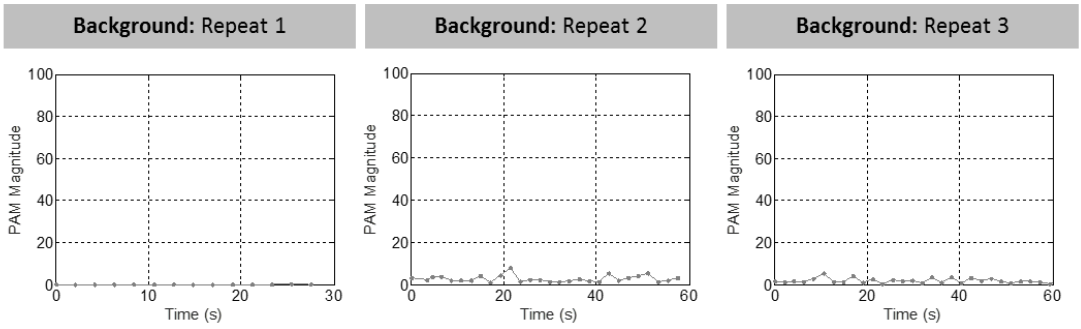

Figure 4.21 *PAM magnitude data for background noise.*

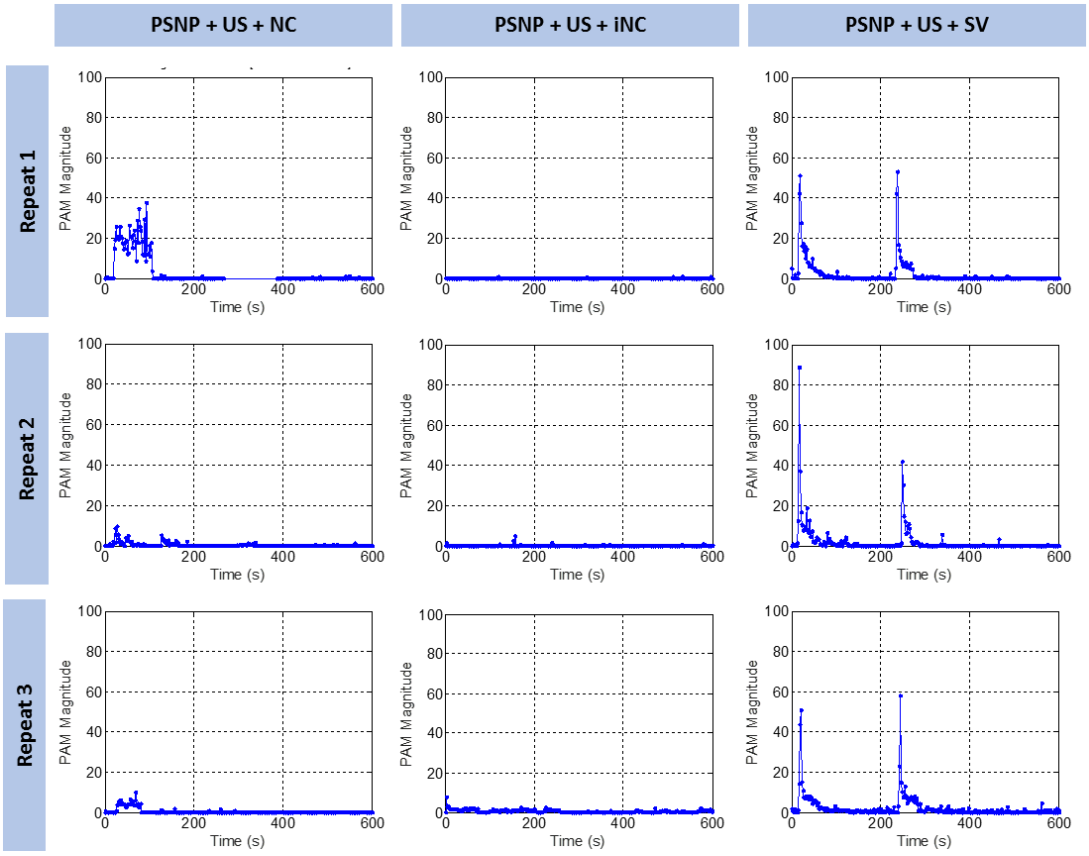

Figure 4.22 *PAM magnitude data for polystyrene nanoparticle (PSNP) treatment groups. The staggered injection of SV occurs at t = 10 s and t = 220 s.*

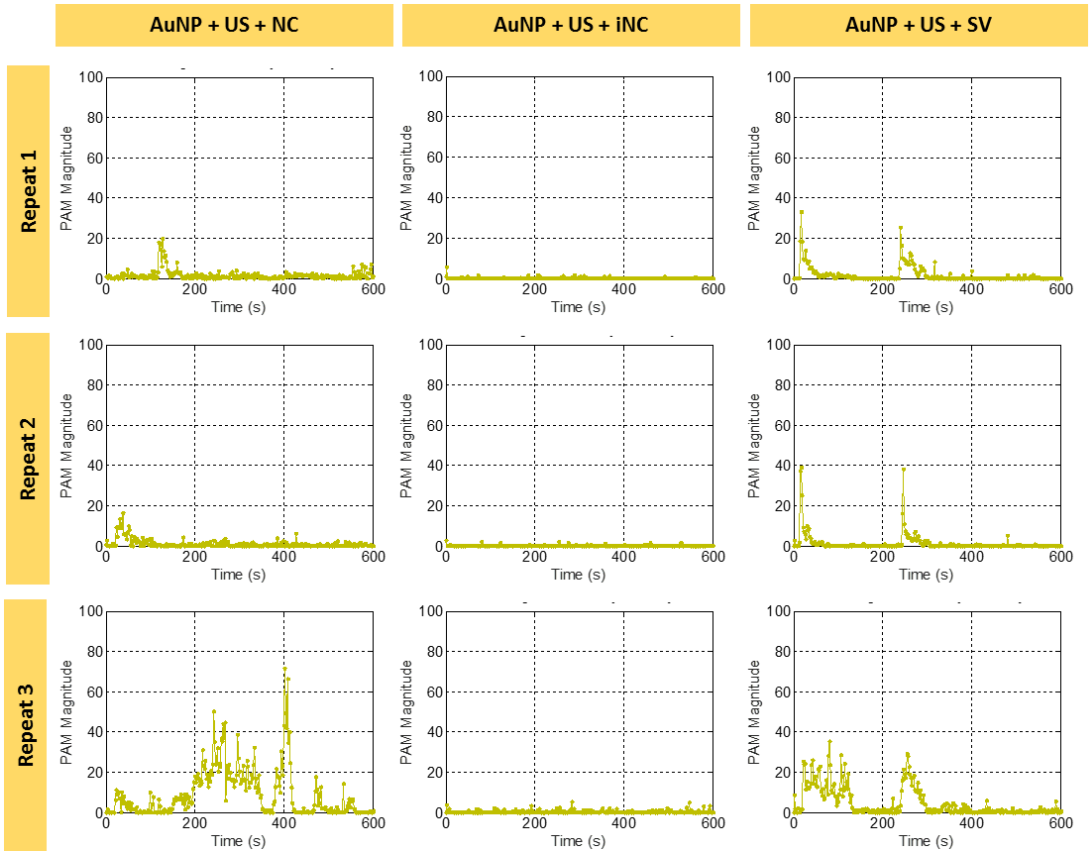

Figure 4.23 *PAM magnitude data for gold nanoparticle (AuNP) treatment groups. The staggered injection of SV occurs at t = 10 s and t = 220 s.*

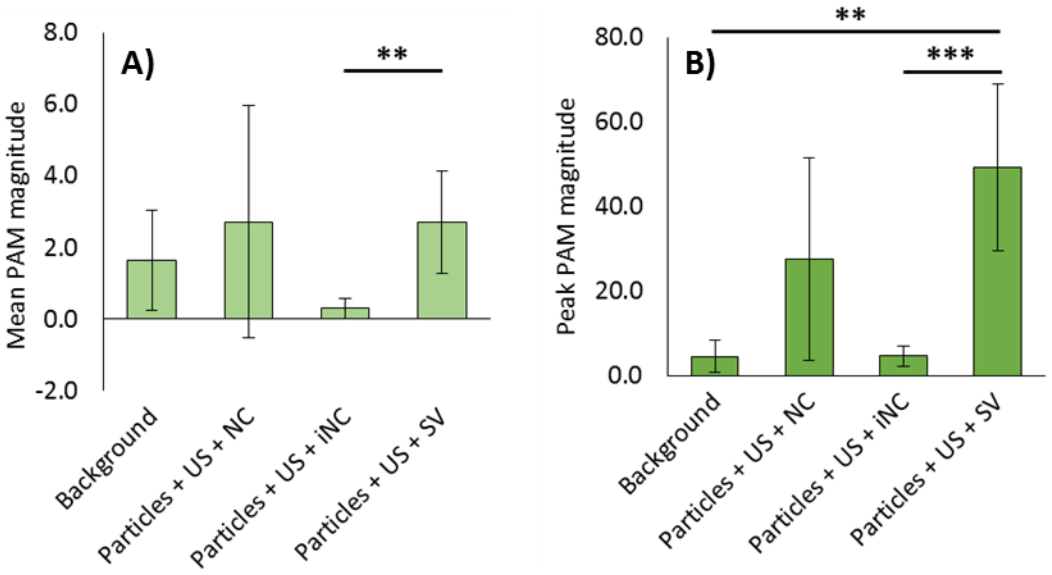

Figure 4.24 *Summary of time-averaged cavitation emissions detected for each experimental group quantified as **(A)** mean PAM magnitude and **(B)** peak PAM magnitude. Error bars show 1 standard deviation of PAM magnitude. Statistical significance was assessed using one-way ANOVA testing:* $**$ $(p < 0.01)$, $***$ $(p < 0.001)$, $(n = 6)$.

4.3.2.2 *In Vivo* Imaging System

Fluorescence images were captured using the IVIS for live animals before treatment and after treatment. Subsequently, after the animals were culled, IVIS images were also captured of the excised tumours. Figure 4.25 illustrates the image analysis sequence including the underlying black and white photograph (figure 4.25(A)), with the fluorescence colour map overlaid (figure 4.25(B)) and finally the white drawn contour selecting the region of interest (ROI) (figure 4.25(C)).

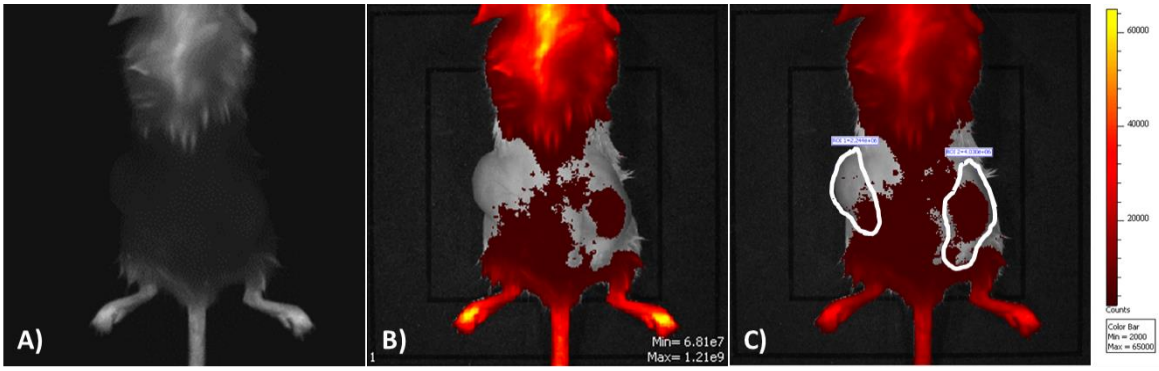

Figure 4.25 *IVIS image analysis sequence of a live anaesthetised animal, including **(A)** black and white photograph, **(B)** fluorescence colour map overlay and **(C)** contoured regions of interest.*

IVIS images of the live anaesthetised animals are summarised in figure 4.26 and quantified in terms of average counts – the average number of photons detected per pixel within the treated tumour ROI – contoured as illustrated in figure 4.25(C).

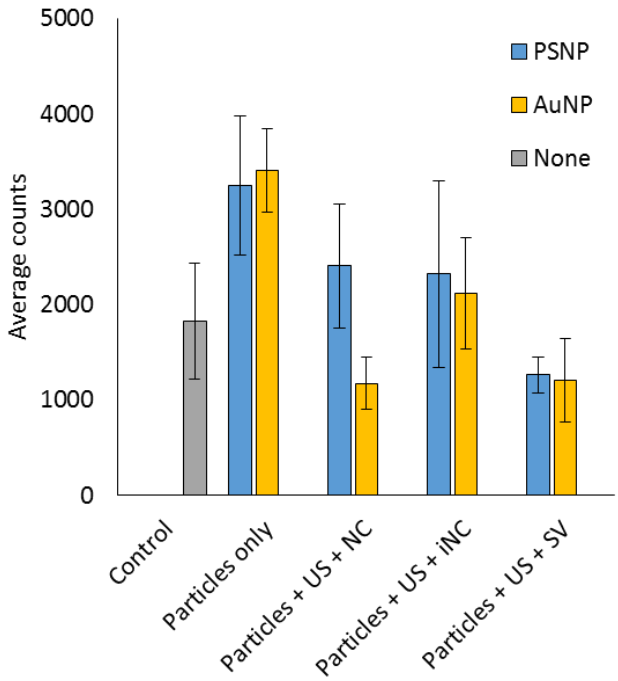

Figure 4.26 *Average counts per ROI as detected by IVIS in live animal imaging of treated tumours post-ultrasound exposure. Error bars show 1 standard deviation of average counts. Statistical significance was assessed using one-way ANOVA testing with no statistical significance found* $(n = 3)$.

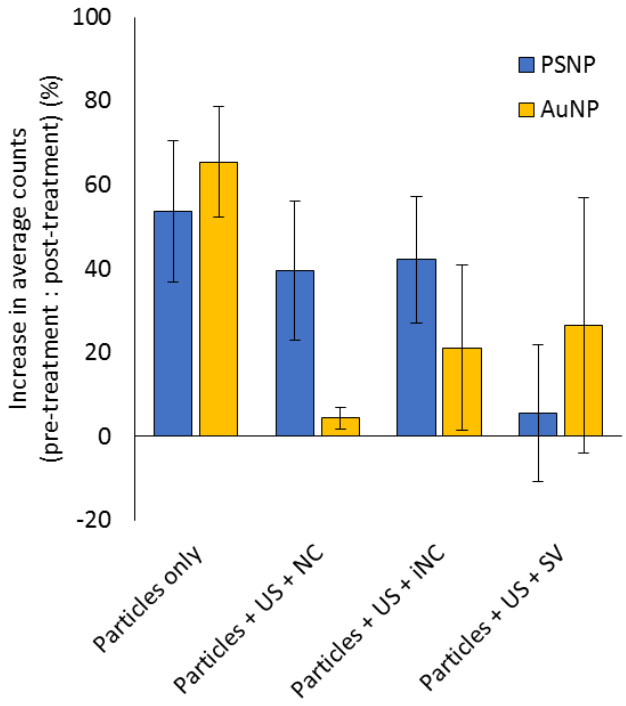

Figure 4.27 *Percentage increase in average counts as detected by IVIS in live-animal imaging comparing pre- and post-treatment of the same tumour ROIs. Error bars show 1 standard deviation of average counts. Statistical significance was assessed using one-way ANOVA testing with no statistical significance found* $(n = 3)$.

Average counts per ROI detected in the treated tumours in live animal imaging showed a large spread in counts and no statistical significance between treatment groups (figure 4.26). When pre- and post-treatment IVIS images were compared for each animal, an increase in average counts was seen in all but one case, but no statistical significance was found between treatment groups, with all ultrasound groups producing a smaller mean increase in average counts than particles alone (figure 4.27).

IVIS images of the excised tumours were post-processed in the same way (figure 4.28). Unlike the whole animal imaging which used a 1 s exposure time, the following tumour images were captured at a 3 s exposure time to enhance fluorescence detection. Figure 4.29 illustrates the increase in average counts within the ROI with increasing exposure time.

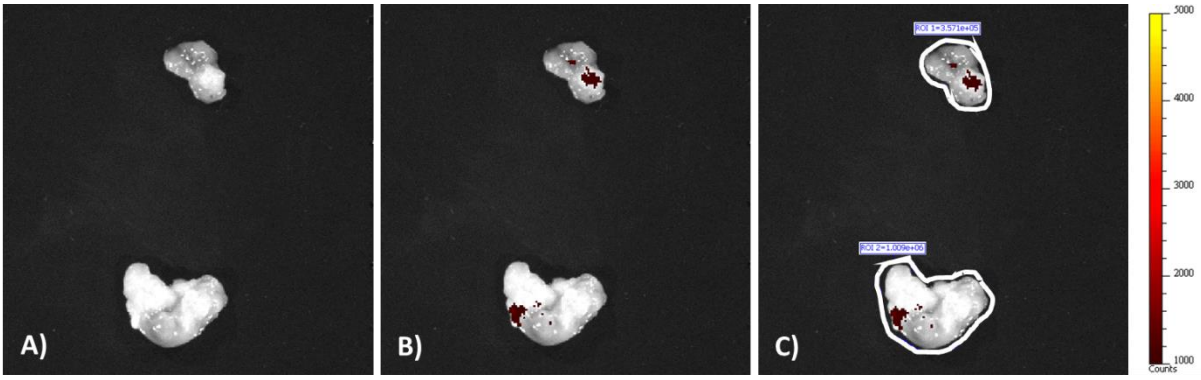

Figure 4.28 *IVIS image analysis sequence of excised tumours, including* ***(A)*** *black and white photograph,* ***(B)*** *fluorescence colour map overlay and* ***(C)*** *contoured region of interest, at 1 s exposure time.*

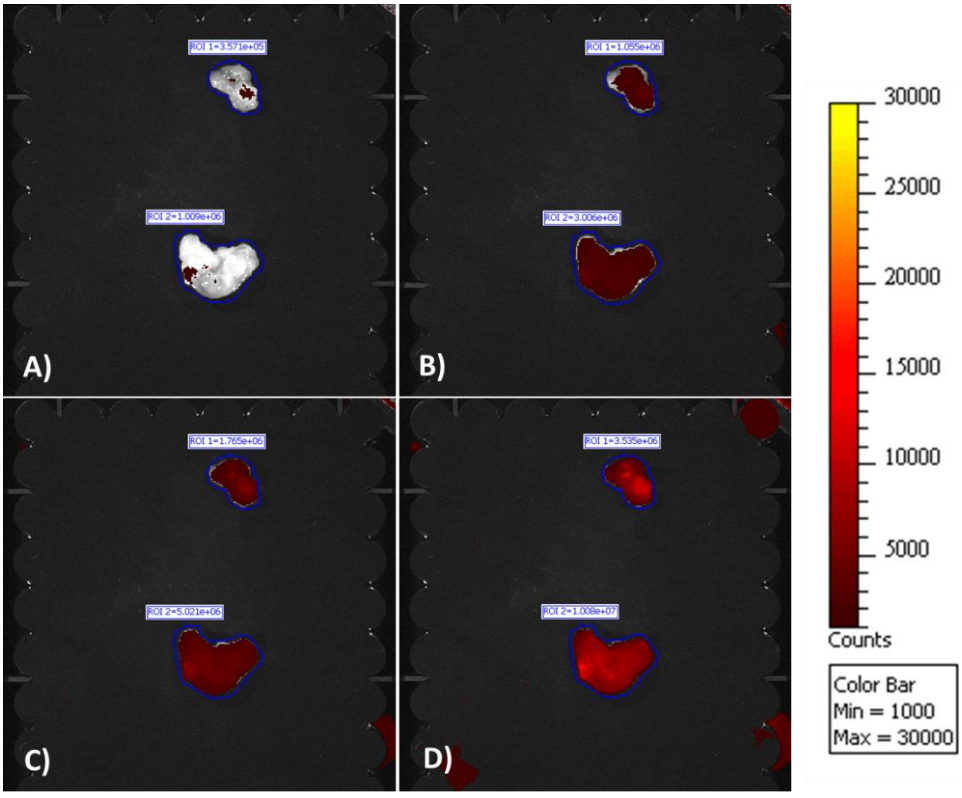

Figure 4.29 *IVIS images of excised tumours at increasing exposure times –* ***(A)*** *1 s,* ***(B)*** *3 s,* ***(C)*** *5 s and* ***(D)*** *10 s.*

Imaging the tumours *ex vivo* allowed for higher exposure times and more sensitive fluorescence detection. Figure 4.30 shows the average counts detected for the excised tumours in each experimental group. When compared to the control tumour samples, a

statistically significant increase in average counts was detected for polystyrene nanoparticles co-delivered with NanoCups in the presence of ultrasound. However, no significance was found between the gold nanoparticle groups.

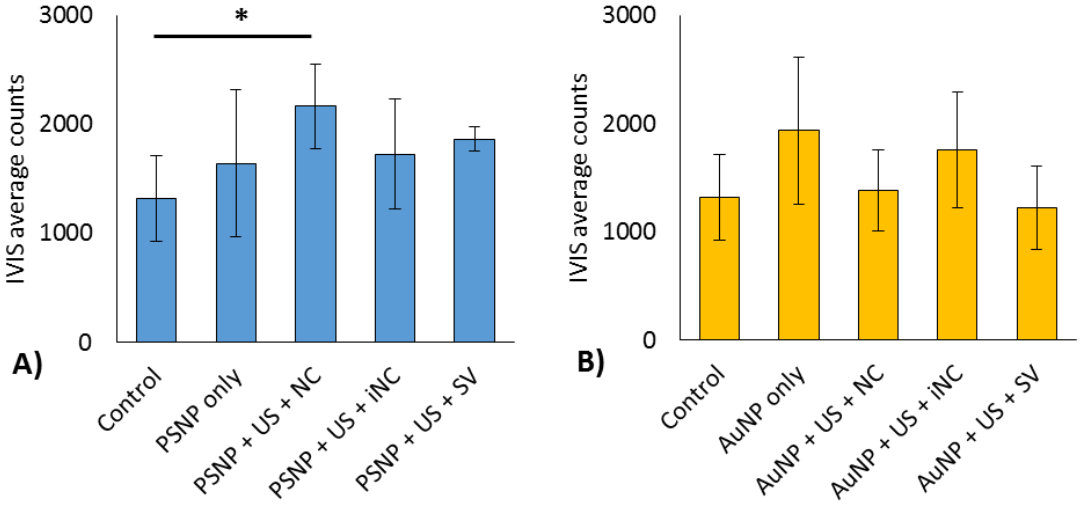

Figure 4.30 *Summary of IVIS data from excised tumours showing average counts for each set of treatments group detecting* ***(A)*** *PSNP and* ***(B)*** *AuNP delivery respectively. Error bars show 1 standard deviation of average counts and statistical significance is assessed using one-way ANOVA testing:* $*$ $(p < 0.05)$, $(n = 3)$.

4.3.2.3 Microplate reader

Homogenised tumour samples were assessed for fluorescence content using a microplate reader, excitation wavelength 640 nm and emission filter at 680 nm, the combination identified as optimal for detection of the Cy5 fluorophore.

A wide variation in tumour composition was found during homogenisation. Many tumours were highly vascularised (producing a dark red homogenate), whilst others had very little blood and produced homogenate much lighter in colour (figures 4.31 and 4.32). This variation in composition led to a wide distribution of absorbance values, from 1.40 to 3.01 (measured at the Cy5 emission wavelength 680 nm). Figure 4.32 shows absorbance spectra of four

different types of tumour sample, categorised as (A) 'pale', (B) 'pink', (C) 'orange' and (D) 'red', with colours dependent on haemoglobin content. The red region marked on figure 4.32 shows where the characteristic absorbance peak for red blood cells lies (520 – 580 nm). As expected, this peak is most prominent in the sample with highest blood content (figure 4.32(D)).

It can be seen that opacity rather than colour dominates the absorbance, where 'pale' and 'red' samples show the highest absorbance values at 680 nm although they are very different in colour. The amount of light transmitted through the sample is influenced by both absorption and scattering. It is possible that this variation in absorbance level influenced the fluorescence measurements, falsely reducing the fluorescence intensity.

However, regardless of the variation in absorbance, if the fluorescent material had been intense and stable enough, and present in sufficient quantity, the influence of background absorbance would be insignificant. Furthermore, poorly vascularised tumours will inevitably show lower uptake, even when assisted by cavitation.

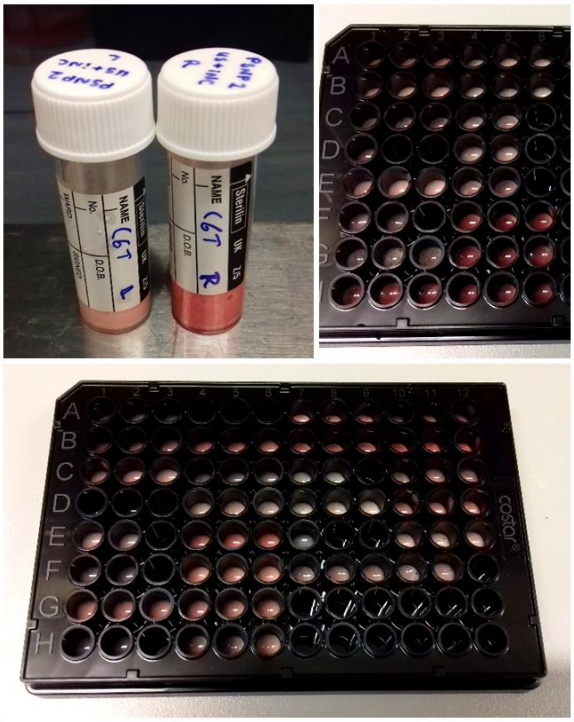

Figure 4.31 *Tumour homogenate, showing the contrast in homogenate colouring between samples in clear sample tubes and a black 96-well plate.*

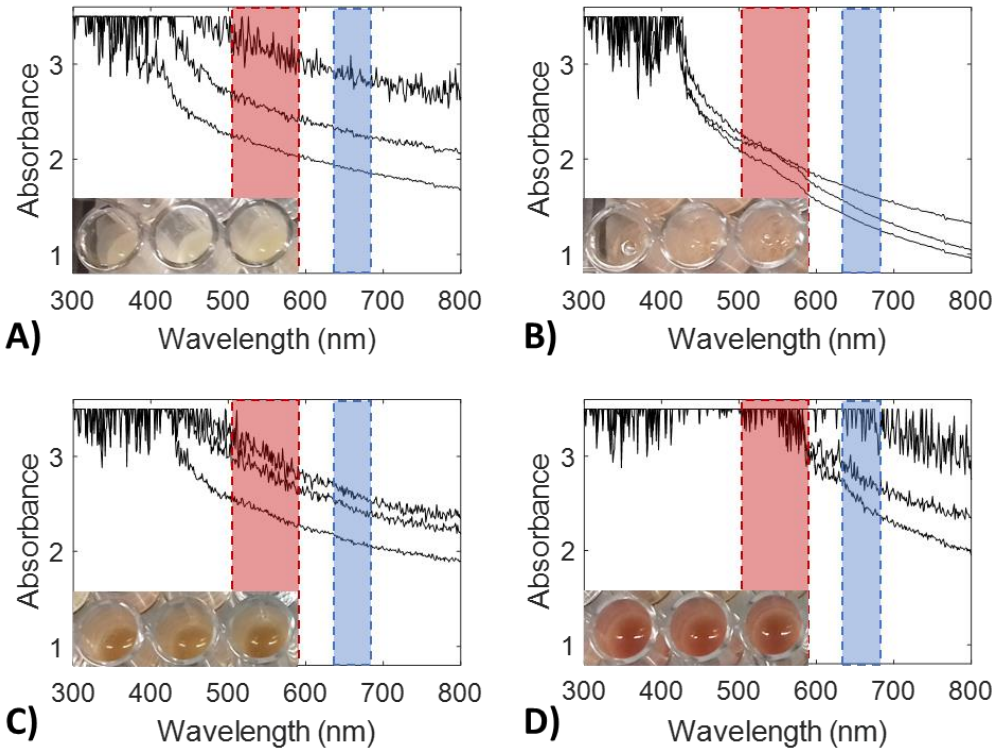

Figure 4.32 *Absorbance spectra of tumour tissue samples illustrating differences in colour, opacity and vascularity of **(A)** pale, **(B)** pink, **(C)** orange and **(D)** red samples. The red region indicates the characteristic spectral band of red blood cell absorbance and the blue region indicates excitation and emission wavelengths of Cy5 fluorophore.*

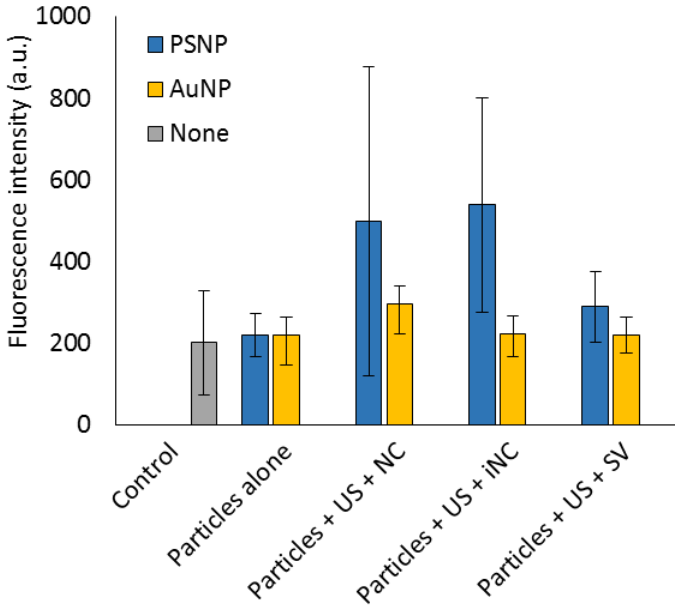

Figure 4.33 *Microplate reader fluorescence intensity values of tumour homogenate in each treatment group. Error bars show 1 standard deviation of fluorescence intensity. Statistical significance was assessed using one-way ANOVA testing with no statistical significance found* $(n = 3)$.

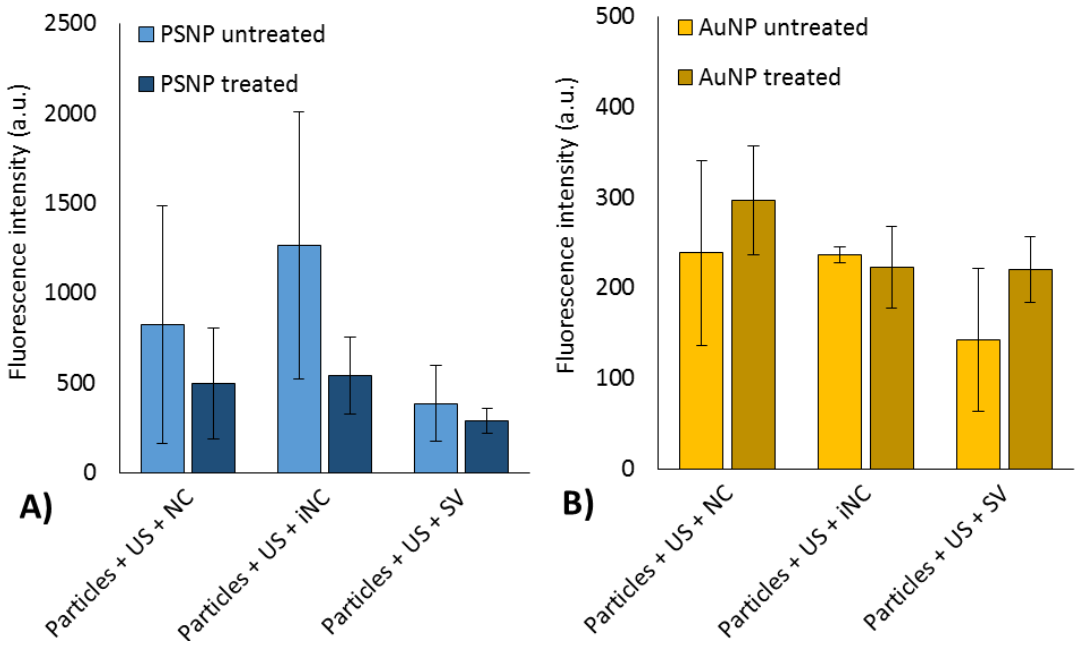

Figure 4.34 *Microplate reader fluorescence intensity values comparing untreated and treated tumours within the same animal for* ***(A)*** *PSNP and* ***(B)*** *AuNP respectively. Error bars show 1 standard deviation of fluorescence intensity. Statistical significance is assessed using one-way ANOVA testing with no statistical significance found* $(n = 3)$.

No statistical significance was found between experimental groups of homogenised tumour samples (figure 4.33). Many groups showed extremely large discrepancies in values potentially stemming from the wide distribution in tumour size, composition and homogenate colouring.

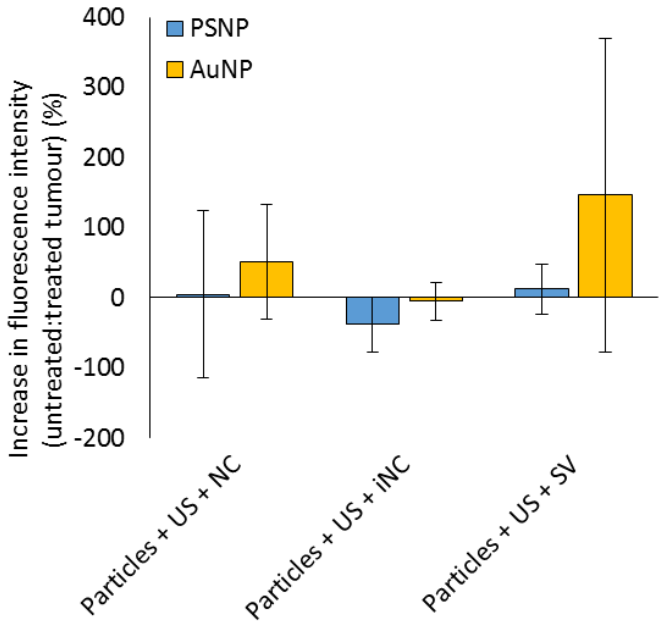

Figure 4.35 *Microplate reader fluorescence intensity values comparing untreated and treated tumours within the same animal. Error bars show 1 standard deviation of fluorescence intensity. Statistical significance is assessed using one-way ANOVA testing with no statistical significance found* $(n = 3)$.

Similarly, when the internal control tumour (the untreated tumour) of each animal was used to assess the increase in fluorescence intensity, comparing untreated and treated tumours (figure 4.34) i.e. $\left(\frac{treated-untreated}{untreated} \times 100\ \%\right)$, no statistical significance was found. Figure 4.35 shows the increase in fluorescence intensity comparing untreated and treated tumours. Although the trend in figure 4.35 may suggest a greater enhancement in the AuNP groups, the error bars are too large to draw a meaningful conclusion.

4.4 Discussion

4.4.1 Cavitation detection

The bistatic HIFU configuration was able to successfully and accurately deliver acoustic energy into the anaesthetised animal at sufficient intensities to activate micro- and nano-scale cavitation agents. The orthogonal arrangement of linear arrays achieved passive cavitation mapping within the tumour, successfully monitoring and localising cavitation activity throughout the 10-minute ultrasound treatment. Figure 4.36 shows an example PAM acquisition during treatment, where the PAM map alone allows PAM magnitude to be visualised (figure 4.36(A)), and overlaying this PAM map (shown in blue) with the B-mode image (shown in grey scale) allows localisation of the HIFU focus within the tumour volume (the white speckle region) (figure 4.36(B)).

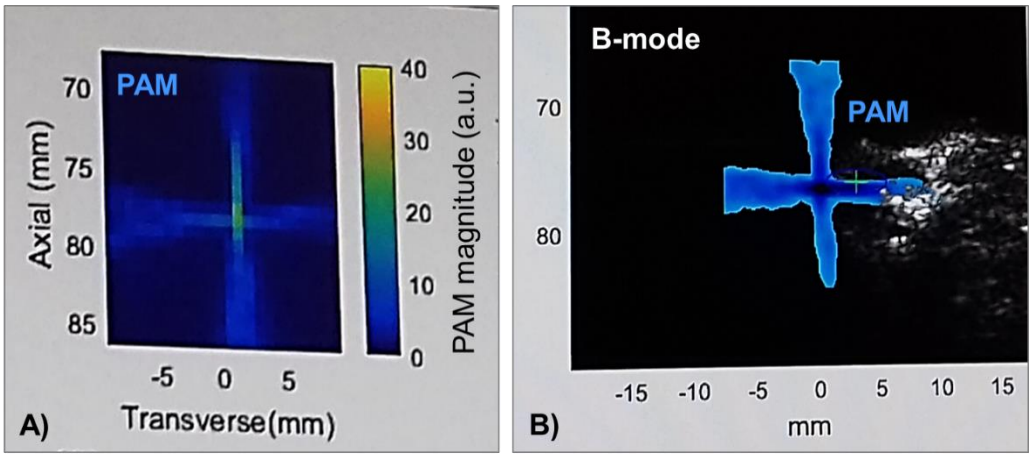

Figure 4.36 *Example PAM acquisition during treatment, including **(A)** the PAM map alone illustrating the colour map assigned to PAM magnitude and **(B)** the B-mode image of the tumour region overlaid with the PAM map for localisation and co-registration.*

NanoCups were found to induce a more sustained cavitation response, generating a larger mean PAM magnitude compared to SonoVue®. It is likely that this effect would have been even more prominent if a single injection of SonoVue® had been used. On average SonoVue® produced a larger peak response compared to NanoCups, but the injected population was

destroyed more rapidly, consistent with previous studies (Kwan *et al.* 2015). The persistence of cavitation activity exhibited by NanoCups can be attributed to their high concentration (10^5 more cavitation nuclei per mL than SonoVue®) and the potential for multiple inertial cavitation events from a single agent (as has been seen in Brandaris high-speed camera footage) (Kwan *et al.* 2016).

4.4.2 *In Vivo* Imaging System

Although the live animal imaging did not have sufficient sensitivity to detect the Cy5-labelled particles *in vivo*, the *ex vivo* samples of excised tumours did show a statistically significant increase in fluorescence pixels within the tumour ROI, when control and treated tumours were compared for Cy5-PSNP (figure 4.30), due to the higher sensitivity of *ex vivo* imaging (longer exposure duration and less light attenuation through surrounding tissue).

However, a statistically significant increase in fluorescence was not found for Cy5-AuNP. There is no evidence to suggest that the pharmacokinetics of Cy5-PSNP and Cy5-AuNP would be different, since size and zeta potential remained constant throughout previous stability studies. We can therefore assume that Cy5-AuNP were present in the tumour, but the fluorescence signal had dropped sufficiently that they were no longer detectable through IVIS *in vivo* or *ex vivo* (see sections 4.5.2 and 5.3.3). Furthermore, using an intratumoral injection of the fluorescent particles could have been beneficial in providing a positive control for this study.

4.4.3 Microplate reader

Tumour tissue samples were successfully excised and snap-frozen on dry ice before being homogenised 24 – 48 hours later. During this time the samples were stored in dark conditions.

Every effort was made during homogenisation to work in a dark environment, including foil-wrapped sample tubes and a blacked-out hood for sample preparation. However, the microplate reader fluorescence results suggest that significant decay in fluorophore emissions occurred, with extremely low fluorescence values and no statistical significance found between control and treatment groups. Furthermore there was no longer any correlation between the two independent fluorescence measurement techniques (figure 4.37) – IVIS and the microplate reader. This is particularly surprising since such good correlation was measured during the IVIS calibration study (figure 4.15), further indicating a decay of fluorescence intensity in the homogenised samples.

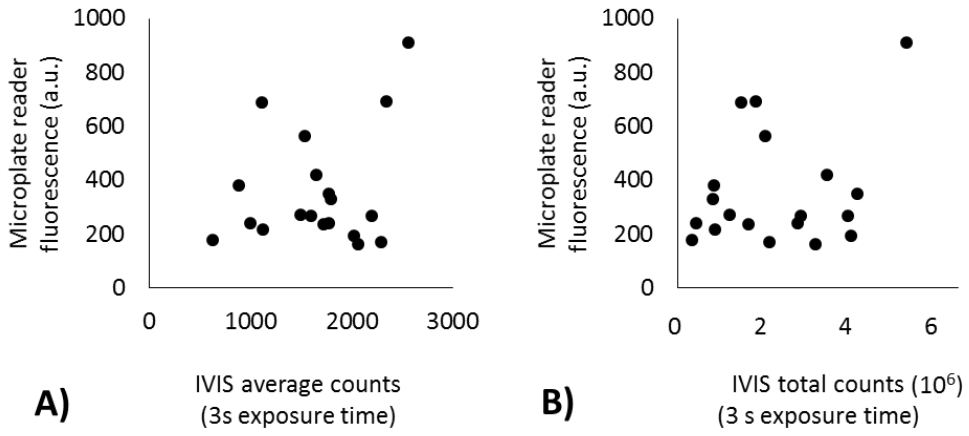

Figure 4.37 *Correlation between two independent fluorescence measurements – the microplate reader fluorescence detection of homogenised tumour samples 48 hours after treatment, and the IVIS fluorescence detection summarised as **(A)** average counts and **(B)** total counts over the tumour ROI.*

There are several possible reasons for this fluorescence decay. Firstly, as was described in the stability study in section 4.2.2, the instability of the Cy5 fluorophore is highly dependent on the surrounding buffer, depending on concentration and salt content. Since the fluorophore was stored directly in the tumour sample, the immediate surrounding buffer could not be adjusted.

Secondly, excessive light exposure is likely to lead to photobleaching. Although every precaution was taken to minimise light exposure, the fluorescent injectate was exposed to light at several points during the experiment: whilst the injection was prepared in the clear syringe, whilst running through the clear tubing of the cannula, whilst in the superficial regions of the circulatory system of the animal during treatment, during IVIS imaging post-treatment and finally during tumour resection. As described in section 4.2.2, no noticeable photobleaching was observed during IVIS imaging in the control study, but each of these experimental stages are likely to have a cumulative effect on the photobleaching and fluorescence emissions of the fluorophore.

Thirdly, it is possible that during the freezing and thawing process carried out before homogenisation the Cy5 fluorophore, in the protein-rich environment of the tumour, underwent aggregation, forming protein-dye conjugates, which in turn led to significant light adsorption. This kind of light adsorption by dye conjugates is well documented (Berlier *et al.* 2003) and has been shown to lead to diminished fluorescence emissions.

Future studies should explore alternative fluorescence and bioluminescence techniques, such as those that have been previously demonstrated in ultrasound delivery studies, including green fluorescent protein (GFP) (Lee *et al.* 2017), paying particular attenuation to their stability in protein-rich environments and in sub-zero storage conditions. Furthermore, electron microscopy and histology offer valuable insights into the biodistribution of nano-scale constructs without the need for fluorescence. With proper sample preservation and preparation, histology could be used to show penetration distances of density-contrasting nanoparticles from nearby vasculature.

4.4.4 *In vivo* tumour model

A key limitation of this study was found to be the variability in the tumour model, both from animal to animal, and within each animal. This large variability was seen in size and vascularity, making the comparison between experimental groups difficult and bringing into question the validity of the internal control tumour. When imaged with B-mode ultrasound it quickly became clear whether an animal had a well perfused tumour or not. Often larger tumours would exhibit a 'bright' tumour shell (indicating a well-vascularised periphery) and a 'dark' solid tumour centre (indicating a poorly perfused and potentially necrotic centre). Without a well-perfused tumour the potential for nanoparticle delivery is limited, even with the assistance of ultrasound and cavitation.

Furthermore, no correlation was found between fluorescence uptake (as detected by IVIS count) and tumour size, suggesting that tumour size is not an indicator of vascularity (figure 4.38). Although total counts show some correlation between fluorescence uptake and tumour weight (figure 4.38(A)), this metric is inherently biased since it sums fluorescent pixels across the whole tumour volume. In contrast, when average fluorescence uptake is considered (figure 4.38(B)) and the tumour size is accounted for, no correlation is found.

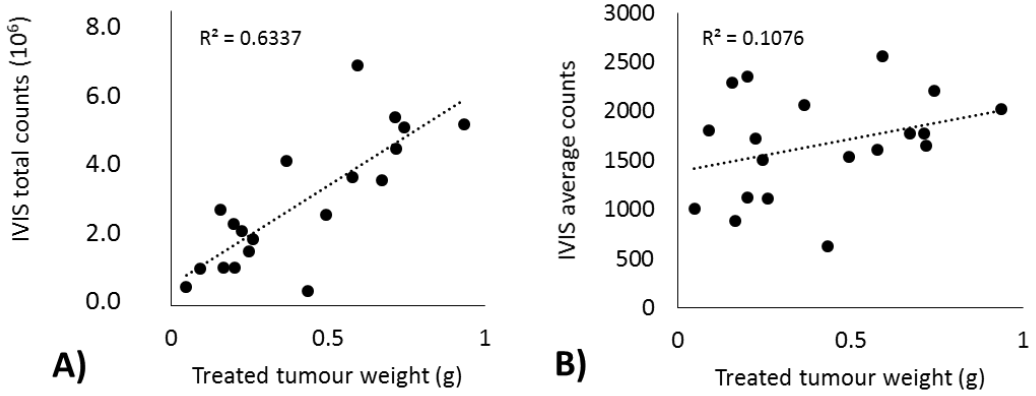

Figure 4.38 *Correlation between tumour weight and fluorescence uptake, as quantified by IVIS imaging in **(A)** total counts and **(B)** average counts.*

Going forward, establishing a system whereby tumours are assessed for perfusion before treatment is likely to be very beneficial (see sections 4.5.2 and 5.3.3). One example method of assessing perfusion uses high frequency ultrasound and microbubble contrast agents. The VisualSonics system (FUJIFILM, Toronto, Canada) is able to perform this assessment in real time and could offer a valuable diagnostic step in future ultrasound-enhanced delivery studies. This system could be utilised in the first instance to assess which tumours have grown sufficiently and are ready for treatment, and in future studies to learn which tumour models tend to be well perfused and inform our choice of cell line and animal when inoculating.

4.4.5 Acoustic monitoring

In the previous chapter we saw how bubbles can be used as sensors – producing acoustic emissions that could be used as potential predictors of successful delivery and the extent of delivery. However, in this pilot *in vivo* study cavitation emissions were not found to be a good indicator of fluorescence uptake (figure 4.39). Most probably, this is due to limitations in fluorescence detection discussed above, rather than a fundamental limitation of acoustic monitoring *per se*. However, it should not be ruled out that acoustic emissions may not be a good indicator of delivery.

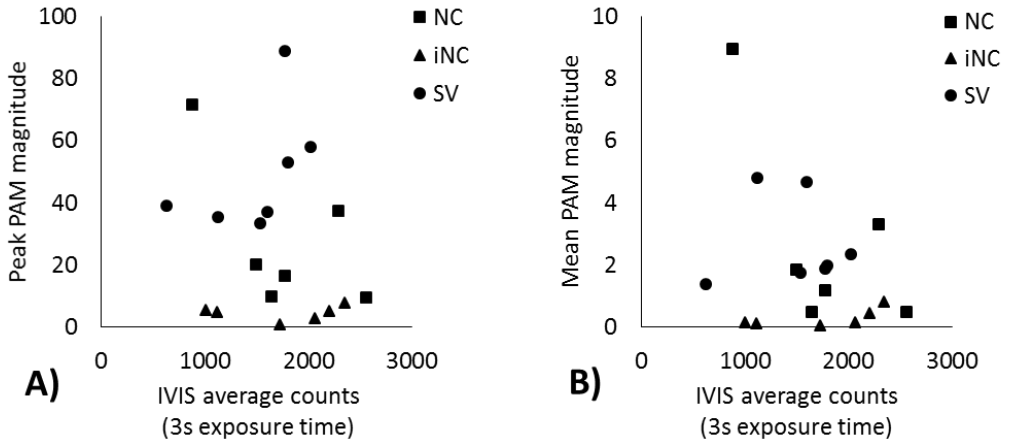

Figure 4.39 *Correlating acoustic emissions and fluorescence uptake, quantified as **(A)** peak PAM magnitude and **(B)** mean PAM magnitude with IVIS average counts from ex vivo tumours.*

4.5 Conclusions and future work

4.5.1 Density-enhanced delivery

Unfortunately the limitations of the *in vivo* methodology utilised in this study meant that is was not possible to answer definitively the main research question: whether ultrasound-mediated delivery of nanoparticles is influenced by density *in vivo*. The feasibility of fabricating fluorescently labelled density-contrasting biocompatible nanoparticles, the implementation of a bistatic HIFU setup to activate cavitation agents within the target site, and the detection of ultrasound-enhanced fluorescent nanoparticle uptake in *ex vivo* tumours through IVIS imaging were all successfully demonstrated. However, large discrepancies in the tumour model, including size and perfusion, alongside insufficient levels of fluorescence uptake, resulted in large uncertainties and consequently low statistical significance.

4.5.2 Future work

The key limitations of the current approach that need to be addressed are: the assessment of tumour perfusion, optimisation of nanoparticle fabrication and alternative markers for drug delivery.

Assessing tumour perfusion

Previously the assessment of perfusion has been based purely on size – where a tumour that is too small is assumed to not be mature enough to have developed vasculature, and a tumour that is too big is assumed to have a necrotic core (Ackerman 1974, Cataland *et al.* 1962). However, the results of the current study demonstrate that size alone is not an adequate indicator of perfusion (figure 4.38(B)).

High-frequency ultrasound imaging with microbubble contrast agents could be used to pre-image tumours to assess their perfusion. This assessment of perfusion could become the first stage in the experimental work flow, answering the question – 'is this a likely candidate for successful ultrasound-mediated drug delivery?' – and ensuring consistency of perfusion across experimental groups. Furthermore, the assessment of tumour perfusion will aid our understanding on the most appropriate tumour models to use for ultrasound-mediated delivery studies, enabling us to choose the optimal combination of cell line and animal to imitate human tumours for clinical relevance.

Nanoparticle fabrication

The current study highlights the importance of a well-characterised and stable fluorescent construct for use in *in vivo* delivery studies. By increasing the fluorophore loading a low particle concentration is required in the injected dose, and the likelihood of detection increases. Furthermore, the stability of the construct is paramount, not only in the storage buffer but throughout the entire experimental procedure. Particular consideration should be given to biological sample preservation and freezing of the fluorophore.

Alternative markers for drug delivery

Previous work has shown fluorescent markers to be an effective method for monitoring drug delivery; however, the current work was not able to produce a fluorescent construct with sufficient stability. Alternative fluorophores that have been successfully implemented include DiI (1,1'-Dioctadecyl-3,3,3',3'-Tetramethylindocarbocyanine Perchlorate ('DiI'; $DiIC_{18}(3)$)), and bioluminescence markers, such as red fluorescent proteins (RFPs). Both alternatives can be imaged with IVIS because of their characteristic long wavelength emissions, and are compatible with *ex vivo* fluorescence techniques (Crake *et al.* 2016, Troy *et al.* 2004). Further future developments for this *in vivo* work are discussed in section 5.3.3.

References

Ackerman, N.B., '*The blood supply of experimental liver metastases. IV. Changes in vascularity with increasing tumor growth*', Surgery, 1974, 75(4), 589-596.

Alexis, F., Pridgen, E., Molnar, L.K. and Farokhzad, O.C., *'Factors affecting the clearance and biodistribution of polymeric nanoparticles'*, Molecular Pharmaceutics, 2008, 5(4), 505-515.

Bazan-Peregrino, M., Rifai, B., Carlisle, R.C., Choi, J., Arvanitis, C.D., Seymour, L.W. and Coussios, C.C., *'Cavitation-enhanced delivery of a replicating oncolytic adenovirus to tumors using focused ultrasound'*, Journal of Controlled Release, 2013, 169(1), 40-47.

Berlier, J.E., Rothe, A., Buller, G., Bradford, J., Gray, D.R., Filanoski, B.J., Telford, W.G., Yue, S., Liu, J., Cheung, C.Y. and Chang, W., '*Quantitative comparison of long-wavelength Alexa Fluor dyes to Cy dyes: fluorescence of the dyes and their bioconjugates*', Journal of Histochemistry and Cytochemistry, 2003, 51(12), 1699-1712.

Buckingham, M.J., Berknout, B.V. and Glegg, S.A., '*Imaging the ocean with ambient noise',* Nature, 1992, 356(6367), 327.

Cataland, S., Cohen, C. and Sapirstein, L.A.,. *'Relationship Between Size and Perfusion Rate of Transplanted Tumors'*, Journal of the National Cancer Institute, 1962, 29(2), 389-394.

Coviello, C., Kozick, R., Choi, J., Gyöngy, M., Jensen, C., Smith, P.P. and Coussios, C.C., '*Passive acoustic mapping utilizing optimal beamforming in ultrasound therapy monitoring*', The Journal of the Acoustical Society of America, 2015, 137(5), 2573-2585.

Crake, C., Owen, J., Smart, S., Coviello, C., Coussios, C.C., Carlisle, R. and Stride, E., *'Enhancement and Passive Acoustic Mapping of Cavitation from Fluorescently Tagged Magnetic Resonance-Visible Magnetic Microbubbles In Vivo*'. Ultrasound in Medicine and Biology, 2016, 42(12), 3022-3036.

Elbes, D., Paverd, C., Cleveland, R. and Coussios, C., '*Sub-millimeter bistatic passive acoustic mapping*', The Journal of the Acoustical Society of America, 2017, 141(5), 3550-3551.

Gyongy, M., Arora, M., Noble, J.A. and Coussios, C.C., '*Use of passive arrays for characterization and mapping of cavitation activity during HIFU exposure*', In Ultrasonics Symposium, 2008, IUS 2008, 871-874.

Hwang, H., Kim, H. and Myong, S., '*Protein induced fluorescence enhancement as a single molecule assay with short distance sensitivity*', Proceedings of the National Academy of Sciences, 2011, 108(18), 7414-7418.

Kim, M., Schmitt, S.K., Choi, J.W., Krutty, J.D. and Gopalan, P., '*From self-assembled monolayers to coatings: Advances in the synthesis and nanobio applications of polymer brushes*', Polymers, 2015, 7(7), 1346-1378.

Kunjachan, S., Pola, R., Gremse, F., Theek, B., Ehling, J., Moeckel, D., Hermanns-Sachweh, B., Pechar, M., Ulbrich, K., Hennink, W.E. and Storm, G., '*Passive versus active tumor targeting using RGD-and NGR-modified polymeric nanomedicines*', Nano letters, 2014, 14(2), 972-981.

Kwan, J.J., Myers, R., Coviello, C.M., Graham, S.M., Shah, A.R., Stride, E., Carlisle, R.C. and Coussios, C.C., *'Ultrasound-Propelled Nanocups for Drug Delivery'*, Small, 2015, 11(39), 5305-5314.

Kwan, J.J., Lajoinie, G., de Jong, N., Stride, E., Versluis, M. and Coussios, C.C., '*Ultrahigh-Speed Dynamics of Micrometer-Scale Inertial Cavitation from Nanoparticles*', Physical Review Applied, 2016, 6(4), 044004.

Lee, J.Y., Crake, C., Teo, B., Carugo, D., de Saint Victor, M., Seth, A. and Stride, E., '*Ultrasound-Enhanced siRNA Delivery Using Magnetic Nanoparticle-Loaded Chitosan-Deoxycholic Acid Nanodroplets',* Advanced Healthcare Materials, 2017, 6(8).

Mo, S., Carlisle, R., Laga, R., Myers, R., Graham, S., Cawood, R., Ulbrich, K., Seymour, L. and Coussios, C.C., '*Increasing the density of nanomedicines improves their ultrasound-mediated delivery to tumours*', Journal of Controlled Release, 2015, 210, 10-18.

Moh, L.C., Losego, M.D. and Braun, P.V., '*Solvent quality effects on scaling behavior of poly (methyl methacrylate) brushes in the moderate-and high-density regimes*', Langmuir, 2011, 27(7), 3698-3702.

Myers, R., Coviello, C., Erbs, P., Foloppe, J., Rowe, C., Kwan, J., Crake, C., Finn, S., Jackson, E., Balloul, J.M. and Story, C., *'Polymeric cups for cavitation-mediated delivery of oncolytic vaccinia virus'*, Molecular Therapy, 2016, 24(9), 1627-1633.

Norton, S.J. and Won, I.J., '*Time exposure acoustics*', IEEE Transactions on Geoscience and Remote Sensing, 2000, 38(3), 1337-1343.

PMI Nutrition International, '*The Impact of Laboratory Animal Diets on Autofluorescence Imaging in Animals'*, LabDiet®, 2015.

Smyth, J.W.P., Fleeton, M.N., Sheahan, B.J. and Atkins, G.J., '*Treatment of rapidly growing K-BALB and CT26 mouse tumours using Semliki Forest virus and its derived vector'*, Gene Therapy, 2005, 12(2), 147-159.

Staveley, L.A.K., '*The characterization of chemical purity: organic compounds'*, 1971, Butterworths Scientific Publications, London.

Stennett, E.M., Ciuba, M.A., Lin, S. and Levitus, M., '*Demystifying PIFE: The photophysics behind the protein-induced fluorescence enhancement phenomenon in Cy3*', The Journal of Physical Chemistry Letters, 2015, 6(10), 1819-1823.

Synnevag, J.F., Austeng, A. and Holm, S., '*Adaptive beamforming applied to medical ultrasound imaging*', IEEE Transactions on Ultrasonics, Ferroelectrics, and Frequency Control, 2007, 54(8).

Thomenius, K.E., '*Evolution of ultrasound beamformers*', In Ultrasonics Symposium, IEEE Proceedings, 1996, 2, 1615-1622.

Troy, T., Jekic-McMullen, D., Sambucetti, L. and Rice, B., *'Quantitative comparison of the sensitivity of detection of fluorescent and bioluminescent reporters in animal models'*, Molecular imaging, 2004, 3(1), 15353500200403196.

Wu, S.K., Chu, P.C., Chai, W.Y., Kang, S.T., Tsai, C.H., Fan, C.H., Yeh, C.K. and Liu, H.L., *'Characterization of Different Microbubbles in Assisting Focused Ultrasound-Induced Blood-Brain Barrier Opening'*, Scientific Reports, 2017, 7.

Chapter 5: **Conclusions and future work**

The overall aim of the research described in this thesis was to investigate the influence of nanoparticle density in the context of ultrasound-mediated drug delivery. The main objective of the work was to test the hypothesis that increasing particle density increases penetration depth of nanoparticles under ultrasound exposure. In this final chapter an overview of the research is presented, along with key limitations and suggested avenues for future work.

5.1 Research overview

As outlined in Chapter 1, a significant barrier to successful drug delivery in cancer therapy is the limited penetration of nanoscale therapeutics beyond the immediate vicinity of blood vessels. This limits the region of a tumour that can be treated, leading to ineffective therapy and potentially the development of drug resistance. Many groups have shown the ability of sound and microbubbles to enhance the delivery of an injected drug to a specific tissue site using focused ultrasound. Strategies such as tailoring nanoparticle size and shape to promote passage through leaky tumour vessels, and using surface charge or ligands to target receptors on cancer cells, have also been studied. However, to date little attention has been paid to the influence of particle density. This thesis set out to fill this knowledge gap by posing the question: *'Is it possible, simply by increasing the density of a drug, to help a therapeutic penetrate deeper into tissue under the exposure of ultrasound?'*

A combination of numerical simulations, *in vitro* and *in vivo* experimental models were utilised to address this question. The penetration depth of nanoparticles of different densities was first predicted using a computational model assessing the acoustic and fluid dynamic forcing terms on a spherical nanoparticle. These predictions were confirmed experimentally using a series of *in vitro* models, density-contrasting nanoparticles, nano- and micro-scale cavitation

agents, high-intensity focussed ultrasound and passive cavitation detection in various tissue phantoms. Finally, experiments were performed in a tumour-bearing mouse model.

5.1.1 Specific research questions

In order to explore the influence of nanoparticle characteristics in ultrasound-mediated drug delivery, this thesis has explored the following subsidiary questions:

1) How does nanoparticle density influence the ultrasound-mediated transport and penetration depth of density-contrasting nanoparticles?

2) What influence does the choice of ultrasound exposure parameters have on the transport of density-contrasting nanoparticles, and is this dominated by acoustic streaming and radiation force effects, or by cavitation-mediated microstreaming?

3) What influence does the choice of cavitation agent have on the cavitation-enhanced transport of density-contrasting nanoparticles?

4) Can acoustic emissions be used to predict the transport and penetration depth of density-contrasting nanoparticles?

5) What is the influence of nanoparticle density on ultrasound-mediated drug delivery *in vivo*?

5.2 Conclusions and contributions

5.2.1 Chapter 2

Research questions 1 and 2 were explored in Chapter 2 using a simple computation model to assess the dominant forces on a nanoparticle exposed to ultrasound, and validated using an *in vitro* tissue phantom. For the first time particle density was shown to influence ultrasound-mediated transport. In this chapter denser particles were shown to exhibit significantly greater ultrasound-mediated transport than their lower density counterparts using an *in vitro*

tissue phantom, where a fivefold increase in density resulted in a 43 % increase in peak particle penetration depth.

Three sets of bespoke density-contrasting nanoparticles were fabricated during this research project, each set tailored to three different experimental configurations used in Chapter 2, Chapter 3 and Chapter 4 respectively. To the author's knowledge, this was the first time nanofabrication had been used to create a set of fluorescent nano-scale tools to test a density transport hypothesis.

A computational model, designed to predict the penetration depth of particles, supported the experimental observations. This simulation showed that a denser particle will be transported further when exposed to ultrasound and cavitating microbubbles than its less dense counterpart. Furthermore, in a comparison of excitation frequencies of 0.5 and 1.6 MHz, the simulation showed greater transport under the lower frequency regime where forcing from microstreaming was predicted to be greatest.

In agreement with previous studies, cavitation-enhanced delivery was found to achieve significantly greater penetration depths than particles in non-cavitation regimes. Using the computational model, microstreaming occurring in the fluid region was identified as the dominant force in this propulsion. As limited penetration depth is a key barrier to successful drug delivery, these findings offer an important new consideration in the design of therapeutic agents used in combination with ultrasound and cavitation nuclei.

5.2.2 Chapter 3

Research questions 2, 3 and 4 were studied in Chapter 3 using a developed *in vitro* model to mimic a flowing blood vessel. The predicted influence of nanoparticle density on ultrasound-

mediated transport was validated in this three-dimensional flow-vessel phantom, utilising three density-contrasting nanoparticles with unique fluorescent tags and comparing two cavitation agents.

A trend between nanoparticle density and extravasation depth was discernible, with the densest particles consistently penetrating the furthest. However, the trend was found to be less statistically significant than in the static system described in Chapter 2. Density-enhanced transport did not always show statistical significance in the flow channel phantom, and was found to be limited by the threshold for mechanical damage in the phantom medium.

Furthermore, the choice of cavitation agent often had a greater influence on penetration depth than particle density. Comparing micro-scale and nano-scale cavitation agents revealed that the smaller and more stable agent, NanoCups, resulted in more sustained cavitation activity and deeper particle penetration depths when compared to SonoVue®.

Using acoustic emissions to predict the delivery of nanoscale agents will be fundamental to the clinical application of this technology. In answering research question 4, Chapter 3 illustrated that total acoustic energy and nanoparticle peak penetration distance can be correlated. A power-law trend was found to be the most appropriate relationship in correlating acoustic emissions with nanoparticle penetration depth.

5.2.3 Chapter 4

Chapter 4 addressed research question 5 through the bio-distribution of fluorescent nanoparticles in a murine tumour model under the exposure of ultrasound and cavitation. Cavitation agents were activated and detected within the target tumour site using a bistatic transmission and detection setup. Biocompatible fluorescent nanoparticles were fabricated

and characterised for use *in vivo*. These mock therapeutics were successfully detected in *ex vivo* tumours through IVIS imaging.

However, cavitation emissions and uptake of fluorescent nanoparticles were not found to correlate. Furthermore, no statistical significance was found between measures of the accumulation of polystyrene and gold core particles in tumours. Ultimately, the influence of nanoparticle density on ultrasound-mediated drug delivery *in vivo* could not be determined owing to experimental limitations: the wide distribution of tumour samples and low fluorescence uptake.

5.3 Future work

To develop the study of density-enhanced ultrasound-mediated delivery of nanoparticles, a number of suggestions are made for potential future work.

5.3.1 *In silico*

Several significant simplifications are made in the current computational model which could be improved in future work. Firstly, in predicting the *in vitro* results, the porosity of agar should be considered, where at certain agar concentrations pore size becomes comparable to the diameter of agent travelling through it. Expressions such as Darcy's Law may be appropriate for small molecular agents, but larger agents will require consideration of additional viscous and shearing effects. Investigation into a more accurate constitutive equation to describe the porous viscoelastic material of agar is recommended. Gaining a better understanding of this material will inform the analysis of *in vitro* experiments and assess how accurately agar can model living tissue.

Furthermore, for simulations to offer helpful insights *in* vivo, living tissue should be considered. *In vivo* complex cellular barriers, such as the endothelial layer, are pivotal in determining which therapeutics will leave the vasculature, where the pore size in the endothelium acts as a sieve, setting a size threshold for any traversing therapeutic (a consideration that could be easily added to a delivery simulation). In addition to the endothelium, the tumour environment is also highly pressurised – an additional forcing term not considered in the current model. A tissue model combining viscoelasticity, porosity, a 'leaky' endothelium and a pressurised environment could be explored to more accurately mimic the tumour environment. The model of acoustic propagation through a porous dissipative media developed by Biot (1956, 1962) could be implemented to achieve this.

As discussed in Chapter 1, the unique behaviour of a cavitating microbubble is complex, and the behaviour of a *population* of bubbles is even more so. Predicting the nonlinear behaviour of these resonant systems has been achieved to various levels of accuracy by a series of dynamic bubble models, from the Rayleigh-Plesset expression (Plesset 1960) to the Keller-Miksis model (Keller *et al.* 1980). However, analytical expressions describing the microstreaming induced by this nonlinear, often high-amplitude, behaviour have yet to be realised. A fully coupled simulation, including a population of nonlinear coated microbubbles, radiated pressure field and microstreaming behaviour could offer important insights into cavitation-induced drug delivery at low and high pressure amplitudes.

Ultimately the clinical applicability of a stationary, free, single-bubble single-particle system is limited. Firstly the translational motion of the bubble is likely to be significant, and microstreaming effects produced by this motion could be added to the current simulation using the expressions relating to the translational mode developed by Doinikov (2010). The translational motion of the bubble will be dominated by the primary radiation force it

experiences (a much greater forcing term for the microbubble than the nanoparticle since the size of the bubble tends to that of the ultrasound wavelength, particularly during the expansion phase) which is likely to push the bubble against the far wall of the vessel (as was also observed experimentally on B-mode imaging in Chapter 3). An appreciation of this positioning could be simulated by adjusting the bubble's initial location relative to the tissue boundary.

Furthermore, *in vivo*, when the bubble becomes large relative to the vessel size, the system is confined within viscoelastic boundaries, altering the response of the bubble and shifting the resonance frequency (Sassaroli *et al.* 2005). An appreciation of this effect could be included in the model by adding additional inertia terms dependent on the vessel geometry relative to the bubble size.

5.3.2 *In vitro*

A clear limitation of the work presented in this thesis is the lack of a therapeutic. Future work in nanotechnology should involve the fabrication of density-modified nano-scale drug-carriers. Methods for density modification of drug-carriers include dense coatings, small particle coatings and single nanoparticle attachment (figure 5.1).

Firstly, encapsulating the drug inside a dense coating may be achieved using a lipid or polymer shell formulation. An example of this is found in the formation of magnetic droplets, where iron oxide nanoparticles are embedded in the lipid shell of the droplet (Lee *et al.* 2015, 2017), for the purpose of magnetic targeting, which shows this would be a feasible strategy. Secondly, the use of small, dense nanoparticles (on the order of 5 – 10 nm) to decorate a larger therapeutic has also been proved previously. As discussed above, Mo *et al.* (2015) decorated an adenovirus with a coating of small gold nanoparticles. However, this particular

attachment technique was found to inhibit therapeutic efficacy *in vivo*. Therefore, careful consideration of linkers and binding sites is necessary.

Single particle attachment may offer an attractive alternative, offering the density enhancement but requiring only a single binding site. However, limitations may include increased overall construct size and effective clearance of the larger dense nanoparticle. Although each potential strategy outlined has associated advantages, it should be ensured that the chosen technique does not compromise therapeutic efficacy.

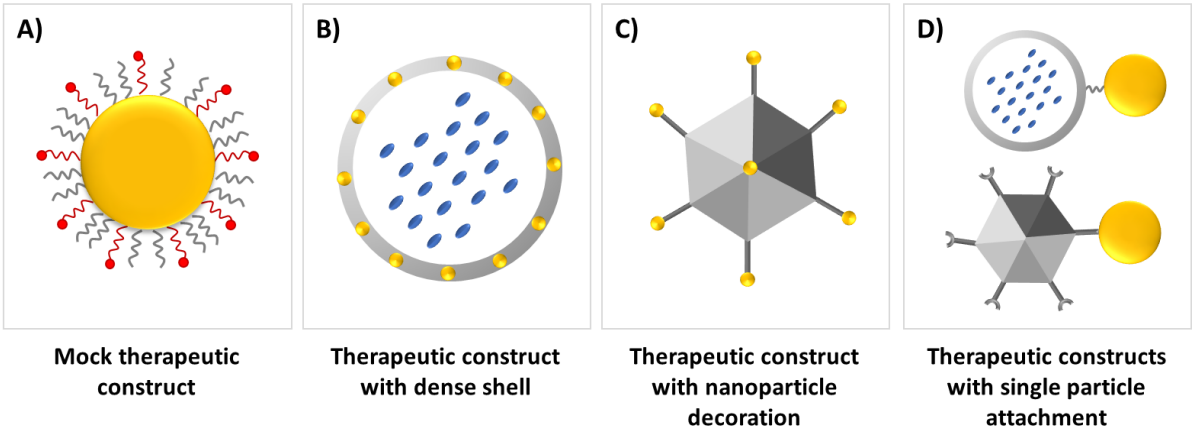

Figure 5.1 *Methods for density-modification of drug-carriers including **A)** solid dense nanoparticle core, **B)** dense shell, **C)** dense nanoparticle decoration and **D)** single particle attachment strategies.*

5.3.3 *In vivo*

A key limitation of the *in vivo* work described in Chapter 4 was the low fluorescence signal detected from the Cy5-labelled nanoparticles. To address this limitation alternative biodistribution analysis methods are recommended, namely histology with blood vessel staining, and alternative markers such as more robust fluorophores, radioactive tracers and biological markers. Furthermore, implementing one of the potential density-modified

constructs outlined in section 5.3.2 would enable a therapeutic efficacy study to be carried out. An experimental design similar to that described in Chapter 4 would be recommended. In developing this work further it will be important to optimise the tumour model – firstly, by assessing perfusion of the tumour to ensure consistency across experimental groups and secondly, by reconsidering the current murine tumour model. Many studies have highlighted the limitations of a murine model, namely rapidity of growth, irregularity of structure and integrity of the vasculature, leading to a greater EPR effect than that found in most human solid tumours (Yuan *et al.* 1994, Bae *et al.* 2011). Lammers *et al.* (2012) recommends 'establishing a well-defined panel of animal models' to allow systematic testing of therapeutics in a range of tumour models, including subcutaneous xenograft and metastatic tumour models.

5.3.4 Clinical relevance and development

Ultrasound for enhancing drug delivery is growing in clinical acceptance, both through thermal (Lyon *et al.* 2017) and mechanical (Dimcevski *et al.* 2016) techniques. The potential for using clinically available components such as SonoVue® and diagnostic ultrasound systems, once utilised for ultrasound contrast imaging, are now finding applications in ultrasound-mediated drug delivery. Using existing clinically-approved components in this way enables relatively swift implementation both from a practical and regulatory perspective.

For the current doctoral work to have clinical relevance, the same approach of using clinically approved components should be sought. Firstly, the use of diagnostic imaging probes for the delivery and monitoring of therapy should be implemented. However, for meaningful monitoring, further work is required to correlate acoustic emissions and bio-effects. Understanding this relationship, the relative thresholds and optimal signal processing methods will be vital for assessing successful treatment. Secondly, the density-modification of

therapeutics should utilise clinically approved pharmaceuticals. The repackaging of these agents with a density-modification strategy (figure 5.1) should enable enhanced transport without compromising therapeutic potency.

References

Bae, Y.H. and Park, K., *'Targeted drug delivery to tumors: myths, reality and possibility'*, Journal of Controlled Release, 2011, 153(3), 198.

Biot, M.A.,. '*Theory of propagation of elastic waves in a fluid-saturated porous solid. II. Higher frequency range'*, Journal of the Acoustical Society of America, 1956, 28(2), 179-191.

Biot, M.A., '*Generalized theory of acoustic propagation in porous dissipative media*', Journal of the Acoustical Society of America, 1962, 34(9A), 1254-1264.

Dimcevski, G., Kotopoulis, S., Bjånes, T., Hoem, D., Schjøtt, J., Gjertsen, B.T., Biermann, M., Molven, A., Sorbye, H., McCormack, E. and Postema, M., '*A human clinical trial using ultrasound and microbubbles to enhance gemcitabine treatment of inoperable pancreatic cancer*', Journal of Controlled Release, 2016, 243, 172-181.

Keller, J.B., and Miksis, M., '*Bubble oscillations of large amplitude*', The Journal of the Acoustical Society of America, 1980, 68(2), 628-633.

Lammers, T., Kiessling, F., Hennink, W.E. and Storm, G., *'Drug targeting to tumors: principles, pitfalls and (pre-) clinical progress',* Journal of Controlled Release, 2012, 161(2), 175-187.

Lee, J.Y., Carugo, D., Crake, C., Owen, J., de Saint Victor, M., Seth, A., Coussios, C. and Stride, E., *'Nanoparticle-Loaded Protein–Polymer Nanodroplets for Improved Stability and Conversion Efficiency in Ultrasound Imaging and Drug Delivery'*, Advanced Materials, 2015, 27(37), 5484-5492.

Lee, J.Y., Crake, C., Teo, B., Carugo, D., de Saint Victor, M., Seth, A. and Stride, E., '*Ultrasound-Enhanced siRNA Delivery Using Magnetic Nanoparticle-Loaded Chitosan-Deoxycholic Acid Nanodroplets*', Advanced Healthcare Materials, 2017, 6(8), 1601246.

Lyon, P.C., Griffiths, L.F., Lee, J., Chung, D., Carlisle, R., Wu, F., Middleton, M.R., Gleeson, F.V. and Coussios, C., '*Clinical trial protocol for TARDOX: a phase I study to investigate the feasibility of targeted release of lyso-thermosensitive liposomal doxorubicin (ThermoDox®) using focused ultrasound in patients with liver tumours*', Journal of Therapeutic Ultrasound, 2017, 5(28), 1-8.

Mo, S., Carlisle, R., Laga, R., Myers, R., Graham, S., Cawood, R., Ulbrich, K., Seymour, L. and Coussios, C.C., '*Increasing the density of nanomedicines improves their ultrasound-mediated delivery to tumours*', Journal of Controlled Release, 2015, 210, 10-18.

Plesset, M.S. and Hsieh, D.Y., *'Theory of gas bubble dynamics in oscillating pressure fields'*, The Physics of Fluids, 1960, 3(6), 882-892.

Sassaroli, E. and Hynynen, K., '*Resonance frequency of microbubbles in small blood vessels: a numerical study*', Physics in Medicine and Biology, 2005, 50(22), 5293.

Yuan, F., Salehi, H.A., Boucher, Y., Vasthare, U.S., Tuma, R.F. and Jain, R.K., *'Vascular permeability and microcirculation of gliomas and mammary carcinomas transplanted in rat and mouse cranial windows'*, Cancer Research, 1994, 54(17), 4564-4568.

Appendix

A1. HIFU transducer and coupling cone calibration

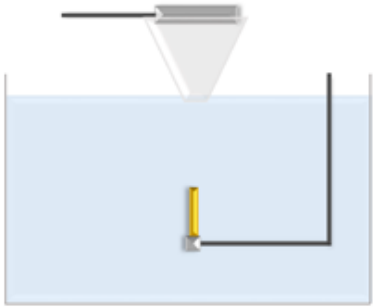

Figure A1.1 *Schematic of calibration configuration using HIFU transducer (H-107F-18, Sonic Concepts, USA) with water-filled coupling cone suspended above a water tank with needle hydrophone (Precision Acoustics, Dorchester, UK) submerged below.*

Calibration at fundamental frequency (0.5 MHz)				
Hydrophone sensitivity at 0.5 MHz 47.08 (mV/MPa)				
Input		**Output**		
Signal generator	**Voltage probe**	**Hydrophone pressures**		
mVpp	**Vpp**	**MPa**	**MPa (p+)**	**MPa (p-)**
10	6	0.24	0.11	-0.13
15	8.9	0.34	0.16	-0.17
20	11.8	0.44	0.21	-0.23
25	14.4	0.54	0.26	-0.27
30	17	0.65	0.33	-0.32
35	19.6	0.76	0.37	-0.38
40	22.5	0.88	0.44	-0.43
45	25.1	0.98	0.49	-0.49
50	27.6	1.09	0.55	-0.55
55	30.5	1.20	0.60	-0.60
60	33.1	1.31	0.66	-0.65
65	36.1	1.41	0.71	-0.69
70	38.6	1.51	0.77	-0.75
75	41.5	1.63	0.83	-0.79
80	44.4	1.74	0.89	-0.85
85	47.2	1.86	0.95	-0.90
90	49.8	1.94	1.00	-0.93
95	52.1	2.06	1.04	-1.00
100	55.1	2.17	1.10	-1.07

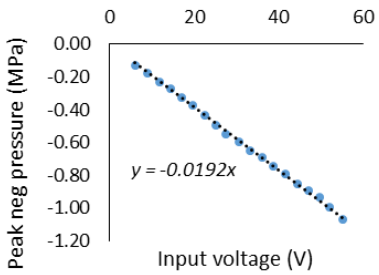

Figure A1.2 *Calibration at 0.5 MHz.*

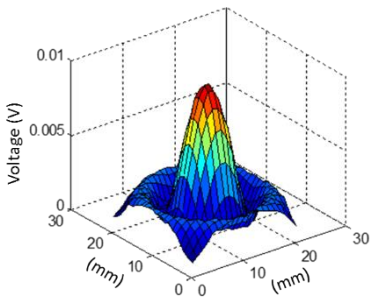

Figure A1.3 *Axial profile at 0.5 MHz.*

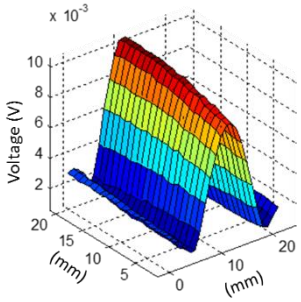

Figure A1.4 *Transverse profile at 0.5 MHz.*

Calibration at third harmonic frequency (1.6 MHz)				
Hydrophone sensitivity at 1.6 MHz 68.53 (mV/MPa)				
Input		**Output**		
Signal generator	**Voltage probe**	**Hydrophone pressures**		
mVpp	**Vpp**	**MPa**	**MPa (p+)**	**MPa (p-)**
10	5.8	0.53	0.27	-0.27
15	8.4	0.81	0.40	-0.41
20	10.7	1.07	0.54	-0.53
25	13.8	1.33	0.68	-0.65
30	16.1	1.59	0.82	-0.80
35	19.1	1.88	0.95	-0.91
40	21.6	2.13	1.09	-1.03
45	24.5	2.38	1.24	-1.16
50	26.5	2.65	1.37	-1.27
55	28.4	2.92	1.53	-1.39
60	31.7	3.16	1.66	-1.51
65	34.8	3.42	1.81	-1.61
70	36.7	3.69	1.94	-1.72
75	39.5	3.98	2.10	-1.87
80	42.3	4.23	2.25	-1.97
85	44.5	4.47	2.39	-2.09
90	48.1	4.74	2.55	-2.20
95	50	5.01	2.70	-2.31
100	53.3	5.28	2.85	-2.41

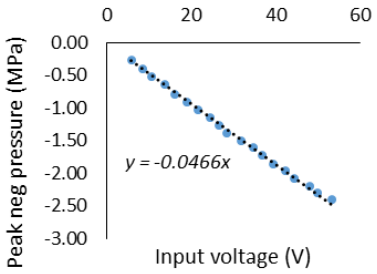

Figure A1.5 *Calibration at 1.6 MHz.*

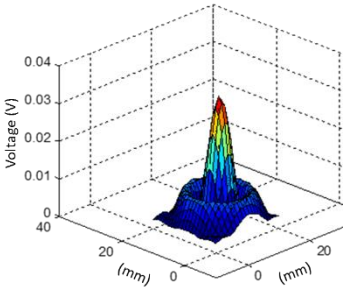

Figure A1.6 *Axial profile at 1.6 MHz.*

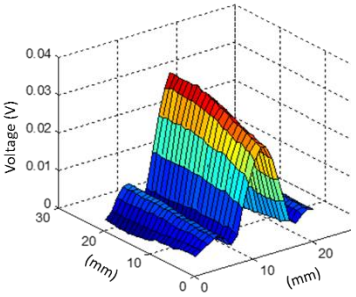

Figure A1.7 *Transverse profile at 1.6 MHz.*

A2. Gold nanoparticle fabrication protocol

Protocol: Gold 100 nm nanoparticles

Reference: Liz-Marzan *et al.*, '*Tuning Size and Sensing Properties in Colloidal Gold Nanostars*', Langmuir, 2010, 26(18), 14943-14950.

Scope: This protocol describes the method to fabricate 100 nm gold nanoparticles with a star-like structure. This protocol produces 3x the quantity described by Liz-Marzan (2010).

Materials:

Item	Product code	Supplier
Polyvinylpyrrolidone (PVP) (Mw 10,000)	PVP10	Sigma
N,N-Dimethylformamide (DMF)	648531	Sigma
Gold(III) chloride trihydrate (HAuCl4)	520918	Sigma
Sodium borohydride (NaBH4) powder	S678	Fisher Scientific

Part 1: Synthesis of gold seeds *(~20 nm diameter)*

- ❑ Prepare 0.1136 M HAuCl4 solution
  38.6 mg HAuCl4 in 1 mL DI H2O
- ❑ 22 uL of HAuCl4 solution + 47.5mL of DMF/H20 (18:1 v/v) + 17 mg PVP + 2.5 mL NaBH4 (10 mM)
- ❑ Stir for 2 hours at room temperature
- ❑ Centrifuge and wash (3 x 30 mins at 9000 g)
- ❑ Re-disperse in 5 mL of ethanol for storage

Part 2: Synthesis of 100 nm gold particles

- ❑ Preparing the 10mM PVP solution in DMF
  - 4.5g PVP (dry) + 45 mL DMF (flammable)
  - Stir with magnetic stir bar and hot plate with gentle heat until dissolved
- ❑ Preparing the aqueous solution of 50mM HAuCl4
  - 0.02g of HAuCl4 + 1mL of Milli-Q water
- ❑ Combining
  - 246µL of the HAuCl4 solution (above) + the PVP-DMF solution
  - + 10µL of pre-made gold seed solution (red)
  - Stir with magnetic stir bar for 1 – 2 hours until blue
- ❑ Washing
  - Centrifuging and washing three times (3x 30 mins at 9000G)

A3. PEGylated density-modified nanoparticle fabrication protocol

Protocol: Cy5-PEGylated 200 nm nanoparticles of polystyrene and gold

Scope: This protocol describes the method to fabricate and characterise two sets of Cy5-PEGylated 200 nm nanoparticles, with a core of polystyrene or gold.

Materials:

Item	Product code	Supplier
Gold nanoparticles (200 nm, stabilized suspension in citrate buffer) (1.9×10^9 particles/mL)	742066-100ML	Sigma
Cy5 PEG Thiol, Cy5-PEG-SH (2000 Da)	PG2-S5TH-2k	Nanocs
Thiol PEG, mPEG-SH (2000 Da)	PG1-TH-2k-1	Nanocs
Phosphate buffer		
Polystyrene beads, amine function (200 nm) (2.4×10^{12} particles/mL)	PS200-AM-2	Nanocs
Cy5 PEG NHS (2000 Da)	PG2-NSS5-2k	Nanocs
Succinimidyl PEG NHS, mPEG-NHS(SC) (2000 Da)	PG1-SC-2k-1	Nanocs
Borate buffer		

Method (1): *Cy5-PEGylated PS nanoparticles*

- ❑ Prepare 5 mL of 20 mM **borate buffer** at pH 8.5
  0.1 M, 100 mL borate buffer stock
  - 100 mL DI + 0.618g boric acid, 0.13g sodium tetraborate
  - Measure pH
  - Dilute to 20 mM (i.e. 2 mL 0.1M in 10 mL DI)

- ❑ Prepare the 1 mg of PEG by dissolving in 100uL of DMSO in the following proportions 5 % labelled (**Cy5-PEG-NHS**), 95 % unlabelled (**mPEG-NHS(SC)**)
- ❑ Spin down PS (amine-modified) particles and re-disperse in 5 mL borate buffer at desired concentration of $5x10^{10}$ particles/mL
- ❑ Combine particle solution and PEG solution stirring rapidly for ~4 hours

Method (2): *Cy5-PEGylated Au nanoparticles*

- ❑ Prepare 5 mL of 20 mM **phosphate buffer** at pH 7.4
  0.1 M, 100 mL sodium phosphate buffer stock
  - 100 mL DI + 1.10g sodium phosphate dibasic + 0.27g sodium phosphate monobasic
  - Measure pH
  - Dilute to 20 mM (i.e. 2 mL 0.1M in 10 mL DI)

- ❑ Prepare the 1 mg of PEG by dissolving in 100uL of DMSO in the following proportions 5 % labelled (**Cy5-PEG-Thiol**), 95 % unlabelled (**mPEG-SH**)
- ❑ Spin down particles and re-disperse in 5 mL phosphate buffer at desired concentration of $1x10^{10}$ particles/mL
- ❑ Combine particle solution and PEG solution stirring rapidly overnight

Purification: by centrifugation – using LoBind tubes, 14000 RPM, 30 mins, 3 repeats.

Characterisation: DLS (size and zeta potential), plate reader (fluorescence and absorbance), NanoSight (concentration), IVIS (fluorescence detection *in vivo*).

A4. MATLAB code for bubble dynamics and nanoparticle transport modelling

A4.1 Dynamic bubble model with viscoelastic shell

```
% MODIFIED KELLER-MIKSIS EQUATIONS
% including a thin elastic shell
%
% Based on
% J.B.Keller and M.Miksis, 'Bubble Oscillations of Large Amplitude',
% JASA (1980)
% P. Marmottant, 'A model for large amplitude oscillations of coated
% bubbles accounting for buckling and rupture', JASA (2005)
%
% Harriet Lea-Banks, December 2014
clear all
close all

%% Defining variables
% Global variables
global a_e c chi eps f k o P p_0 rho vis vsh

% Parameters
% as defined in Marmottant (2005)
f0 = 114*10^3; %2.9*10^6;                   % Driving frequency (2.9MHz)
P = 70*10^3; %130*10^3;                     % Driving pressure (130kPa)

% Constants
% Dimensional values (0 denotes dimensioned)
a_e = 10*10^-6; %0.975*10^(-6);             % Equilibrium radius
chi0 = 0.5;                                 % (N/m) Shell elasticity
kappa_s = 15*10^(-9);                       % (N) Shell friction (3*vsh0*eps0)
vsh0 = 1;                                   % (kg/ms) Shell viscosity
eps0 = 0.1*10^-6; %0.02*10^(-6);            % (m) Shell thickness
rho0 = 1000;                                % (kg/m^3) Fluid density
vis0 = 0.001;                               % (kg/ms) Fluid viscosity
k = 1.095;                                  % Polytropic gas exponent

p_s = 1*(10^5);                             % (Pa) Static pressure
p_v = 0.0233*(10^5);                        % (Pa) Vapour pressure
p_0 = p_s - p_v;

c0 = 1480;                                  % (m/s) Speed of sound
o0 = 0.0725;                                % (N/m) Surface tension

% Nondimensionalization
c = c0/(a_e*f0*2*pi);                       % where m/s = a_e*(w0*2*pi)
n = 10;                                     % Number of cycles
run_t = n/f0;                               % Run time
t = run_t*2*pi*f0;                          % Total time
rho = rho0*(a_e*2*pi*f0)^2/p_0;             % Liquid density
o = o0/(a_e*p_0);                           % Surface tension
vis = vis0*f0*2*pi/p_0;                     % Viscosity
f = f0/(2*pi*f0);                           % Excitation frequency
P = P/p_0;                                  % Excitation pressure

eps = eps0/a_e;                             % Shell thickness
vsh = vsh0*f0*2*pi/p_0;                     % Shell viscosity
chi = chi0/(a_e*p_0);                       % Shell elasticity

p_0 = p_0/p_0; % ! Over-writes
a_e = a_e/a_e; % ! Over-writes

%% Ordinary differential equations
tspan = [0 t]; %[0 t];
options = odeset('MaxStep',0.01);
[T,X] = ode15s(@shell,tspan,[a_e 0], options);
% ode15s proves quicker than ode45 since the problem is 'stiff'
% where X(:,1) = radius and (X:,2) = radial velocity
figure
plot(T,X(:,1),'b')
title('Radial Displacement - Keller-Miksis Model with Shell')
xlabel('Dimensionless time vector (T)')
ylabel('Radius (a/a_e)')
```

```
function dx = shell(t,x)
% The radius function determines the dimensionless radius (a)
% as defined by the Keller-Miksis equations
%
% Harriet Lea-Banks, November 2014

% Dimensionless global variables
global a_e c chi eps f k o P p_0 rho vis vsh

% Initial conditions
% dx_1=x_2 , x_1(0)=a_e
% dx_2=((x_2)^3)/2... , x_2(0)=0

w = sin(2*pi*(t)*f);
dx = zeros(2,1);
dx(1) = x(2);

% Non-linear surface tension = (o + 2*chi*((x(1)/a_e) - 1))
dx(2) = ((1/2)*x(2)^(3)...
    + x(2)*((p_0 + 2*(o + 2*chi*((x(1)/a_e) - 1))*a_e^(-1))*(a_e*x(1)^(-1))^(3*k) -
p_0)*rho^(-1)...
    - c*((3/2)*x(2)^2 ...
    + 4*vis*x(2)*(rho*x(1))^(-1)...
    - ((p_0 + 2*(o + 2*chi*((x(1)/a_e) - 1))*a_e^(-1))*(a_e*x(1)^(-1))^(3*k) -
p_0)*rho^(-1)...
    + 2*(o + 2*chi*((x(1)/a_e) - 1))*(x(1)*rho)^(-1)...
    + 4*(3*eps*vsh)*x(2)*((x(1)^2)*rho)^(-1))...
    - x(1)*x(2)*(3*k*(p_0 + 2*(o + 2*chi*((x(1)/a_e) - 1))*a_e^(-1))*(a_e*x(1)^(-
1))^(3*k)*x(1)^(-1))*rho^(-1)...
    + ((1 + x(2)*c^(-1))*P*c*rho^(-1)*sin((2*pi*f)*(t+(x(1)*c^(-1))))))...
    *(4*vis*rho^(-1) - x(1)*(x(2)-c))^(-1);
```

A4.2 Transport of nanoparticles

```
% TRANSPORT
% -> FUNCTIONS: Keller.m, Rad.m, Stream.m, MicroStream.m, Vel_rad.m, Vel_theta.m
% A model of a particle suspended in a fluid, in close proximity to a
% microbubble, within an ultrasonic field.
%
% F_R1 = Acoustic radiation force from the primary sound field
% (governed by a sinusoidal incident wave of pressure P_A)
% F_R2 = Acoustic radiation force scattered from the pulsating bubble
% (governed by the Keller Miksis model)
% F_D1 = Drag force from primary sound field
% F_D2 = Drag force from pulsating bubble
% (governed by Stokes equation and the Doinikov microstreaming function)
%
% Harriet Lea-Banks, January 2015
clear all
close all

%% PARAMETERS
global P_A f_0 w_0 I k_L R_0 o0 p_v d chi c_i vis_i rho_i y p_s c_0 vis_0 rho_0 R_p V_p
rho_p n Total step r R dR ddR v_s_theta v_s_rad v_ms_theta v_ms_rad v_sR v_msR v_sT
v_msT

% ACOUSTIC parameters
P_A = 1*(10^6);       % Incident acoustic pressure (Pa)(1bar = 1*10^5Pa)
f_0 = 0.5*10^6;       % Incident acoustic frequency (100kHz)
    % Previously: 309*10^3, where excitation frequency f_0 = f_0*0.37 (Keller-Miksis
numerical solution)
w_0 = f_0*2*pi;         % Incident acoustic frequency (rad/s)
I = 1000;               % Incident acoustic intensity (W/m^2)
% BUBBLE parameters
R_0 = 1.5*10^(-6);      % Equilibrium bubble radius (10um)
o0 = 72.5*10^(-3);      % Surface tension (N/m)
p_v = 0.0233*(10^5);    % Vapour pressure (Pa)
d = 0.1;                % Damping coefficient
chi = 10;               % Damping factor
% GAS parameters
c_i = 343;              % Speed of sound in air (m/s)
vis_i = 1.84*10^(-5);   % Viscosity of air (kg/ms)
rho_i = 1.21;           % Density of air (kg/m^3)
y = 1.4;                % Polytropic exponent
```

```
p_s = 1*(10^5);          % Static pressure (Pa)
% FLUID parameters
c_0 = 1484;              % Sound speed in fluid (m/s)
vis_0 = 0.001;           % Fluid dynamic viscosity (kg/ms)
rho_0 = 998;             % Fluid density (kg/m^3)
% PARTICLE parameters
R_p = 100*10^(-9);       % Particle radius (100 nm)
V_p = (4/3)*pi*R_p^3;    % Particle volume (nm^3)
rho_p = 19300;           % Particle density (kg/m^3) (Density of gold)
% PROGRAM parameters
n = 10;                  % Number of cycles
run_t = n/f_0;           % Run time
Total = run_t*2*pi*f_0; % Total time
step = 0.1;             % Time step
obs_points = [1*10^(-8)]; %, 1*10^(-9), 1*10^(-10)]; % Observation points - radial
distances

for rr = 1:length(obs_points)
  r = obs_points(rr);

 %% F_AR_2 Acoustic Radiation Force
 % due to scattering from the pulsating bubble
 % Radial displacement (R) and radial velcity (dR)
 % as determined by the Keller Miksis model
 [R, dR, T] = Keller(R_0, f_0);
 ddR = diff(dR);                                    % Radial acceleration (dv/dt)
 len = length(R);                                   % Correcting length
 R = R(1:len-1);
 dR = dR(1:len-1);

 p_scat = rho_0*((R.^2).*ddR + 2*R.*dR.^2)/r;       % Scattered pressure field

 % Acoustic radiation force dependent on particle volume and pressure gradient
 F_AR_2 = V_p*dp_scat;                              % Time dependent force
 FAR2 = mean(F_AR_2);                               % Mean force

 %% F_AR_1 Acoustic Radiation Force
 % due to a attenuation OR a pressure perturbation in the primary sound field
 % Acoustic radiation force dependent on particle volume and pressure gradient
 F_AR_1 = V_p*dp_L;                                 % Time dependent force
 FAR1 = mean(F_AR_1);                               % Mean force

 %% F_D_1 Fluid drag force
 % due to acoustic streaming
 % Acoustic streaming velocity (select Nyborg, Eckart, Wu&Du or Doinikov)
 [v_s_rad] = Stream(R_0, f_0);
 % F_D_1 = 6*pi*vis_0*R_p(v_p - v_s);

 %% F_D_2 Fluid drag force
 % due to microstreaming
 % Microstreaming velocity (select Wu&Du or Doinikov)
 [v_ms_theta, v_ms_rad] = MicroStream(R_0, f_0);
 % F_D_2 = 6*pi*vis_0*R_p(v_p - v_ms);
end


function [R,dR,T] = Keller(a_e,f_0)
% KELLER-MIKSIS EQUATIONS
% Based on the paper
% J.B.Keller and M.Miksis, 'Bubble Oscillations of Large Amplitude',
% 1980 (JASA)
%
% Harriet Lea-Banks, October 2014

%% Defining variables
% Global variables
global o01 k01 rho_01 c_01 step Total P_A vis_0 p_s P_A1 vis_01 f_01 o0 p_v c_0 rho_0
p_0 p_01 a_e1

% Additional parameters
p_0 = p_s - p_v;
k01 = o0+1;                          % Gas characteristic

% Nondimensionalization
c_01 = c_0/(a_e*f_0*2*pi);           % where m/s = a_e*(w_0*2*pi)
rho_01 = rho_0*(a_e*2*pi*f_0)^2/p_0; % Liquid density
```

```
o01 = o0/(a_e*p_0);                    % Surface tension
vis_01 = vis_0*f_0*2*pi/p_0;           % Viscosity
f_01 = f_0/(2*pi*f_0);                 % Excitation frequency
P_A1 = P_A/p_0;                        % Incident acoustic pressure
p_01 = p_0/p_0;
a_e1 = a_e/a_e;

%% Ordinary differential equations
tspan = [0:step:Total];
options = odeset('MaxStep',0.01);
[T,X] = ode15s(@Rad,tspan,[a_e1 0], options);
% ode15s proves quicker than ode45 since the problem is 'stiff'
% where X(:,1) = radius and (X:,2) = radial velocity

% Redimensioning
% R = X(:,1)*a_e;
% dR = X(:,2)*(a_e*f_0*2*pi);
% T = T;

% Keeping nondimensioned
R = X(:,1);
dR = X(:,2);
T = T;

function dx = Rad(t,x)
% The radius function determines the dimensionless radius (a)
% as defined by the Keller-Miksis equations
%
% Harriet Lea-Banks, October 2014

% Dimensionless global variables
global o01 k01 rho_01 c_01 P_A1 vis_01 f_01 p_01 a_e1

% Initial conditions
% dx_1=x_2 , x_1(0)=a_e
% dx_2=((x_2)^3)/2... , x_2(0)=0

w = sin(2*pi*(t)*f_01);

dx = zeros(2,1);
dx(1) = x(2);
dx(2) = ((1/2)*x(2)^(3)...
    + x(2)*((p_01 + 2*o01*a_e1^(-1))*(a_e1*x(1)^(-1))^(3*k01) - p_01)*rho_01^(-1)...
    - c_01*((3/2)*x(2)^2 ...
    + 4*vis_01*x(2)*(rho_01*x(1))^(-1)...
    - ((p_01 + 2*o01*a_e1^(-1))*(a_e1*x(1)^(-1))^(3*k01) - p_01)*rho_01^(-1)...
    + 2*o01*(x(1)*rho_01)^(-1))...
    - x(1)*x(2)*(3*k01*(p_01 + 2*o01*a_e1^(-1))*(a_e1*x(1)^(-1))^(3*k01)*x(1)^(-
1))*rho_01^(-1)...
    + ((1 + x(2)*c_01^(-1))*P_A1*c_01*rho_01^(-1)*sin((2*pi*f_01)*(t+(x(1)*c_01^(-
1))))))...
    *(4*vis_01*rho_01^(-1) - x(1)*(x(2)-c_01))^(-1);


function [u_1] = Stream(P_A,f_0)
% ACOUSTIC STREAMING: from a plane wave
% Streaming function as defined by Nyborg (1965),
%
% Harriet Lea-Banks, June 2015

% Defining parameters
global I d chi c_i vis_i rho_i c_0 vis_0 rho_0 R_0 obs_points

%% PLANE WAVE IN UNBOUNDED MEDIUM (Nyborg, 1965)
i = sqrt(-1);

P_A = 1*(10^6);            % Incident acoustic pressure (Pa)(1bar = 1*10^5Pa
f_0 = 1.6*10^6;            % Incident acoustic frequency (100kHz)
c_0 = 1484;
rho_0 = 998;
I = (P_A^2)/(2*rho_0*c_0); % Incident acoustic intensity (W/m^2)

w = 2*pi*f_0;              % Angular frequency
lam = (c_0/f_0);           % Wavelength
k = (2*pi)/lam;            % Wavenumber
n = 10;                    % No. of cycles
```

```
t = 0:0.01*(n/f_0):(n/f_0);% Time
x = 1*10^-9;               % Space (0:0.02:2)*10^-2;
                           %(If a single x value is chosen, attenuation cannot act)

u_0 = I/P_A;               % Particle velocity amplitude
a = 50;                    % Absorption coefficient (dB) water
n = 0.001;                 % Dynamic viscosity (kg/ms) water

% u_1 = u_0*exp(-a*x).*sin(w*t-k*x);     % Velocity field
% F1 = -n*diff(u_1,2);                   % Streaming force

%% PLANE WAVE IN A CYLINDRICAL TUBE (Eckart, 1948)
r = 0.01*10^-3;            % Radial location (0 < r < r_1)
r_0 = 5*10^-3;             % Cylinder radius (1 cm diameter)
r_1 = 1.5*10^-3;           % Beam radius (3 mm focus [-6 dB] width)
N = 3;                     % Bulk viscosity (=0 for an ideal gas)
n = 0.001;                 % Dynamic viscosity (kg/ms) water

P_1 = P_A*exp(-a*x).*sin(w*t-k*x);  % Pressure field
b = (4/3) + (N/n);                  % 'Viscosity number'
K = (b*k)/(2*rho_0^2*c_0^3);        %
G = 0.5*K*P_1.^2*r_1^2;             %

u_1 = G*[0.5*(1 - r^2/r_1^2) - ...  % Steaming velocity
    (1 - r_1^2/(2*r_0^2))*(1 - r^2/r_0^2) - log(r_1/r_0)];
F2 = -n*diff(u_1,2);                % Streaming force


% STREAMING
% Streaming function as defined by Doinikov and Bouakaz,
% considering an air bubble in water, where all fluid inside and outside
% the bubble is modelled as viscous and heat-conducting
%
% Based on
% A.Doinikov and A.Bouakaz, 'Acoustic microstreaming around a gas bubble',
% JASA 2010, 127(2) 703-709
%
% Harriet Lea-Banks, October 2015
clear all
close all

%% Setting the scene
% Functions and values required to calculate fundamental parameters

i = sqrt(-1);
f = 100*10^3;              % Acoustic frequency (100 kHz)
w = 2*pi*f;                % Angular frequency
t = 1;
A = 1;                     % Amplitude of the velocity potential of the incident wave
R_0 = 33*10^(-6);          % Bubble equilibrium radius (33 um)

c_i = 330;                 % Sound speed in internal gas (m/s)
c_o = 1500;                % Sound speed in external fluid (m/s)
y_i = 1.4;                 % Ratio of specific heats of internal gas
y_o = 1.007;               % Ratio of specific heats of external fluid
rho_i = 1.2;               % Density of internal gas (kg/m^3)
rho_o = 1000;              % Density of external fluid (kg/m^3)
sig = 0.072;               % Surface tension (N/m)

vis_ni = 1.8*10^(-5);      % Shear viscosity of internal gas (kg/m/s)
vis_no = 0.001;            % Shear viscosity of external fluid (kg/m/s)
vis_bi = 1.6*10^(-5);      % Bulk viscosity of internal gas (Pa/s)
vis_bo = 0.0026;           % Bulk viscosity of external fluid (Pa/s)
vis_ki = vis_ni/rho_i;     % Kinematic viscosity of internal gas (kg/m/s)
vis_ko = vis_no/rho_o;     % Kinematic viscosity of external fluid (kg/m/s)

chi_i = 2.8*10^(-5);           % Damping factor
chi_o = 1.4*10^(-7);           % Damping factor
d_vi = sqrt(2*(vis_ni/rho_i)/w); % Viscous boundary layer thickness (m)
d_vo = sqrt(2*(vis_no/rho_o)/w); % Viscous boundary layer thickness (m)
alpha_i = 3.665*10^(-3);       % Volume thermal expansion coefficient of internal gas
(K^-1)
alpha_o = 2.1*10^(-4);         % Volume thermal expansion coefficient of external
fluid (K^-1)
K_i = 0.034;                   % Thermal conductivity of internal gas (J/s/m/K)
K_o = 0.58;                    % Thermal conductivity of external fluid (J/s/m/K)
```

```
% Wave numbers (complex scalar values)
   % Coefficients used in the wave numbers (k_1, k_2, k_3)
    B_3o = 1 - (i*w*y_o)*(vis_bo + 4*vis_no/3)/(rho_o*c_o^2);
    B_2o = i*w*(y_o - 1 + B_3o)/(y_o*chi_o*B_3o);
    B_1o = y_o*w^2/(c_o^2*B_3o);
    B_3i = 1 - (i*w*y_i)*(vis_bi + 4*vis_ni/3)/(rho_i*c_i^2);
    B_2i = i*w*(y_i - 1 + B_3i)/(y_i*chi_i*B_3i);
    B_1i = y_i*w^2/(c_i^2*B_3i);
   % 1. Sound wave number
    k_1o = (((B_1o + B_2o)/2)*(1 - (1 - (4*i*w*B_1o)/(y_o*chi_o*(B_1o +
B_2o)^2))^(1/2)))^(1/2);
    k_1i = (((B_1i + B_2i)/2)*(1 - (1 - (4*i*w*B_1i)/(y_i*chi_i*(B_1i +
B_2i)^2))^(1/2)))^(1/2);
   % 2. Thermal wave number
    k_2o = (((B_1o + B_2o)/2)*(1 + (1 - (4*i*w*B_1o)/(y_o*chi_o*(B_1o +
B_2o)^2))^(1/2)))^(1/2);
    k_2i = (((B_1i + B_2i)/2)*(1 + (1 - (4*i*w*B_1i)/(y_i*chi_i*(B_1i +
B_2i)^2))^(1/2)))^(1/2);
   % 3. Viscous wavenumber
    k_3o = (1 + i)/d_vo;
    k_3i = (1 + i)/d_vi;
   % Nondimensional wavenumbers (x_j = k_j[m^-1] * R_0[m])
    x_1o = k_1o*R_0;
    x_2o = k_2o*R_0;
    x_3o = k_3o*R_0;
    x_1i = k_1i*R_0;
    x_2i = k_2i*R_0;
    x_3i = k_3i*R_0;

   % Extending the list of wavenumbers [k_0:k_4]
   % by setting k_0 = k_1 and k_4 = k_3
   % (which are necessary for Jn_k0 and Jn_k4,
   % which in turn are needed for djn_x1 and djn_x3)
    k_0o = k_1o; k_0i = k_1i;
    k_4o = k_3o; k_4i = k_3i;
    x_0o = k_0o*R_0; x_0i = k_0i*R_0;
    x_4o = k_4o*R_0; x_4i = k_4i*R_0;

% Mode (n)
n = 1;
r = 0:90;
theta = 0:90;

% Unit azimuth vector of the spherical coordinate system
E_eps = -sind(r) + cosd(theta);

% LEGENDRE POLYNOMIAL (Pn)
   % Pn1 = (1/ ((2^n)*factorial(n)))...
   %     *diff((cosd(theta).^2 -1).^n, cosd(theta), n);
    syms x dx(x)
    dx(x) = diff((x.^2 -1).^n, x, n);
    x = cosd(theta);
    Pn = (1/ ((2^n)*factorial(n)))*dx(x);
    Pn1 = double(Pn);

% SPHERICAL BESSEL FUNCTION (Jn)
    Jn_x1i = cosd(n*theta - x_1i*sind(theta)); Jn_x2i = cosd(n*theta -
x_2i*sind(theta));
    Jn_x3i = cosd(n*theta - x_3i*sind(theta));
    Jn_x1o = cosd(n*theta - x_1o*sind(theta)); Jn_x2o = cosd(n*theta -
x_2o*sind(theta));
    Jn_x3o = cosd(n*theta - x_3o*sind(theta));
    Jn_k1r = cosd(n*theta - k_1i*r.*sind(theta)); Jn_k2r = cosd(n*theta -
k_2i*r.*sind(theta));
    Jn_k3r = cosd(n*theta - k_3i*r.*sind(theta));
    Jn_x0i = cosd(n*theta - x_0i*sind(theta)); Jn_x0o = cosd(n*theta -
x_0o*sind(theta));
    Jn_x4i = cosd(n*theta - x_4i*sind(theta)); Jn_x4o = cosd(n*theta -
x_4o*sind(theta));
    % dJn(x)/dx = 1/2(J(n-1)(x) - J(n+1)(x))
        % ---> Internal streaming
    jn_x1i = (1/pi)*trapz(Jn_x1i); djn_x1i = (1/2)*(Jn_x0i - Jn_x2i); % requires k_0
    jn_x2i = (1/pi)*trapz(Jn_x2i); djn_x2i = (1/2)*(Jn_x1i - Jn_x3i);
    jn_x3i = (1/pi)*trapz(Jn_x3i); djn_x3i = (1/2)*(Jn_x2i - Jn_x4i); % requires k_4
        % ---> External streaming
```

```
    jn_x0o = (1/pi)*trapz(Jn_x0o); jn_x1o = (1/pi)*trapz(Jn_x1o);
    jn_x2o = (1/pi)*trapz(Jn_x2o); jn_x3o = (1/pi)*trapz(Jn_x3o);
    jn_x4o = (1/pi)*trapz(Jn_x4o);
    djn_x1o = (1/2)*(Jn_x0o - Jn_x2o); % requires k_0
    djn_x2o = (1/2)*(jn_x1o - jn_x3o);
    djn_x3o = (1/2)*(Jn_x2o - Jn_x4o); % requires k_4
    jn_k1or = (1/pi)*trapz(Jn_k1r); jn_k2or = (1/pi)*trapz(Jn_k2r);
    jn_k3or = (1/pi)*trapz(Jn_k3r);

% SPHERICAL HANKEL FUNCTION (Hn)
% dHn(x)/dx = 1/2(H(n-1)(x) - H(n+1)(x))
    hn_x0o = (-jn_x0o - exp(-n*i*pi)*jn_x0o)/(i*sin(n*pi));
    hn_x1o = (-jn_x1o - exp(-n*i*pi)*jn_x1o)/(i*sin(n*pi));
    hn_x2o = (-jn_x2o - exp(-n*i*pi)*jn_x2o)/(i*sin(n*pi));
    hn_x3o = (-jn_x3o - exp(-n*i*pi)*jn_x3o)/(i*sin(n*pi));
    hn_x4o = (-jn_x4o - exp(-n*i*pi)*jn_x4o)/(i*sin(n*pi));
    dhn_x1o = (1/2)*(hn_x0o - hn_x2o); % requires k_0
    dhn_x2o = (1/2)*(hn_x1o - hn_x3o);
    dhn_x3o = (1/2)*(hn_x2o - hn_x4o); % requires k_4
    hn_k1or = (-jn_k1or - exp(-n*i*pi)*jn_k1or)/(i*sin(n*pi));
    hn_k2or = (-jn_k2or - exp(-n*i*pi)*jn_k2or)/(i*sin(n*pi));
    hn_k3or = (-jn_k3or - exp(-n*i*pi)*jn_k3or)/(i*sin(n*pi));

   % Defining u_ij(n) and v_ij(n)
    g = 2*(vis_ni - vis_no)/(vis_ni*x_3i^2);
    g1 = sig*(n - 1)*(n + 2)/(rho_i*w^2*R_0^3);
    g2 = x_3i*djn_x3i/jn_x3i;
    g3 = alpha_i*B_3o*(alpha_o*B_3i*(B_1i - k_1i^2)*(B_1i - k_2i^2)...
        *(x_1i*djn_x1i*jn_x2i - x_2i*djn_x2i*jn_x1i)).^(-1);

    f1 = (B_1o - k_1o^2)*((B_1i - k_1i^2)*x_1i*jn_x2i.*djn_x1i.*g3...
        - (B_1i - k_2i^2)*x_2i*jn_x1i.*djn_x2i) - n*(n + 1)*g - rho_o/rho_i;
    f2 = n*(n + 1)*g + (B_1o - k_1o^2)*g3*(k_1i^2 -
k_1i^2)*x_1i.*djn_x1i*x_2i.*djn_x2i;
    f3 = (B_1o - k_1o^2).*g3*(K_o/K_i)*(k_1i^2 - k_2i^2)*jn_x1i*jn_x2i + 2*g - g1;
    f4 = 1 - n*(n + 1)*g - (B_1o - k_1o^2).*g3*(K_o/K_i)...
        .*((B_1i - k_2i^2)*x_1i.*djn_x1i*jn_x2i - (B_1i -
k_1i^2)*x_2i.*djn_x2i*jn_x1i);

    v11 = f3;
    v12 = (B_1o - k_2o^2)*g3*(K_o/K_i)*(k_1i^2 - k_2i^2)*jn_x1i*jn_x2i + 2*g - g1;
    v13 = -n*(n + 1)*g;
    v21 = f4;
    v22 = 1 - n*(n + 1)*g - (B_1o - k_2o^2).*g3*(K_o/K_i)...
        .*((B_1i - k_2i^2)*x_1i.*djn_x1i*jn_x2i - (B_1i -
k_1i^2)*x_2i.*djn_x2i*jn_x1i);
    v23 = n*(n + 1)*g;
    v31 = g*(1 - g2) - g1;
    v32 = v31;
    v33 = 1 + g*(g2 + 1 - n - n^2);

    u11 = f1;
    u12 = (B_1o - k_2o^2).*g3.*((B_1i - k_1i^2)*x_1i.*djn_x1i*jn_x2i...
        - (B_1i - k_2i^2)*x_2i.*djn_x2i*jn_x1i) - n*(n + 1)*g - rho_o/rho_i;
    u13 = n*(n + 1)*(g - g1);
    u21 = f2;
    u22 = n*(n + 1)*g + (B_1o - k_2o^2).*g3*(k_1i^2 -
k_1i^2)*x_1i.*djn_x1i*x_2i.*djn_x2i;
    u23 = n*(n + 1)*(1 - rho_o/rho_i - (n^2 + n - 1)*g);
    u31 = 1 - rho_o/rho_i + g*(g2 + 1 - n - n^2);
    u32 = u31;
    u33 = 1 + n*(n + 1)*(g - g1) - (1 + g2)*(rho_o/rho_i + (n^2 + n - 1)*g);

%% First-order velocity
% ---> a) 'Velocity of the SCATTERED sound wave field'
% Scattered field matrices
% to calculate the 'linear scattering coefficients'
% (Velocity vectors are converted to scalar values by removing NaNs and choosing the
median value)
u12 = median(u12,2); u13 = u13; u21 = median(u21,2); u22(isnan(u22))=[]; u22 =
median(u22,2); u23 = u23; u31 = median(u31,2); u32 = median(u32,2); u33 =
median(u33,2); v11 = median(v11,2); v12 = median(v12,2); v13 = v13; v21 =
median(v21,2); v22 = median(v22,2); v23 = v23; v31 = median(v31,2); v32 =
median(v32,2); v33 = median(v33,2);
% Forming the square matrices u_ij and v_ij
u_ij = [u11,u12,u13; u21,u22,u23; u31,u32,u33];
```

```
v_ij = [v11,v12,v13; v21,v22,v23; v31,v32,v33];
h_n = [hn_x1o,hn_x1o,hn_x1o; hn_x2o,hn_x2o,hn_x2o; hn_x3o,hn_x3o,hn_x3o];
dh_n = [dhn_x1o,dhn_x1o,dhn_x1o; dhn_x2o,dhn_x2o,dhn_x2o; dhn_x3o,dhn_x3o,dhn_x3o];
x_j = [x_1o,x_1o,x_1o; x_2o,x_2o,x_2o; x_3o,x_3o,x_3o];
Da_ij_m = zeros(1,3);
a_mn = zeros(1,3);
for m = 1:3
    a_ij = u_ij*h_n + x_j*v_ij*dh_n; % Square matrix (i,j = 1,2,3)
    b_i = -u_ij(:,1)*jn_x1o - v_ij(:,1)*x_1o*djn_x1o(1); % Column vector (i = 1,2,3)
    Da_ij = det(a_ij); % Determinant of the matrix a_ij(n)
    a_ij(:,m) = b_i; % Forming the modified matrix a_ij(nm)
    Da_ij_m(m) = det(a_ij); % Determinant of the modified matrix a_ij(nm)
    alpha_mn(m) = Da_ij_m(m)/Da_ij; % Scattering coefficients ?_mn
end
% Defining the scalar and vorticity potential velocities
An = A*(2*n + 1)*i^n; % Defining the incident wave

%% VECTORS
    % Scattered scalar potential velocity
    PHI_s = exp(-i*w*t)*An*(alpha_mn(1)*hn_k1or + alpha_mn(2)*hn_k2or)*Pn1;
    % Scattered vorticity potential velocity
     % PSI_s = exp(-i*w*t)*E_eps*An*alpha_mn(3)*hn_k3or.*Pn1;
    PSI_s = exp(-i*w*t)*An*alpha_mn(3)*hn_k3or.*Pn1;
% Calculating the velocity of the scattered sound wave field (v_s)
v_s = gradient(PHI_s) + gradient(PSI_s);
% ---> b) 'Velocity of the INCIDENT sound wave field' (v_I)
    % Incident scalar potential velocity
    PHI_I = exp(-i*w*t)*An*jn_k1or*Pn1;
% Calculating the velocity of the incident sound wave field (v_I)
v_I = gradient(PHI_I);
% First-order velocity (r,theta)
v_1 = v_I + v_s;
%% Second-order velocity
% Building-block functions
Wr = (R_0^3/(4*vis_ko))...
    *real(conj(v_1).*(gradient(v_1)) + (gradient(conj(v_1))).*v_1...
    - conj(v_I).*(gradient(v_I)) - (gradient(conj(v_I))).*v_I);

Wtheta = (R_0^3/(4*vis_ko))...
    *real(conj(v_1).*(gradient(v_1)) + (gradient(conj(v_1))).*v_1...
    - conj(v_I).*(gradient(v_I)) - (gradient(conj(v_I))).*v_I);

CHI_r = integral(Wr.*Pn1.*sind(theta));
CHI_theta = (-1/(n*(n + 1)))*trapz(Wtheta.*Pn1.*sin(theta));
% Integration with respect to (y) for Nn(x,m)
for m = (-n):(n+3);
    for y = 1:x;
        N(y,m) = (y^m)*(CHI_r(y) + m*CHI_theta(y));
    end
    Nn(:,m) = trapz(N(:,m));
end

RHO_I = i*rho_o*k_1o^2.*PHI_I/w;
RHO = (-i*rho_o/w)*gradient(v_1);
u = (R_0^2/(4*rho_o))*trapz(real(gradient(conj(RHO).*v_1 - conj(RHO_I).*v_I))...
    .*Pn1*cosd(theta)*sind(theta));

% Integration with respect to (y) for Kn(x,m)
for m = (1-n):0;
    for y = 1:x; %(x=r/R0)
        K(y,m) = (y^m)*u(y);
    end
    Kn(:,m) = trapz(K(:,m));
end

% (V_I) The velocity produced by the incident sound field in the ambient liquid
% when the particle is absent, for a plane travelling wave:
V_I = (-abs(k_1o*A)^2/(2*w))*real(k_1o)*exp(i*k_1o.*r - i*conj(k_1o).*r);
U = (R_0/2).*V_I - (R_0/4*w^2)*real(conj(gradient(v_1(:,1)))*gradient(v_1(1,:)));

a_n = trapz(U(r).*Pn1.*sind(theta));
b_n = (-1/(n*(n + 1)))*trapz(U(theta).*Pn1.*sin(theta));

C_phi(n) = (n*(2*n - 1)/2*(n + 1))*K + (n*(2*n + 1)/4*(2*n + 3))*N...
    - (n/4)*N + ((2*n + 1)*(n - 2)/2*(n + 1))*a_n + (n*(2*n + 1)/2)*b_n;
C_psi(n) = (4*n^2 - 1)*(N/(2*(2*n - 1)) - N/(2*(2*n + 1)) - ((K + a_n)/(n + 1)) - b_n);
```

```
%%
% Once the previous code has iterated through 'n'
% (producing the matrices Kn(x,m) and Nn(x,m)) then...
x = r/R_0;
% for n = 1:
PHI_n = (1/x^(n+1))*(K(x,n+2) - C_phi(n)) - x^n*(K(x,1-n) - K(end,1-n));
PSI_n = (1/(2*(2*n + 3)))*...
    ((1/x^(n + 1))*N(x,n+3) - x^(n + 2)*(N(x,-n) - N(end,-n)))...
    + (1/(2*(2*n - 1)))*(x^n*(N(x,2-n) - N(end,2-n)) - x^(1-n)*(N(x,n+1) - C_psi(n)));
V_r = (1/R_0)*((gradient(PHI_n) + (n*(n + 1)/x)*PSI_n)*Pn1);
V_theta = (1/R_0)*(PHI_n/x + PSI_n/x + gradient(PSI_n))*Pn1;
PHI = PHI_n*Pn1;
PSI = E_eps*PSI_n*Pn1;
V = gradient(PHI) + gradient(PSI);


function [u_2theta0, u_2r0] = MicroStream(R_0,f)
% MICROSTREAMING: 2nd order
% Streaming function as defined by Wu and Du,
%
% Based on
% J. Wu and G. Du, 'Streaming Generated by a Bubble in an Ultrasound Field'
% JASA 1997, 101(4) 1899-1907
%
% Harriet Lea-Banks, January 2015

%% Defining parameters
global I d chi c_i vis_i rho_i c_0 vis_0 rho_0 obs_points

w = 2*pi*f; % Angular frequency
% lambda_o = c_0/f;            % Wavelength in water (m)
% lambda_i = c_i/f;            % Wavelength in air (m)
k_o = w/c_0; %(2*pi)/lambda_o; % Wavenumber in water
k_i = w/c_i; %(2*pi)/lambda_i; % Wavenumber in air

lambda = rho_i/rho_0;
v_i = vis_i/rho_i;             % Dynamic viscosity air (kg/ms)
v_o = vis_0/rho_0;             % Dynamic viscosity water (kg/ms)
B_i = sqrt(w/(2*v_i));         % 1/Inner boundary thickness (m)
B_o = sqrt(w/(2*v_o));         % 1/Outer boundary thickness (m)

u_0 = sqrt((I*2)/(rho_0*c_0)); % (0.036) 'Velocity amplitude of the sound source'
sigma = k_o/k_i;               % Shear stress
%r = 40*10^(-6); %R_0 + 2/B_o; % Distance from the bubble surface
alpha = (B_o*vis_0)/(B_i*vis_i);
g_o = (lambda - 1)/(1 + alpha); % -0.00469
g_i = alpha*(1 - lambda)/(1 + alpha); % 0.994

%% Streaming velocities outside the bubble
theta = 90[0:1:180];
for j = 1:length(theta)
    % Legendre polynomial of degree 2
    P2 = (3*cosd(theta(j))^2 - 1)/2;
    % Tangential velocity
    % n = 0 mode (pulsation)
    u_2theta0(j) = -((u_0^2)*chi*k_o*obs_points)/(4*lambda*sigma)...
        *(g_o*exp(-B_o*(obs_points-R_0))/(B_o*v_o))...
        *(cosd(B_o*(obs_points-R_0)) + sind((B_o)*(obs_points-R_0)))*sind(theta(j));
    % n = 1 mode (translation)
    u_2theta1(j) = ((9*u_0^2)/4)*((g_o*exp(-B_o*(obs_points-R_0))/(B_o*v_o))...
        *(cosd(B_o*(obs_points-R_0)) - sind(B_o*(obs_points-R_0)))...
        - (((g_i*rho_i)/vis_0) +
(g_o/v_o))*(R_0^2/obs_points))*cosd(theta(j))*sind(theta(j));

    % Radial velocity
    % n = 0 mode (pulsation)
    u_2r0(j) = (u_0^2*k_i*R_0^2*g_o*cosd(theta(j)))/(2*obs_points^2*B_o^2*v_o)...
        *(chi/(lambda*sigma))*(exp(-B_o*(obs_points-R_0))*cosd(B_o*(obs_points-R_0))-
1);
    % n = 1 mode (translation)
    u_2r1(j) = ((-9*u_0^2*R_0)/(2*obs_points^2))*((g_o/(B_o^2*v_o))*exp(-
B_o*(obs_points-R_0))...
        *sind(B_o*(obs_points-R_0)) + (((g_i*rho_i*R_0)/vis_0) + ((g_o*R_0)/v_o))*(R_0
- obs_points))*P2;
end
```